工學博士學位論文

Fabrication of three-dimensional reduced graphene oxide network for thermal energy storage/supercapacitor applications

3차원 환원된 그래핀 옥사이드 구조체의 제조 및 열에너지 저장/슈퍼캐패시터 응용

2016年 2月

서울大學校 大學院

化學生物工學部

李 忠 炫

Fabrication of three-dimensional reduced graphene oxide network for thermal energy storage/supercapacitor applications

by

Choonghyeon Lee

Submitted to the Graduate School of Seoul National University in Partial Fulfillment of the Requirements for the Degree of Doctor of Philosophy

February, 2016

Thesis Adviser: Jyongsik Jang

ABSTRACT

Graphene, the 2-dimensional carbon allotrope with one-atom-thick layer of carbon elements, has drawn a lot of intention since the breakthrough of the isolation of single graphene sheet in 2004. The graphene material possesses outstanding properties, *e.g.,* large specific surface area, mechanical stability, and superb thermal/electrical conductivity and so on. Especially, the large surface area and mechanical stability of graphene have triggered huge attention on preparation of three-dimensional (3D) architecture of graphene for various applications. Up to date, various synthetic pathways for preparing 3D graphene network have been developed. However, simple preparation of graphene in multi-dimensional scale with low-cost and environmental-friendly way still remains as a challenge.

This dissertation describes the two pathways in the preparation method of 3D reduced graphene oxide (RGO) network utilizing plasma reduction method and L-ascorbic acid (L-AA) reduction method. As a ‘plasma reduction method’, the 3D plasma-reduced GO (PRGO) structures with increased surface area are successfully fabricated using a rapid thermal exfoliation and deoxygenation process on graphene oxide (GO) film *via* atmospheric plasma reduction. This

reduction process do not require high thermal energy or toxic chemical agent previously used in traditional GO reduction methodology. In ‘L-AA reduction approach’, 3D graphene monoliths are spontaneously formed during the mild L-AA reduction of GO solution. The pore size and the density of the graphene monolith can be easily controlled by adjusting the concentration of initial GO solution used. By using L-AA as an environmental-friendly reducing agent, cylinder-like graphene monoliths are easily prepared. The novel approaches can be used as an alternate methodology for fabrication of 3D RGO network with rational design and controlled physical properties. In this research, the 3D PRGO films and 3D graphene monolith materials were utilized as active materials for supercapacitor electrode and foothold of phase change materials (PCMs) for latent heat storage. The novel methods presented here might allow application of multi-dimensional graphene architecture in chemical/biological sensor, active material for secondary ion batteries and so on.

KEYWORDS: Carbon nanomaterials; Graphene; Multi-dimensional; Plasma reduction; L-ascorbic acid; Supercapacitor electrode; phase change materials

STUDENT NUMBER: 2011–22930

List of Abbreviations

2D : 2-dimensional

3D : 3-dimensional

AAO : anodic aluminum oxide

BET : Brunauer–Emmett–Teller

CMG : chemically modified graphene

CND : carbon nanodots

CNFs : carbon nanofibers

CV : cyclic voltammetry

CVD : chemical vapor deposition

DSC : differential scanning calorimetry

EA : elemental analysis

EDLC : electric double layer capacitance

EG : epitaxial graphene

FT-IR : Fourier transform infrared

GO : graphene oxide

ITO : indium tin oxide

L-AA : L-ascorbic acid

LIB : lithium-ion battery

PCM : phase change material

PCNFs : platelet carbon nanofibers

PDMS : poly(dimethylsiloxane)

PMMA : poly(methylene methacrylate)

PRGO : plasma-reduced GO

pRGO : partially reduced GO

RGO : reduced graphene oxide

SEM : scanning electron microscopy

SiC : silicon carbide

TEM : transmission electron microscopy

TGA : thermogravimetric analysis

UHV : ultrahigh vacuum

UV-Vis : ultraviolet-visible spectroscopy

VDP : vapor deposition polymerization

XPS : X-ray photoelectron spectroscopy

XRD : X-ray diffraction

List of Figures

List of Tables

Table of Contents

1. INTRODUCTION

1.1. Background

1.1.1. Properties of graphene

Among the various carbon nanomaterials, including carbon nanotube (CNT), carbon nanodots (CND) (Figure 1) [1-3], graphene, the carbon allotrope composed of a one-atom-thick planar sheet of carbon elements, has been regarded as a 'next-generation' material for its outstanding properties. Since the isolation of single graphene sheet by Geim and Novoselov in 2004 [4], the graphene material has been thoroughly studied and following properties were found: graphene is composed of sp^2 carbon atoms which are organized in hexagonal honeycomb lattice structure and possess superb characteristics, such as high electron mobility (with experimentally reported values in excess of 15,000 $cm^2 V^{-1} s^{-1}$ [5], high modulus, large thermal/electric conductivity and tremendous specific surface area and *etc*. The crystalline graphene can be a semi-metal or zerogap semiconductor which can be used in electronic devices. The increased attention in graphene is primarily due to a host of superb characteristics that have been mentioned above.

Successful preparation of high-quality graphene with controlled scale still remains as a challenge toward practical application of graphene. Therefore, researchers have utilized versatile methods to synthesize single layer of

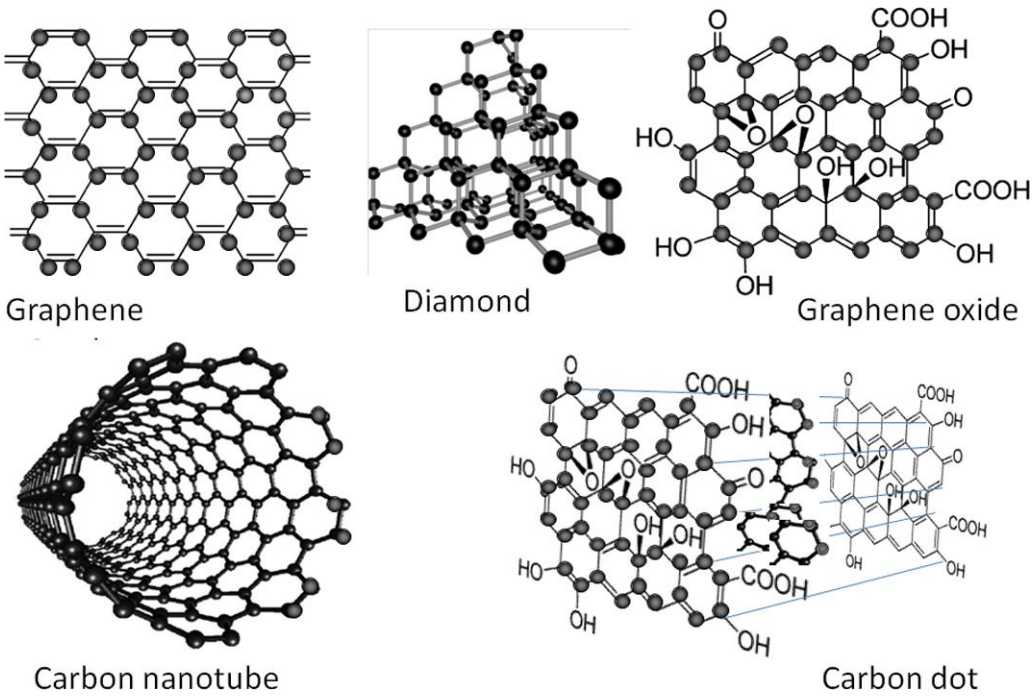

Figure 1. Structures of various carbon materials: Diamond, carbon nanotube (CNT), carbon dot, graphene and graphene oxide. Reprinted with permission from ref 3. Copyright 2012 Elsevier.

graphene (Figure 2) [6]. Synthesis methods can be classified into micromechanical exfoliation, epitaxial growth using SiC surfaces (along with chemical vapor deposition (CVD)) and liquid-phase exfoliation. Each pathway has its own advantages and disadvantages, and can be choosed according to following criteria: cost, scalability, purpose and *etc*. At first, production of single or few-layer graphene in experimental scale has been achieved by micromechanical exfoliation of highly oriented pyrolytic graphite [4]. This method is also known as 'scotch-tape method' or repeated peeling of graphite, since the methodology involves repeated steps of peeling graphene layers off of highly oriented pyrolytic graphite with adhesive tape, and subsequent pressing of the tape onto suitable substrate [7]. This method enabled researchers to investigate the single-layer morphology of graphene [8-9]. However, large-scale production of graphene is not archievable and the high-quality graphene layer can only be prepared with trial-and-error peeling process.

Epitaxial graphene (EG) growth on silicon carbide (SiC) surfaces is a useful bottom-up approach to be applied in nanoelectronics and it has been demonstrated on various metallic substrates [10]. The EG growth can be defined as a large-area growth of single graphene layer on SiC wafer by high temperature (in the range of 1200–1600 ℃) evaporation of silicon (Si) in ultra-

high vacuum (UHV) [10-13]. Si atoms on the wafer surface sublimate at high temperature and the exposed carbon atoms reconstruct to form hexagonal sp^2 carbon structure. EG has been reported to be grown on both the carbon-terminated and Si-terminated surfaces, though films grow much faster on the carbon face [14]. This method enables preparation of wafer-sized large graphene with carrier mobility values of *ca.* 2000 $cm^2 V^{-1} s^{-1}$ [15]. However, preparation of SiC wafer and experimental set-up of high-temperature furnace for Si sublimation are needed.

And also, Chemical vapor deposition (CVD) growth of graphene onto metal substrate has been applied as a means of producing large-area high-quality graphene [16]. Large-area graphene films with minute structural defects and decreased inter-sheet junction contact resistance can be prepared by deposition and pyrolysis of hydrocarbon-containing precursors like methane (CH_4) [17-19]. Furthermore, the CVD method can realize fabrication of template-mediated multi-dimensional graphene architecture by using commercial nickel or copper foam. Nonetheless, the CVD method requires furnace set-up, relatively expensive metal substrates/templates and additional substrate to be transferred upon, such as Poly(dimethylsiloxane) (PDMS) or Poly(methyl methacrylate) (PMMA) sheets.

Additionally, exfoliation of graphite into few-layer graphene sheets in

liquid-phase has been archived by bath-sonication of graphite powder in N-methylpyrrolidone (NMP) [20]. Nonetheless, the yield of graphene sheets is relatively low compared with the methods described above.

Since the methods mentioned here requires complex experimental set-up and relatively low amount of graphene material is produced, the researchers have came up with mass-production of graphene varieties: preparation of graphite oxide and subsequent exfoliation into few-layered graphene oxide (GO). After production of GO, the GO can be reduced to reduced graphene oxide (RGO) by diverse reduction methods. The details of preparation of GO and RGO are described in the next section.

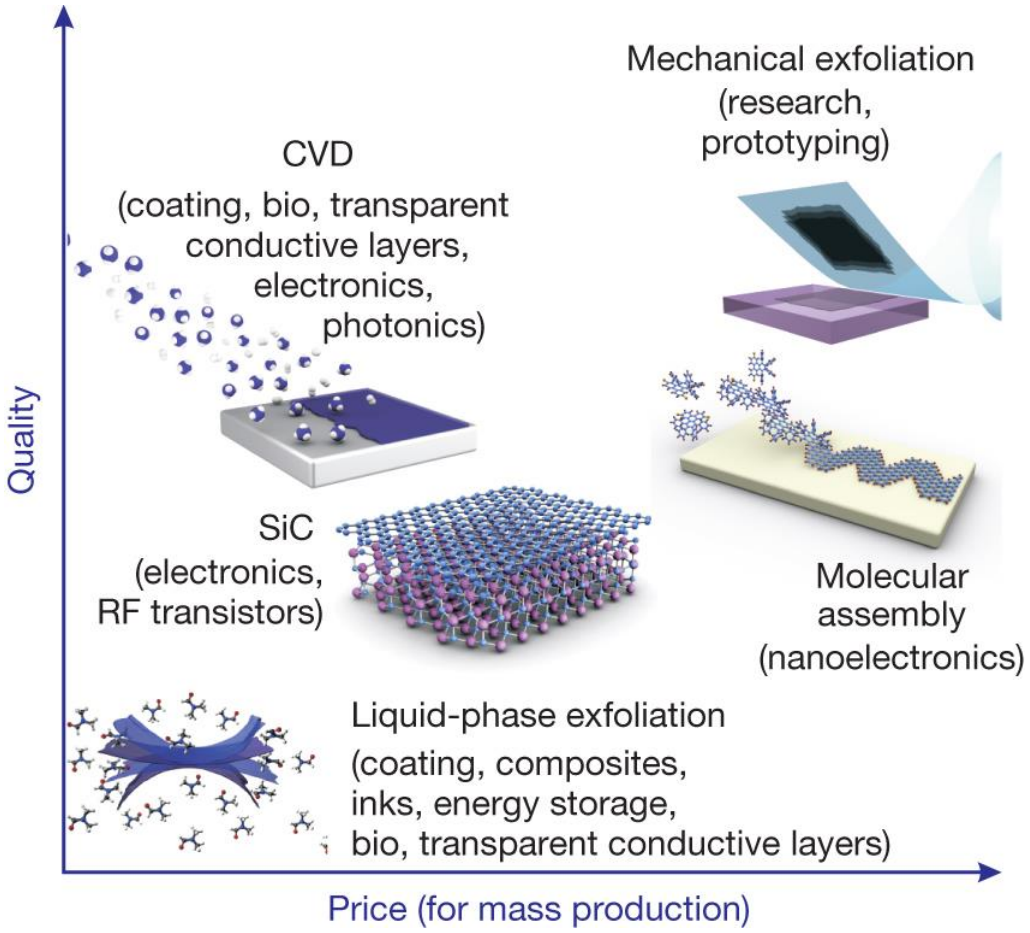

Figure 2. The synthesis method of graphene by various methodologies. Reprinted with permission from Ref 6. Copyright 2012 Right Managed by Nature Publishing Group.

1.1.2. Synthesis of reduced graphene oxide (RGO) from graphene oxide (GO)

The graphene synthesis methodologies described in section 1.1.1 have enabled researchers to produce high-quality graphene sheets or films in lab-scale quantity. However, due to several shortcomings of production of graphene, a 'Top-down approach' has been alternatively used: chemical exfoliation of graphite flake in acidic media to produce graphitic oxide [21]. In this method, chemical reagents, such as potassium permanganate, are inserted between the graphene layers of bulk graphite to reduce the van der Waals force [22]. Among various graphite oxidation methods [21,23-24], a modified version of Hummers' method has been extensively used to prepare graphite oxide for its fast reation time and less toxic solution condition. After successful reaction, the d-spacing value of inter-layer rises from 3.4 ~ 3.5 Å in graphite to above 6 Å, possibly due to formation of oxygen-related groups and diminished van der Waals force between the layers. Finally, single or few layers of graphene oxide (GO) can be obtained after bath sonication and the resultant GO can be readily dispersed in polar solvents (usually water) to produce stable colloidal dispersion.

Since GO sheets possess several defects in C-C hexagonal lattice and are functionalized with various oxygen-related groups, such as epoxy, carbonyl

(C=O), hydroxyl (-OH) and carboxyl (-COOH) groups, the material is intrinsically insulating. Therefore, many methods which involves removal of oxygen from the GO surface and restoration of graphitic honeycomb lattice have been developed to prepare reduced graphene oxide (RGO), or sometimes defined as chemically modified graphene (CMG). These reduction methods described below are promising routes to accomplish mass-production of graphene in experimental/industrial scale.

1.1.2.1. Chemical reduction

Preparation of RGO or CMG by chemical reduction method involves reaction of the chemical reagents with GO. The chemical agents react with GO to annihilate functional groups and repair the structural defect on GO plane. The usual chemical reduction occurs in relatively moderate annealing condition. Therefore, this method offers a promising way of producing RGO in less-expensive and large-scale aspect, compared with other RGO synthesis pathway (Table 1) [25]. Chemical reduction of GO with hydrazine has been extensively used by graphene researchers after Stankovich *et al.*'s work [26]. The relatives of hydrazine, such as phenylhydrazine [27], also work as a good reducing agent to produce high-quality RGO and the highest C/O ratio after hydrazine reduction was reported to be around 12.5 with electric conductivity of ~ 100

S/cm. Metal hydrides, e.g. $LiAlH_4$ or $NaBH_4$, also work as strong reducing agents [28-29]. However, the metal hydrides reacts vigorously with water, the typical solvent for GO dispersion, and causes safety issues. Hydriodic acid (HI) also act as a very strong reducing agent and is reported to produce RGO with C/O ratio exceeding 15 [30-32]. The strong advantage of HI as a reducing agent is that high-quality RGO can be prepared even in room temperature, regardless of target GO structure (powder, film and etc). These strong reducing agents overall produce high-quality RGO with gram-scale, but the respective reagents are often classified as ‘harmful’, ‘toxic’ or ‘corrosive’ materials, with toxic side products to be washed away.

Besides of reagents above, hydroquinone [33], thiourea [34], various metal/acid mixtures [35-36], and L-gluthathione [37] can be used in reduction of GO to produce RGO. Strong alkali solutions, such as NaOH and KOH solution, are as well applied in RGO synthesis [38]. However these reagents are often classified as ‘weak’ or ‘mild’ reducing agents compared with hydrazine, HI and metal hydrides.

Table 1. Summarized reduction pathways of GO to RGO. Reprinted with permission from ref 25. Copyright 2011 Elsevier.

Table 1 – Comparison of the reducing effect of GO by different methods.

Ref. no.	Reduction method	Form	C/O ratio	σ (S/cm)
[56]	Hydrazine hydrate	Powder	10.3	2
[69]	Hydrazine reduction in colloid state	Film	NA[b]	72
[70]	150 mM $NaBH_4$ solution, 2 h	TCF	8.6	0.045
[71]	Hydrazine vapor	Film	~8.8	NG
	Thermal annealing at 900 °C, UHV[a]		~14.1	NG
[55]	Thermal annealing at 1100 °C, UHV	TCF	NA	$\sim 10^3$
[72]	Thermal annealing at 1100 °C in Ar/H_2	TCF	NA	727
[42]	Multi-step treatment:	Powder	(I) 4.78	(I) 0.823
	(I) $NaBH_4$ solution		(II) 8.57	(II) 16.6
	(II) Concentrated H_2SO_4 180 °C, 12 h		(III) >246	(III) 202
	(III) Thermal annealing at 1100 °C in Ar/H_2			
[73]	Vitamin C	Film	12.5	77
	Hydrazine monohydrate		12.5	99.6
	Pyrogallol		NA	4.8
	KOH		NA	1.910^{-3}
[58]	55% HI reduction	Film	>14.9	298

[a] UHV: ultra high vacuum.
[b] NA: not available.

1.1.2.2. Plasma reduction

Compared with traditional chemical reduction method, the plasma-assisted reduction offer a novel advantage in the process condition. The plasma-assisted condition can be completed in low temperature (usually in room temperature) and the experiment proceeds in dry process, which insures the purity of graphene. When the GO materials, in powdery or film, is exposed to plasma, they will be subject to a flux of reactive species working on the surface [39]. The species in plasma flux, including ions (Ar^+, H^+, $C_xH_y^+$), radicals (H•, CH_n•) and neutrals, are dependent on the operating parameters such as flow rate or plasma power. This reactive flux reacts with oxygen-related groups on the suface to create volatile gases, such as CO and CO_2, thus removing the oxygen groups on the GO surface. Ion bombardment on the GO surface also causes rapid thermal exfoliation/deoxygenation process to produce RGO from GO *via* microwave plasma [40]. However, traditional plasma-assisted reduction requires high vacuum condition for fine-quality treatment on GO and substrate or support on GO film is needed. Therefore, the plasma set-up in atmospheric condiction has been realized for simpler reduction step without vacuum process (Figure 3) [41].

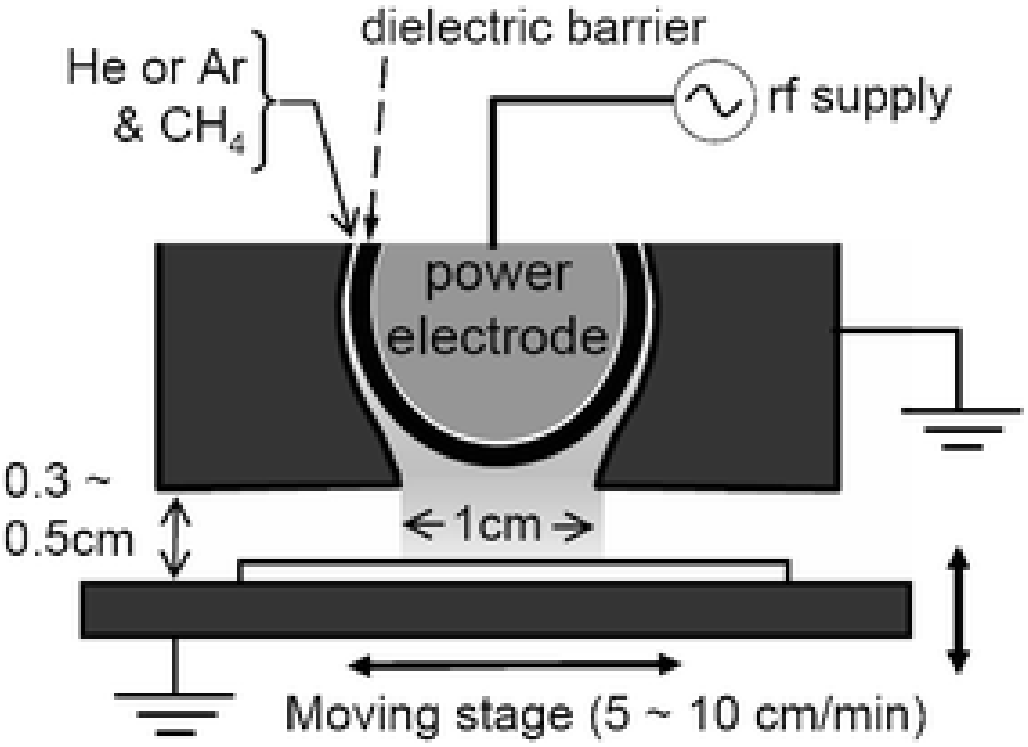

Figure 3. Atmospheric plasma apparatus set-up. Reprinted with permission from Ref 42. Copyright 2006 Right Managed by Royal Society of Chemistry.

1.1.2.3. Mild reduction *via* L-ascorbic acid (L-AA)

The reduction methods described in section 1.1.2.1 involves utilization of strong, toxic reducing agents. Therefore, environmental-friendly reduction of GO has been investigated. L-ascorbic acid (L-AA), also known as Vitamin C, can be applied as a mild reducing agent [43]. The Figure 4 describes the proposed reduction mechanism of GO via L-AA reduction. As L-AA with two hydroxyl groups interact with epoxide and hydroxyl groups on C-C hexagonal rings, the oxygen and hydrogen atoms are annihilated in the form of water. Then the L-AA/ring composition breaks and L-AA is detached in the form of dehydroascorbic acid with two carbonyl groups. As can be seen from the proposed mechanism, the L-AA reduction produce side products only composed of C and O, with no hetero-atom produced [44]. In the Figure 5, the graphene hydrogel made from L-AA resembles the shape of the reactor used, and this phenomenon indicates possible morphology manipulation of 3D graphene gel by adjusting the shape of the reactor [45]. Li *et al.* also found that a mult-step process of 1) L-AA reduction, 2) freezing, 3) thawing and 4) subsequent freeze-drying (also known as lyophilization) resulted in production of 3D RGO monolith [46]. The highest C/O ratio and electric conductivity of L-AA reduced GO were 12.5 and 77 S/cm, respectively [43]. These values are comparable with the values of hydrazine-reduced GO in section 1.1.2.1.

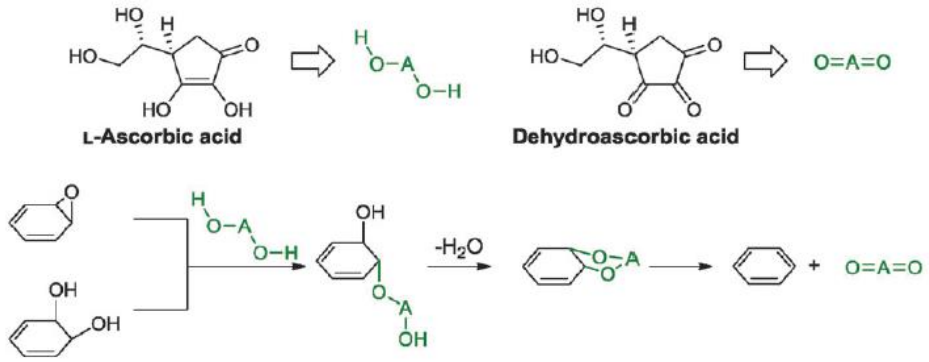

Figure 4. Proposed reduction mechanism of mild reduction via L-AA. Reprinted with permission from Ref 44. Copyright 2013 Right Managed by Royal Society of Chemistry.

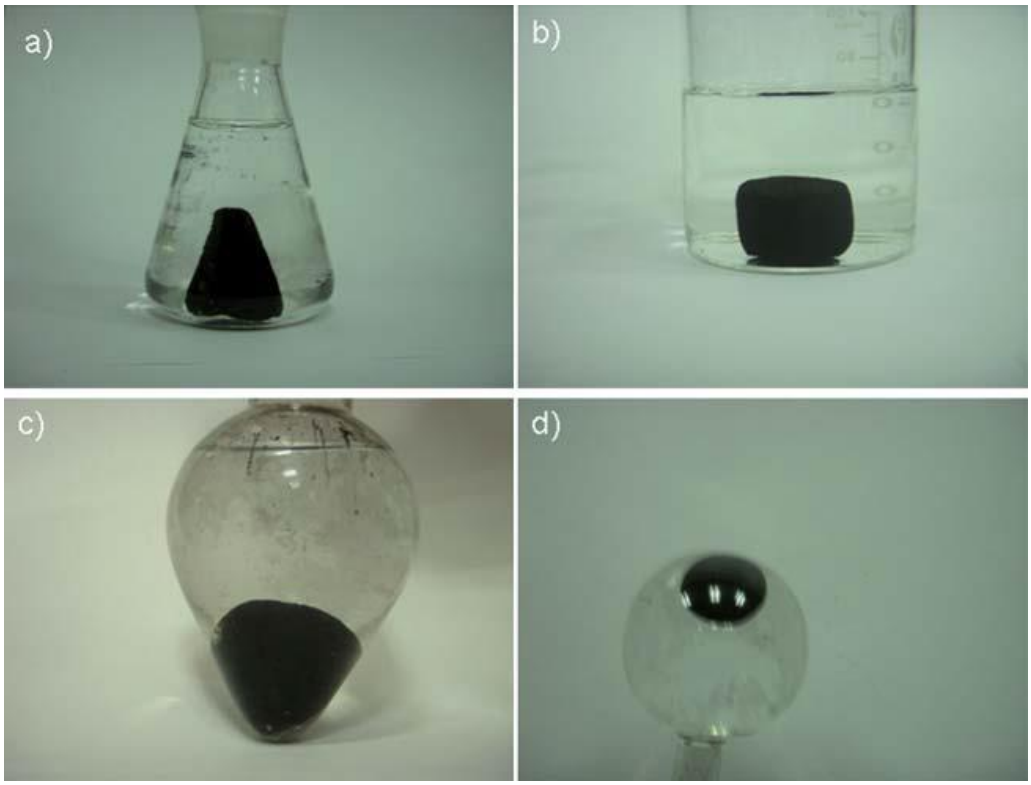

Figure 5. Digital photograph of RGO gel. The shape of the RGO gel depend on the shape of the reactor. Reprinted with permission from Ref. [45]. Copyright 2011 Right Managed by Royal Society of Chemistry.

1.1.2.4. Other reduction methods

Thermal annealing of GO in inert condition to produce RGO has been exploited as a mean of synthesizing high-quality RGO. Using argon (Ar) or nitrogen (N_2) as inert gas, the GO is heated in closed furnace up to 1100 ^oC for complete carbonization [47]. Additionally, using hydrogen (H_2) as reaction gas, GO materials are heated up to 2800 ^oC for graphitization of GO to graphene. The graphitized graphene shows high thermal conductivity of 1100 W/m•K, due to complete annihilation of oxygen-functional groups on basal plane and restoration of sp^2 C-C structure [48]. Zhu *et al.* reported that application of microwave to GO powder resulted in sudden reduction of GO to RGO with expanded structure [49].

Electrochemical reduction utilizes electrochemical force to remove oxygen-related functional groups on GO produce RGO. A previous work has shown that CMG can be functionalized with metal nanoparticles by electrodeposition process [50], direct application of electrochemistry in modifying the structure of GO or graphene has recently been realized [51] In electrochemical reduction, toxic reducdants like hydrazine are not required and harmful byproducts are not generated. In typical electrochemical reduction process, the GO film deposited on various substrates, including indium tin oxide (ITO), polymer, glass and *etc*, is used and the electrodes are positioned at opposite sides of the

GO film. Then linear sweep voltammetry proceedes in a buffer solution to produce RGO film in 300 s [52].

1.1.3. Preparation of 3-dimensional RGO framework

Although many outstanding performances of graphene material, such as ballistic electron transport, superior electric conductivity, come from its 2-dimensional planar nature, the need for preparation of multi-dimensional graphene structure has increased recently for its potential use in other fields. Since the graphene, or RGO, possess increased specific surface area, enhanced electric conductivity and strong mechanical properties compared with traditional building blocks for 3D structure, researchers have indulged in preparation of 3D graphene architecture for biological, energy applications and *etc*.

Synthesis method of 3D RGO network can be classified as follows: CVD on active-metal template, freeze-drying, solvothermal reduction, 3D printing and *etc* (Methods summarized in Table 2) [53]. At first, commercial nickel (Ni) or copper (Cu) foams are utilized as sacrificial artificial template to prepare 3D graphene foam. By using the reactive interface of 3D metallic substrate, graphitic foam is prepared after traditional CVD process utilizing hydrocarbons as graphene precursor [16, 54]. Although graphene foam possesses high electric/thermal conductivity and flexibility, the fabrication process requires sophisticated experimental set-up and high-cost metal foam. In the meantime, freeze-drying process, or sometimes called as freeze-casting and lyophilization,

utilizes volumetric expansion of ice in freezing of water to push away dispersed GO sheets. These re-organized GO sheets create porous GO network when all ice undergoes sublimation process at high vacuum/low temperature condition [55]. By adjusting the concentration of GO solution and varieties of dispersed solute, the porosity and mechanical properties of resultant network differentiates. Solvothermal reduction of GO to RGO also creates 3D network structure of RGO in experimental scale [56-58]. The solvothermal method utilizes the vapor pressure of vaporized organic solvents at the temperature higher than the boiling point of the corresponding solvent. This high vapor pressure inside the sealed container induces partly removes the oxygen-related groups on GO plane and also repairs the disoriented structure of GO, thus realizing reduction of GO. Using polar solvents like N,N-dimethylformamide (DMF), N-methylpyrrolidone (NMP) and water, the graphene network with C/O ratio reaching 14 can be prepared [25]. 3D printing, which allows precise control in architecture and mechanical properties of printed product, can also shine a light on preparation of 3D RGO network for various applications. Kim *et al.* found that controlled extrusion of GO solution through micropipette produced free-standing GO nanowire without supporting material and the GO nanowire was facily reduced with hydrazine treatment [59]. Zhu *et al.* also reported that periodic microlattices of RGO can be fabricated by direct GO ink

writing on isooctane and subsequent supercritical (SC) drying [60]. The storage and loss modulus of resultant microlattices were changed according to the concentration of GO ink and added amount of silica. Nonetheless, the methods described here usually require unique apparatus, e.g. sealed container or 3D printer, and are tedious processes.

Table 2. Preparation of 3-dimensional graphene network. Reproduced with permission from Ref 53. Published by The Royal Society of Chemistry.

Table 1 Comparison of various structures of 3D graphene materials with their preparation methods, properties and applications

Structures	Synthetic methods	Properties	Applications	Ref.
3D graphene networks	CVD using $NiCl_2 \cdot 6H_2O$ as catalyst precursor	Surface area: ~560 $m^2 g^{-1}$, electrical conductivity: ~12 S cm^{-1}	Absorbent	38
	CVD based on Ni foam template	Surface area: ~850 $m^2 g^{-1}$, electrical conductivity: 10 S cm^{-1}, tensile strain: ~95%		37
	Self-assembly of GO sheets induced by hydrothermal reaction	Electrical conductivity: ~0.0025 S cm^{-1}, compressive strength: ~0.042 MPa, compression modulus: ~0.26 MPa	Catalysis	74
Graphene fibers	Wet-spinning	Surface area: ~884 $m^2 g^{-1}$, electrical conductivity: 2600–4900 S cm^{-1}, specific tensile strength: 188 kN m kg^{-1}, compression modulus: 3.3 MPa	Conductive wire	166
	Wet-spinning	Electrical conductivity: 8–10 S cm^{-1}, tensile strength: 140–150 MPa	Micro-pump	168
	Wet-spinning	Electrical conductivity: ~35 S cm^{-1}, tensile strength: ~182 MPa, Young's modulus: 8.7 GPa	Conductive wire	164
Graphene tubes	Hydrothermal using Cu wire as template	Electrical conductivity: 10 S cm^{-1}, tensile strength: ~180 MPa	Self-powered micromotor	173
	CVD using AAO as template	Electrical conductivity: 950 S m^{-1}, thermal conductivity: 8.28 W m^{-1} K^{-1}	Heat transfer and thermal energy storage	83
3D porous graphene films	Leavening strategy	Sheet resistance: <100 Ω sq^{-1}, tensile strength: ~3.2 MPa	Supercapacitor	45
	Assembly of chemically modified graphene using PS particles as template	Surface area: 194.2 $m^2 g^{-1}$, electrical conductivity: 1024 S cm^{-1}	Supercapacitor	100
Graphene balls	Aerosol-assisted capillary compression process	Surface area: 82 $m^2 g^{-1}$, compression strength: >55 MPa	Microbial fuel cell	177
	CVD using PS ball as template	Surface area: 508 $m^2 g^{-1}$, electrical conductivity: 6.5 S m^{-1}	Supercapacitor	44
Honeycomb-like 3D graphenes	Freeze-casting	Electrical conductivity: ~0.12 S m^{-1}, compression strength: ~8 kPa (plateau state), 18 kPa (80% strain), for sample with density of 5.1 mg cm^{-3}		184
	Self-assembly	Electrical conductivity: 649 S m^{-1}	Supercapacitor	197

1.1.4. Application fields

By using various synthetic method described in previous section, 3D RGO network has been utilized in various application. Since the RGO itself is highly conductive and possess large surface area due to micro-pores present in graphene surface, the 3D RGO network are often exploited as active materials in electrodes of energy devices like lithium-ion battery (LIB) and supercapacitor. And also the carbonaceous surface of RGO work as a support for various heterogeneous materials, ranging from inorganic, organic to metallic materials. 3D RGO network is readily fuuctionalized with silica, conducting polymer or novel metal like palladium (Pd) and platinum (Pt) and the resultant composites are endowed with new physicochemical properties. As described below, the composites are used as hybrid supercapacitors with synergistic effect of pseudo-capacitance and electric double layer capacitance, and are utilized as enzymatic sensor or catalyst materials. When biological receptor or DNA are functionalized, the 3D RGO network play a role as a scaffold for cell differentiation. Superior thermal/chemical stabilities and electric/thermal conductivities of 3D RGO network are applied in encapsulation of phase change materials (PCMs) for further industrial applications.

1.1.4.1. Biological application

The controlled fabrication of bio-compatible scaffold for tissue engineering and bio-catalysis has been thoroughly investigated by many researchers. Among the host of materials, carbon-based materials have been extensively used due to their superior physical properties and flexibility in architecture design. For instance, carbon fiber-based scaffold prepared by combined method of electrospinning and freeze-drying was used as an artificial graft for bone growth [61]. Along with other carbon materials, graphene and its varieties have been used to prepare 3D network due to bio-compatibility, ease in surface modification and mechanical stability. By using metal foam as a hard template for 3D graphene network, osteogenic differentiation using human mesenchymal stem cell [62] and detection of Parkinson's disease [63] were investigated. Instead of using expensive CVD-graphene foam, GO-derived hydrogels work as a graphene scaffold for bio-appication. Hou *et al.* demonstrated that immersion of graphene hydrogel into a N,N-dimethylacrylamide (DMAA)-based solution and subsequent polymerization resulted in cross-linked hydrogel of graphene surface and PDMAA polymer. (Figure 6) [64]. This graphene-polymer hydrogel was further treated with near-infrared (NIR) laser and self-healing behavior of the hydrogel was observed. This self-healing material can be applied as an artificial tissue in human body.

Chen *et al.* also found that Fe_2O_3-impregnated RGO hydrogel exhibit large surface area and magnetic property, which are suitable for biocatalytic transformation of glycyrrhizin [65]. Overall, utilizing GO-derived hydrogel offers a novel route to incorporate various bio-compatible additives for specific bio-applications.

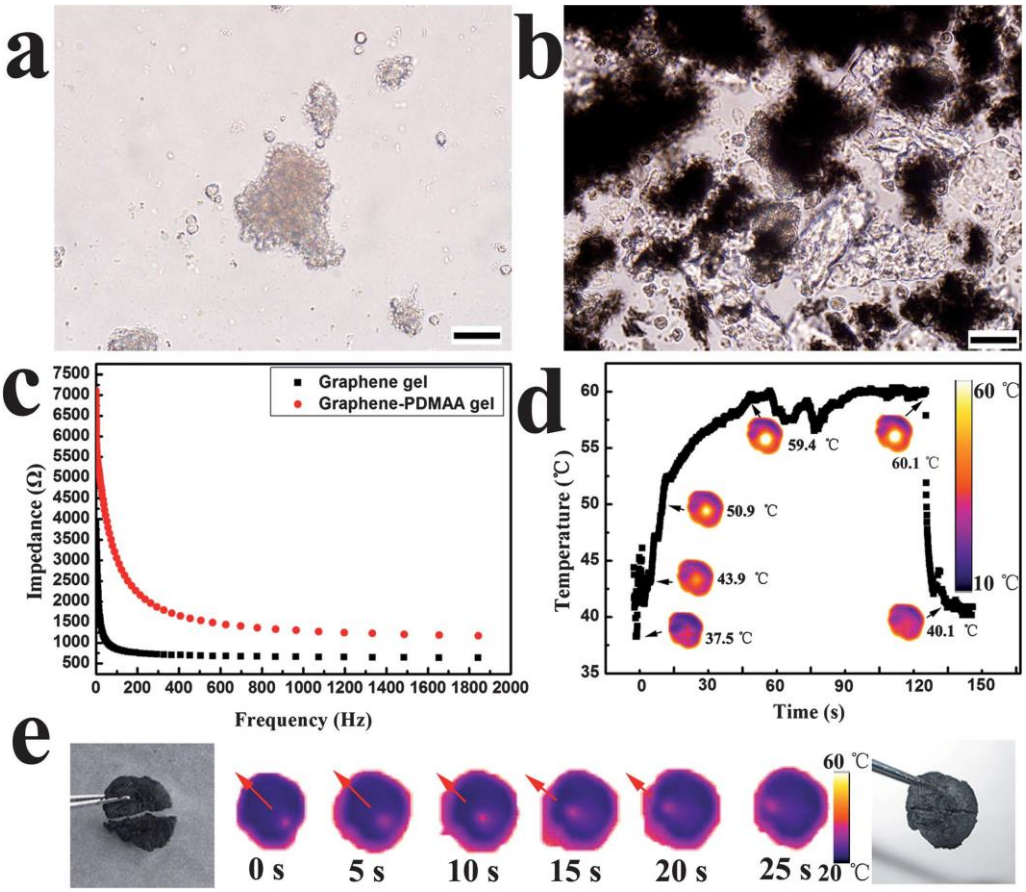

Figure 6. Self-healing of graphene–PDMAA gels under NIR laser irradiation and their infrared thermal images. Reproduced with permission from Ref 65. Copyright 2012, Royal Society of Chemistry.

1.1.4.2. Supercapacitor

Supercapacitors, comprising of pseudo-capacitor and electric double-layer capacitor (EDLC), are a class of energy storage devices which exhibit large power density and energy density simultaneously (Figure 7). Carbon-based EDLCs demonstrate several advantages, such as low-cost, high energy density and intrinsic robust nature [66-70]. Among the carbon nanomaterials used for EDLC electrodes, such as CNT, activated carbon, carbon nanofiber (CNF) and mesoporous carbon, graphene has emerged as an alternative due to intrinsically high specific surface area, large flexibility, high electric conductivity and outstanding mechanical stability. These excellent properties of graphene make it suitable for application in supercapacitor electrode. Multi-dimensional graphene structure is also appreciated, due to increased surface area for efficient electrolyte diffusion. Furthermore, replacing graphene to RGO has attracted researchers for cost-effectiveness and facile scalability of RGO for industrial application.

Lee *et al.* proposed preparation of metal-oxide nanofiber coated RGO network by freeze-drying and thermal reduction methodologies [71]. By dispersing metal-oxide nanofibers in GO solution and subsequent freeze-drying, 3D GO network with well-decorated metal-oxide nanofiber was prepared and additionally reduced. The final nanostructure exhibited high specific

capacitance of 446 F/g due to hybridization of pseudo-capacitance of metal-oxide nanofiber and EDLC capacitance of RGO. Wu *et al.* took a different approach of producing 3D RGO network by mixing of ammonia boron trifluoride (NH_3BF_3) with GO solution prior to hydrothermal reduction [72]. Nitrogen and boron element in NH_3BF_3 play a role as a dopant on RGO network, thus increasing charge transfer between original carbon atoms and doped nitrogen/boron atoms. This nitrogen/boron doped 3D RGO network was applied as a solid-state supercapacitor with polyvinyl alcohol (PVA)/sulfuric acid electrolyte, showing specific capacitance of 26.2 F/g. Chen *et al.* added organic amine or ammonia in GO solution and subsequent hydrothermal reduction of the corresponding solution for 12 h at 180 ^oC [73]. The resultant hydrogel electrode exhibited high power density of 205 kW/kg and specific capacitance of 113.8 F/g. At last, 3D porous MnO_2/RGO composite film prepared by RGO coating on polystyrene (PS) microsphere template and MnO_2 deposition also worked as a supercapacitor electrode due to large surface area of initial PS template [74].

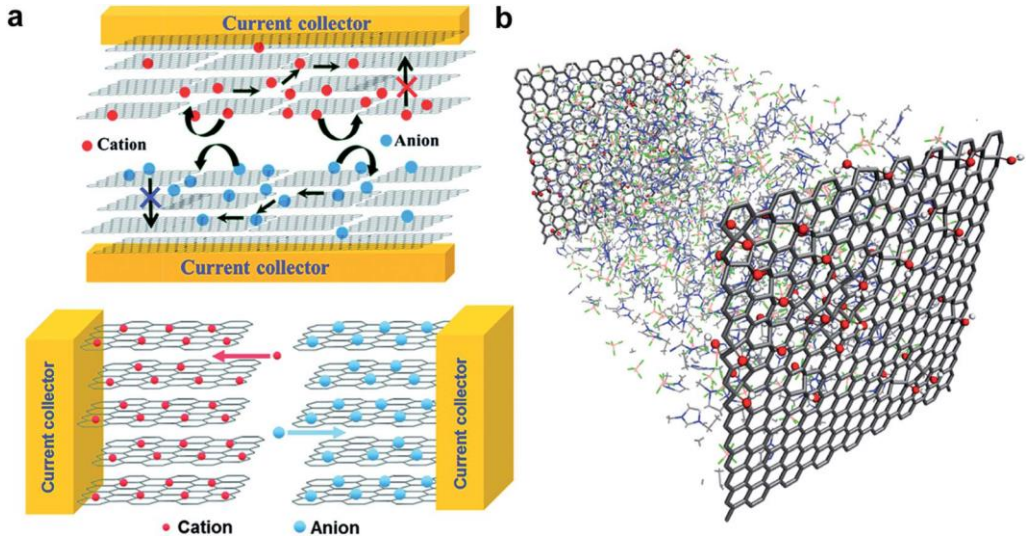

Figure 7. Preparation of supercapacitor: supercapacitor mechanism. Reproduced from Ref 66. with permission from the Royal Society of Chemistry.

1.1.4.3. Sensor

Due to increase in specific surface area and surface reactivity, preparation of novel material in nano-regime and its sensor application has always been a primary interest among nanomaterial researchers. Advent of graphene era has aroused a huge attention toward the fabrication of graphene-based sensors for chemical/biological detection for superior electric conductivity, large specific surface area of graphene itself [75-77]. Besides graphene, GO and RGO-based sensors are also thoroughly investigated, due to facile immobilization of enzyme, active metal nanomaterials or other bio-receptor molecules on functional groups of GO or RGO. The previous studies have shown that the preparation of 3D architecture also presents increased sensing performance [78]. 3D RGO network has also been applied in strain sensor application, where intrinsically robust nature and high electric conductivity of graphene have been exploited.

For example, 3D RGO micropillar structure on PDMS template was fabricated and tyrosinase enzyme was immobilized on the RGO surface to be utilized as a phenol detection sensor [79]. To obtain 3D structure of RGO, PDMS micropillars were prepared by photolithography technique and negative GO sheets were adsorbed on positively functionalized PDMS, followed by chemical reduction. Using this method, target phenol molecules were detected

in detection limit of 50 nM. Similar form of RGO micropillar arrays were prepared by Penmatsa *et al.* and hydrogen peroxide (H_2O_2) was detected with this fine-coated RGO micropillar structure [80]. Penmatsa *et al.* used electrostatic spray deposition method to obtain fine RGO coating on micropillar array. On the other hand, Liu *et al.* employed inorganic nanoparticles for efficient detection of nitrogen dioxide (NO_2) [81]. Utilizing $SnCl_4$ as a tin oxide precursor and GO as a RGO precursor, the $SnCl_4$/GO solution undergoes hydrothermal reduction for 10 h at 200 ^oC to synthesize SnO_2/RGO aerogel. The SnO_2/RGO aerogel selectively respond to 50 ppm NO_2 gas due to unique electron transfer from the aerogel to NO_2 gas to form NO gas.

The 3D RGO gel can be used in detection of bio-molecules, such as glucose. Yuan *et al.* reported preparation of bimetallic PdCu nanoparticle on RGO hydrogel to detect glucose without addition of enzyme on the surface [82]. Using mild hydrothermal reduction of Pd/Cu precursor/GO solution, as-prepared PdCu/RGO hydrogel can detect glucose molecules at the detection limit of 20 μM in the presene of chloride ions.

Additionally, a hierarchically structured RGO foam fabricated from freeze-drying of GO suspension and subsequent thermal treatment (Figure 8) [83]. Since the material possesses macroporous honeycomb-like structure and

exhibits superior compression recovery, it was utilized as a strain-gauge sensor. As compressive strain applied on the RGO foam, the electrical resistance of the material showed linear change behavior along with fast response time. The preparation of RGO foam illuminates a promising route in preparation of real-time monitoring device for human health.

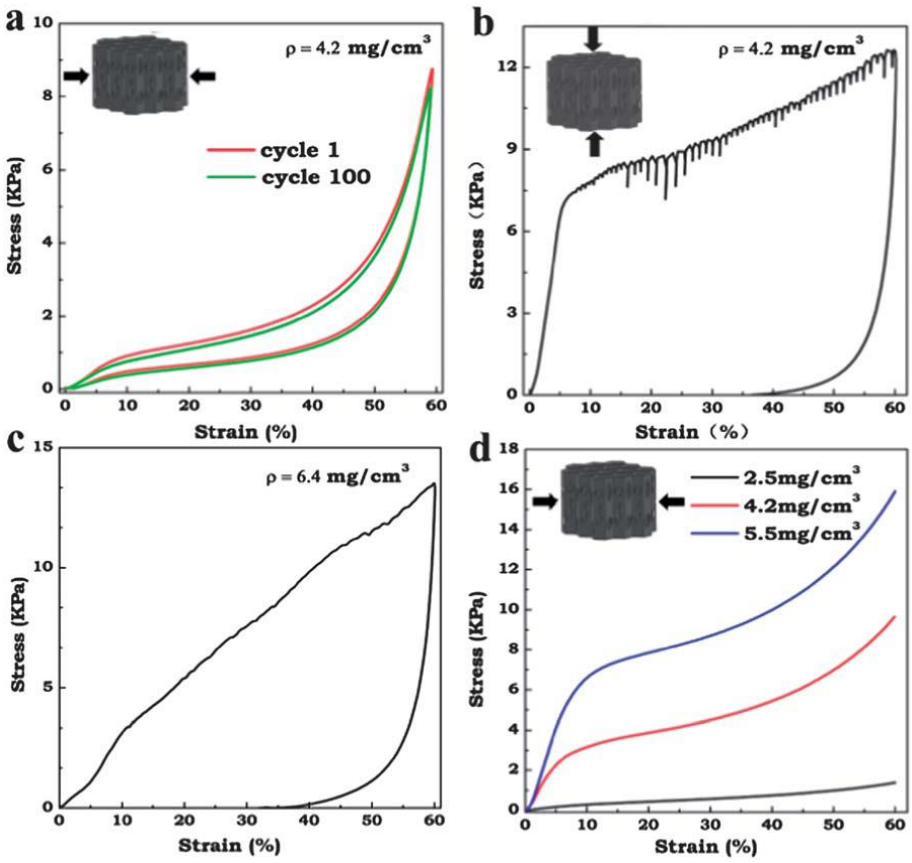

Figure 8. Typical compressive stress–strain curves of the ReG foam: a) in-plane direction and b) out-of-plane direction. c) A typical compressive stress–strain curve of the graphene foam prepared by the hydrothermal method. d) Stress– strain curves of the ReG foams with different density values along the in-plane direction. Reproduced from Ref 83 with permission from the Royal Society of Chemistry.

1.1.4.4. Latent heat storage

Thermal energy control in nano-electronics and industrial plant has been regarded as a critical issue. And also, utilization of surplus solar energy and storage of solar energy as thermal energy have been investigated, due to vast amount of solar energy projected by the sun [84]. Phase change materials (PCMs) are a class of materials that display different physicochemical properties when the ‘phase’ of corresponding material change from one to another [85]. These PCMs undergoes structural change in phase transition, and are applied in fields of non-volatile memory device [86], solar energy storage [87], controlled drug release [88] and *etc*. In case of thermal energy management, many organic materials like paraffin, fatty acid and eutectic mixtures are applied as PCMs due to large latent heat storage in solid-liquid phase transition (Figure 9 and 10). These organic PCMs exhibit a variety of thermophysical properties according to the number of carbon atoms or intrinsic chemical structure (Table 3 and 4). However, the organic PCMs tend to lose their stable shape when phase changes from solid to liquid, which is not appreciated in practical application. And the PCMs exhibit relatively low thermal/electric conductivities and these properties lower the thermal energy transfer rate.

Therefore, use of graphene in multi-dimensional structure can greatly

enhance the weak properties of current PCM used. Ye *et al.* reported preparation of RGO aerogel encapsulating paraffin [89]. The paraffin-encapsulated RGO aerogel was prepared by mixing of paraffin/cyclohexane solution and GO/water solution to obtain GO/paraffin emulsion. This emulsion was then reduced by hydrothermal method and resultant gel was lyophilized acquire paraffin/RGO aerogel. Since the paraffin PCM is directly 'embedded' in porous RGO aerogel structure, the shape-stability of paraffin is maintained during the latent heat storage process. Besides paraffin, fatty acids are a class of PCMs frequently used among researchers. Zhong *et al.* also synthesized RGO aerogel by hydrothermal reduction of GO solution, and molten octadecanoic acid was impregnated into the RGO aerogel by immersion technique [90]. The octadecanoic acid/RGO aerogel showed increased thermal conductivity of 2.635 W/mK at RGO loading fraction of 20 volume %, which is a 14 times value of pristine octadecanoic acid. Nonetheless, the results described above utilizes hydrothermal reduction which requires tightly sealed container and the RGO loading fraction should be very high for appreciable increase in thermal/electric conductivity values.

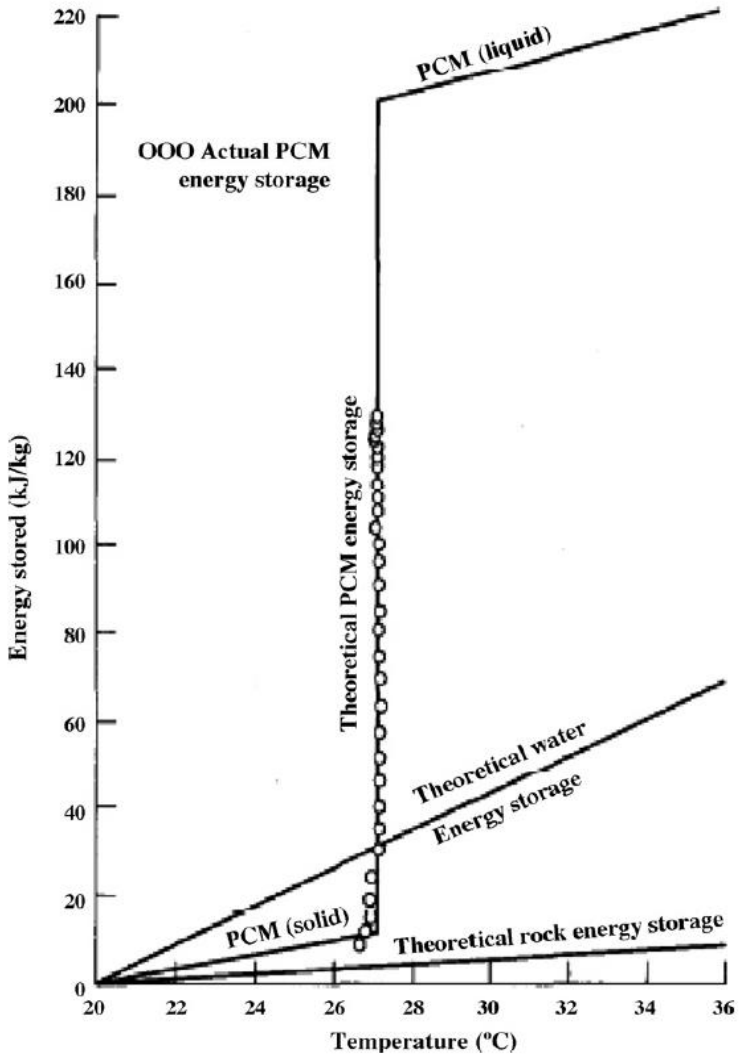

Figure 9. Performance comparison of PCM, water and rock storage system. Reprinted with permission from ref 85. Copyright 2007 Elsevier.

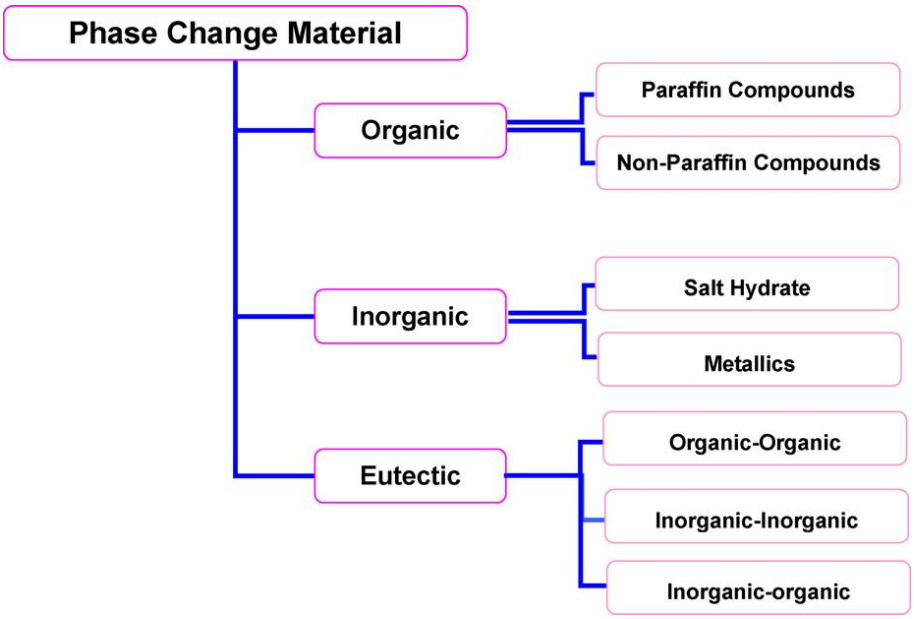

Figure 10. Categorization of phase change materials: Organic, inorganic and eutectic PCMs. Reprinted with permission from ref 85. Copyright 2007 Elsevier.

Table 3. Thermophysical parameters of paraffin according to number of carbon atoms in the paraffin structure. Reprinted with permission from ref 85. Copyright 2007 Elsevier.

Melting point and latent heat of fusion: paraffins

No. of carbon atoms	Melting point (°C)	Latent heat of fusion (kJ/kg)	Group[a]
14	5.5	228	I
15	10	205	II
16	16.7	237.1	I
17	21.7	213	II
18	28.0	244	I
19	32.0	222	II
20	36.7	246	I
21	40.2	200	II
22	44.0	249	II
23	47.5	232	II
24	50.6	255	II
25	49.4	238	II
26	56.3	256	II
27	58.8	236	II
28	61.6	253	II
29	63.4	240	II
30	65.4	251	II
31	68.0	242	II
32	69.5	170	II
33	73.9	268	II
34	75.9	269	II

[a] Group I, most promising; group II, promising; group III, less promising; — insufficient data.

Table 4. Thermophysical properties of non-paraffin organic PCMs. Reprinted with permission from ref 85. Copyright 2007 Elsevier.

Melting point and latent heat of fusion: non paraffins

Material	Melting point (°C)	Latent heat (kJ/kg)	Group[a]
Formic acid	7.8	247	III
Caprilic acid	16.3	149	–
Glycerin	17.9	198.7	III
D-Lattic acid	26	184	I
Methyl palmitate	29	205	II
Camphenilone	39	205	II
Docasyl bromide	40	201	II
Caprylone	40	259	II
Phenol	41	120	III
Heptadecanone	41	201	II
1-Cyclohexylooctadecane	41	218	II
4-Heptadacanone	41	197	II
p-Joluidine	43.3	167	–
Cyanamide	44	209	II
Methyl eicosanate	45	230	II
3-Heptadecanone	48	218	II
2-Heptadecanone	48	218	II
Hydrocinnamic acid	48.0	118	–
Cetyl alcohol	49.3	141	–
α-Nepthylamine	50.0	93	–
Camphene	50	238	III

1.2. Objectives and Outline of the Study

1.2.1. Objectives

In the previous section, the significance of 3D graphene network was introduced from the academic viewpoint and practical applications. The goal of this dissertation is to present two different synthetic methodologies to fabricate 3D reduced graphene oxide (RGO) networks in terms of 'plasma-reduction' and 'L-AA reduction'. Furthermore, the formation mechanism of the respective 3D RGO networks is systematically investigated, and their application fields are also presented: electrochemical energy storage application of the plasma-reduced GO film and latent heat storage application of the plasma-reduced GO film and L-AA-reduced graphene monolith as support material for organic PCMs.

1.2.2. Outline

This dissertation involves the following subtopics:

I. Preparation of 3-dimensional expanded RGO film *via* atmospheric plasma treatment on GO film
    1. Preparation of GO film *via* vacuum suction of GO solution
    2. Preparation of HRGO film *via* hydrazine-reduction
    3. Fabrication of 3-dimensional expanded RGO film *via* atmospheric

plasma

II. Fabrication of 3-dimensional RGO monolith *via* reduction of GO with L-ascorbic acid (L-AA)

1. Preparation of graphene oxide
2. Reduction of graphene oxide solution with L-AA

III. Applications

1. Fabrication of 3-dimensional, expanded RGO film as a free-standing supercapacitor electrode
2. Fabrication of free-standing 3D RGO film embedded with organic PCMs for latent heat storage
3. Fabrication of 3-dimensional graphene monolith with paraffin *via* L-AA reduction for PCM application

A detailed outline of the study is as follows:

1. As a ‘plasma-reduction’, the free-standing 3D expanded reduced graphene oxide (RGO) films are fabricated using a rapid thermal exfoliation and deoxygeneation process of graphene oxide (GO) thin film *via* brief atmospheric plasma treatment. To obtain 3D RGO structure, the GO thin film prepared from vacuum suction of GO solution is used as a starting material. The 3D RGO films are formed by brief atmospheric plasma

treatment on GO film, with sufficient argon flow. The electrons in the plasma glow reacts with oxygen-functional groups of GO surface and the sudden elimination of oxygen groups result in rapid reduction of GO. Due to formation of oxygen-related gases during thermal exfoliation, the RGO sheets are expanded outward to form 3D network of physically linked RGO sheets. In addition, the 3D RGO films can be formed without any toxic reducing agent and possess increased specific surface area.

2. As an ‘L-AA reduction’, 3D graphene monoliths are formed spontaneously during the mild L-ascorbic acid (L-AA) reduction of GO solution. Although the actual mechanism of formation of 3D graphene structure remains unknown, the spontaneous production of 3D graphene monolith by L-AA help reduce the additional step to convert 2D graphene sheets into 3D architecture. The pore size and density of the 3D graphene monoliths can be easily tuned by manipulating the concentration of GO solution. This new methodology can illuminate a great possibility for fabricating 3D graphene network material with controlled architecture.
3. The 3D expanded RGO film prepared from brief atmospheric plasma reduction is utilized as an active material for supercapacitor electrode. The utilization of carbon nanomaterials as electric double layer capacitor (EDLC) has attracted a great deal of interest because of the high surface

area and large electric conductivity of carbon nanomaterials. The increased contact area of electrolyte-electrode interface and superb electric conductivity of carbon nanomaterials help obtain large specific capacitance of carbon-EDLC system. Furthermore, the intrinsic strong nature of carbon materials is also an advantage, since long-term stability of electrode is required. In this study, as-prepared 3D RGO structure showed excellent electrochemical properties and good cyclability, for its high surface area and intrinsic physical/chemical stability.

4. The ability to control thermal energy storage is important in many technological applications, especially in electronic micro-devices and industrial plant where latent heat should be carefully controlled for stability of the devices and machines. In particular, phase change materials (PCMs) have received much attention due to their unique thermophysical properties. The PCMs, including paraffin or metal hydrates, store or release thermal energy during the phase-phase transition process. Among the PCMs, the organic PCMs like paraffin, fatty acid and polymers are less-expensive and can be processed easily. However, the thermal/electric conductivities and shape-stability of the organic PCMs are usually very low. In this work, a simple and effective pathway is demonstrated to study the latent heat storage properties of the organic PCMs/3D plasma-RGO (PRGO) film

comoposites assisted by immersion method. The PCM/PRGO composites demonstrate increased thermal/electric conductivities with retained latent heat of fusion.

5. The 3D pRGO monoliths prepared from mild L-AA reduction of GO solution are utilized as a support of paraffin. Due to low-cost and large latent heat of fusion, paraffin has been exploited as a representative PCM in industrial application. However, the paraffin itself has low thermal/electric conductivities and low shape-stability during solid-liquid transition. Therefore, the 3D pRGO monoliths are immersed in molten paraffin and the solidified paraffin is adsorbed in the 3D RGO monoliths to produce paraffin/pRGO composites. The pore size and the density of the 3D pRGO monoliths are adjusted by using different concentration of GO solution in initial reduction process. As the concentration of GO solution increases, the density of the resultant monolith increases and the physical properties of the corresponding paraffin/pRGO composite enhanced. This simple immersion method provides the feasible candidate for the practical applications of 3D RGO network in PCM industries.

2. EXPERIMENTAL DETAILS

2.1. Preparation of 3-dimensional expanded RGO film *via* atmospheric plasma treatment on GO film

2.1.1. Preparation of GO film *via* vacuum suction of GO solution

200 mesh Graphite (≤ 74 μm) was purchased from Alfa Aesar, USA. Sodium nitrate ($NaNO_3$, 99 %) and hydrazine monohydrate (N_2H_4•H_2O, 98 %) were purchased from the Sigma-Aldrich Co. Potassium permanganate ($KMnO_4$, 99.3 %) and phosphorus pentoxide (P_2O_5, extra pure) were acquired from the Junsei Chemical Co. Sulfuric acid (H_2SO_4, 95 %), hydrochloric acid (HCl, 35~37 %) and hydrogen peroxide (H_2O_2, 30~35.5 %) were supplied from the Samchun Chemical Co. Potassium persulfate ($K_2S_2O_8$, 99 %) was purchased from the Kanto Chemical Co.

Initially, graphene oxide (GO) solution was prepared by a slightly modified Hummers' method [91]. For pre-oxidation process, 5 g of graphite powder, 2.5 g of P_2O_5 and 2.5 g of $K_2S_2O_8$ was mixed with 30 ml of H_2SO_4 in a flask and the whole solution was heated at 80℃ for 6 h. The solution was filtered through mixed cellulose acetate filter (ADVANTEC) with excess deionized water and remaining residue was stored in vacuum oven for 24 h. The 2.5g of $NaNO_3$ was then dissolved in 115 ml of H_2SO_4 with vigorous stirring. The dried graphite powder was poured into well-mixed $NaNO_3$/H_2SO_4 solution

with vigorous stirring, while kept in ice bath. In this state, 15 g of $KMnO_4$ was slowly added to the solution for 30 min, while keeping the temperature lower than 20℃. After 30 min, ice bath was removed and whole solution was heated at 45℃ for 12 h, turning the color of solution to brownish gray. Then 230 ml of deionized water was slowly poured into the paste, keeping the temperature below 40℃. 700 ml of deionized water was poured again and 25 ml of H_2O_2 was added dropwise to the solution, forming bright yellow color in solution. This graphitic oxide solution was washed with 10 wt % HCl solution for three times and deionized water for several times until the pH of solution turned into 7. This solution was ultrasonicated for 1 h to exfoliate graphitic oxide into GO. Then the solution was centrifugated at 4000 rpm for 30 min to exclude residue. The GO solution was dried in vacuum oven and GO powder was obtained.

After complete drying, the GO powder was re-dissolved in ultra-pure water to make 0.2 wt% GO solution. The aqueous GO 0.2 wt% solution was vacuum-filtered through 47mm AAO membrane (Whatman®) with vacuum-suction apparatus for 12 h. After complete suction, GO film was peeled off from the AAO membrane and was kept from humidity.

2.1.2. Preparation of HRGO film via hydrazine-reduction

The hydrazine-reduced GO (HRGO) film was prepared *via* vapor phase treatment of hydrazine on GO film. The GO film prepared from chapter 2.1.1 was put in a glass jar and 0.1 ml of hydrazine solution was dropped inside of the jar, while kept away from the GO film. The jar was sealed with teflon tape and was put in a dry oven. The hydrazine reduction proceeded for 6 h at 100 ^{o}C. As-prepared HRGO film was then put in a vacuum oven before further use.

2.1.3. Fabrication of 3-dimensional expanded RGO film *via* atmospheric plasma

In order to produce 3-dimensionally expanded plasma-reduced GO (PRGO) film, the dried GO film was treated with atmospheric plasma using handheld plasma apparatus. An atmospheric plasma curtain was produced by radio-frequency discharge on cathode ray tube of handheld plasma apparatus with 13.56 MHz radio-frequency and inert argon flow (Flow rate : 8 L/min). The distance from the surface of GO film and the cathode ray tube was set up to be 1 cm. After luminous plasma curtain was produced, the GO film was exposed to plasma curtain for up to 20 seconds. After 20 second-exposure, PRGO film was produced with sudden change of color from gray to black. The as-prepared PRGO film was kept in vacuum oven before further use.

2.2. Fabrication of 3-dimensional RGO monolith *via* reduction of GO with L-ascorbic acid (L-AA)

2.2.1. Preparation of graphene oxide

200 mesh Graphite (≤ 74 μm) was supplied from Alfa Aesar. Hydrogen peroxide (H_2O_2, 30~35.5 %), sulfuric acid (H_2SO_4, 95 %) and hydrochloric acid (HCl, 35~37 %) were acquired from the Samchun Chemical Co. Potassium permanganate ($KMnO_4$, 99.3 %) and phosphorus pentoxide (P_2O_5, extra pure) were purchased from the Junsei Chemical Co. L-ascorbic acid (99 %), sodium nitrate ($NaNO_3$, 99 %) and hydrazine solution (35 % in H_2O) were purchased from the Sigma-Aldrich Co. Potassium persulfate ($K_2S_2O_8$, 99 %) was purchased from the Kanto Chemical Co.

Graphene oxide (GO) solution was prepared by a slightly modified Hummers' method [91]. Solid $NaNO_3$ (0.5 g) was mixed with H_2SO_4 (23 ml) at vigorous stirring. Fine graphite powder (1 g) was then poured into well-mixed $NaNO_3$/ H_2SO_4 solution with vigorous stirring in ice bath. After thorough mixing for 1 h, $KMnO_4$ (3 g) was slowly poured into the solution, while keeping the temperature lower than 40 ^oC. After 30 min, ice bath was removed and whole solution was heated at 45 ^oC for 12 h, turning the black solution to brownish gray paste. Then deionized water (46 ml) was slowly poured into the paste, keeping the temperature below 20 ^oC using ice bath. Then deionized

water (140 ml) was additionally poured and H_2O_2 (5 ml) was slowly dropped to the solution, forming graphitic oxides in solution. The H_2O_2 reacts with the residual metal ions in the solution and cleave them away. This graphitic oxide solution was washed with 10 wt % aqueous HCl solution for three times and deionized water for several times until the pH of solution turned to 7. This solution was ultra-sonicated for 1 h at 450 W power to exfoliate graphitic oxide into GO. Then the solution was centrifugated at 4000 rpm for 30 min to exclude residue. As-prepared GO solution was dried as powder and kept in vacuum oven before further use.

2.2.2. Reduction of graphene oxide solution with L-AA

After complete drying, the GO powder was re-dissolved in ultra-pure water to prepare 0.01, 0.05 and 0.5 wt% GO solution. The 3D pRGO monolith was synthesized by the reduction method presented by Li's group with slight modification [46]. L-ascorbic acid (L-AA) powder was added to the corresponding GO solution, to make the weight ratio of GO in the corresponding solution to L-ascorbic acid as 2 to 1. After L-AA addition, the solution was stirred vigorously for 30 min until all the L-AA powder dissolved. After complete mixing, the solution was put in a glass jar and the jar was stored in 100 ^{o}C oven for 30 min to obtain 3D pRGO monoliths with different pore sizes, according to the different initial concentration of GO solution used. After thermal treatment, the 3D pRGO monoliths were kept in ice bath for 30 min and then moved to 200 ^{o}C oven for 8 h. The 3D pRGO monoliths were then lyophilized for 48 h. Finally, the lyophilized 3D pRGO monoliths were stored in vacuum oven to be kept away from moisture.

2.3. Applications

2.3.1. 3-dimensional expanded RGO film as a free-standing supercapacitor electrode

The GO film and HRGO film were fabricated by the method described in chapter 2.1.1 and 2.1.2, respectively. The 3-dimensional expanded RGO film was prepared by the method described in chapter 2.1.3.

For microscopic analyses, scanning electron microscope (SEM) images were obtained with a JSM-6701F (JEOL, Japan). High-resolution transmission electron microscope (HR-TEM) images were acquired with a JEM-3010 transmission electron microscope. For HR-TEM analysis, few mg of samples were readily dispersed in ethanol and was transfered on copper grid. All X-ray photoelectron spectroscopy (XPS) analyses were conducted with a Thermo-VG (Sigma Probe, UK). Thermogravimetric analysis (TGA) spectra were obtained with a Perkin-Elmer Pyris TGA 6 thermogravimetric analyzer. All TGA analyses were conducted in inert nitrogen atmosphere and the target temperature was 700 ^{o}C at the ramping rate of 10 ^{o}C/min. UV-Vis absorption spectroscopy measurements were performed with a Lambda 35 (Perkin-Elmer) UV-Vis spectrometer. For UV-Vis analyses, the samples were readily dispersed in distilled water. X-ray diffraction (XRD) was conducted using a Bruker New D8 Advance with a Cu-Kα radiation source (λ: 1.5406 Å) at 12

kW power. All XRD analyses were done using the film-type samples, without any modification. Brunauer–Emmett–Teller (BET) surface areas of PRGO films were measured using a ASAP 2000 Micromeritics surface area analyzer (Micromeritics Co., USA). Fourier-Transform Infrared (FT-IR) spectra measurement was conducted with a Perkin-Elmer Frontier FT-NIR/MIR Spectrometer, using universal-ATR mode.

All plasma treatment was conducted using a MyPL 200 handheld plasma apparatus with 13.56 MHz radio-frequency glow discharge and 8 L/min argon flow (APP Co. Ltd., Korea). The distance between the target GO film and the cathode ray tube of the handheld plasma apparatus was set to be 1 cm. The applied plasma power was varied from 100 W to 200 W, and the operating time was fixed at 20 sec.

The cyclic voltammetry (CV) and galvanostatic charge/discharge tests of GO, HRGO and PRGO films were conducted with a Wonatech WBCS 3000 potentiostat/galvanostat instrument to study the electrochemical performances of the samples. All electrochemical measurements were performed in a 3-electrode system with 1M H_2SO_4 solution as the electrolyte at room temperature, where the counter and reference electrodes were Pt wire and Ag/AgCl, respectively. The film itself was directly employed as the working electrode for all sample species. The potential range for CV and galvanostatic

charge/discharge tests was 0.0 to 0.8 V. The electrochemical behavior was first characterized by the CV test at scan rates ranging from 10 mV/s to 250 mV/s. After that, the galvanostatic charge/discharge test of the PRGO film was carried out at a current density of 1, 3 and 5 A/g to precisely evaluate the gravimetric capacitance, C_m (F/g). The gravimetric capacitances (C_m) were calculated by using the equation $C_m = (I \times \Delta t)/(m \times \Delta V)$, where C_m is the gravimetric capacitance in F/g , I is the constant discharge current in mA, Δt is the discharge time in second, m is the total mass of the active material in mg, ΔV is the potential window in V. The cycle stability of the PRGO film was measured by the galvanostatic charge/discharge test at a current density of 1 A/g in 1M H_2SO_4 solution.

2.3.2. 3-dimensional expanded RGO film as a foothold for organic phase change materials

The 3-dimensional expanded RGO film (PRGO film) was prepared by the method described in chapter 2.1.3. For this experiment, polyethylene glycol (M.W. 20000, extra pure) was acquired from Junsei Chemical Co. Fluorene (98%) and octanoic acid (98%) were purchased from Sigma-Aldrich Chemical Co. Paraffin (C_nH_{2n+2}, melting point: 42~44 ^oC) were purchased from Kanto Chemical Co. All of the reagents were used as received without further purification.

For fabrication of the PCM/PRGO composites, solid paraffin and PEG flake, 10 g respectively, were stuffed in 70 ml glass bottle and heated to 60 ^oC and 75 ^oC for melting of the solid PCMs, respectively. The PRGO films were then immersed in the molten paraffin and PEG for 30 min. After complete adsorption of molten PCMs, the PRGO films stuffed with paraffin and PEG were retracted from the glass bottle and were dried in room temperature (RT) to obtain the paraffin/PRGO composite and PEG/PRGO composite, respectively. 40 ml of octanoic acid (in liquid state) was also poured to 70 ml glass bottle and the PRGO film was then immersed in the liquid octanoic acid at RT for 30 min. After complete soaking for 30 min, the PRGO film stuffed

with octanoic acid was collected out and was dried in RT to obtain the octanoic/PRGO composite.

For microscopic analyses, scanning electron microscope (SEM) images were acquired with a JSM-6701F (JEOL, Japan). Fourier-Transform Infrared (FT-IR) spectra measurement was conducted with a Perkin-Elmer Frontier FT-NIR/MIR Spectrometer, using universal-ATR mode. The PCM/PRGO composites were pelletized and the corresponding pellet was measured. X-ray diffraction (XRD) measurement was conducted using a Bruker New D8 Advance with a Cu-Kα radiation source (λ: 1.5406 Å) at 12 kW power. Differential scanning calorimetry (DSC) measurement was conducted with a Perkin-Elmer differential scanning calorimeter DSC 6000. The long-term thermal cyclability of the PCM/PRGO composites was also evaluated with a Perkin-Elmer differential scanning calorimeter DSC 6000. Thermogravimetric analysis (TGA) spectra were obtained with a Perkin-Elmer Pyris TGA 6 thermogravimetric analyzer. All TGA analyses were operated in inert nitrogen atmosphere at ramping rate of 10 ^{o}C/min. The thermal conductivity of the PCM/PRGO composites were determined by modified Flynn and Levin method using a Perkin-Elmer differential scanning calorimeter DSC 6000 [92-93]. For the thermal conductivity measurement, fluorine pellet (5 mm diameter) was utilized as sensor material. The pristine PCMs and the

PCM/PRGO composites were cut into thin, round pellet by razor blade with 6.5 mm diameter. For thermal conductivity measurement, the thickness of sample must be measured. For the DSC analyses, two kinds of experiments were conducted: First, melting curves of the sole fluorine pellet was measured. After then, the melting curves of the PCMs and the composites were measured by using fluorine pellet and sample pellet in one alumina holder. The contact between fluorine pellet and sample pellet must be firm in order to obtain accurate result. After measurement, the slope values of the melting curve were calculated and was converted to thermal resistance to determine the thermal conductivity of the samples. The electric conductivity of the PCM/PRGO composites was measured using a four-point probe system (Mode Systems Co., Korea) equipped with a current source meter (Keithley 2400, Keithley Co., USA).

2.3.3. 3-dimensional pRGO monolith for adsorption of paraffin as a phase change material

The 3-dimensional pRGO monoliths were prepared by the method described in chapter 2.2.2. In this work, paraffin (C_nH_{2n+2}, melting point: 42~44 ^oC) were aquired from Kanto Chemical Co. All of the reagents were used as received without further purification.

For fabrication of paraffin/RGO composites, 10 g of solid paraffin was added to 70 ml glass bottle and the bottle was heated up to 60 ^oC until all paraffin melted. The 3D pRGO monoliths with different pore sizes were then immersed in the molten paraffin for 30 min until the 3D pRGO monoliths were completely soaked with liquid paraffin. After 30 min, the 3D pRGO monoliths with stuffed paraffin were collected out of the molten paraffin and were dried in room temperature to obtain the paraffin/pRGO composites.

For microscopic analysis, scanning electron microscope (SEM) analyses were conducted with a JSM-6701F (JEOL, Japan). X-ray diffraction (XRD) was conducted using a Bruker New D8 Advance with a Cu-Kα radiation source (λ: 1.5406 Å) at 12 kW power. Fourier-Transform Infrared (FT-IR) spectra were acquired with a Perkin-Elmer Frontier FT-NIR/MIR Spectrometer, using universal-ATR measurement on pelletized samples. Differential scanning calorimetry (DSC) measurement was done with a Perkin-Elmer differential

scanning calorimeter DSC 6000. Thermogravimetric analysis (TGA) spectra were obtained with a Perkin-Elmer Pyris TGA 6 thermogravimetric analyzer. All TGA measurements were operated in inert nitrogen atmosphere. The thermal conductivity of paraffin/RGO composites was measured by the DSC-based method described in chapter 2.3.2. The electric conductivity of the paraffin/pRGO composites was measured using a four-point probe system (Mode Systems Co., Korea) equipped with a current source meter (Keithley 2400, Keithley Co., USA).

3. RESULTS AND DISCUSSION

3.1. 3-dimensional, expanded RGO film as a free-standing supercapacitor electrode

3.1.1. Preparation of PRGO film *via* atmospheric plasma

In Figure 11, the process of plasma-assisted reduction of GO film to produce 3D expanded PRGO film is demonstrated. In this work, GO powder was prepared *via* a slightly modified Hummers' method. Among the various oxidation pathways of graphite, the Hummers' method enables mass-production of graphitic oxide with less harmful residues to be washed. The produced graphitic oxide solution was readily ultra-sonicated and few-layer GO powers were obtained after repeated washing. The GO was dispersed in water to prepare 0.2 wt % aqueous GO solution (Figure 11a). This dilute solution was vacuum-suctioned on AAO membrane to produce few μm-thick GO thin film (Figure 11b). This GO film was then treated with atmospheric argon plasma for 20 sec using hand plasma apparatus with 13.56 MHz radio-frequency (RF). When the plasma reached the surface of GO film, the color of the film surface changed suddenly from brownish grey to black, forming expanded PRGO film (Figure 11c). During this plasma treatment, argon plasma curtain induce sudden thermal exfoliation and deoxygenation on GO film to produce 3-dimensionally expanded structure of RGO.

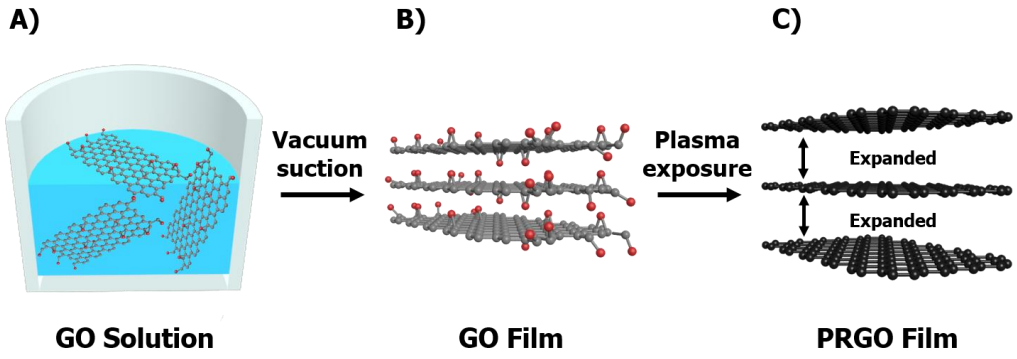

Figure 11. Schematic illustration of preparation of PRGO film. a) Dilute GO solution prepared by Hummers' method; b) GO thin film prepared by vacuum-filtration of the GO solution on AAO. Red dots stand for oxygen-related groups on GO structure; c) Expanded structure of PRGO film produced by atmospheric argon plasma treatment on GO thin film for 20 sec at 200W plasma power.

In SEM image of GO thin film (Figure 12a), GO sheets were stacked vertically to produce 10 μm-thick GO film after vacuum-suction of 10 ml 0.2 wt% GO solution onto AAO membrane. After brief atmospheric plasma treatment on GO film for 20 sec, the as-reduced GO sheets in the PRGO film expanded outward and the distance between individual RGO sheets increased. In Figure 12b, overall thickness of as-prepared PRGO film reached *ca.* 400 μm after plasma treatment. Digital photograph of the PRGO film (Figure 13) demonstrate that the structure of free-standing RGO film with 38 mm diameter was well preserved after plasma-reduction. The film demonstrated flexibility and change in color, referring to successful reduction of GO. In Figure 14, the transmission electron microscopy (TEM) analysis on PRGO film demonstrated that the planar RGO sheet was observed after brief plasma treatment on GO sheet.

The reduction mechanism of GO film by brief plasma treatment can be described as a combined effect of rapid thermal exfoliation and deoxygenation process. When atmospheric argon plasma curtain reaches the GO surface, various reactive species, such as electrons and ions, in plasma detach the oxygen-related functional groups (epoxide, carbonyl, carboxyl and hydroxyl groups) from the surface. These oxygen groups were rapidly eliminated compared to previous vacuum plasma process [39, 41, 95], which is verified by

rapid transition of color of the GO film. Additionally, this sudden deoxygenation generate oxygen-related gases like CO or CO_2 from oxygen groups and these gases evolve into stacked graphene sheets and induce high pressure to expand adjacent graphene sheets outward. Judging from the SEM results, atmospheric argon plasma treatment on GO film and subsequent reduction showed similar behavior with expansion of GO sheets in thermal reduction process [25].

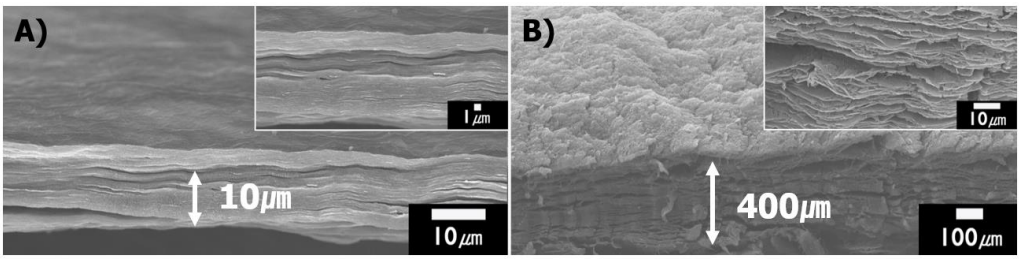

Figure 12. SEM images of GO film and PRGO film. a) x2000 SEM image of GO thin film (Inset: magnified image of GO thin film); b) x100 SEM image of PRGO film after 200W plasma treatment for 20 sec (Inset: magnified image of PRGO film).

.

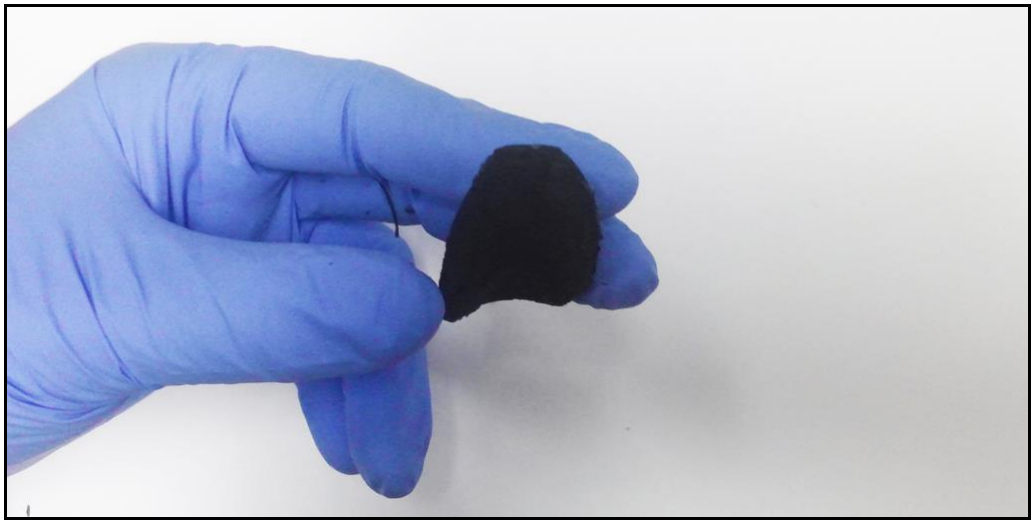

Figure 13. Digital photograph of the free-standing PRGO film.

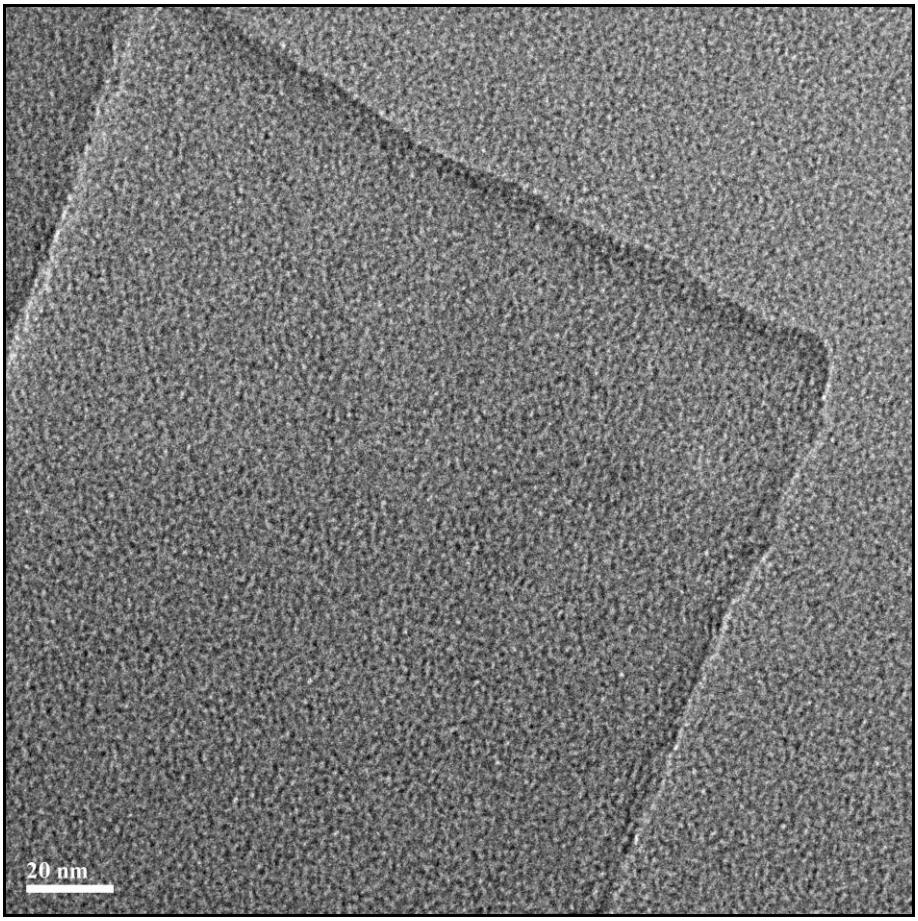

Figure 14. TEM image of PRGO film (Plasma treatment condition: 200W power for 20 sec).

3.1.2. Characterization of PRGO film

X-ray photoelectron spectroscopy (XPS) C1s analysis on PRGO film with different applied plasma power was conducted to investigate the effect of plasma condition on the degree of reduction of GO film (Figure 15 and 16). In the GO film spectrum, a distinct peak for single/double bond between carbon and carbon (C-C/C=C)) at 284.5 eV and a peak for C-O single bond at 286.5 eV is emphasized, as reported in previous work [41]. However, at plasma power exceeding 110 W, the C-O single bond peak was decreased and C-C/C=C bond peak was increased, which stands for cleavage of oxygen groups and restoration of C-C graphitic structure. Although C=O double bond peak at 287.8 eV and carboxyl (COOH) peak at 290 eV were still observed in the C1s spectra, the peak intensity of overall oxygen-related group was decreased (Figure 15). As the applied power increased to 200W, the percentage of carbon element on the surface of resultant PRGO film rose from 80.0 % at the power of 100W to 91.1 % at 200W. Meanwhile, the percentage of oxygen element declined from 20 % at 100W to 8.9 % at 200W (Figure 16). As a result, O/C ratio of PRGO film surface decreased to 0.116 when the applied power reached 200 W. The C1s XPS results indicate that the plasma reduction of GO completed in 20 sec with more than 110 W plasma power, reaching lowest O/C ratio of 0.116 at applied power of 200W.

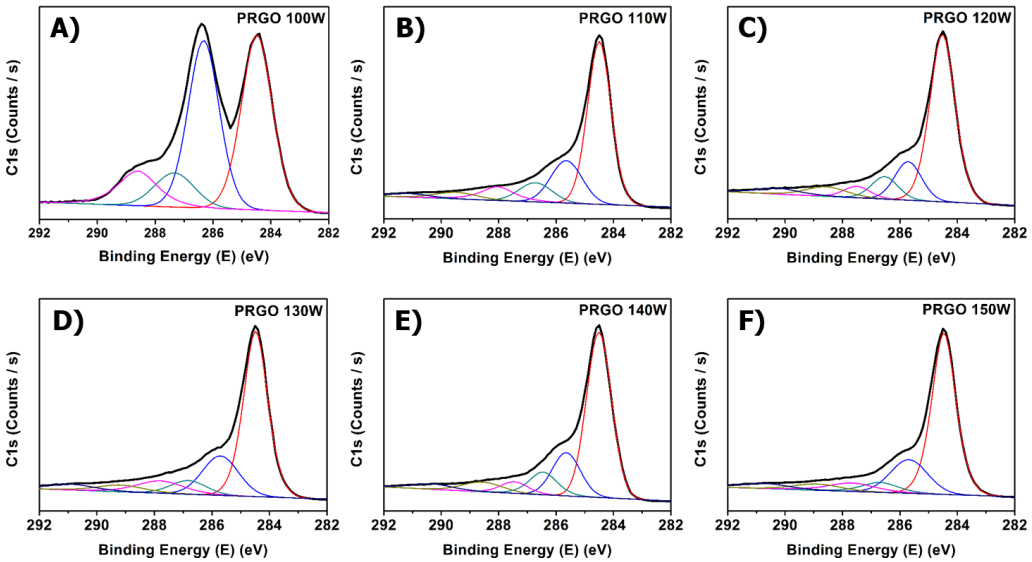

Figure 15. Deconvoluted XPS C1s spectra of PRGO film with varying applied plasma power from 100 to 150 W. a) 100W treatment; b) 110W treatment; c) 120W treatment; d) 130W treatment; e) 140W treatment; f) 150W treatment.

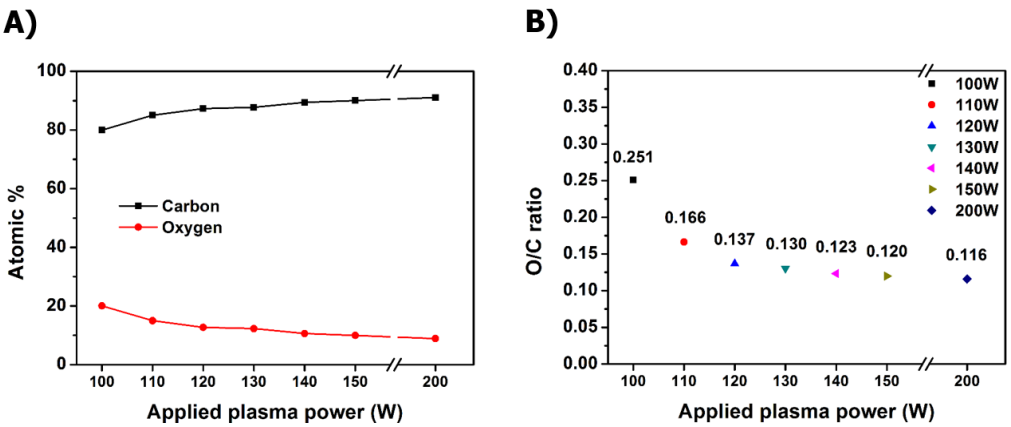

Figure 16. XPS analyses of PRGO film after plasma treatment. a) Atomic percentage of carbon (C) and oxygen (O) calculated from XPS analysis on PRGO film; b) O/C ratio values of PRGO film plotted over various applied plasma power (ranging from 100W to 200W). All plasma processing was conducted within 20 sec.

N1s XPS analyses were additionally conducted to clarify the effect of reduction on the surface atomic structure of PRGO film. Especially, hydrazine-reduced GO (Further denoted as HRGO) was prepared to compare the degree of reduction and the hetero-atom doping effect (Figure 17). For the comparison, HRGO films were synthesized by vapor-phase reduction of GO film with 0.1 ml hydrazine solution at 100 ℃ for 6 h. PRGO film produced at 200W plasma power (Further denoted as PRGO 200W) was used for this comparison experiment due to its lowest O/C ratio. In Figure 17a, a small N1s peak around 400 eV in overall XPS spectrum is present in HRGO, while a negligible N1s peak is detected in overall XPS spectrum of PRGO 200W. In Figure 18b, various nitrogen-related peaks, from pyridinic (*ca.* 399 eV) to pyrrolic (*ca.* 400.2 eV) and quaternary nitrogen (*ca.* 401.3 eV) peak, were spotted in deconvoluted HRGO N1s spectrum. In PRGO 200W spectrum, small nitrogen-related peaks were found and GO also showed small peak in N1s spectrum. These results indicate that the use of nitrogen-containing reducing agent like hydrazine or its relatives in reduction of GO might lead to considerable doping of nitrogen elements in target graphene structure, while atmospheric argon plasma treatment resulted in a minute hetero-atom incorporation on graphene structure. Since the atmospheric plasma treatment proceeded in normal atmospheric condition, N_2 gases in the air might be converted to nitrogen-

related reactive species and the reactive species might contact with graphene structure for insignificant nitrogen-doping on PRGO 200W.

UV-Vis measurement on GO, HRGO and PRGO 200W was done to study atomic structural change of PRGO film after plasma reduction process (Figure 18). First, the corresponding samples were finely dispersed in water and bath-sonicated prior to measurement. In UV-Vis spectra, the red-shift of broad absorption peak from 230 nm of GO to 283 nm of PRGO 200W after 200W plasma treatment reveals that C-C/C=C bonding was re-generated in plasma reduction process [96]. This vathochromic shift of absorption peak of PRGO 200W exceeds that of absorption peak of HRGO, suggesting superior reduction effect of plasma reduction.

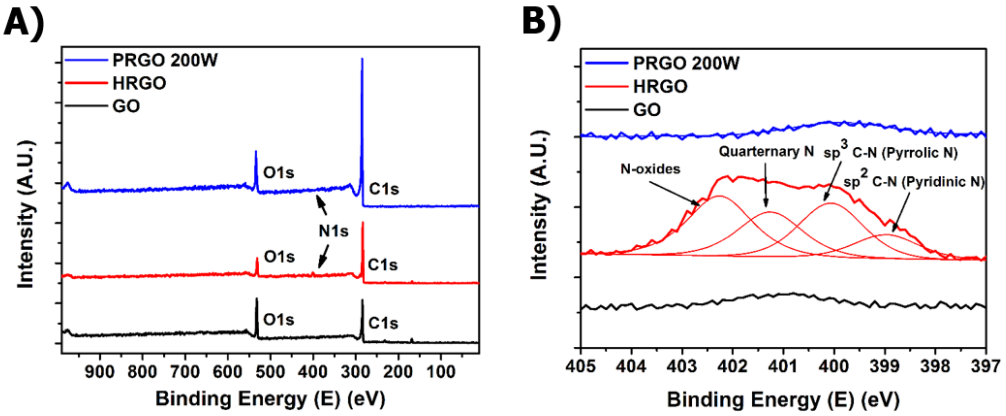

Figure 17. a) XPS wide spectra of GO, HRGO and PRGO 200W; b) deconvoluted XPS N1s spectra of GO, HRGO and PRGO 200W.

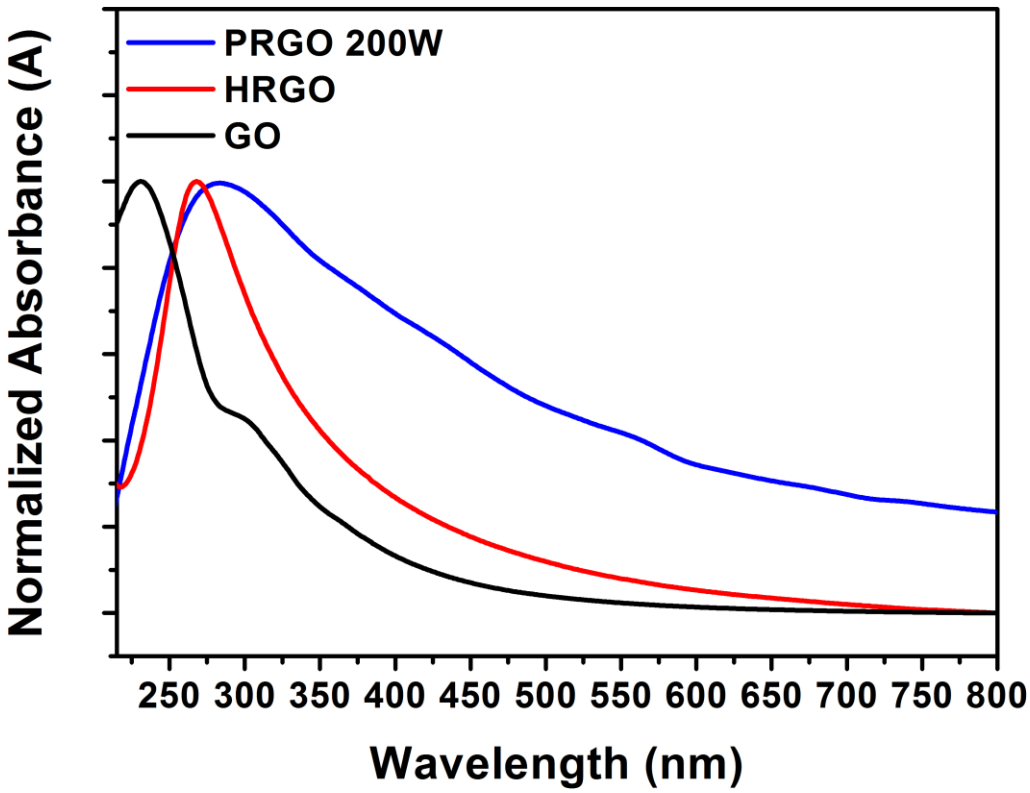

Figure 18. UV-Vis spectra of GO, HRGO and PRGO 200W.

C1s XPS analyses were additionally conducted to scrutinize the structural change of GO film after chemical and plasma reduction, in the viewpoint of change in oxygen-related functional groups on the surface (Figure 19). The peak area values were calculated by intergration of area under each deconvoluted C1s peak. In Figure 19, the C-O single bond peak at 286.5 eV occupied 14.1 % of peak area in GO film spectrum, while the C-C/C=C bond peak area percentage at 284.5 eV was 45.9 %. After each reduction process, corresponding C-O single bond peak area in HRGO and PRGO 200W diminished to 9 and 8.1 %, respectively. Meanwhile, the C-C/C=C bond peak area at 284.5 eV increased from to 48.8 % and 53.7 %, respectively. The result suggests that the plasma reduction exhibited better cleavage of oxygen-related groups after reduction process and the overall graphene structure is more repaired in plasma reduction.

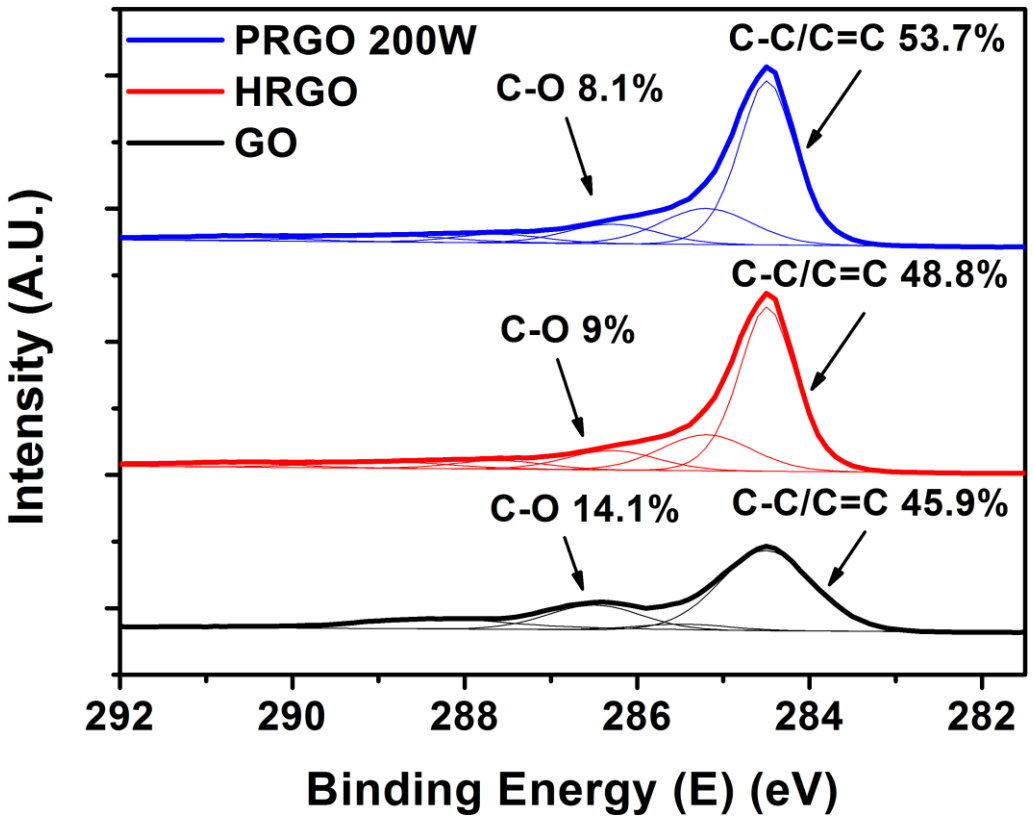

Figure 19. Comparison graph of XPS C1s spectra of GO, HRGO and PRGO 200W.

X-ray diffraction (XRD) analyses on GO film revealed that GO thin film possesses a well-ordered, stacked layers of GO sheets, as can be seen from a sharp d_{001} peak (Figure 20). The exact 2Θ value for the d_{001} peak was 10.22, corresponding to a d-spacing value of 8.65 Å, and this value is due to presence of water molecule layer with hydrogen bonding on two GO sheets [97]. In the XRD spectra of HRGO and PRGO 200W, the characteristic peak of GO at 2Θ = 10 to 12 is absent, and a new broad peak is observed at 2Θ = 24.73 and 24.78 for HRGO and PRGO 200W, respectively. These values correspond to the d-spacing of 3.60 Å and 3.59 Å, which are comparable with the d-spacing of 3.35 Å for graphite. The change in the value of d-spacing can be attributed to cleavage of oxygen groups on basal plane and restoration of π-π interaction between neighboring RGO sheets. These broad peak also indicates the existence of 3D-expanded structure of PRGO and the restoration of the graphitic structure after plasma reduction, almost similar with the ordered structure of graphite. Supplementary Brunauer–Emmett–Teller (BET) analysis exhibited that PRGO 200W sample showed Type IV hysteresis with high surface area of 312 m^2/g after plasma reduction process (Figure 21). From these results, the plasma reduction of GO thin film at 200W power generated a graphitic ordered 3D RGO structure with high surface area.

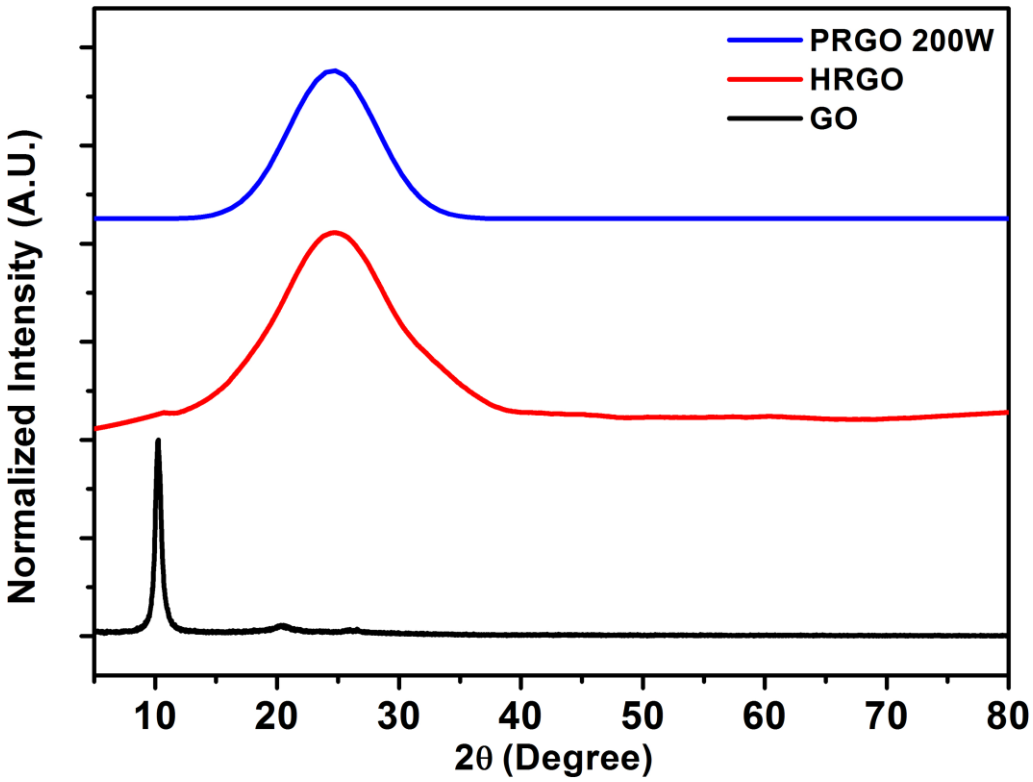

Figure 20. Normalized XRD spectra of GO, HRGO and PRGO 200W.

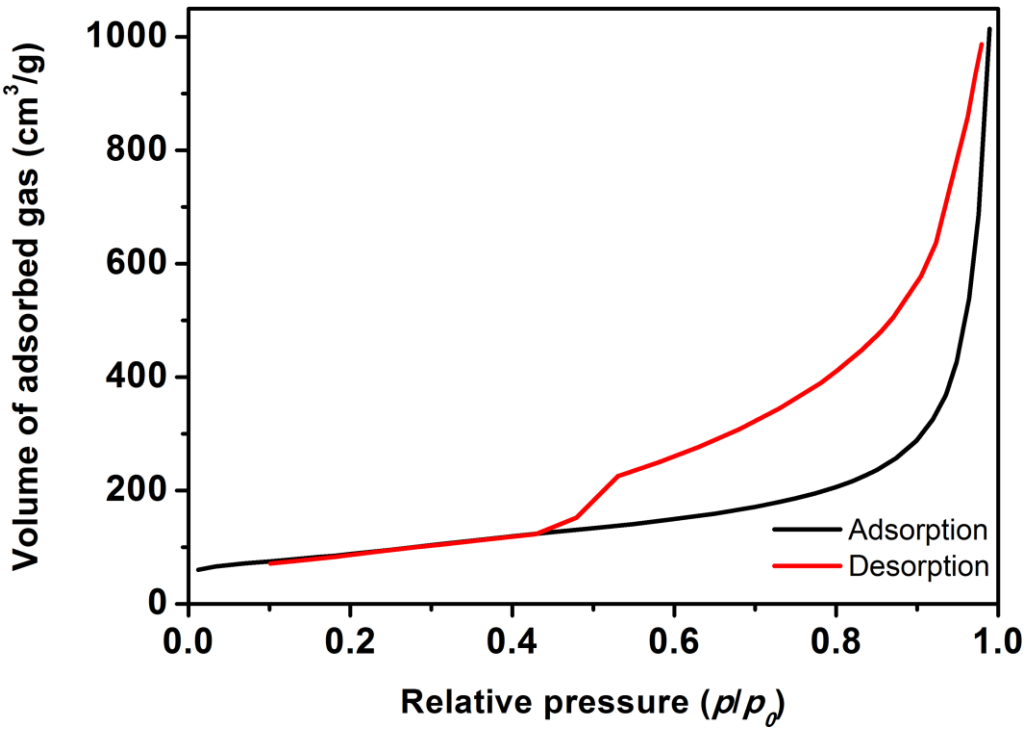

Figure 21. Brunauer–Emmett–Teller (BET) curve of PRGO 200W.

In the following Fourier-Transform infrared (FT-IR) analysis, a broad peak at *ca.* 3400 cm^{-1} was assigned to the O-H stretching of hydroxyl group and a small peak at *ca.* 1715 cm^{-1} was designated for C=O double bond vibration of carbonyl group on GO in GO FT-IR spectrum (Figure 22). The intensity of these peaks were diminished in the FT-IR spectra of HRGO and PRGO 200W, which indicates the cleavage of oxygen-related groups after the hydrazine/plasma reduction.

Figure 23 describes the Raman analyses results of GO, HRGO and PRGO 200W. The Raman spectra of GO, HRGO and PRGO 200W displayed G peaks for E_{2g} vibration of sp^2 C-C structure at *ca.* 1595 cm^{-1} and D peaks for structural defects at *ca.* 1344 cm^{-1}. In previous work, the I_D/I_G ratio of chemically reduced GO after reduction was calculated to be larger than that of GO due to smaller sp^2 domain [26]. However, in this study, the I_D/I_G ratio decreased from 0.97 of GO to 0.83 of the PRGO 200W, in comparison with 1.15 of the hydrazine-reduced HRGO. It can be assumed from the Raman results that production of RGO by plasma reduction with atmospheric argon plasma prompted the removal of structural defects and the conversion of sp^3 to sp^2 C-C structure, leading to increase in the G peak [98]. Therefore, this brief plasma treatment can produce RGO structure with less deformation compared with that from traditional chemical reduction pathway.

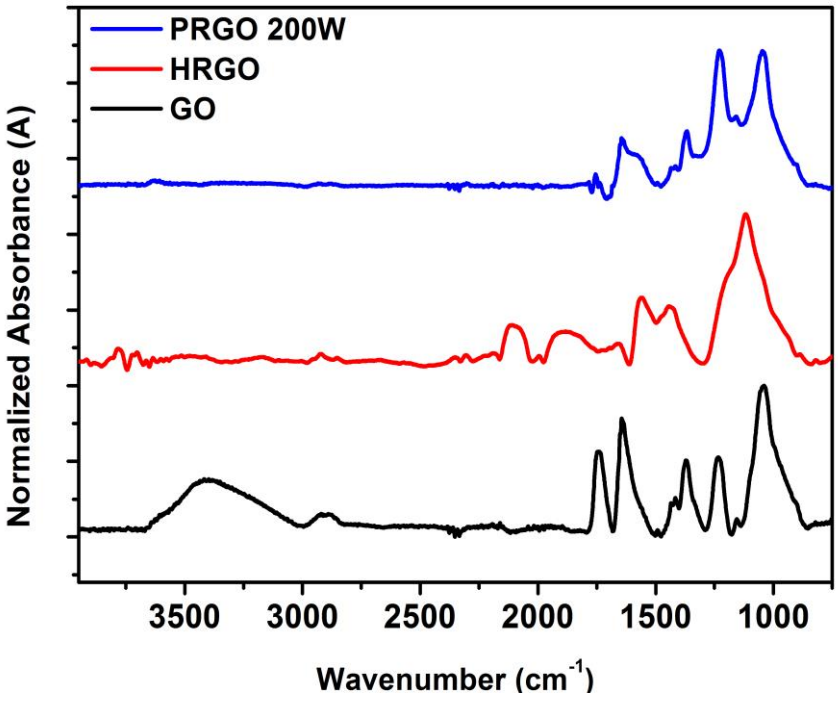

Figure 22. Normalized FT-IR spectra of GO, HRGO and PRGO 200W.

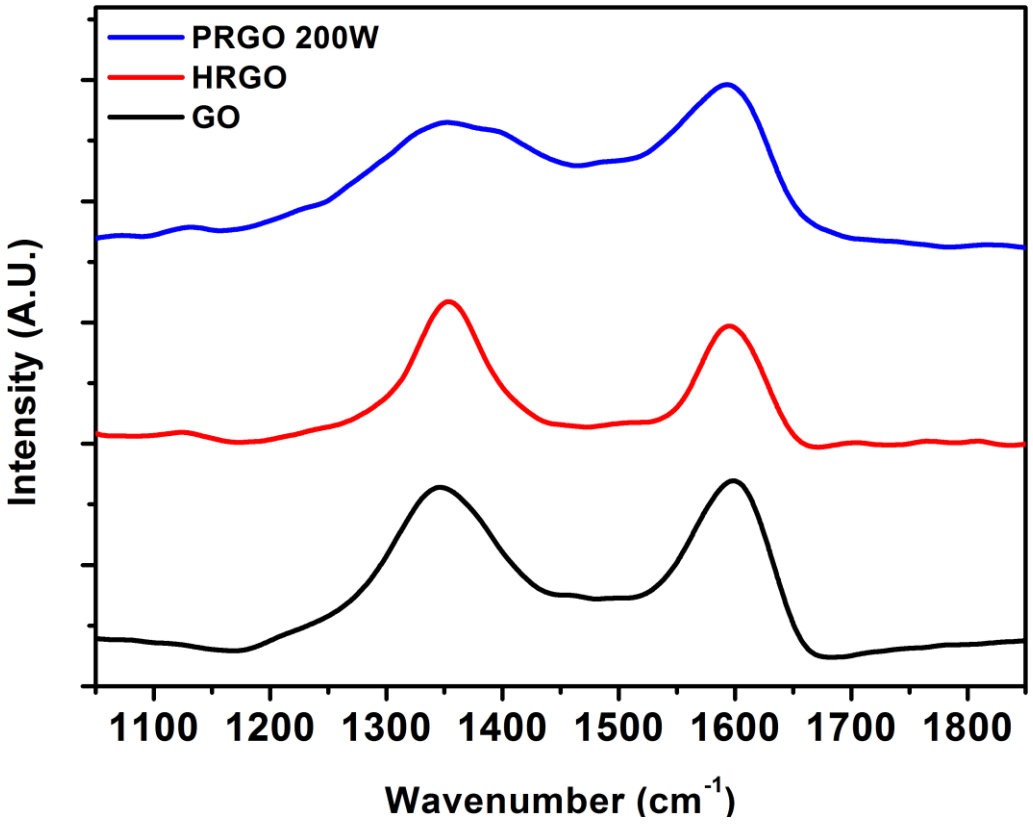

Figure 23. Raman spectra of GO, HRGO and PRGO 200W.

In order to evaluate the processability of as-prepared PRGO 200W for future application in solution-based process, PRGO 200W film was ground to flakes and was dispersed in following various organic solvents: Toluene, dimethyl formamide (DMF), 2-propanol (also known as IPA), N-methyl-2-pyrrolidone (NMP), water, ethanol, tetrahydrofuran (THF), n-hexane, acetone and acetonitrile. The concentration was set to be 0.05 wt% for each solution. The ground PRGO 200W flakes were readily dispersed in each solvent by vigorous mixing for 30 min and the mixed solutions in vials were placed on the flat table for 30 min. After 30 min, the PRGO 200W flakes were observed to be finely dispersed in all solvents except n-hexane (Figure 24). After placing the solution vials on the flat table for 7 days, the dispersability of PRGO 200W in the organic solvent decreased, which is witnessed by precipitated PRGO solutes in toluene, water, THF, n-hexane and acetone. The PRGO 200W flakes were observed to be well-dispersed in 2-propanol and NMP after 7 day storage.

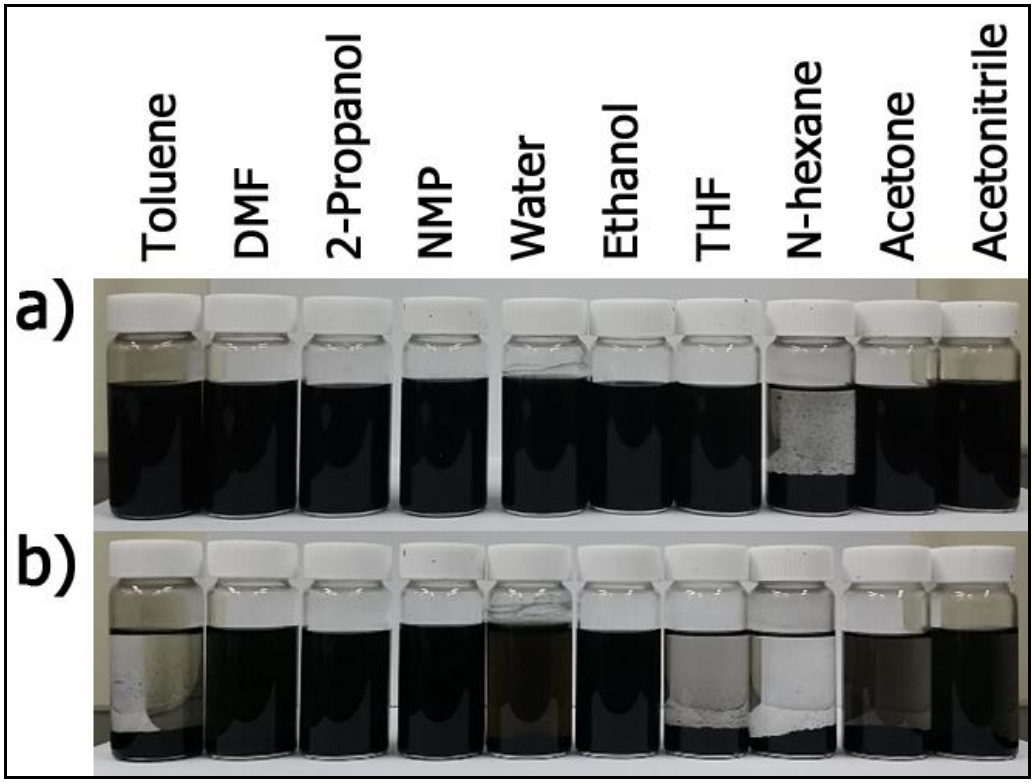

Figure 24. Dispersion result of PRGO 200W in various organic solvents. a) Digital photograph of PRGO 200W powder dispersion in toluene, DMF, 2-propanol, NMP, water, ethanol, THF, n-hexane, acetone and acetonitrile taken after 30 min dispersion. b) Digital photograph of PRGO 200W powder dispersion in the same solvents taken after 7 days later.

Additional thermo-gravimetric analysis (TGA) was conducted to evaluate the thermal stability of GO, HRGO and PRGO 200W up to 700 ℃ (Figure 25). The weight loss curve of GO in Figure 25 exhibited a linear, continuous loss of weight up to around 300 ℃ due to gasification of oxygen-functional groups on the GO basal plane as CO or CO_2 gases. The GO, HRGO and PRGO 200W all displayed a weight loss starting from ca. 550 ℃ and this loss can be attributed to thermal degradation of C-C structure of graphene [99]. Nonetheless, the PRGO 200W exhibited only 13 % weight reduction up to 700 ℃, comparable with 14 % weight loss of HRGO produced from harsh hydrazine reduction. Judging from these data, the atmospheric plasma treatment induced successful cleavage of oxygen-related groups on GO surface to produce thermally stable RGO structure. Plus, the PRGO 200W demonstrates the enhanced thermal barrier property comparable with hydrazine-treated RGO.

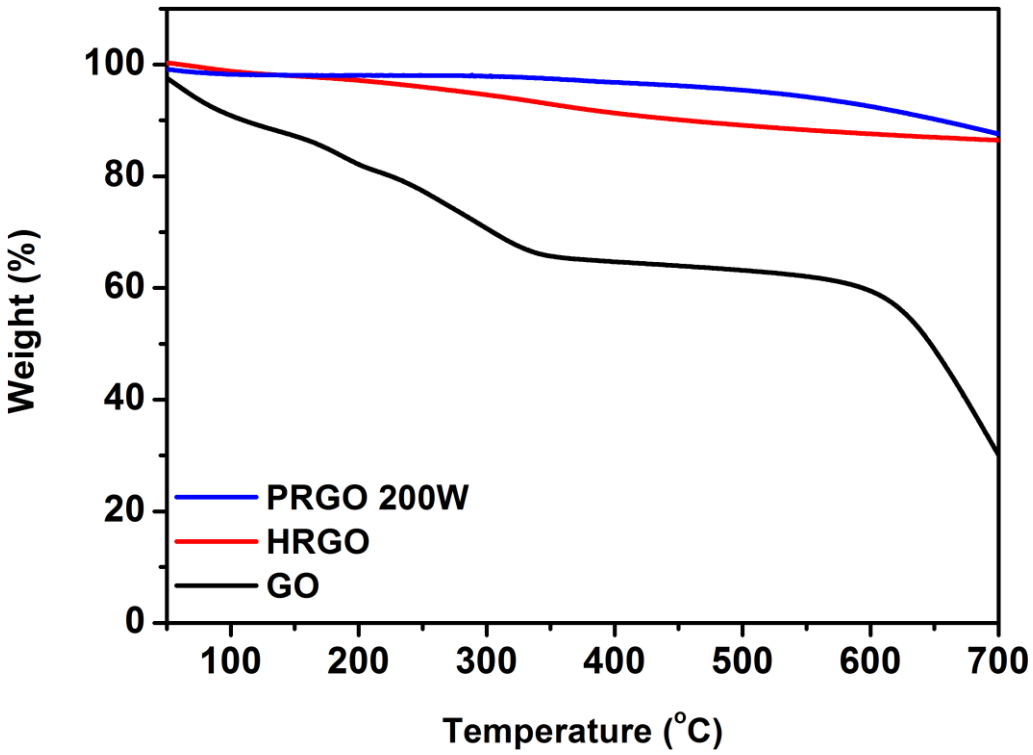

Figure 25. Thermogravimetric analysis (TGA) spectra of GO, HRGO and PRGO 200W.

3.1.3. Supercapacitor performance of PRGO film

Figure 26a displays electrochemical evaluation results of the GO, HRGO and PRGO 200W at the scan rate of 50 mV/s. All electrochemical tests, cyclic votammetry (CV), cyclability test and galvanostatic charge-discharge test, were proceeded using free-standing film samples as working electrodes in 3-electrode system. The CV measurement showed that the PRGO 200W electrode demonstrates larger capacitance than GO and HRGO, which is indicated by larger CV curve area.

In the galvanostatic measurement at current density of 1 A/g, the PRGO 200W electrode displayed a tri-angular charge-discharge curve with minute internal resistance (IR) drop, possibly due to the removal of oxygen-functional groups from GO surface (Figure 26b). In comparison with GO and HRGO, the PRGO 200W electrode exhibited gravimetric capacitance of 150 F/g at current density of 1 A/g. This enhancement in capacitance value of PRGO 200W can be attributed to successful restoration of sp^2 hexagonal lattice in RGO structure and increased surface area of 3D PRGO structure. The capacitance of PRGO 200W electrode in this work surpasses the electrochemical performance of the hydrazine-reduced GO electrodes in previous works [100-102] and the gravimetric capacitance of 100 F/g of the RGO electrode prepared from microwave reduction method [103].

The detailed electrochemical behavior of PRGO 200W electrode was additionally evaluated by conducting CV measurement by changing scan rates from 10 mV/s to 250 mV/s (Figure 26c). As scan rate increased from 10 mV/s to 250 mV/s, the area under CV curve gradually decreased, which means that the analogous specific capacitance also reduced. The decrease in the capacitance at higher scan rates of PRGO 200W can be explained by the limitation of diffusion inside the micro-pores of PRGO 200W at higher rates. Lastly, the long-term stability of PRGO 200W electrode was evaluated at a scan rate of 50 mV/s. After cycling test for 1000 cycles, 82 % retention of initial capacitance of PRGO 200W electrode was determined, demonstrating acceptable stability as a supercapacitor electrode material (Figure 27).

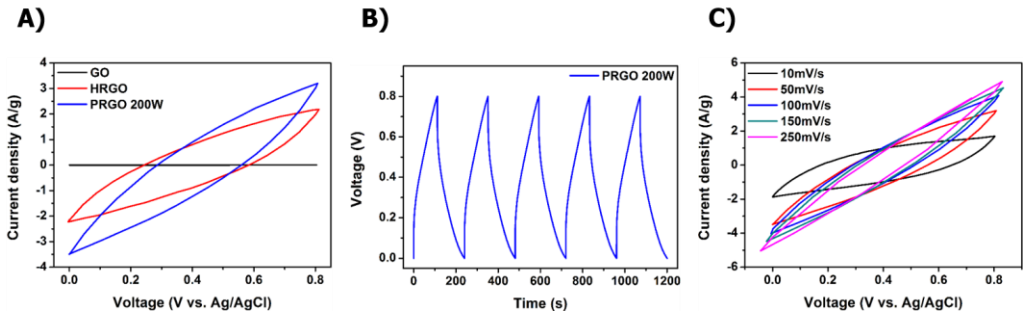

Figure 26. Electrochemical characterization of PRGO film. a) Cyclic voltammetry (CV) graph of GO, HRGO and PRGO 200W at 50 mV/s scan rate; b) 5-consecutive charge-discharge curve of PRGO 200W at 1 A/g current density; c) Cyclic voltammetry graph of PRGO with various scan rates, from 10 to 250 mV/s. All electrochemical analyses were conducted using 1M H_2SO_4 liquid electrolyte in 3-electrode system.

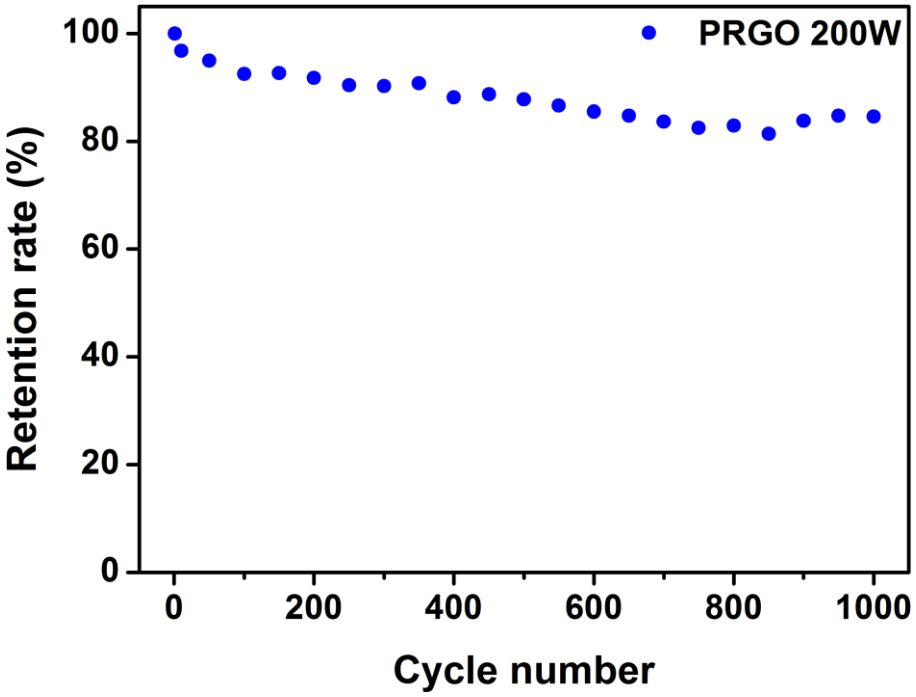

Figure 27. Cyclability test of PRGO 200W for 1000 cycles.

In conclusion, a novel type of 3-dimensional, expanded PRGO structure was prepared *via* brief and direct atmospheric argon plasma treatment on GO thin film. The thin GO film with 10 μm thickness was transformed into 3-dimensionally expanded PRGO film with up to 400 μm thickness without any toxic chemical treatment. The 3D PRGO film was produced with applied plasma power exceeding 110 W in less than 20 seconds, and the lowest O/C ratio for PRGO film was approximately 0.116 at 200W plasma power. Systematic surface analyses announced that oxygen-related functional groups were cleaved from RGO sheet after combined process of rapid thermal exfoliation and deoxygenation. The PRGO 200W was then used as a free-standing supercapacitor electrode, displaying 150 F/g of specific capacitance at the current density of 1 A/g and 82 % of initial capacitance was retained after 1000 charge-discharge cycles. Considering the longer plasma exposure time, complex device set-up, and high vacuum condition needed for plasma reduction reported in previous works, this rapid, environmental-friendly method can illuminate a novel way of producing 3D RGO structure for energy storage applications.

3.2. Fabrication of free-standing 3D RGO film embedded with organic PCMs for latent heat storage

3.2.1. Preparation of PCM/PRGO composites

Figure 28 describes the preparation of the PCM/PRGO composites by simple immersion of the 3D PRGO network in liquid-state organic PCMs. At first, dried GO powders synthesized by a modified Hummers' method were readily dispersed in deionized water and the concentration of the GO solution was set to 0.2 wt %. Prior to synthesis of expanded PRGO network, the 0.2 wt% GO solution (10 ml) was vacuum-filtered on commercialized AAO membrane (Pore size: 100 to 300 nm) for 12 h to acquire GO thin film (Figure 28a). As-prepared GO film was peeled off from the membrane and was reduced with atmospheric plasma apparatus to synthesize the PRGO network. (Figure 28b). The fabrication of as-synthesized PRGO network is realized by rapid thermal exfoliation/deoxygenation during the atmospheric plasma treatment and the oxygen-related groups on the GO surface are annihilated to make physically-linked RGO network [40]. The 3D, expanded structure of PRGO network was realized by production of oxygen-derived gas, such as CO_2, in the rapid thermal exfoliation process. These gases evolve into the stacked graphene sheets and induce sudden pressure to drive the graphene framework outward. Due to increased distance between RGO sheets during the thermal

exfoliation process, various organic PCMs are readily impregnated into the network by a facile immersion method (Figure 28c).

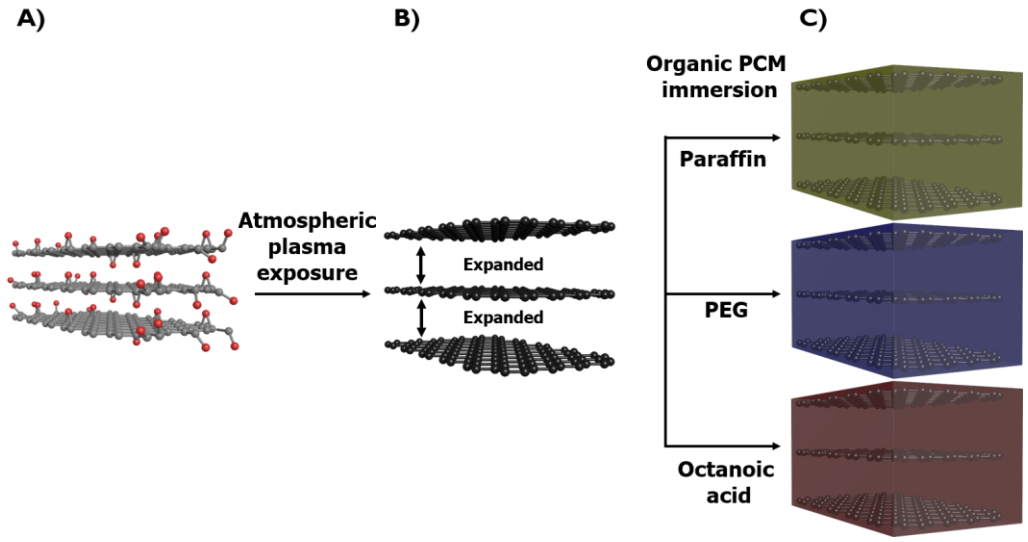

Figure 28. Fabrication process of the PCM/PRGO composites. a) Illustration of proposed chemical structure of GO film. Red dots indicate oxygen-related groups; b) PRGO network prepared by plasma treatment on GO film; c) Preparation of the PCM/PRGO composites by immersion of PRGO network into each PCM (in liquid state) for 30 min.

The surface morphologies of the as-prepared PCM/PRGO composites were investigated by scanning electron microscopy (SEM) in order to evaluate the successful introduction of organic PCMs into PRGO network (Figure 29). The surfaces of the 3D PRGO network prepared from atmospheric plasma reduction on GO film display cork-like expanded structure of connected graphene sheets (Figure 29a) [46]. As illustrated above, the open, percolated structure of PRGO network with inter-layer distances ranging from *ca.* 500 nm to few μm provides an opportunity of sufficient organic PCM introduction in the network by simple immersion. Figure 29b to 29d exhibits SEM images of the three PCM/PRGO composites after immersion process. The open structures of pristine PRGO network are successfully saturated with paraffin (Figure 29b), polyethylene glycol (PEG) (Figure 29c) and octanoic acid (Also known as caprylic acid) materials (Figure 29d). The three different reagents all represent organic PCMs, which require a shape-stabilizer for further industrial application. From the SEM results, the PRGO network provides a room for adsorption of organic PCMs with enhanced shape stability.

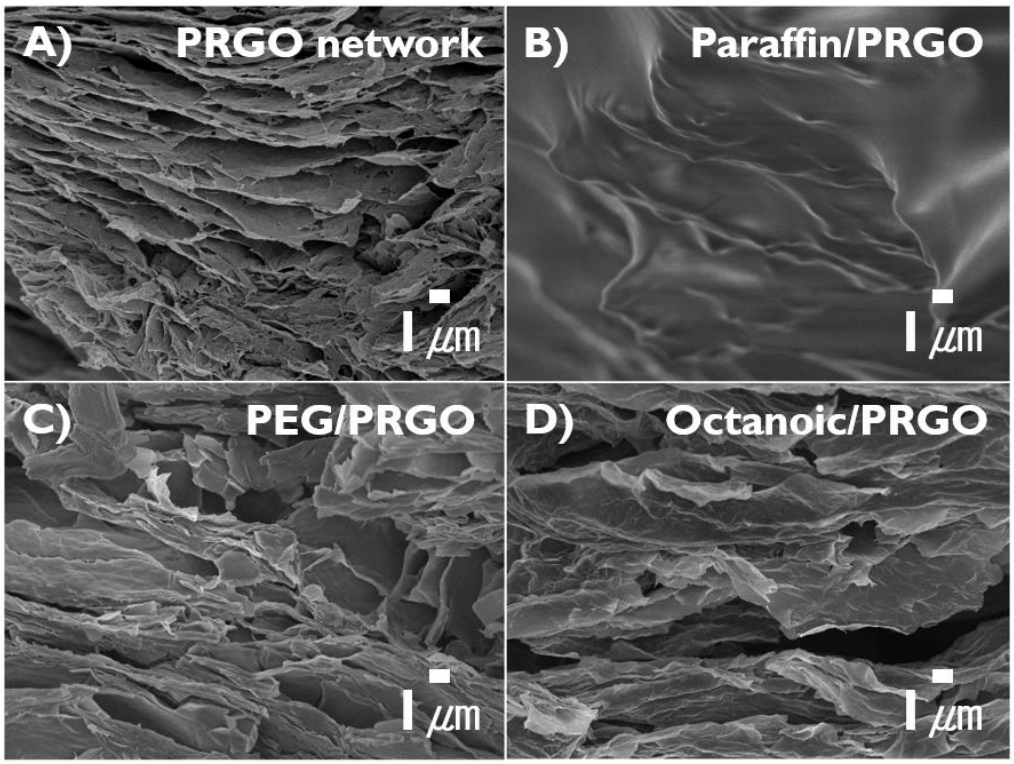

Figure 29. SEM images of the PCM/PRGO composites. a) Pristine PRGO network; b) paraffin/PRGO; c) PEG/PRGO and d) Octanoic/PRGO.

3.2.2. Characterization of PCM/PRGO composites

X-Ray diffraction (XRD) analyses were conducted to understand the structrural change after immersion of organic PCMs in 3D PRGO network to form PCM/PRGO composites. In Figure 30, the XRD spectra presents a broad peak at *ca.* 25° for PRGO network spectrum and this peak stands for typical RGO structure with d-spacing of 3.56 Å [90]. In the XRD spectra of the PCM/PRGO composites, two protruding peaks of paraffin at 21° and 23° are displayed in paraffin/PRGO, while two peaks att 19.2° and 23.4° for PEG and a broad peak at 20.5° for octanoic acid are present in PEG/PRGO and octanoic/PRGO, respectively. According to the previous works, the three PCM/PRGO composites display almost the same XRD d-spacing values with the result of pristine PCMs [104-105]. The XRD results also demonstrate that the introduction of paraffin, PEG and octanoic acid into the 3D PRGO network resulted in no substantial structural change of the corresponding PCM, while almost no PRGO peak was found due to extremely lower concentration (less than 4 wt %) of PRGO network composition in the composites.

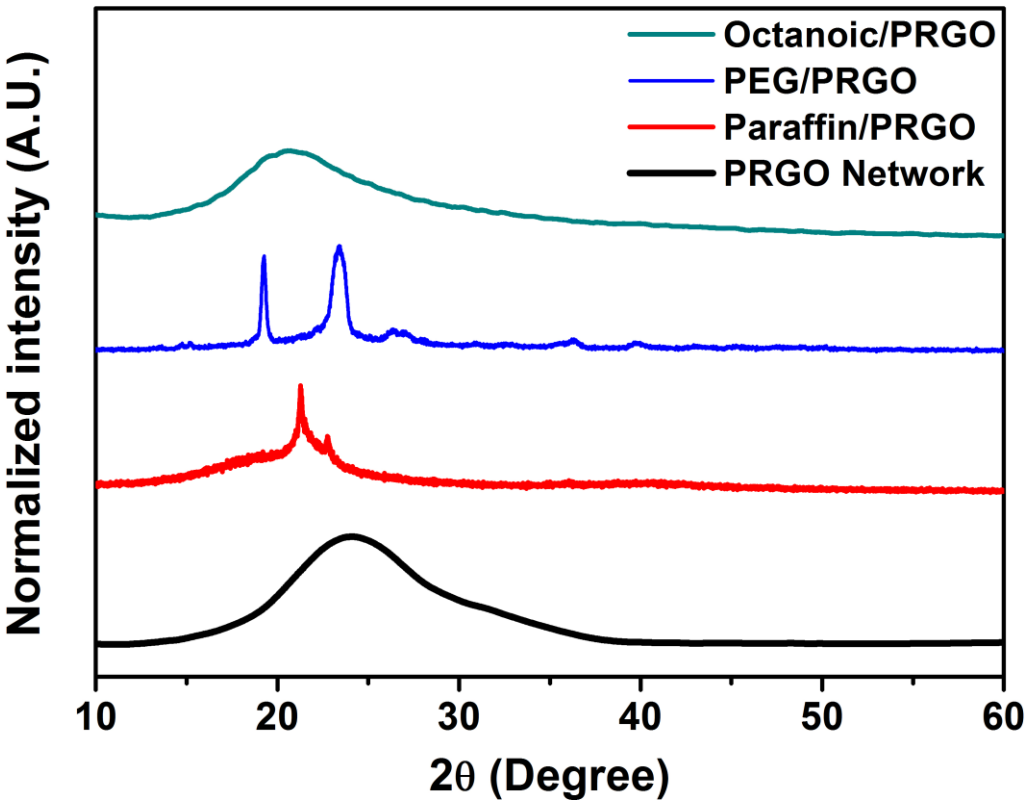

Figure 30. Normalized XRD analysis graph of the PCM/PRGO composites.

To verify the successful introduction of organic PCMs in the PRGO network, additional FT-IR analyses on the PCM/PRGO composites were conducted (Figure 31). In the FT-IR spectra of the PCM/PRGO composites, the two distinct peaks at *ca.* 2850 cm^{-1} and 2940 cm^{-1} for the paraffin/PRGO composite stand for the -CH bond stretching of the structure of paraffin (C_nH_{2n+2}) inside the PRGO network [106-107]. In the PEG/PRGO composite, the stretching peak of the -CH bonds at 2860 cm^{-1}, the C=O double bond vibration peak at 1635 cm^{-1}, the deformation peak of the -CH bonds at 1467 and 1341 cm^{-1}, the hydroxyl (-OH) group bending peak at 1280 and 1240 cm^{-1} and the C–O stretching vibration peak at *ca.* 1148 cm^{-1} in the PEG/PRGO composite all indicate the characteristic -CH chains and hydroxyl groups of PEG polymer backbone in the composite [105]. In the octanoic/PRGO composite FT-IR spectrum, two protruding peaks for the stretching vibration of -CH groups at 2860 cm^{-1} and 2920 cm^{-1}, a sharp C=O carbonyl peak at 1710 cm^{-1} and a small C-O stretching peak at 1270 cm^{-1} represent alkyl chains and the carboxyl groups of octanoic acid in the octanoic/PRGO composite [108]. Owing to small weight fraction of the PRGO network in the PCM composites, a distinct FT-IR peak for the PRGO network was not found. The FT-IR analyses again show that the pristine PCMs are well adsorbed in the PRGO network without significant change in chemical structure.

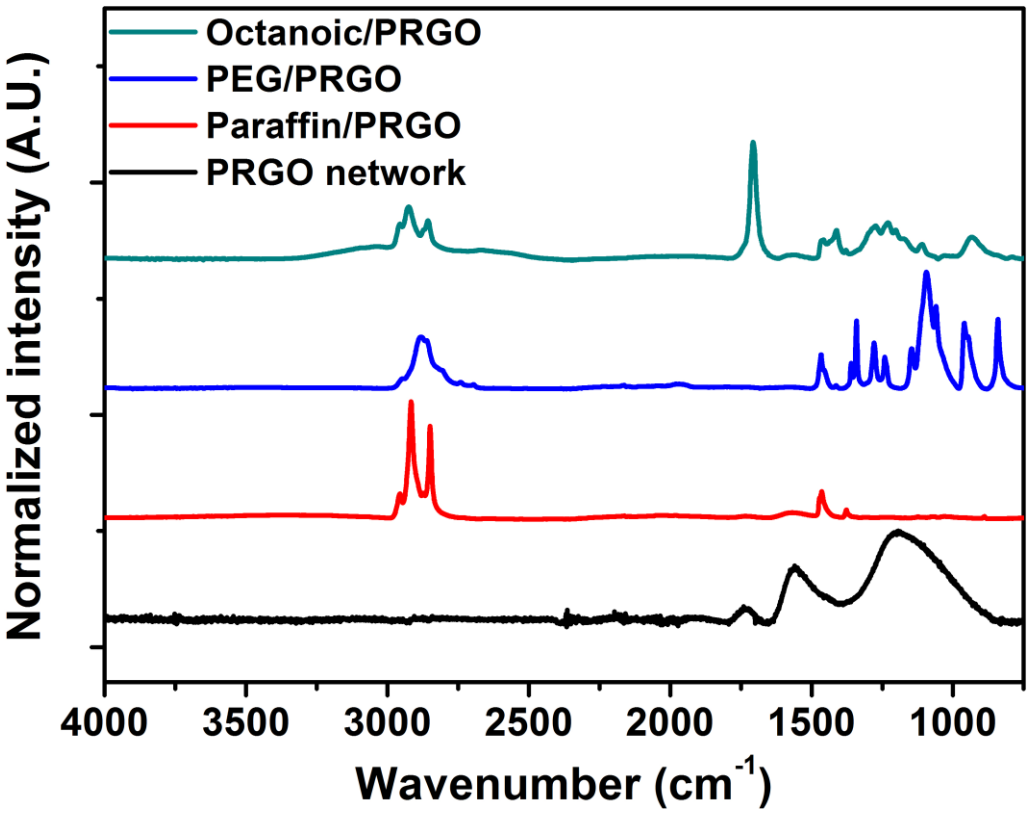

Figure 31. Normalized ATR-FT-IR curve of the PCM/PRGO composites.

The thermophysical properties of the PCM/PRGO composites were evaluated by differential scanning calorimetry (DSC) examination. The change in heat flow was recorded as a function of temperature change (Figure 32). The peak melting temperature and the value of latent heat of fusion for the pristine PCMs and the PCM/PRGO composites were measured as well. In the pristine PCM measurement, three combined peaks protruded at pristine paraffin spectrum, showing peak melting temperature at *ca.* 51 ℃ to completely consume *ca.* 119 J/g heat energy for solid-to-liquid phase transition. The DSC curves of pristine PEG and octanoic acid also demonstrated energy consumption of *ca.* 191 J/g and 144 J/g, at 70 ℃ and 18 ℃, respectively. Especially, the PEG polymer possesses the largest heat of fusion in course of thermal cycling process. In the DSC analyses on the PCM/PRGO composites, the paraffin/PRGO composite displayed an endothermic melting process starting at 26 ℃ and ending at 50 ℃ to completely consume 115 J/g heat energy for solid-to-liquid phase transition. The PEG/PRGO and octanoic/PRGO composites exhibited heat absorption of 184 J/g and 140 J/g, respectively, after DSC measurement at ramping rate of 5 ℃/min (Summarized in Table 5). By comparing the values, the latent heat of fusion of the PCMs after formation of the composites was almost retained. In the previous works, the values of latent heat of fusion were significantly lowered due to

incorporation of large amount of heterogeneous fillers in the PCM matrix, with decreasing weight fraction of the PCMs and the overall thermal stability [109-111]. Nonetheless, since the 3D PRGO network possesses less than 5 % weight fraction of the overall composites, the values of overall latent heat of fusion for the PCM/PRGO composites remain intact.

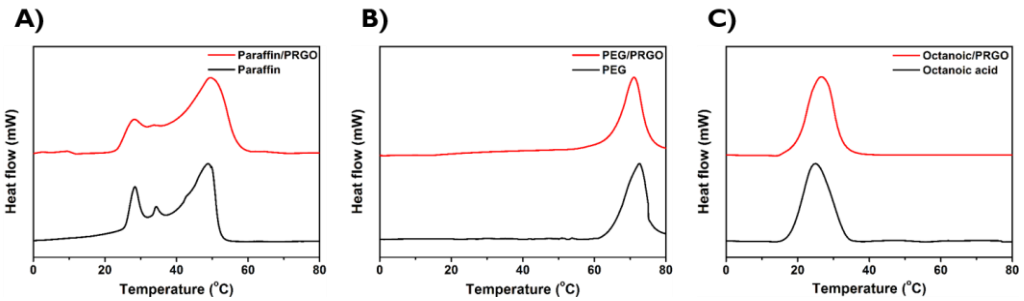

Figure 32. DSC curve of the PCM/PRGO composites.

Table 5. Summarized value of the DSC analysis on the PCM/PRGO composites.

Sample	Peak melting temperature(^{o}C)	Latent heat of fusion (△H)
Paraffin	49.2	119.2
Paraffin/PRGO	49.0	115.3
PEG	72.7	190.9
PEG/PRGO	71.0	184.0
Octanoic acid	25.2	144.4
Octanoic/PRGO	25.0	140.1

The thermal stability of the PCM/PRGO composites was further studied with thermogravimetric analysis (TGA) experiments. Figure 33 displays the TGA curves of the pristine PCMs and the prepared PCM/PRGO composites. Pristine paraffin exhibits a single-step weight loss starting at 201 ℃ and the maximum weight loss behavior at 275 ℃, due to thermal decomposition of the paraffin chain. The paraffin/PRGO composite species also exhibit a one-stage weight loss behavior and the maximum weight loss increased up to 290 ℃. For the pristine PEG, the weight loss begins at 318 ℃ and the maximum weight loss occurs at 383 ℃, while the PEG/PRGO exhibits the maximum weight loss at 391 ℃. For the octanoic/PRGO, the maximum weight loss was increased up to 145 ℃ from 138 ℃ of the pristine octanoic acid. The PRGO network is robust enough to protect the impregnated PCMs from degrading at the ordinary boiling point, thus enhancing the onset decomposition temperature of composite PCMs.

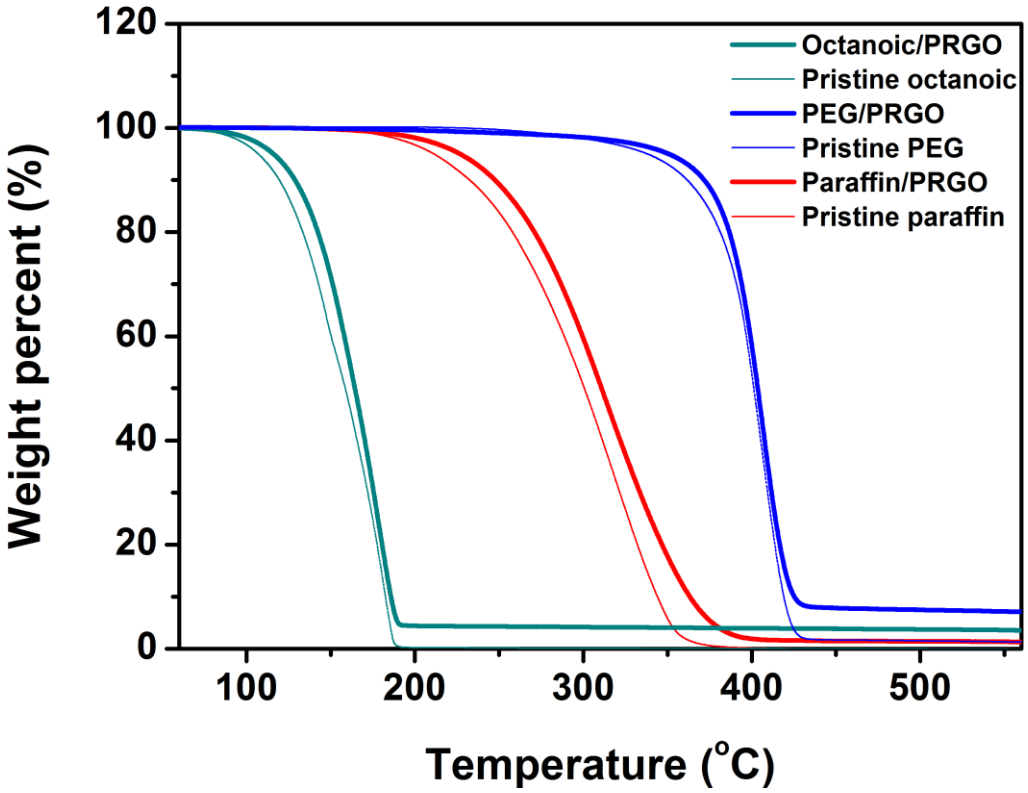

Figure 33. TGA graph of the PCM/PRGO composites. The TGA experiments were conducted in inert N_2 atmosphere.

3.2.3. Enhanced PCM performance of PCM/PRGO composites

The long-term thermal cyclability of the PCM/PRGO composites was examined by DSC measurement for 30 cycles (Figure 34). In the DSC graph, the shape of the DSC curve for 1st cycle and the DSC curves for the later cycles are slightly different for all three composites, with changes in the position of protruding peak. The slight modification in DSC curves can be explained as a re-positioning of the PCM materials in the PRGO network, followed by stabilization. Furthermore, after recurring DSC measurement on the three PCM/PRGO composites for 30 cycles, less than 3 % reduction in the value of latent heat of fusion was measured, as presented in Figure 35. The minute reduction in the latent heat of fusion for the three PCM/PRGO composites can be attributed to slight PCM evaporation phenomena during the 30-cycle DSC measurement [112]. From the DSC cyclability results, the PRGO network worked as a successful shape-stabilizer/container, and re-positioning of the PCM materials in the overall composites induced insignificant change in the amount of latent heat of fusion.

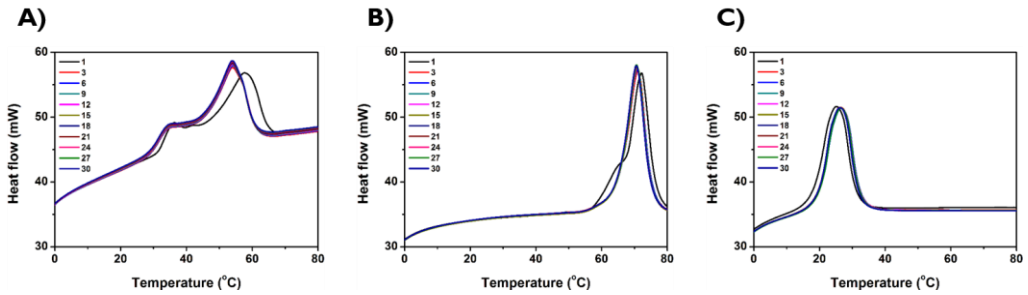

Figure 34. DSC heating curves of the PCM/PRGO composites for 1 to 30 cycle. a) DSC curves of the paraffin/PRGO composite; b) DSC curves of the PEG/PRGO composite; c) DSC curves of the octanoic/PRGO composite. All experiments were conducted in inert N_2 atmosphere.

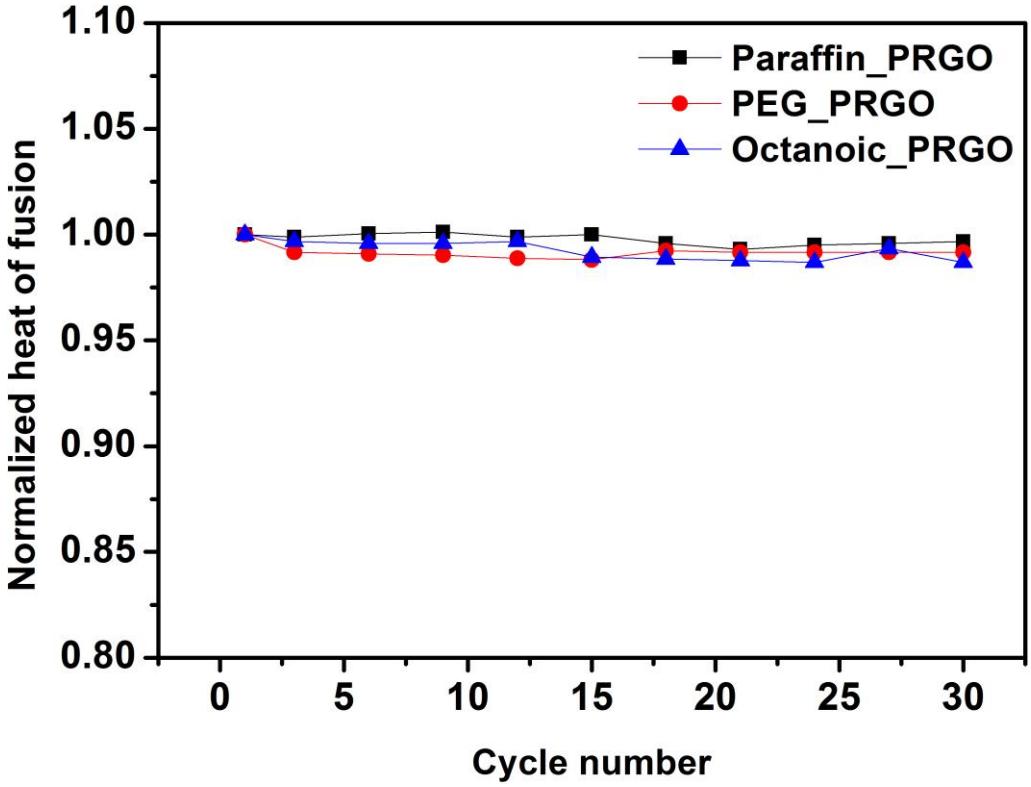

Figure 35. Normalized value of latent heat of fusion of the PCM/PRGO composites after 30-cycle DSC measurement.

The influence of the introduction of PRGO network on the thermal/ electric conductivities of the PCM/PRGO composites were studied (Figure 36, Figure 37 and Table 6). The thermal conductivity of the pristine PCMs and the PCM/PRGO composites was measured by the method using DSC [92-93]. Using fluorine (melting point: 112 ℃) as a reference material, thermal conductivity of the PCM/PRGO composites was determined by the difference in the slope of the DSC endothermic curves of fluorine and the target material. The thermal conductivity measurement was done three times for each sample and the calculated thermal conductivity values were averaged (Figure 36). By DSC mode calculation, thermal conductivities of the paraffin/PRGO, PEG/PRGO and octanoic/PRGO were calculated to be 0.62, 0.06 and 0.38 W/ m•K, respectively (Table 6). Compared with the thermal conductivity values of the pristine PCMs, where the values are 0.24, 0.04 and 0.146 W/ m•K for the paraffin, PEG and octanoic acid, the thermal conductivities of the PCM/PRGO composite increased by up to *ca.* 2.5-fold (Figure 37). Considering the small weight fraction of the PRGO network in the composites, the 2.5-fold increase in the thermal conductivity of the PCM/PRGO composites overwhelm the previous work using RGO aerogel as a filler for PCM [89].

The electric conductivity of the PCM/PRGO composites were also calculated by 4-probe method. Owing to the insulating properties of traditional

PCMs, the utilization of the PCMs in electronic devices has been restricted. In this work, the PCM/PRGO composites exhibited enhanced electric conductivity values ranging from $5*10^{-3}$ to $8*10^{-2}$ S/cm (Table 6). From these conductivity measurement results, the PCM/PRGO composites offer a potential use in thermal energy storage application due to the increased heat transfer action by greater thermal/electric conductivity.

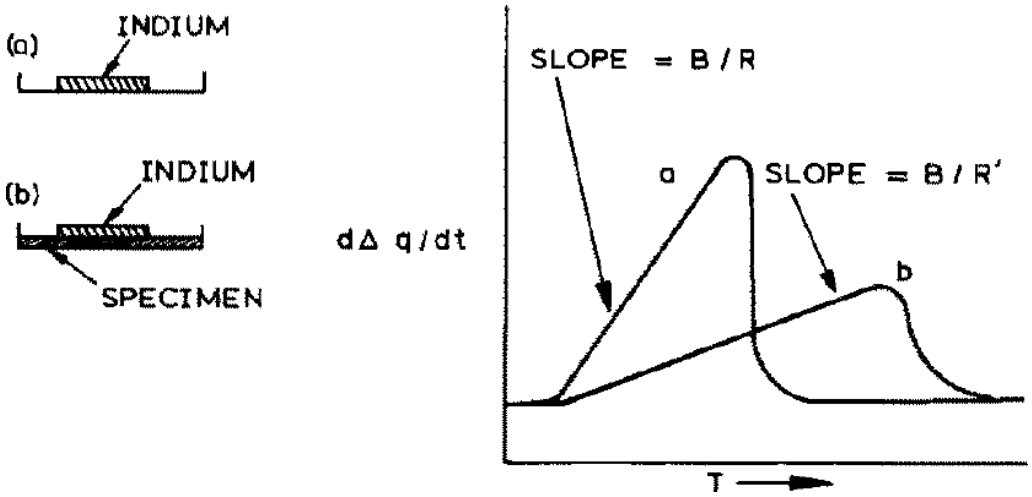

Figure 36. DSC curves for melting of indium: a) indium; b) indium+specimen sheet. Reprinted with permission from ref 92. Copyright 1988 Elsevier.

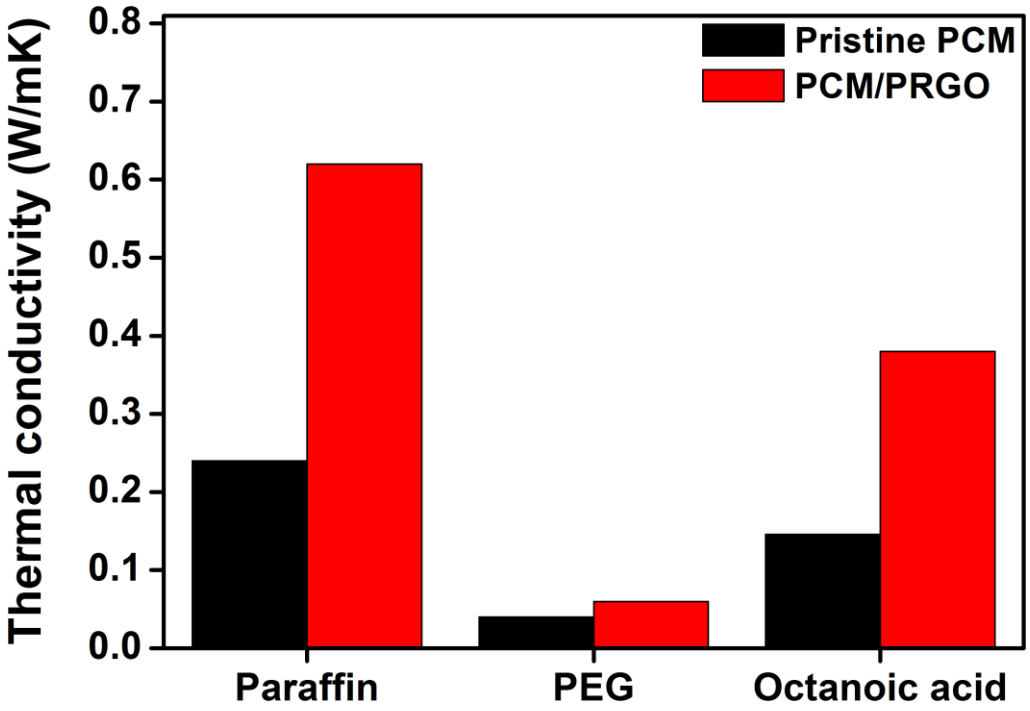

Figure 37. Comparison graph of thermal conductivity values of pristine PCMs and the PCM/PRGO composites.

Table 6. Physical parameters of the PCM/PRGO composites.

Sample	Thermal conductivity (W/m·K)	Electric conductivity (S/cm)
Pristine paraffin	0.24	- (insulating)
Paraffin/PRGO	0.62	$5.23 * 10^{-3}$
Pristine PEG	0.04	- (insulating)
PEG/PRGO	0.06	$5.45 * 10^{-3}$
Pristine octanoic acid	0.146	- (liquid state)
Octanoic acid/PRGO	0.38	$8.33 * 10^{-2}$

Herein, the PCM/PRGO composites comprised of 1) 3D PRGO network generated by atmospheric plasma reduction on GO film and 2) three different organic PCMs (paraffin, PEG and octanoic acid) were prepared by facile immersion of the as-fabricated PRGO network in liquid-state organic PCMs. Instead of compact structure of stacked GO sheets, open, percolated PRGO network with inter-connected RGO sheets enable simple impregnation of liquid-state PCMs into the network by capillary forces. The PRGO network work as a shape-stabilizer and property enhancer of the organic PCMs. Compared with each pristine PCM, the PCM/PRGO composites exhibited increased shape-stability and the values of latent heat of fusion were retained owing to low weight fraction of PRGO network in the composites. At last, the PCM/PRGO composites exhibited enhanced thermal/electric conductivities, demonstrating up to 2.5-fold increase of thermal conductivities compared with pristine PCMs. This methodology opens a promising route in use of the RGO-incorporated PCMs in industrial thermal energy control of solar panel and lithium ion batteries.

3.3. Fabrication of 3-dimensional graphene monolith with paraffin *via* L-AA reduction for PCM application

3.3.1. Preparation of paraffin/pRGO composites

Figure 38 illustrates the preparation of the paraffin/pRGO composites by simple immersion method. At first, the dried GO powders synthesized from a slightly modified Hummers' method were dissolved in DI water and the concentration of the GO solution was set to 0.01, 0.05, and 0.5 wt % (Figure 38a). The porous structure of partially reduced graphene oxide (pRGO) monoliths are not generated at the higher concentration of GO than 0.5 wt %. To fabricate pRGO monoliths, the GO solution was mixed with L-ascorbic acid (L-AA) powder with vigorous stirring (mass ratio of GO: L-AA = 2:1). After complete mixing, the L-AA/GO solution was transferred to appropriate vessel and kept in 100 ºC oven for 30 min. The pRGO monolith was then formed in shape of black cylinder floating on the water (Figure 38b) [46]. After freezing for 30 min and thawing for 30 min, the pRGO monoliths were further lyophilized to eliminate water residue on the monoliths. Li *et al.* described that the reduced GO sheets are pushed away by ice to form cork-like structure in freezing step, and the ice are eliminated in thawing & lyophilization process (Figure 39). The as-prepared 3D pRGO monolith samples were then immersed in molten paraffin at 60 ºC for 30 min to obtain the paraffin/pRGO composites

(Figure 38c). Due to percolated, open structure of pRGO monoliths, molten paraffin is easily impregnated into the monolith and solidifies.

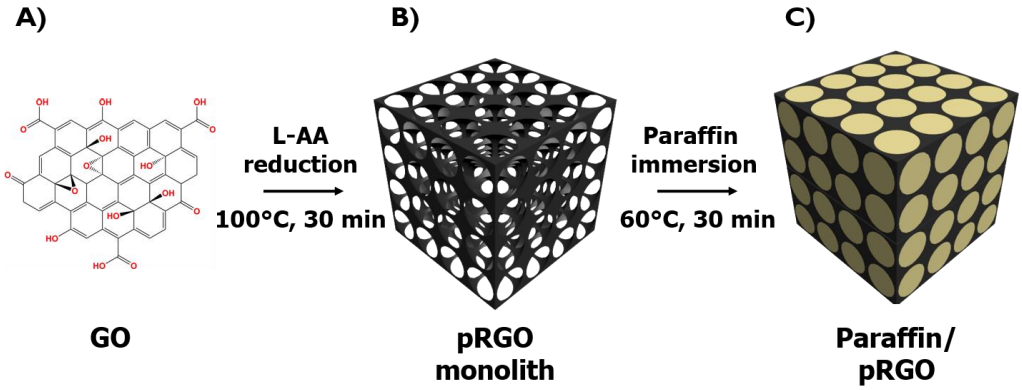

Figure 38. Schematic illustration of the preparation of the paraffin/pRGO composites. a) GO powders were dispersed in distilled water with varying concentration; b) Porous pRGO monolith formed after reduction of GO solution with L-AA at 100 ºC for 30 min; c) Paraffin/pRGO composite obtained after immersion of cylindrical pRGO monolith in molten paraffin for 30 min.

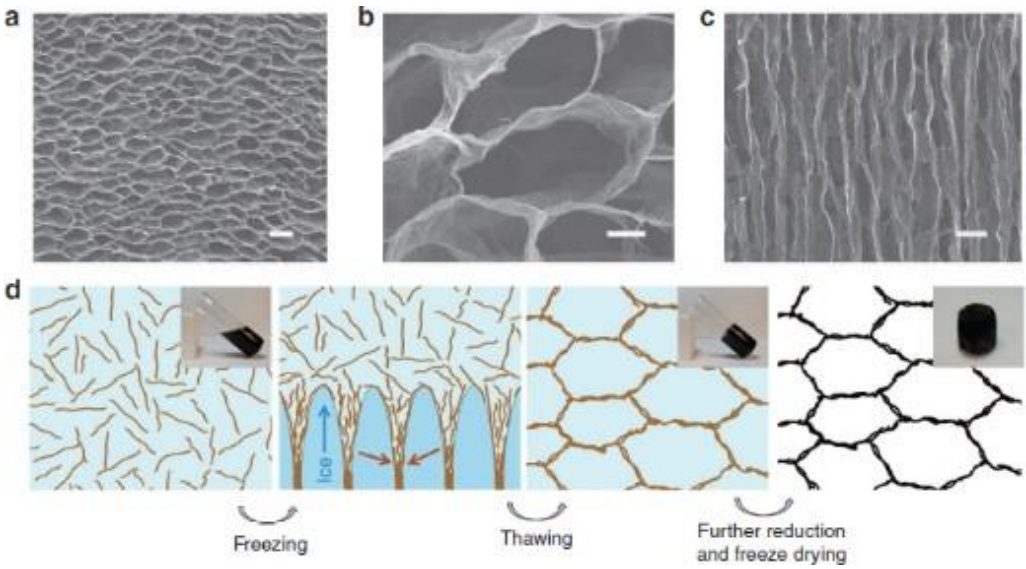

Figure 39. Formation mechanism of pRGO monolith via L-AA reduction of GO. Reprinted with permission from Ref 46. Copyright 2012 Right Managed by Nature Publishing Group.

The micro-scale morphologies of the pristine pRGO monoliths and the paraffin/pRGO composites were examined by SEM analyses (Figure 40). In Figure 40a to 40c, the SEM images of pristine pRGO monoliths synthesized from reduction of GO solutions with different concentration (0.01, 0.05 and 0.5 wt %) exhibited cork-shaped micro structure of inter-connected RGO sheets. In the inset images of Figure 40, the average pore size reduced as the initial GO concentration increases, from *ca.* 2 ~ 5 μm of pRGO_0.01 to *ca.* 0.5 ~ 1 μm of pRGO_0.05. During this reaction process, the dispersed RGO sheets are accumulated to generate diverse shape of micro-porous scaffold with respect to the GO solution concentration and the shape of vessel [45-46]. Figure 40d to 40f displays SEM images of the paraffin/pRGO composites. From the SEM analyses, the micro-pores of the three different pRGO monoliths were soaked with paraffin materials, which are seen to be glittering in the SEM images. From the results, it can be inferred that the pores of pRGO monolith provided a room for paraffin packing, and the interaction between solidified paraffin and the surface of pRGO monolith was sturdy enough to preserve the overall composite structure.

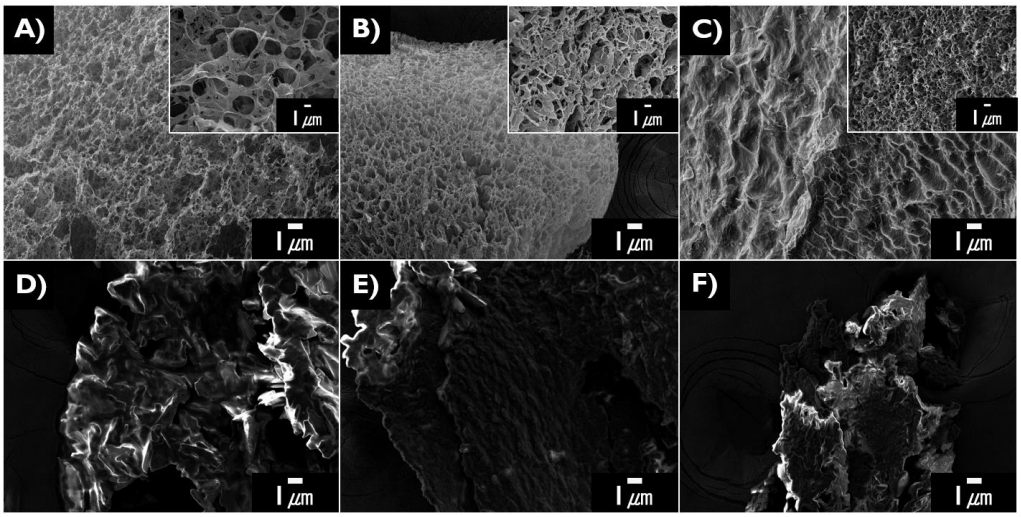

Figure 40. SEM images of a) pristine pRGO_0.01, b) pristine pRGO_0.05 and c) pristine pRGO_0.5 (Inset images: X5000 magnification of each pristine pRGO sample); SEM images of d) paraffin/pRGO_0.01, e) paraffin/pRGO_0.05 and f) paraffin/pRGO_0.5.

3.3.2. Characterization of paraffin/pRGO composites

XRD analysis (Figure 41) was conducted to verify successful immersion of paraffin materials in pRGO monolith. In Figure 41, the XRD graph for the paraffin/pRGO composites shows two prominent peaks at 21° and 23°, the characteristic peaks of pristine paraffin [104]. Concurrently, the pristine pRGO monoliths exhibited broad peak at *ca.* 25° for typical RGO structure [90]. The broad peak demonstrates the various degree of reduction or pRGO sheets in the monolith. In the XRD graph, characteristic d_{002} peak for the paraffin/pRGO composites was not changed significantly. The result indicates that the immersion of molten paraffin into the pRGO monolith and solidification induced no crucial structural change of the intrinsic paraffin material. And also almost no pRGO-related peak was detected in the XRD curve of the paraffin/pRGO composites, due to lower fraction (less than 5 wt %) of pRGO scaffold weight in the composites.

Additional FT-IR investigation on the paraffin/pRGO composites were done to verify successful introduction of paraffin in the pRGO monoliths (Figure 42). Two small peaks at 1050 cm^{-1} and 1715 cm^{-1} were observed and these peaks respectively indicate minute C-O stretching vibration and C=O double bond vibration. The mild reduction by L-AA on GO left small fraction of carboxyl groups, while annihilating hydroxyl groups on basal plane. The FT-

IR spectrum of pristine paraffin displays two strong -CH peaks at *ca.* 2850 cm^{-1} and 2940 cm^{-1} and these peaks represent the alkyl chain structure of paraffin. In the FT-IR spectra of the paraffin/pRGO composites, only two protruding peaks at *ca.* 2850 cm^{-1} and 2940 cm^{-1} again prove that the alkyl chain structure of paraffin remains inside the pRGO monolith. From these results, the FT-IR analyses show that the paraffin materials were successfully incorporated in the composite without modification in chemical structure, with trivial pRGO-related peaks were found due to low fraction of pRGO in the composites.

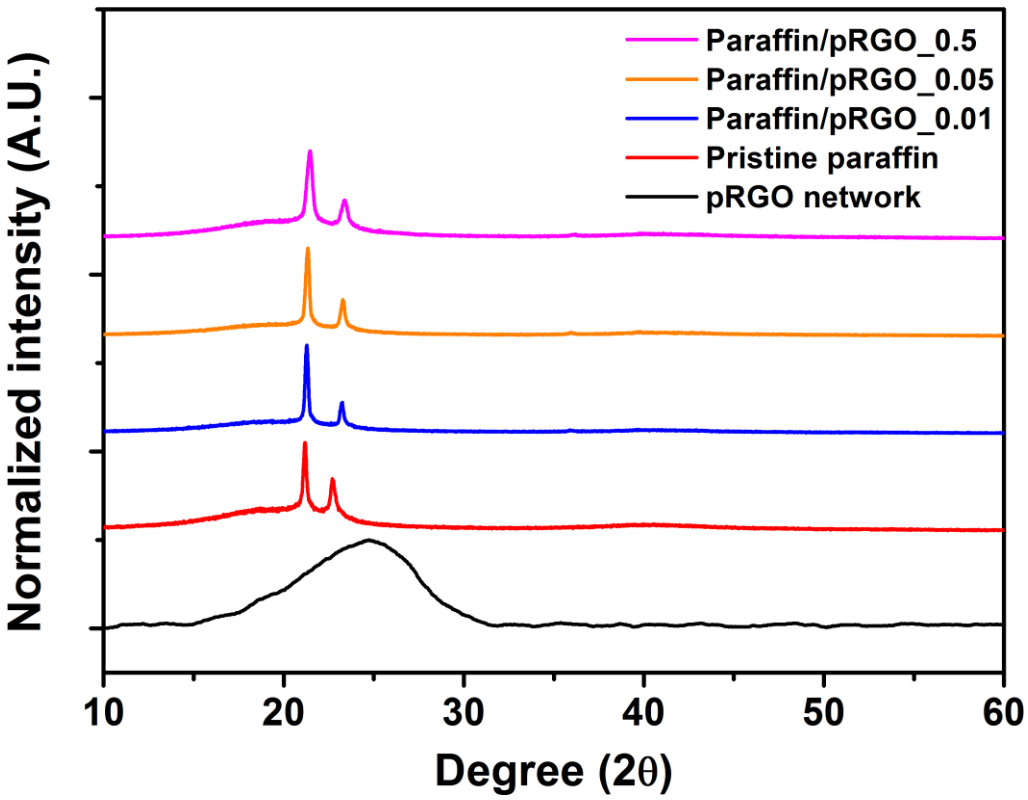

Figure 41. Normalized XRD analysis graph of the paraffin/pRGO composites.

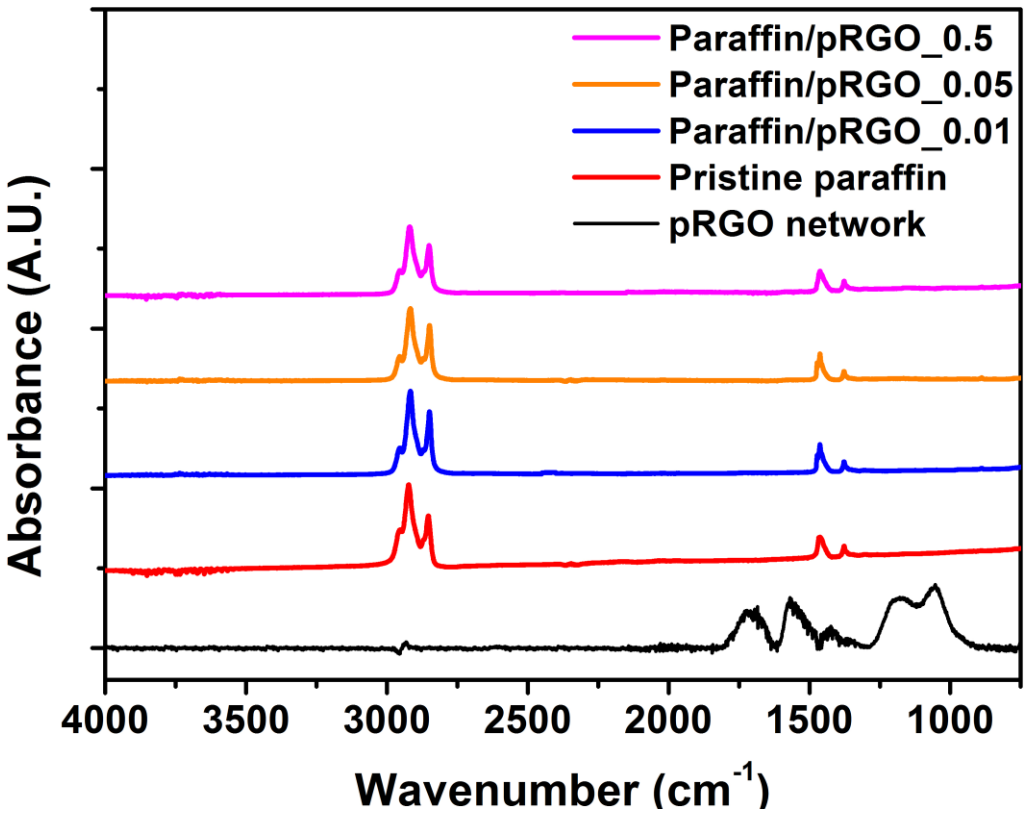

Figure 42. FT-IR curve of the paraffin/pRGO composites.

The thermal behavior of the paraffin/pRGO composites were examined by adjusting condition parameters such as the initial concentration of corresponding pRGO monolith. The change in heat flow was recorded as a function of temperature change in differential scanning calorimetry (DSC) examination (Figure 43). The peak melting temperature and the value of latent heat of fusion were also measured. In the case of DSC analyses on the pristine paraffin and the paraffin/pRGO composites, the pristine paraffin exhibited heat of fusion of 119.2 J/g after DSC measurement at ramping rate of 10 ℃/min. In case of the paraffin/pRGO composites, the latent heat of fusion after formation of the composites was almost maintained, exhibiting 116.0 J/g, 115.9 J/g and 115.2 J/g for paraffin/pRGO_0.01, paraffin/pRGO_0.05 and paraffin/pRGO_0.05, respectively. The peak melting temperature of the composites demonstrated slight change, ranging from 48.8 to 49.7 ℃. In previous works, the value of latent heat of fusion might be lowered due to incorporation of large amount of graphitic fillers in the PCM matrices, decreasing the thermal stability. Nonetheless, the 3D pRGO monolith occupies less than 4 % weight of the overall composites, with the overall latent heat of fusion maintained.

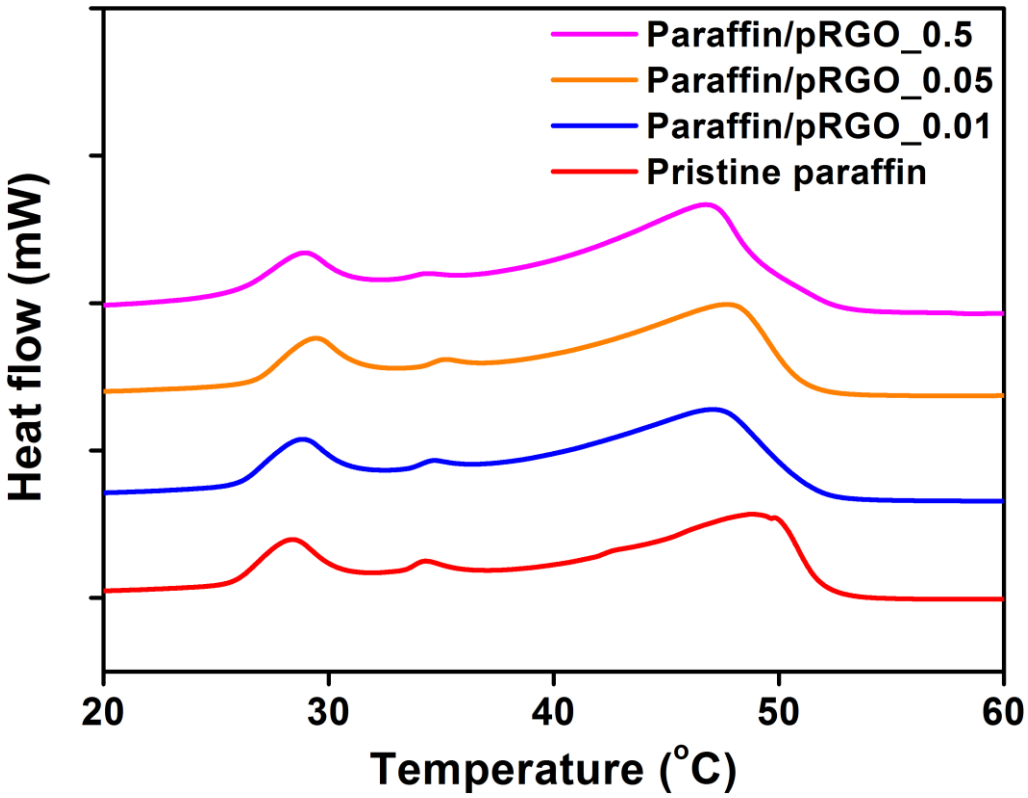

Figure 43. DSC curve of the paraffin/pRGO composites. The DSC experiments were conducted in inert N_2 flow.

Table 7. Summarized value of the DSC analysis on the paraffin/pRGO composites.

Sample	Peak melting temperature(^{o}C)	Latent heat of fusion (ΔH)
Paraffin	48.8	119.2
Paraffin/pRGO 0.01	48.5	116.0
Paraffin/pRGO 0.05	47.5	115.9
Paraffin/pRGO 0.5	46.8	115.2

The thermal barrier properties of the paraffin/pRGO composites was studied by TGA analyses to measure the maximum weight loss temperature (Figure 44). In the TGA graph, the weight loss occurring at a temperature range from 200 to 400 ℃ is due to thermal degradation of the alkyl chains of paraffin molecules, and the remaining weight fraction over 500 ℃ belongs to the pRGO monoliths.

The detailed 1st derivative thermogram of the TGA weight-loss curves of the paraffin/pRGO composites (Figure 45) presents that the value of onset decomposition temperature of the paraffin/pRGO composites increased from 216.32 ℃ of the pristine paraffin to 236.54 ℃ of the paraffin/pRGO_0.5 sample, and the maximum weight loss temperatue also increased from 289.82 ℃ to 332.45 ℃ (Summarized in Table 8). Since the pRGO monolith made from 0.01 wt % GO solution is relatively lower in density, its fraction in the paraffin/pRGO_0.01 is extremely low and therefore increase in onset decomposition temperature was relatively small, from 216.32 to 216.8 ℃. Nonetheless, the gradual increase in the onset decomposition temperature and maximum weight loss temperature indicates that the paraffin/pRGO composites acquired higher thermal stability by introducing pRGO monoliths as thermal barrier materials.

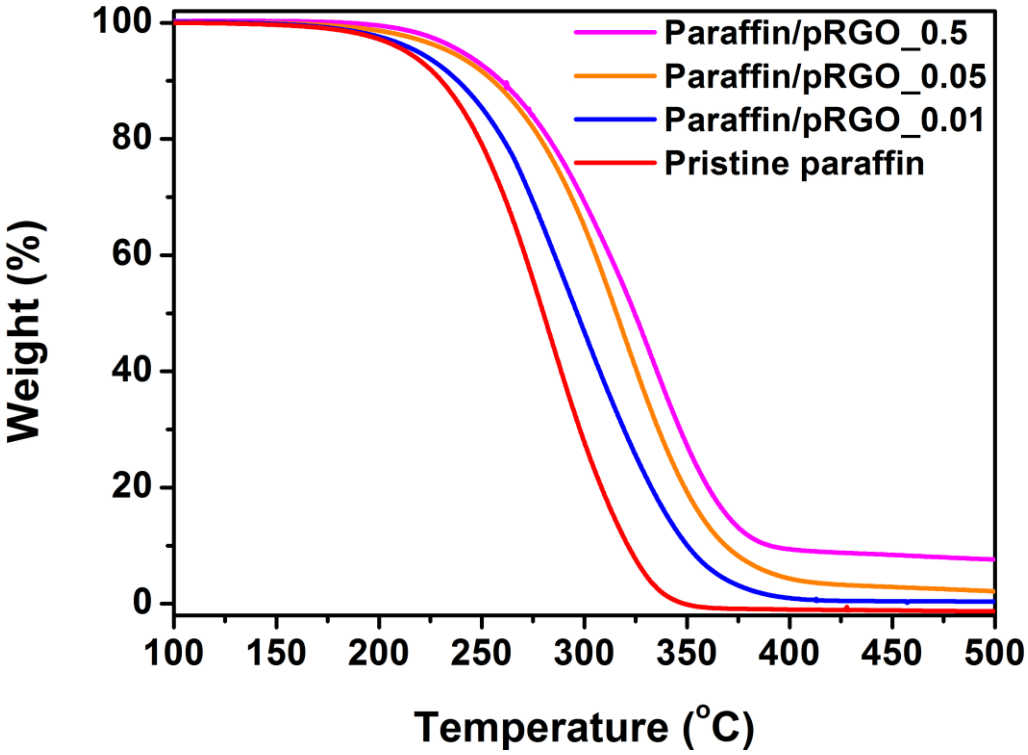

Figure 44. TGA graph of the paraffin/pRGO composites. The TGA experiments were conducted in inert N_2 atmosphere.

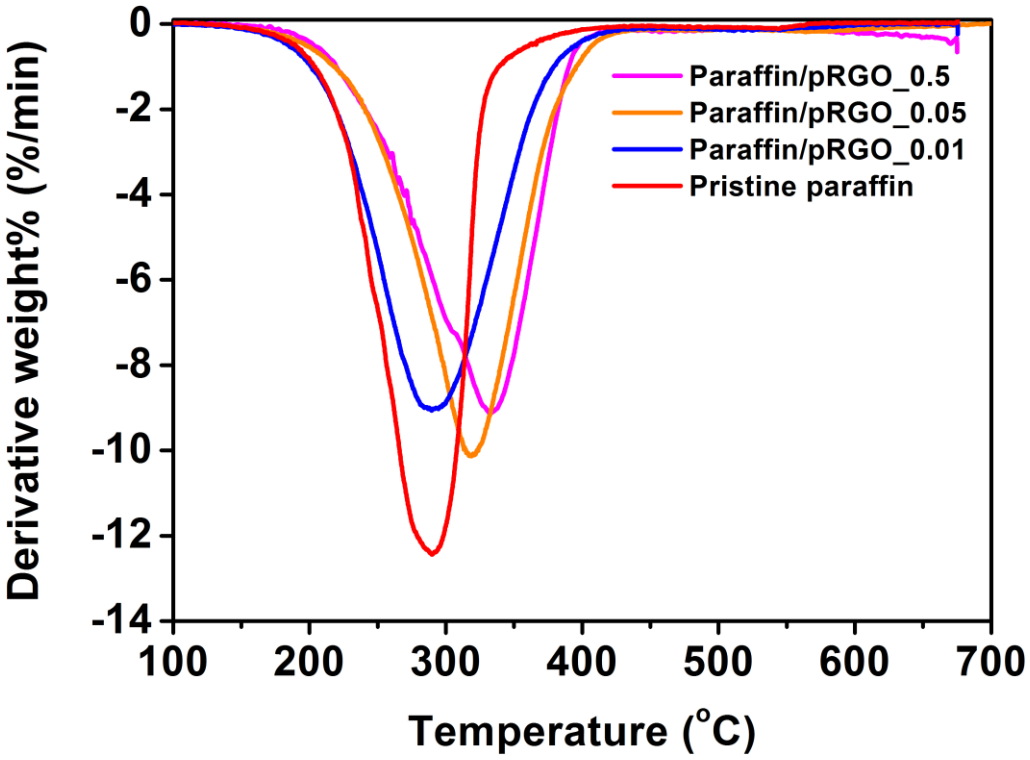

Figure 45. 1st derivative graph of the TGA curve.

Table 8. Onset decomposition temperature and maximum weight loss temperature of the paraffin/pRGO composites after TGA analyses.

Sample	Onset decomposition temperature (ºC)	Maximum weight loss temperature (ºC)
Paraffin	216.32	289.82
Paraffin/pRGO 0.01	216.8	290.31
Paraffin/pRGO 0.05	235.51	318.32
Paraffin/pRGO 0.5	236.54	332.45

3.3.3. Enhanced PCM performance of paraffin/pRGO composites

The long-term cycling stability of the paraffin/pRGO composites was carefully examined by DSC cycling for 30 solid–liquid phase-transition cycles (Figure 46). In Figure 46, the 1st DSC cycle of the paraffin/pRGO materials exhibited a protruding peak at 32 ^{o}C. As cycling test proceeded to 30 times, however, the intensity of protruding peak at 32 ^{o}C was slightly diminished and the peak positions were slightly modified. Overall, the DSC heat flow curves stabilized from 3rd cycle to 30th cycle. From the DSC curves, it can be concluded that the paraffin chain was re-organized in the cycling process and the chain stabilized after sufficient cycling. In the viewpoint of heat storage capability, only *ca.* 2 % reduction in the value of latent heat of fusion was observed for the paraffin/pRGO_0.01. The *ca.* 1 % reduction in latent heat of fusion for the paraffin/pRGO_0.05 and the paraffin/pRGO_0.5 was also found (Figure 47). This small reduction in the latent heat of fusion for the paraffin/pRGO composites can be attributed to minute loss during the DSC process owing to evaporation of PCMs [112]. Overall, this results indicate that the paraffin/pRGO composites maintain their heat storage capacity for long cycling process.

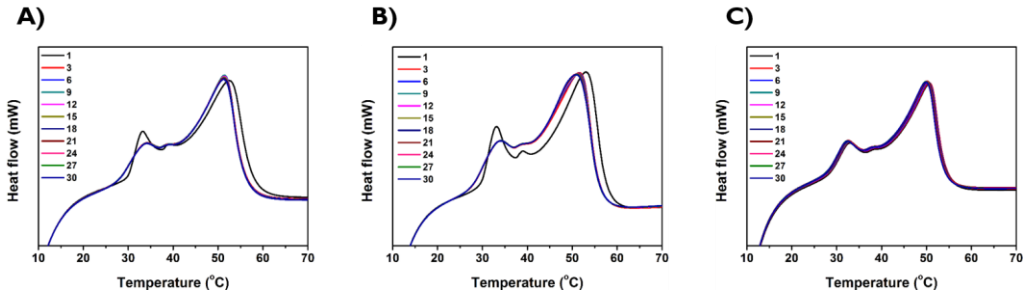

Figure 46. a) DSC curve of the paraffin/pRGO_0.01 after 30 solid–liquid phase-transition. The DSC experiments were conducted in N_2 flow; b) DSC curve of the paraffin/pRGO_0.05 after 30 solid–liquid phase-transition; c) DSC curve of the paraffin/pRGO_0.5 after 30 solid–liquid phase-transition.

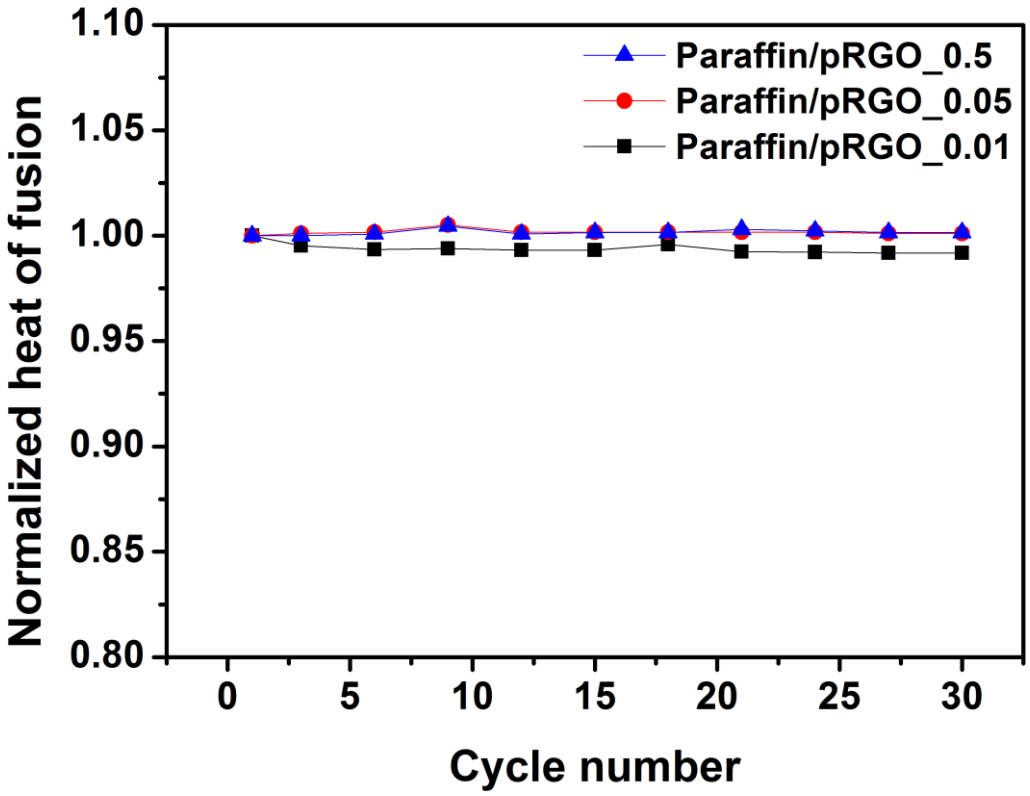

Figure 47. Normalized latent heat of fusion values of the paraffin/pRGO composites.

The enhancement in the thermal/electric conductivities of the paraffin/pRGO composites were investigated with DSC-based thermal conductivity measurement method and 4-probe method (Figure 48 and Table 9). The thermal conductivity of the pristine paraffin and the paraffin/pRGO composites was calculated by DSC-based method [92-93] (Details described in section 3.2.3). By DSC calculation, thermal conductivities of the pristine paraffin and paraffin/pRGO_0.01, paraffin/pRGO_0.05 and paraffin/pRGO_0.5 were calculated to be 0.24, 0.52, 0.68 and 0.97 W/ m•K, respectively (Table 9). In comparison with the thermal conductivity values of the pristine paraffin, the thermal conductivity measurement of the paraffin/pRGO composites exhibited *ca.* 4 times increase in thermal conductivity (Figure 48). Considering the small weight fraction of the pRGO monolith in the composites, the 4-fold increase in the thermal conductivity of the paraffin/pRGO composites might provide a promising route in enhancement in the rate of heat uptake and release in thermal energy storage process.

On account of the basic insulating properties of paraffin, the paraffin utilization in electronic devices has been quite obstructed. Nonetheless, introduction of super-conductive pRGO monolith in PCM might open a new route in the future application of pRGO-reinforced PCMs in electronic devices.

To investigate the enhancement in electric conductivity of the paraffin/pRGO compsites, the electric conductance was measured by 4-probe method. For electric conductivity measurement, all samples were cut into flat, round pellet with known thickness. From the conductivity measurement, the paraffin/pRGO composites showed increased electric conductivity values from $3.8*10^{-3}$ to $4.2*10^{-1}$ S/cm as the initial GO concentration increased from 0.01 to 0.5 wt % (Table 9). This result is due to the fact that the densely packed pRGO sheets of the pRGO monolith from highest GO concentration induced higher electric conductance. From these conductivity measurement results, the paraffin/pRGO composites present a promising route in application of RGO-reinforced paraffin PCM in various thermal/electronic application.

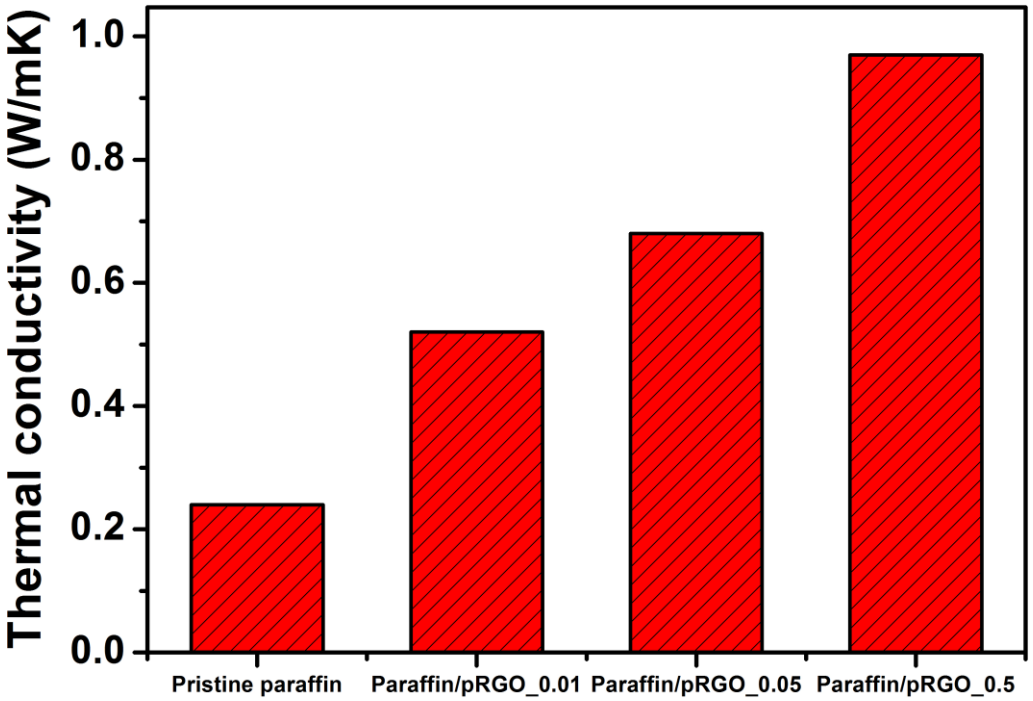

Figure 48. Comparison graph of thermal conductivity values of pristine paraffin and the paraffin/pRGO composites.

Table 9. Physical parameters of the paraffin/pRGO composites.

Sample	Thermal conductivity (W/(m·K))	Electric conductivity (S/cm)
Pristine paraffin	0.24	-
Paraffin/pRGO_0.01	0.52	$3.8*10^{-3}$
Paraffin/pRGO_0.05	0.68	$8.5*10^{-2}$
Paraffin/pRGO_0.5	0.97	$4.2*10^{-1}$

In summary, the composite materials composed of paraffin and 3D pRGO monoliths were successfully prepaerd by two-step process: 1) fabrication of pRGO monolith by mild L-AA reduction of three different GO solutions (0.01, 0.05 and 0.5 wt %) and 2) subsequent immersion of the pRGO monoliths in molten paraffin for complete soaking. These paraffin/pRGO composites were then applied as phase change material (PCM) with increased thermophysical/electric properties. Compared with conventional paraffin, the paraffin/pRGO composites exhibited greatly enhanced thermal stability and retained latent heat of fusion. The thermal stability of all composites was observed to improve with increasing primary concentration of GO solution (0.01 to 0.5 wt %) in reduction process, due to excellent barrier properties of denser graphene network from 0.5 wt % solution. Additionally, the paraffin/pRGO composites showed superb thermal/electric conductivities, showing a promising pathway for industrial and practical applications such as thermal energy storage device for solar panel and nano-electronics.

4. CONCLUSIONS

1. Free-standing, 3D expanded plasma-reduced graphene oxide (PRGO) films are synthesized using a rapid thermal exfoliation/deoxygeneation process of graphene oxide (GO) thin film *via* brief atmospheric plasma treatment. This synthetic methodology is termed as 'plasma reduction' throughout this dissertation. The 3D PRGO films are formed by brief atmospheric plasma treatment (less than 20 sec) on GO film, with sufficient argon flow. Due to sudden formation of oxygen-related gases during thermal exfoliation, the RGO sheets are expanded outward to form 3D network of physically linked RGO sheets. Systematic analyses confirmed that the 3D PRGO films can be formed without any hetero-atom incorporation and possess increased specific surface area.
2. 3D RGO monoliths are formed spontaneously during the mild reduction of GO using L-ascorbic acid (L-AA). This reduction method is referred as 'L-AA reduction' throughout this dissertation. The spontaneous production of 3D RGO monolith by L-AA reduction facilitates the conversion of 2D graphene sheets into 3D architecture. The pore size and density of the 3D RGO monoliths can be easily adjusted by manipulating the concentration of GO solution. This new methodology can illuminate a great possibility for fabricating 3D graphene network material with

controlled architecture.

3. The 3D expanded PRGO film prepared from plasma reduction is utilized as an active material for supercapacitor electrode. The increased contact area of electrolyte-electrode interface and high electric conductivity of 3D PRGO films help obtain large specific capacitance of carbon-EDLC system. By 200W plasma treatment, PRGO film possess lowest O/C ratio of 0.116 and highest surface area of 312 m^2/g. In this study, as-prepared 3D PRGO structure showed largest specific capacitance of 150 F/g at 1 A/g and maintained 82 % capacitance retention after 1000 cycles, for its high surface area and intrinsic physical/chemical stability. In comparison with the RGO film prepared with harsh hydrazine treatment, the PRGO film exhibited superior performance and the plasma reduction method illuminates a promising pathway for environmental-friendly production of supercapacitor electrode.
4. The 3D expanded PRGO films prepared by 200W atmospheric plasma treatment are utilized as supporting material for various organic phase change materials (PCMs). In this work, three representative organic PCMs, paraffin, polyethylene glycol and octanoic acid, are incorporated into the 3D PRGO film by simple immersion method. In order to enhance the intrisically low thermal/electric conductivities and shape-stability of

the organic PCMs, the 3D PRGO film act as a property-enhancer and shape-stabilizer simultaneously. The composite material of PCM and PRGO demonstrate increase in thermal/electric conductivities with retained latent heat of fusion. Thermal cyclability test confirmed that the composite materials maintain its latent heat of fusion after 30 cycles, showing its potential application in nano-electronics and energy storage devices.

5. The 3D pRGO monoliths prepared from mild reduction of GO solution using L-AA are utilized as a property-enhancer/shape-stabilizer of paraffin. Although paraffin has been used as representative PCM for its low-cost and large latent heat of fusion, the material possesses quite low thermal/electric conductivities and exhibit low shape-stability during solid-liquid transition. Therefore, the molten paraffin is impregnated into 3D pRGO monoliths by simple immersion and then solidified to produce paraffin/RGO composites. The pore size and the density of the 3D pRGO monoliths are adjusted by using different concentration of GO solution (from 0.01 to 0.5 wt %) in initial reduction process. As the concentration of GO solution increases, the density of the resultant monolith increases and the physical properties of the corresponding paraffin/pRGO composite enhanced, showing 3-fold enhancement of thermal

conductivity. Due to low fraction of pRGO monolith in the composites, the overall latent heat of fusion is retained. This simple immersion pathway provides the possible candidate for the practical applications of 3D RGO network in PCM industries.

In summary, two different methods in preparation of 3D RGO network were demonstrated as plasma reduction and L-ascorbic acid (L-AA) reduction of GO. In plasma reduction, the 3D expanded RGO film is produced from brief atmospheric argon plasma treatment on GO film due to rapid thermal exfoliation/deoxygenation process. The degree of reduction is controlled by adjusting applied plasma power on GO film. In L-AA reduction, 3D, cylindrical RGO monoliths were manufactured using mild reduction of GO with L-AA. The density and pore size of the resultant monoliths were readily controlled with change in concentration of GO solution. These new reduction pathways do not require a high temperature annealing process, and the reduction proceeds in non-toxic way. The simple process can be used as an alternative tool for the fabrication of multi-dimensional RGO structure with controlled design.

The 3D RGO networks prepared by the two methods described in this dissertation have been successfully applied in electrochemical/thermal energy storage application. The outstanding properties of these materials may be beneficial in further applications related to electrochemical energy storage and conversion, chemical/biological/pressure sensor, bio-compatible support, nano-electronic devices, and management in thermal energy storage.

REFERENCES

[1] J. H. Chen, C. Jang, S. Xiao, M. Ishigami, M. S. Fuhrer, *Nat. Nanotechnol.*, **2008**, *3*, 206.

[2] A. K. Geim, P. Kim, *Sci. Am.*, **2008**, *298*, 90.

[3] A. P. Demchenko, M. O. Dekaliuk, *Methods Appl. Fluoresc.*, **2013**, *1*, 042001.

[4] K. S. Novoselov, A. K. Geim, S. V. Morozov, D. Jiang, Y. Zhang, S. V. Dubonos, I. V. Grigorieva, A. A. Firsov, *Science*, **2004**, *306*, 666.

[5] M. I. Katsnelson, *Mater. Today*, **2007**, *10*, 20.

[6] K. S. Novoselov, V. I. Fal´ko, L. Colombo, P. R. Gellert, M. G. Schwab, K. Kim, *Nature*, **2012**, *490*, 192.

[7] P. Blake, E. W. Hill, A. H. Castro Neto, K. S. Novoselov, D. Jiang, R. Yang, T. J. Booth, A. K. Geim, *Appl. Phys. Lett.*, **2007**, *91*, 063124.

[8] D. D. L. Chung, *J. Mater. Sci.*, **1987**, *22*, 4190.

[9] X. Lu, M. Yu, H. Huang, R. Ruoff, *Nanotechnology*, **1999**, *10*, 269.

[10] Y. Zhu, S. Murali, W. Cai, X. Li, J. W. Suk, J. R. Potts, R. S. Ruoff, *Adv. Mater.*, **2010**, *22*, 3906.

[11] C. Berger, Z. M. Song, T. B. Li, X. B. Li, A. Y. Ogbazghi, R. Feng, Z. T. Dai, A. N. Marchenkov, E. H. Conrad, P. N. First, W. A. De Heer, *J. Phys. Chem. B*, **2004**, *108*, 19912.

[12] C. Berger, Z. Song, X. Li, X. Wu, N. Brown, C. Naud, D. Mayou, T. Li,

J. Hass, A. N. Marchenkov, E. H. Conrad, P. N. First, W. A. de Heer, *Science*, **2006**, *312*, 1991.

[13] W. A. de Heer, C. Berger, X. Wu, P. N. First, E. H. Conrad, X. Li, T. Li, M. Sprinkle, J. Hass, M. L. Sadowski, M. Potemski, G. Martinez, *Solid State Commun.*, **2007**, *143*, 92.

[14] J. Hass, W. A. de Heer, E. H. Conrad, *J. Phys.: Condens. Matter*, **2008**, *20*, 323202.

[15] K. V. Emtsev, A. Bostwick, K. Horn, J. Jobst, G. L. Kellogg, L. Ley, J. L. McChesney, T. Ohta, S. A. Reshanov, J. Rohrl, E. Rotenberg, A. K. Schmid, D. Waldmann, H. B. Weber, T. Seyller, *Nat. Mater.*, **2009**, *8*, 203.

[16] Z. Chen, W. Ren, L. Gao, B. Liu, S. Pei, H.-M. Cheng, *Nat. Mater.*, **2011**, *10*, 424.

[17] Y. Dedkov, A. Shikin, V. Adamchuk, S. Molodtsov, C. Laubschat, A. Bauer, G. Kaindl, *Phys. Rev. B*, **2001**, *64*, 035405.

[18] P. W. Sutter, J.-I. Flege, E. A. Sutter, *Nat. Mater.*, **2008**, *7*, 406.

[19] Y. S. Dedkov, M. Fonin, C. Laubschat, *Appl. Phys. Lett.*, **2008**, *92*, 052506.

[20] Y. Hernandez, V. Nicolosi, M. Lotya, F. M. Blighe, Z. Y. Sun, S. De, I. T. McGovern, B. Holland, M. Byrne, Y. K. Gun'ko, J. J. Boland, P.

Niraj, G. Duesberg, S. Krishnamurthy, R. Goodhue, J. Hutchison, V. Scardaci, A. C. Ferrari, J. N. Coleman, *Nat. Nanotechnol.*, **2008**, *3*, 563.

[21] W. S. Hummers Jr., R. E. Offeman, *J. Am. Chem. Soc.*, **1958**, *80*, 1339.

[22] C. Soldano, A. Mahmood, E. Dujardin, *Carbon*, **2010**, *48*, 2127.

[23] B. C. Brodie, *Phil. Trans. R. Soc. Lond.*, **1859**, *149*, 249.

[24] L. Staudenmaier, *Ber. Dtsch. Chem. Ges.*, **1898**, *31*, 1481.

[25] S. Pei, H.-M. Cheng, *Carbon*, **2012**, *50*, 3210.

[26] S. Stankovich, D. A. Dikin, R. D. Piner, K. A. Kohlhaas, A. Kleinhammes, Y. Jia, Y. Wu, S. T. Nguyen, R. S. Ruoff, *Carbon*, **2007**, *45*, 1558.

[27] V. H. Pham, T. V. Cuong, T.-D. Nguyen-Phan, H. D. Pham, E. J. Kim, S. H. Hur, E. W. Shin, S. Kim, J. S. Chung, *Chem. Commun.*, **2010**, *46*, 4375.

[28] A. Ambrosi, C. K. Chua, A. Bonanni, M. Pumera, *Chem. Mater.*, **2012**, *24*, 2292.

[29] H.-J. Shin, K. K. Kim, A. Benayad, S.-M. Yoon, H. K. Park, I.-S. Jung, M. H. Jin, H.-K. Jeong, J. M. Kim, J.-Y. Choi, Y. H. Lee, *Adv. Funct. Mater.*, **2009**, *19*, 1987.

[30] P. Cui, J. Lee, E. Hwang, H. Lee, *Chem. Commun.*, **2011**, *47*, 12370.

[31] I. K. Moon, J. Lee, R. S. Ruoff, H. Lee, *Nat. Commun.*, **2010**, *1*, 73.

[32] S. Pei, J. Zhao, J. Du, W. Ren, H.-M. Cheng, *Carbon,* **2010**, *48*, 4466.

[33] G. Wang, J. Yang, J. Park, X. Gou, B. Wang, H. Liu, J. Yao, *J. Phys. Chem. C*, **2008**, *112*, 8192.

[34] Y. Liu, Y. Li, Y. Yang, Y. Wen, M. Wang, *J. Nanosci. Nanotechnol.*, **2011**, *11*, 10082.

[35] Z.-J. Fan, W. Kai, J. Yan, T. Wei, L.-J. Zhi, J. Feng, Y.-m. Ren, L.-P. Song, F. Wei, *ACS Nano*, **2011**, *5*, 191.

[36] X. Mei, J. Ouyang, *Carbon,* **2011**, *49*, 5389.

[37] T. A. Pham, J. S. Kim, J. S. Kim, Y. T. Jeong, *Colloids Surf., A,* **2011**, *384*, 543.

[38] V. H. Pham, H. D. Pham, T. T. Dang, S. H. Hur, E. J. Kim, B. S. Kong, S. Kim, J. S. Chung, *J. Mater. Chem.*, **2012**, *22*, 10530.

[39] M. Baraket, S. G. Walton, Z. Wei, E. H. Lock, J. T. Robinson, P. Sheehan, *Carbon,* **2010**, *48*, 3382.

[40] T. N. Lambert, C. C. Luhrs, C. A. Chavez, S. Wakeland, M. T. Brumbach, T. M. Alam, *Carbon,* **2010**, *48*, 4081.

[41] S. W. Lee, C. Mattevi, M. Chhowalla, R. M. Sankaran, *J. Phys. Chem. Lett.*, **2012**, *3*, 772.

[42] J.-H. Kim, G. Liu, S. H. Kim, *J. Mater. Chem.*, **2006**, *16*, 977.

[43] M. J. Fernández-Merino, L. Guardia, J. I. Paredes, S. Villar-Rodil, P.

Solís-Fernández, A. Martínez-Alonso, J. M. D. Tascón, *J. Phys. Chem. C*, **2010**, *114*, 6426.

[44] C. K. Chua, M. Pumera, *Chem. Soc. Rev.*, **2014**, *43*, 291.

[45] W. Chen, L. Yan, *Nanoscale*, **2011**, *3*, 3132.

[46] L. Qiu, J. Z. Liu, S. L. Chang, Y. Wu, D. Li, *Nat. Commun.*, **2012**, *3*, 1241.

[47] X. Wang, L. Zhi, K. Mullen, *Nano lett.*, **2008**, *8*, 323.

[48] B. Shen, W. Zhai, W. Zheng, *Adv. Funct. Mater.*, **2014**, *24*, 4542.

[49] Y. Zhu, S. Murali, M. D. Stoller, A. Velamakanni, R. D. Piner, R. S. Ruoff, *Carbon*, **2010**, *48*, 2106.

[50] R. S. Sundaram, C. Gomez-Navarro, K. Balasubramanian, M. Burghard, K. Kern, *Adv. Mater.*, **2008**, *20*, 3050.

[51] M. Zhou, Y. Wang, Y. Zhai, J. Zhai, W. Ren, F. Wang, S. Dong, *Chem. Eur. J.*, **2009**, *15*, 6116.

[52] D. R. Dreyer, S. Park, C. W. Bielawski, R. S. Ruoff, *Chem. Soc. Rev.*, **2010**, *39*, 228.

[53] X. Cao, Z. Yin, H. Zhang, *Energy Environ. Sci.*, **2014**, *7*, 1850.

[54] H. Huang, L. Xu, Y. Tang, S. Tang, Y. Du, *Nanoscale*, **2014**, 6, 2426.

[55] Z. Xu, B. Zheng, J. Chen, C. Gao, *Chem. Mater.*, **2014**, *26*, 6811.

[56] Y. Zhou, Q. Bao, L. A. L. Tang, Y. Zhong, K. P. Loh, *Chem. Mater.*,

2009, *21*, 2950.

[57] H. Wang, J. T. Robinson, X. Li, H. Dai, *J. Am. Chem. Soc.,* **2009**, *131*, 9910.

[58] S. Dubin, S. Gilje, K. Wang, V. C. Tung, K. Cha, A. S. Hall, J. Farrar, R. Varshneya, Y. Yang, R. B. Kaner, *ACS Nano,* **2010**, *4*, 3845.

[59] J. H. Kim, W. S. Chang, D. Kim, J. R. Yang, J. T. Han, G. W. Lee, J. T. Kim, S. K. Seol, *Adv. Mater.,* **2015**, *27*, 157.

[60] C. Zhu, T. Y. Han, E. B. Duoss, A. M. Golobic, J. D. Kuntz, C. M. Spadaccini, M. A. Worsley, *Nat. Commun.*, **2015**, *6*, 6962.

[61] S. Ryu, C. Lee, J. Park, J. S. Lee, S. Kang, Y. D. Seo, J. Jang, B. S. Kim, *Angew. Chem. Int. Ed.,* **2014**, *53*, 9213.

[62] S. W. Crowder, D. Prasai, R. Rath, D. A. Balikov, H. Bae, K. I. Bolotin, H. J. Sung, *Nanoscale*, **2013**, *5*, 4171.

[63] H. Y. Yue, S. Huang, J. Chang, C. Heo, F. Yao, S. Adhikari, F. Gunes, L. C. Liu, T. H. Lee, E. S. Oh, B. Li, J. J. Zhang, T. Q. Huy, N. V. Luan, Y. H. Lee, *ACS Nano,* **2014**, *8*, 1639.

[64] C. Hou, Y. Duan, Q. Zhang, H. Wang, Y. Li, *J. Mater. Chem.,* **2012**, *22*, 14991.

[65] L. Chen, B. Wei, X. Zhang, C. Li, *Small,* **2013**, *9*, 2331.

[66] Z. Yu, L. Tetard, L. Zhai, J. Thomas, *Energy Environ. Sci.,* **2015**, *8*, 702.

[67] J. J. Yoo, K. Balakrishnan, J. Huang, V. Meunier, B. G. Sumpter, A. Srivastava, M. Conway, A. L. Reddy, J. Yu, R. Vajtai, P. M. Ajayan, *Nano lett.*, **2011**, *11*, 1423.

[68] S. Han, D. Wu, S. Li, F. Zhang, X. Feng, *Adv. Mater.*, **2014**, *26*, 849.

[69] J. Jang, J. Bae, M. Choi, *Carbon*, **2005**, *43*, 2730.

[70] M. Choi, B. Lim, J. Jang, *Macromol. Res.*, **2008**, *16*, 200.

[71] J. S. Lee, C. Lee, J. Jun, D. H. Shin, J. Jang, *J. Mater. Chem. A,* **2014**, *2*, 11922.

[72] Z. S. Wu, A. Winter, L. Chen, Y. Sun, A. Turchanin, X. Feng, K. Mullen, *Adv. Mater.*, **2012**, *24*, 5130.

[73] P. Chen, J.-J. Yang, S.-S. Li, Z. Wang, T.-Y. Xiao, Y.-H. Qian, S.-H. Yu, *Nano Energy*, **2013**, *2*, 249.

[74] B. G. Choi, M. Yang, W. H. Hong, J. Choi, Y. S. Huh, *ACS Nano*, **2012**, *6*, 4020.

[75] Y. P. Dan, Y. Lu, N. J. Kybert, Z. T. Luo, A. T. C. Johnson, *Nano Lett.*, **2009**, *9*, 1472.

[76] L. H. Tang, Y. Wang, Y. M. Li, H. B. Feng, J. Lu, J. H. Li, *Adv. Funct. Mater.*, **2009**, *19*, 2782.

[77] Y. Ohno, K. Maehashi, Y. Yamashiro, K. Matsumoto, *Nano Lett.*, **2009**, *9*, 3318.

[78] C. Sharma, S. Patil, S. Saurabh, A. Sharma and R. Venkatragavan, *Bull. Mater. Sci.*, **2009**, *32*, 239.

[79] F. Liu, Y. Piao, J. S. Choi, T. S. Seo, *Biosens. Bioelectron.*, **2013**, *50*, 387.

[80] V. Penmatsa, T. Kim, M. Beidaghi, H. Kawarada, L. Gu, Z. Wang, C. Wang, *Nanoscale*, **2012**, *4*, 3673.

[81] X. Liu, J. Cui, J. Sun, X. Zhang, *RSC Adv.*, **2014**, *4*, 22601.

[82] M. Yuan, A. Liu, M. Zhao, W. Dong, T. Zhao, J. Wang, W. Tang, *Sensor Actuat. B-Chem*, **2014**, *190*, 707.

[83] J. Kuang, L. Liu, Y. Gao, D. Zhou, Z. Chen, B. Han, Z. Zhang, *Nanoscale*, **2013**, *5*, 12171.

[84] A. Abhat, *Solar energy*, **1983**, *30*, 313.

[85] A. Sharma, V. V. Tyagi, C. R. Chen, D. Buddhi, *Renew. Sustainable Energy Rev.*, **2009**, *13*, 318.

[86] S. Raoux, W. Welnic, D. Ielmini, *Chem. Rev.*, **2010**, *110*, 240.

[87] S. M. Shalaby, M. A. Bek, A. A. El-Sebaii, *Renew. Sustainable Energy Rev.*, **2014**, *33*, 110.

[88] D. C. Hyun, N. S. Levinson, U. Jeong, Y. Xia, *Angew. Chem. Int. Ed.*, **2014**, *53*, 3780.

[89] S. Ye, Q. Zhang, D. Hu, J. Feng, *J. Mater. Chem. A*, **2015**, *3*, 4018.

[90] Y. Zhong, M. Zhou, F. Huang, T. Lin, D. Wan, *Sol. Energ. Mat. Sol. Cells*, **2013**, *113*, 195.

[91] M. Kim, C. Lee, J. Jang, *Adv. Funct. Mater.*, **2014**, *24*, 2489.

[92] J. H. Flynn, D. M. Levin, *Thermochim, Acta*, **1988**, 126, 93.

[93] C. P. Camirand, *Thermochim, Acta*, **2004**, *417*, 1.

[94] S. W. Lee, C. Mattevi, M. Chhowalla, R. M. Sankaran, *J. Phys. Chem. Lett.*, **2012**, *3*, 772.

[95] M. Cardinali, L. Valentini, P. Fabbri, J. M. Kenny, *Chem. Phys. Lett.*, **2011**, *508*, 285.

[96] Y-K. Kim, M-H. Kim, D-H. Min, *Chem. Commun.*, **2011**, *47*, 3195.

[97] D. A. Dikin, S. Stankovich, E. J. Zimney, R. D. Piner, G. H. Dommett, G. Evmenenko, S. T. Nguyen, R. S. Ruoff, *Nature*, **2007**, *448*, 457.

[98] M. Cheng, R. Yang, L. Zhang, Z. Shi, W. Yang, D. Wang, G. Xie, D. Shi, G. Zhang, *Carbon*, **2012**, *50*, 2581.

[99] C. Zhu, S. Guo, Y. Fang, S. Dong, *ACS Nano*, **2010**, *4*, 2429.

[100] M. D. Stoller, S. Park, Y. Zhu, J. An, R. S. Ruoff, *Nano Lett.*, **2008**, *8*, 3498

[101] S. D. Perera, R. G. Mariano, N. Nijem, Y. Chabal, J. P. Ferraris, K. J. Balkus Jr., *J. Power Sources*, **2012**, *215*, 1.

[102] Q. Wu, Y. X. Xu, Z. Y. Yao, A. R. Liu, G. Q. Shi, *ACS Nano*, **2010**, *4*,

1963.

[103] A. V. Murugan, T. Muraliganth, A. Manthiram, *Chem. Mater.*, **2009**, *21*, 5004.

[104] Q. Tang, J. Sun, S. Yu, G. Wang, *RSC Adv.*, **2014**, *4*, 36584.

[105] C. Wang, L. Feng, H. Yang, G. Xin, W. Li, J. Zheng, W. Tian, X. Li, *PCCP*, **2012**, *14*, 13233.

[106] M. Mehrali, S. T. Latibari, M. Mehrali, H. S. C. Metselaar, M. Silakhori, *Energ, Convers. Manage.*, **2013**, *67*, 275.

[107] D. Wu, W. Wen, S. Chen, H. Zhang, *J. Mater. Chem. A*, **2015**, *3*, 2589.

[108] Y. Konuklu, M. Unal, H. O. Paksoy, *Sol. Energ. Mat. Sol. Cells*, **2014**, *120*, 536.

[109] J.-N. Shi, M.-D. Ger, Y.-M. Liu, Y.-C. Fan, N.-T. Wen, C.-K. Lin, N.-W. Pu, *Carbon*, **2013**, *51*, 365.

[110] F. Yavari, H. R. Fard, K. Pashayi, M. A. Rafiee, A. Zamiri, Z. Yu, R. Ozisik, T. Borca-Tasciuc, N. Koratkar, *J. Phys. Chem. C*, **2011**, *115*, 8753.

[111] J. Wang, H. Xie, Z. Xin, Y. Li, C. Yin, *J. Appl. Phys.*, **2011**, *110*, 094302.

[112] H. Ji, D. P. Sellan, M. T. Pettes, X. Kong, J. Ji, L. Shi, R. S. Ruoff, *Energy Environ. Sci.*, **2014**, *7*, 1185.

국문초록

한 층의 탄소 원자로 이루어진 2차원 탄소 동소체인 그래핀은 지난 2004년의 획기적 발견 이후 전 세계적으로 집중적인 관심을 받아 왔다. 그래핀 물질은 높은 비표면적, 역학적 안정성 그리고 뛰어난 열/전기 전도도 등의 특별한 성능을 보인다. 특히, 그래핀의 높은 비표면적과 역학적 안정성으로 인해 그래핀을 3차원 구조로 제조해 다양한 방면으로 응용하는 연구가 계속 진행되었으며, 지금까지 다양한 3차원 그래핀 구조체의 제조 방법이 개발되어왔다. 하지만, 저비용, 친환경적인 그래핀의 다차원 구조체 제조는 아직 많은 연구가 필요하다.

본 논문에서는 플라즈마 환원방법 / L-아스코르브산 환원방법을 이용하여 3차원의 환원된 그래핀 옥사이드 구조체를 제조하였으며, 이들의 형성 메커니즘을 체계적으로 고찰하였고, 아울러 슈퍼캐패시터 전극과 상변화물질의 지지체로의 응용에 대해 살펴보았다.

플라즈마 환원방법으로, 먼저 흑연을 화학적 박리하여 제조한 그래핀 옥사이드를 물에 분산시킨 후 진공 여과하여 얻은 그래핀 옥사이드 필름에 상압 플라즈마를 20초 간 처리하여 3차원으로 확장된 환원된 그래핀 옥사이드 필름을 제조하였다. 더불어, 사용하는 상압 플라즈마의 출력을 조절함에 따라서 최종적인 환원된 그래핀 옥사이드의 성질 또한 조절 할 수 있었다. 상기 방법은 기존의 환원 방식에서 사용하던 높은 에너지 출력과 하이드라진과 같은 유독성 화합물을 요구하지 않을뿐더러, 기존의

플라즈마 방식에서 필수적인 고진공 조건 없이도 우수한 성능의 그래핀 물질을 신속하게 제조할 수 있다는 장점이 있다.

L-아스코르브산 환원방법으로, 그래핀 옥사이드 용액을 L-아스코르브산을 이용해 환원 시 자발적으로 3차원 환원된 그래핀 옥사이드 구조체가 형성됨을 관찰하였다. 위 방식은 기존의 환원 방식과 달리 그래핀 옥사이드 용액의 환원 과정 중에 3차원 환원된 그래핀 옥사이드 구조체의 형성이 자발적으로 일어나며, 최초의 그래핀 옥사이드 용액의 농도를 조절함에 따라 얻어지는 환원된 그래핀 옥사이드 구조체의 기공 크기와 밀도가 조절됨을 관찰하였다. 또한 L-아스코르브산과 같은 친환경 환원제의 사용으로도 기존의 화학적 환원 방식과 비견될 수준의 고품질 3차원 그래핀 구조체를 제조할 수 있다는 장점이 있다.

본 연구에서 새롭게 개발한 플라즈마 환원방법 / L-아스코르브산 환원방법은 기공 및 밀도 조절이 가능하며 비표면적이 증대된 새로운 종류의 그래핀 구조체 제조에 적용될 수 있으며, 이를 통해 슈퍼캐패시터 전극과 상변화물질를 포함한 여러가지 응용분야에 폭넓게 활용될 수 있을 것으로 사료된다.

주요어: 탄소 나노물질, 그래핀, 다차원, 플라즈마 환원, L-아스코르브산, 슈퍼캐패시터 전극, 상변화 물질

학번: 2011-22930

工學博士學位論文

Fabrication of three-dimensional reduced graphene oxide network for thermal energy storage/supercapacitor applications

3차원 환원된 그래핀 옥사이드 구조체의 제조 및 열에너지 저장/슈퍼캐패시터 응용

2016年 2月

서울大學校 大學院

化學生物工學部

李 忠 炫

Fabrication of three-dimensional reduced graphene oxide network for thermal energy storage/supercapacitor applications

by

Choonghyeon Lee

Submitted to the Graduate School of Seoul National University in Partial Fulfillment of the Requirements for the Degree of Doctor of Philosophy

February, 2016

Thesis Adviser: Jyongsik Jang

ABSTRACT

Graphene, the 2-dimensional carbon allotrope with one-atom-thick layer of carbon elements, has drawn a lot of intention since the breakthrough of the isolation of single graphene sheet in 2004. The graphene material possesses outstanding properties, *e.g.,* large specific surface area, mechanical stability, and superb thermal/electrical conductivity and so on. Especially, the large surface area and mechanical stability of graphene have triggered huge attention on preparation of three-dimensional (3D) architecture of graphene for various applications. Up to date, various synthetic pathways for preparing 3D graphene network have been developed. However, simple preparation of graphene in multi-dimensional scale with low-cost and environmental-friendly way still remains as a challenge.

This dissertation describes the two pathways in the preparation method of 3D reduced graphene oxide (RGO) network utilizing plasma reduction method and L-ascorbic acid (L-AA) reduction method. As a ‘plasma reduction method’, the 3D plasma-reduced GO (PRGO) structures with increased surface area are successfully fabricated using a rapid thermal exfoliation and deoxygenation process on graphene oxide (GO) film *via* atmospheric plasma reduction. This

reduction process do not require high thermal energy or toxic chemical agent previously used in traditional GO reduction methodology. In ‘L-AA reduction approach’, 3D graphene monoliths are spontaneously formed during the mild L-AA reduction of GO solution. The pore size and the density of the graphene monolith can be easily controlled by adjusting the concentration of initial GO solution used. By using L-AA as an environmental-friendly reducing agent, cylinder-like graphene monoliths are easily prepared. The novel approaches can be used as an alternate methodology for fabrication of 3D RGO network with rational design and controlled physical properties. In this research, the 3D PRGO films and 3D graphene monolith materials were utilized as active materials for supercapacitor electrode and foothold of phase change materials (PCMs) for latent heat storage. The novel methods presented here might allow application of multi-dimensional graphene architecture in chemical/biological sensor, active material for secondary ion batteries and so on.

KEYWORDS: Carbon nanomaterials; Graphene; Multi-dimensional; Plasma reduction; L-ascorbic acid; Supercapacitor electrode; phase change materials

STUDENT NUMBER: 2011–22930

List of Abbreviations

2D : 2-dimensional

3D : 3-dimensional

AAO : anodic aluminum oxide

BET : Brunauer–Emmett–Teller

CMG : chemically modified graphene

CND : carbon nanodots

CNFs : carbon nanofibers

CV : cyclic voltammetry

CVD : chemical vapor deposition

DSC : differential scanning calorimetry

EA : elemental analysis

EDLC : electric double layer capacitance

EG : epitaxial graphene

FT-IR : Fourier transform infrared

GO : graphene oxide

ITO : indium tin oxide

L-AA : L-ascorbic acid

LIB : lithium-ion battery

PCM : phase change material

PCNFs : platelet carbon nanofibers

PDMS : poly(dimethylsiloxane)

PMMA : poly(methylene methacrylate)

PRGO : plasma-reduced GO

pRGO : partially reduced GO

RGO : reduced graphene oxide

SEM : scanning electron microscopy

SiC : silicon carbide

TEM : transmission electron microscopy

TGA : thermogravimetric analysis

UHV : ultrahigh vacuum

UV-Vis : ultraviolet-visible spectroscopy

VDP : vapor deposition polymerization

XPS : X-ray photoelectron spectroscopy

XRD : X-ray diffraction

List of Figures

List of Tables

Table of Contents

1. INTRODUCTION

1.1. Background

1.1.1. Properties of graphene

Among the various carbon nanomaterials, including carbon nanotube (CNT), carbon nanodots (CND) (Figure 1) [1-3], graphene, the carbon allotrope composed of a one-atom-thick planar sheet of carbon elements, has been regarded as a 'next-generation' material for its outstanding properties. Since the isolation of single graphene sheet by Geim and Novoselov in 2004 [4], the graphene material has been thoroughly studied and following properties were found: graphene is composed of sp^2 carbon atoms which are organized in hexagonal honeycomb lattice structure and possess superb characteristics, such as high electron mobility (with experimentally reported values in excess of 15,000 $cm^2 V^{-1} s^{-1}$ [5], high modulus, large thermal/electric conductivity and tremendous specific surface area and *etc*. The crystalline graphene can be a semi-metal or zerogap semiconductor which can be used in electronic devices. The increased attention in graphene is primarily due to a host of superb characteristics that have been mentioned above.

Successful preparation of high-quality graphene with controlled scale still remains as a challenge toward practical application of graphene. Therefore, researchers have utilized versatile methods to synthesize single layer of

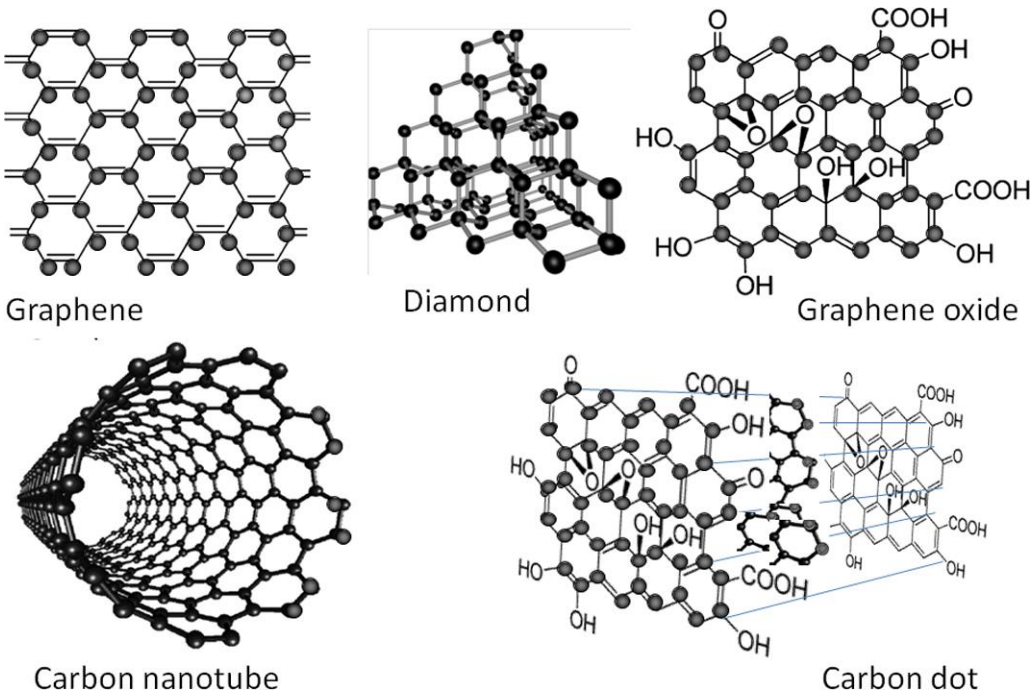

Figure 1. Structures of various carbon materials: Diamond, carbon nanotube (CNT), carbon dot, graphene and graphene oxide. Reprinted with permission from ref 3. Copyright 2012 Elsevier.

graphene (Figure 2) [6]. Synthesis methods can be classified into micromechanical exfoliation, epitaxial growth using SiC surfaces (along with chemical vapor deposition (CVD)) and liquid-phase exfoliation. Each pathway has its own advantages and disadvantages, and can be choosed according to following criteria: cost, scalability, purpose and *etc*. At first, production of single or few-layer graphene in experimental scale has been achieved by micromechanical exfoliation of highly oriented pyrolytic graphite [4]. This method is also known as 'scotch-tape method' or repeated peeling of graphite, since the methodology involves repeated steps of peeling graphene layers off of highly oriented pyrolytic graphite with adhesive tape, and subsequent pressing of the tape onto suitable substrate [7]. This method enabled researchers to investigate the single-layer morphology of graphene [8-9]. However, large-scale production of graphene is not archievable and the high-quality graphene layer can only be prepared with trial-and-error peeling process.

Epitaxial graphene (EG) growth on silicon carbide (SiC) surfaces is a useful bottom-up approach to be applied in nanoelectronics and it has been demonstrated on various metallic substrates [10]. The EG growth can be defined as a large-area growth of single graphene layer on SiC wafer by high temperature (in the range of 1200–1600 ℃) evaporation of silicon (Si) in ultra-

high vacuum (UHV) [10-13]. Si atoms on the wafer surface sublimate at high temperature and the exposed carbon atoms reconstruct to form hexagonal sp^2 carbon structure. EG has been reported to be grown on both the carbon-terminated and Si-terminated surfaces, though films grow much faster on the carbon face [14]. This method enables preparation of wafer-sized large graphene with carrier mobility values of *ca.* 2000 $cm^2 V^{-1} s^{-1}$ [15]. However, preparation of SiC wafer and experimental set-up of high-temperature furnace for Si sublimation are needed.

And also, Chemical vapor deposition (CVD) growth of graphene onto metal substrate has been applied as a means of producing large-area high-quality graphene [16]. Large-area graphene films with minute structural defects and decreased inter-sheet junction contact resistance can be prepared by deposition and pyrolysis of hydrocarbon-containing precursors like methane (CH_4) [17-19]. Furthermore, the CVD method can realize fabrication of template-mediated multi-dimensional graphene architecture by using commercial nickel or copper foam. Nonetheless, the CVD method requires furnace set-up, relatively expensive metal substrates/templates and additional substrate to be transferred upon, such as Poly(dimethylsiloxane) (PDMS) or Poly(methyl methacrylate) (PMMA) sheets.

Additionally, exfoliation of graphite into few-layer graphene sheets in

liquid-phase has been archived by bath-sonication of graphite powder in N-methylpyrrolidone (NMP) [20]. Nonetheless, the yield of graphene sheets is relatively low compared with the methods described above.

Since the methods mentioned here requires complex experimental set-up and relatively low amount of graphene material is produced, the researchers have came up with mass-production of graphene varieties: preparation of graphite oxide and subsequent exfoliation into few-layered graphene oxide (GO). After production of GO, the GO can be reduced to reduced graphene oxide (RGO) by diverse reduction methods. The details of preparation of GO and RGO are described in the next section.

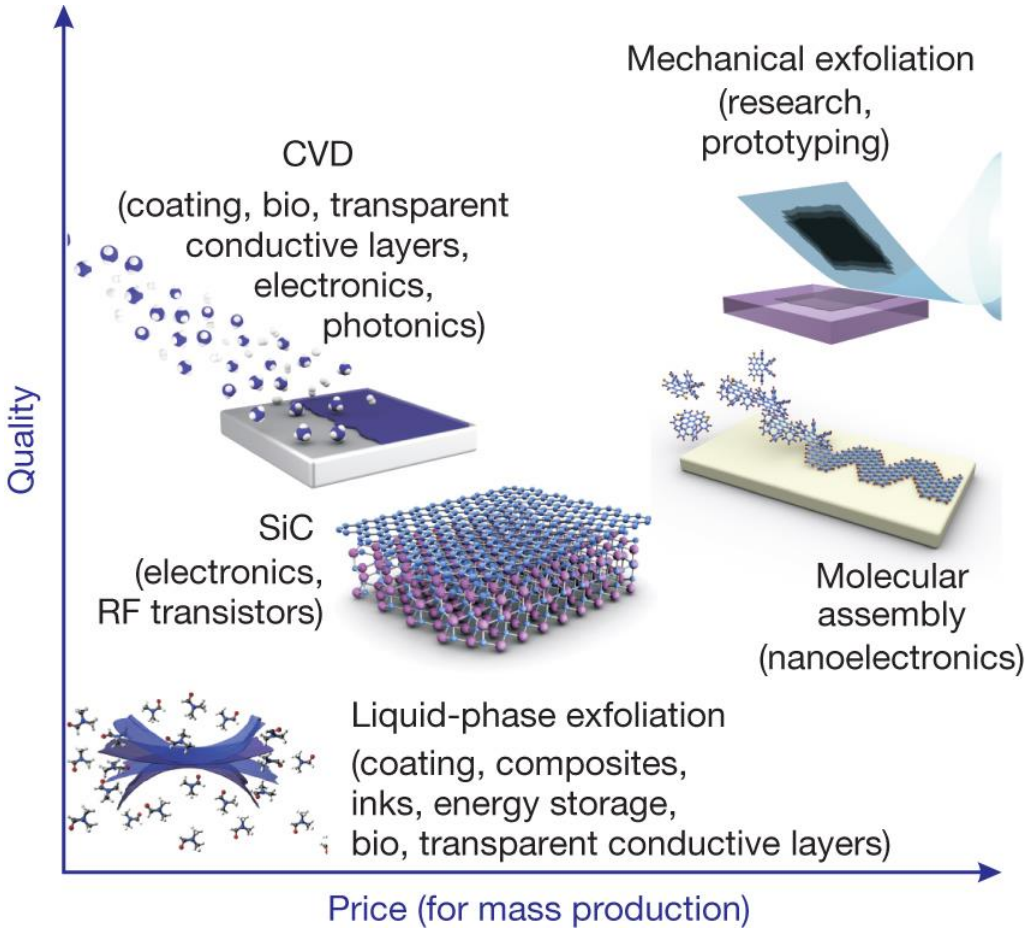

Figure 2. The synthesis method of graphene by various methodologies. Reprinted with permission from Ref 6. Copyright 2012 Right Managed by Nature Publishing Group.

1.1.2. Synthesis of reduced graphene oxide (RGO) from graphene oxide (GO)

The graphene synthesis methodologies described in section 1.1.1 have enabled researchers to produce high-quality graphene sheets or films in lab-scale quantity. However, due to several shortcomings of production of graphene, a 'Top-down approach' has been alternatively used: chemical exfoliation of graphite flake in acidic media to produce graphitic oxide [21]. In this method, chemical reagents, such as potassium permanganate, are inserted between the graphene layers of bulk graphite to reduce the van der Waals force [22]. Among various graphite oxidation methods [21,23-24], a modified version of Hummers' method has been extensively used to prepare graphite oxide for its fast reation time and less toxic solution condition. After successful reaction, the d-spacing value of inter-layer rises from 3.4 ~ 3.5 Å in graphite to above 6 Å, possibly due to formation of oxygen-related groups and diminished van der Waals force between the layers. Finally, single or few layers of graphene oxide (GO) can be obtained after bath sonication and the resultant GO can be readily dispersed in polar solvents (usually water) to produce stable colloidal dispersion.

Since GO sheets possess several defects in C-C hexagonal lattice and are functionalized with various oxygen-related groups, such as epoxy, carbonyl

(C=O), hydroxyl (-OH) and carboxyl (-COOH) groups, the material is intrinsically insulating. Therefore, many methods which involves removal of oxygen from the GO surface and restoration of graphitic honeycomb lattice have been developed to prepare reduced graphene oxide (RGO), or sometimes defined as chemically modified graphene (CMG). These reduction methods described below are promising routes to accomplish mass-production of graphene in experimental/industrial scale.

1.1.2.1. Chemical reduction

Preparation of RGO or CMG by chemical reduction method involves reaction of the chemical reagents with GO. The chemical agents react with GO to annihilate functional groups and repair the structural defect on GO plane. The usual chemical reduction occurs in relatively moderate annealing condition. Therefore, this method offers a promising way of producing RGO in less-expensive and large-scale aspect, compared with other RGO synthesis pathway (Table 1) [25]. Chemical reduction of GO with hydrazine has been extensively used by graphene researchers after Stankovich *et al.*'s work [26]. The relatives of hydrazine, such as phenylhydrazine [27], also work as a good reducing agent to produce high-quality RGO and the highest C/O ratio after hydrazine reduction was reported to be around 12.5 with electric conductivity of ~ 100

S/cm. Metal hydrides, e.g. $LiAlH_4$ or $NaBH_4$, also work as strong reducing agents [28-29]. However, the metal hydrides reacts vigorously with water, the typical solvent for GO dispersion, and causes safety issues. Hydriodic acid (HI) also act as a very strong reducing agent and is reported to produce RGO with C/O ratio exceeding 15 [30-32]. The strong advantage of HI as a reducing agent is that high-quality RGO can be prepared even in room temperature, regardless of target GO structure (powder, film and etc). These strong reducing agents overall produce high-quality RGO with gram-scale, but the respective reagents are often classified as ‘harmful’, ‘toxic’ or ‘corrosive’ materials, with toxic side products to be washed away.

Besides of reagents above, hydroquinone [33], thiourea [34], various metal/acid mixtures [35-36], and L-gluthathione [37] can be used in reduction of GO to produce RGO. Strong alkali solutions, such as NaOH and KOH solution, are as well applied in RGO synthesis [38]. However these reagents are often classified as ‘weak’ or ‘mild’ reducing agents compared with hydrazine, HI and metal hydrides.

Table 1. Summarized reduction pathways of GO to RGO. Reprinted with permission from ref 25. Copyright 2011 Elsevier.

Table 1 – Comparison of the reducing effect of GO by different methods.

Ref. no.	Reduction method	Form	C/O ratio	σ (S/cm)
[56]	Hydrazine hydrate	Powder	10.3	2
[69]	Hydrazine reduction in colloid state	Film	NA[b]	72
[70]	150 mM $NaBH_4$ solution, 2 h	TCF	8.6	0.045
[71]	Hydrazine vapor	Film	~8.8	NG
	Thermal annealing at 900 °C, UHV[a]		~14.1	NG
[55]	Thermal annealing at 1100 °C, UHV	TCF	NA	$\sim 10^3$
[72]	Thermal annealing at 1100 °C in Ar/H_2	TCF	NA	727
[42]	Multi-step treatment:	Powder	(I) 4.78	(I) 0.823
	(I) $NaBH_4$ solution		(II) 8.57	(II) 16.6
	(II) Concentrated H_2SO_4 180 °C, 12 h		(III) >246	(III) 202
	(III) Thermal annealing at 1100 °C in Ar/H_2			
[73]	Vitamin C	Film	12.5	77
	Hydrazine monohydrate		12.5	99.6
	Pyrogallol		NA	4.8
	KOH		NA	1.910^{-3}
[58]	55% HI reduction	Film	>14.9	298

[a] UHV: ultra high vacuum.
[b] NA: not available.

1.1.2.2. Plasma reduction

Compared with traditional chemical reduction method, the plasma-assisted reduction offer a novel advantage in the process condition. The plasma-assisted condition can be completed in low temperature (usually in room temperature) and the experiment proceeds in dry process, which insures the purity of graphene. When the GO materials, in powdery or film, is exposed to plasma, they will be subject to a flux of reactive species working on the surface [39]. The species in plasma flux, including ions (Ar^+, H^+, $C_xH_y^+$), radicals (H•, CH_n•) and neutrals, are dependent on the operating parameters such as flow rate or plasma power. This reactive flux reacts with oxygen-related groups on the suface to create volatile gases, such as CO and CO_2, thus removing the oxygen groups on the GO surface. Ion bombardment on the GO surface also causes rapid thermal exfoliation/deoxygenation process to produce RGO from GO *via* microwave plasma [40]. However, traditional plasma-assisted reduction requires high vacuum condition for fine-quality treatment on GO and substrate or support on GO film is needed. Therefore, the plasma set-up in atmospheric condiction has been realized for simpler reduction step without vacuum process (Figure 3) [41].

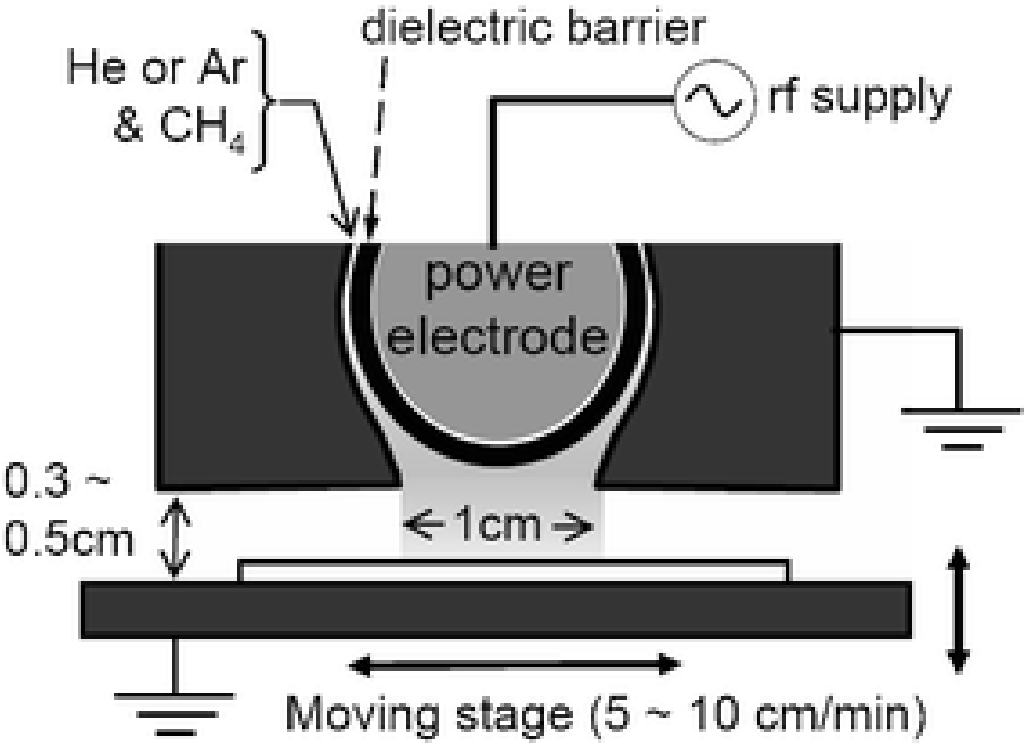

Figure 3. Atmospheric plasma apparatus set-up. Reprinted with permission from Ref 42. Copyright 2006 Right Managed by Royal Society of Chemistry.

1.1.2.3. Mild reduction *via* L-ascorbic acid (L-AA)

The reduction methods described in section 1.1.2.1 involves utilization of strong, toxic reducing agents. Therefore, environmental-friendly reduction of GO has been investigated. L-ascorbic acid (L-AA), also known as Vitamin C, can be applied as a mild reducing agent [43]. The Figure 4 describes the proposed reduction mechanism of GO via L-AA reduction. As L-AA with two hydroxyl groups interact with epoxide and hydroxyl groups on C-C hexagonal rings, the oxygen and hydrogen atoms are annihilated in the form of water. Then the L-AA/ring composition breaks and L-AA is detached in the form of dehydroascorbic acid with two carbonyl groups. As can be seen from the proposed mechanism, the L-AA reduction produce side products only composed of C and O, with no hetero-atom produced [44]. In the Figure 5, the graphene hydrogel made from L-AA resembles the shape of the reactor used, and this phenomenon indicates possible morphology manipulation of 3D graphene gel by adjusting the shape of the reactor [45]. Li *et al.* also found that a mult-step process of 1) L-AA reduction, 2) freezing, 3) thawing and 4) subsequent freeze-drying (also known as lyophilization) resulted in production of 3D RGO monolith [46]. The highest C/O ratio and electric conductivity of L-AA reduced GO were 12.5 and 77 S/cm, respectively [43]. These values are comparable with the values of hydrazine-reduced GO in section 1.1.2.1.

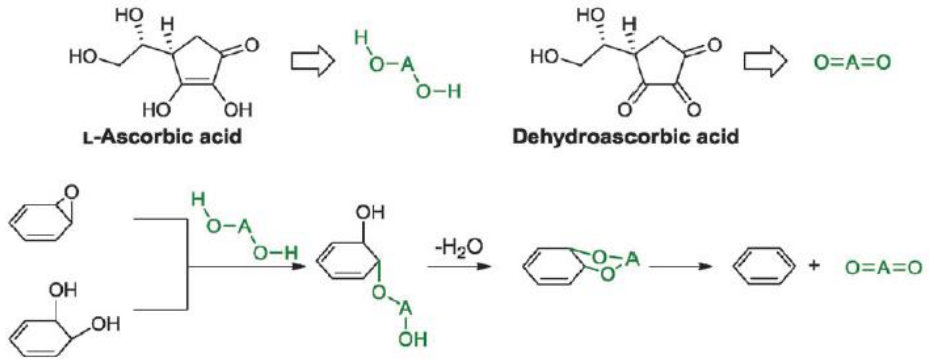

Figure 4. Proposed reduction mechanism of mild reduction via L-AA. Reprinted with permission from Ref 44. Copyright 2013 Right Managed by Royal Society of Chemistry.

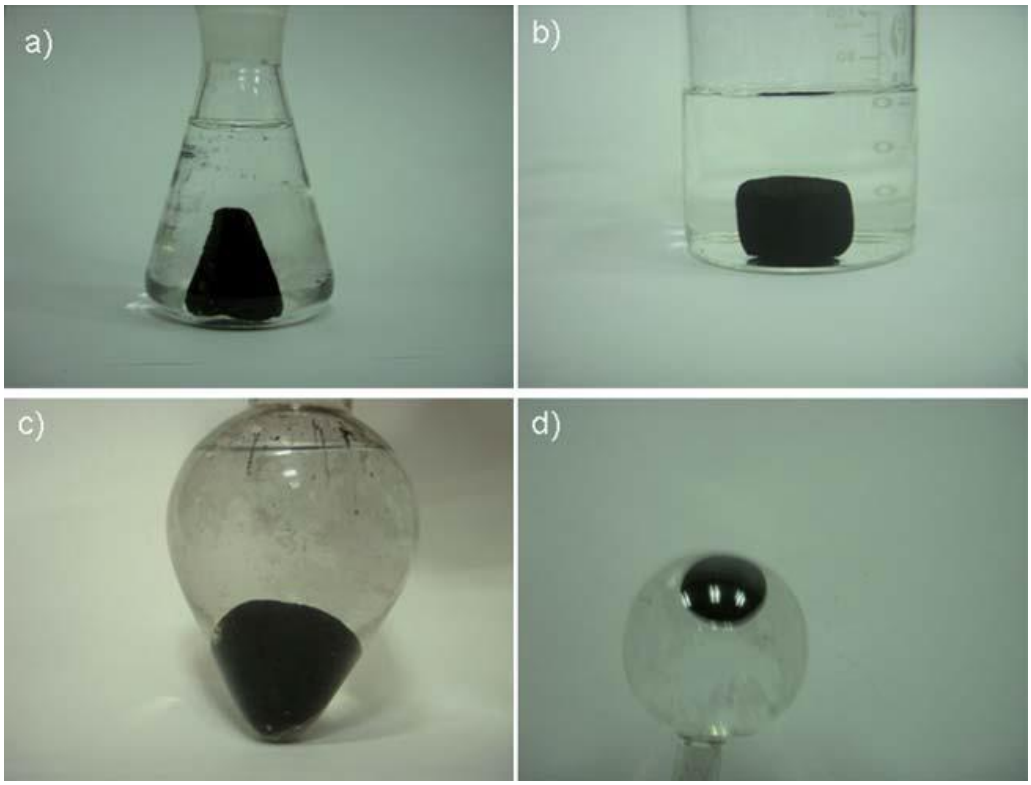

Figure 5. Digital photograph of RGO gel. The shape of the RGO gel depend on the shape of the reactor. Reprinted with permission from Ref. [45]. Copyright 2011 Right Managed by Royal Society of Chemistry.

1.1.2.4. Other reduction methods

Thermal annealing of GO in inert condition to produce RGO has been exploited as a mean of synthesizing high-quality RGO. Using argon (Ar) or nitrogen (N_2) as inert gas, the GO is heated in closed furnace up to 1100 ^oC for complete carbonization [47]. Additionally, using hydrogen (H_2) as reaction gas, GO materials are heated up to 2800 ^oC for graphitization of GO to graphene. The graphitized graphene shows high thermal conductivity of 1100 W/m•K, due to complete annihilation of oxygen-functional groups on basal plane and restoration of sp^2 C-C structure [48]. Zhu *et al.* reported that application of microwave to GO powder resulted in sudden reduction of GO to RGO with expanded structure [49].

Electrochemical reduction utilizes electrochemical force to remove oxygen-related functional groups on GO produce RGO. A previous work has shown that CMG can be functionalized with metal nanoparticles by electrodeposition process [50], direct application of electrochemistry in modifying the structure of GO or graphene has recently been realized [51] In electrochemical reduction, toxic reducdants like hydrazine are not required and harmful byproducts are not generated. In typical electrochemical reduction process, the GO film deposited on various substrates, including indium tin oxide (ITO), polymer, glass and *etc*, is used and the electrodes are positioned at opposite sides of the

GO film. Then linear sweep voltammetry proceedes in a buffer solution to produce RGO film in 300 s [52].

1.1.3. Preparation of 3-dimensional RGO framework

Although many outstanding performances of graphene material, such as ballistic electron transport, superior electric conductivity, come from its 2-dimensional planar nature, the need for preparation of multi-dimensional graphene structure has increased recently for its potential use in other fields. Since the graphene, or RGO, possess increased specific surface area, enhanced electric conductivity and strong mechanical properties compared with traditional building blocks for 3D structure, researchers have indulged in preparation of 3D graphene architecture for biological, energy applications and *etc*.

Synthesis method of 3D RGO network can be classified as follows: CVD on active-metal template, freeze-drying, solvothermal reduction, 3D printing and *etc* (Methods summarized in Table 2) [53]. At first, commercial nickel (Ni) or copper (Cu) foams are utilized as sacrificial artificial template to prepare 3D graphene foam. By using the reactive interface of 3D metallic substrate, graphitic foam is prepared after traditional CVD process utilizing hydrocarbons as graphene precursor [16, 54]. Although graphene foam possesses high electric/thermal conductivity and flexibility, the fabrication process requires sophisticated experimental set-up and high-cost metal foam. In the meantime, freeze-drying process, or sometimes called as freeze-casting and lyophilization,

utilizes volumetric expansion of ice in freezing of water to push away dispersed GO sheets. These re-organized GO sheets create porous GO network when all ice undergoes sublimation process at high vacuum/low temperature condition [55]. By adjusting the concentration of GO solution and varieties of dispersed solute, the porosity and mechanical properties of resultant network differentiates. Solvothermal reduction of GO to RGO also creates 3D network structure of RGO in experimental scale [56-58]. The solvothermal method utilizes the vapor pressure of vaporized organic solvents at the temperature higher than the boiling point of the corresponding solvent. This high vapor pressure inside the sealed container induces partly removes the oxygen-related groups on GO plane and also repairs the disoriented structure of GO, thus realizing reduction of GO. Using polar solvents like N,N-dimethylformamide (DMF), N-methylpyrrolidone (NMP) and water, the graphene network with C/O ratio reaching 14 can be prepared [25]. 3D printing, which allows precise control in architecture and mechanical properties of printed product, can also shine a light on preparation of 3D RGO network for various applications. Kim *et al.* found that controlled extrusion of GO solution through micropipette produced free-standing GO nanowire without supporting material and the GO nanowire was facily reduced with hydrazine treatment [59]. Zhu *et al.* also reported that periodic microlattices of RGO can be fabricated by direct GO ink

writing on isooctane and subsequent supercritical (SC) drying [60]. The storage and loss modulus of resultant microlattices were changed according to the concentration of GO ink and added amount of silica. Nonetheless, the methods described here usually require unique apparatus, e.g. sealed container or 3D printer, and are tedious processes.

Table 2. Preparation of 3-dimensional graphene network. Reproduced with permission from Ref 53. Published by The Royal Society of Chemistry.

Table 1 Comparison of various structures of 3D graphene materials with their preparation methods, properties and applications

Structures	Synthetic methods	Properties	Applications	Ref.
3D graphene networks	CVD using $NiCl_2 \cdot 6H_2O$ as catalyst precursor	Surface area: ~560 $m^2 g^{-1}$, electrical conductivity: ~12 S cm^{-1}	Absorbent	38
	CVD based on Ni foam template	Surface area: ~850 $m^2 g^{-1}$, electrical conductivity: 10 S cm^{-1}, tensile strain: ~95%		37
	Self-assembly of GO sheets induced by hydrothermal reaction	Electrical conductivity: ~0.0025 S cm^{-1}, compressive strength: ~0.042 MPa, compression modulus: ~0.26 MPa	Catalysis	74
Graphene fibers	Wet-spinning	Surface area: ~884 $m^2 g^{-1}$, electrical conductivity: 2600–4900 S cm^{-1}, specific tensile strength: 188 kN m kg^{-1}, compression modulus: 3.3 MPa	Conductive wire	166
	Wet-spinning	Electrical conductivity: 8–10 S cm^{-1}, tensile strength: 140–150 MPa	Micro-pump	168
	Wet-spinning	Electrical conductivity: ~35 S cm^{-1}, tensile strength: ~182 MPa, Young's modulus: 8.7 GPa	Conductive wire	164
Graphene tubes	Hydrothermal using Cu wire as template	Electrical conductivity: 10 S cm^{-1}, tensile strength: ~180 MPa	Self-powered micromotor	173
	CVD using AAO as template	Electrical conductivity: 950 S m^{-1}, thermal conductivity: 8.28 W m^{-1} K^{-1}	Heat transfer and thermal energy storage	83
3D porous graphene films	Leavening strategy	Sheet resistance: <100 Ω sq^{-1}, tensile strength: ~3.2 MPa	Supercapacitor	45
	Assembly of chemically modified graphene using PS particles as template	Surface area: 194.2 $m^2 g^{-1}$, electrical conductivity: 1024 S cm^{-1}	Supercapacitor	100
Graphene balls	Aerosol-assisted capillary compression process	Surface area: 82 $m^2 g^{-1}$, compression strength: >55 MPa	Microbial fuel cell	177
	CVD using PS ball as template	Surface area: 508 $m^2 g^{-1}$, electrical conductivity: 6.5 S m^{-1}	Supercapacitor	44
Honeycomb-like 3D graphenes	Freeze-casting	Electrical conductivity: ~0.12 S m^{-1}, compression strength: ~8 kPa (plateau state), 18 kPa (80% strain), for sample with density of 5.1 mg cm^{-3}		184
	Self-assembly	Electrical conductivity: 649 S m^{-1}	Supercapacitor	197

1.1.4. Application fields

By using various synthetic method described in previous section, 3D RGO network has been utilized in various application. Since the RGO itself is highly conductive and possess large surface area due to micro-pores present in graphene surface, the 3D RGO network are often exploited as active materials in electrodes of energy devices like lithium-ion battery (LIB) and supercapacitor. And also the carbonaceous surface of RGO work as a support for various heterogeneous materials, ranging from inorganic, organic to metallic materials. 3D RGO network is readily fuuctionalized with silica, conducting polymer or novel metal like palladium (Pd) and platinum (Pt) and the resultant composites are endowed with new physicochemical properties. As described below, the composites are used as hybrid supercapacitors with synergistic effect of pseudo-capacitance and electric double layer capacitance, and are utilized as enzymatic sensor or catalyst materials. When biological receptor or DNA are functionalized, the 3D RGO network play a role as a scaffold for cell differentiation. Superior thermal/chemical stabilities and electric/thermal conductivities of 3D RGO network are applied in encapsulation of phase change materials (PCMs) for further industrial applications.

1.1.4.1. Biological application

The controlled fabrication of bio-compatible scaffold for tissue engineering and bio-catalysis has been thoroughly investigated by many researchers. Among the host of materials, carbon-based materials have been extensively used due to their superior physical properties and flexibility in architecture design. For instance, carbon fiber-based scaffold prepared by combined method of electrospinning and freeze-drying was used as an artificial graft for bone growth [61]. Along with other carbon materials, graphene and its varieties have been used to prepare 3D network due to bio-compatibility, ease in surface modification and mechanical stability. By using metal foam as a hard template for 3D graphene network, osteogenic differentiation using human mesenchymal stem cell [62] and detection of Parkinson's disease [63] were investigated. Instead of using expensive CVD-graphene foam, GO-derived hydrogels work as a graphene scaffold for bio-appication. Hou *et al.* demonstrated that immersion of graphene hydrogel into a N,N-dimethylacrylamide (DMAA)-based solution and subsequent polymerization resulted in cross-linked hydrogel of graphene surface and PDMAA polymer. (Figure 6) [64]. This graphene-polymer hydrogel was further treated with near-infrared (NIR) laser and self-healing behavior of the hydrogel was observed. This self-healing material can be applied as an artificial tissue in human body.

Chen *et al.* also found that Fe_2O_3-impregnated RGO hydrogel exhibit large surface area and magnetic property, which are suitable for biocatalytic transformation of glycyrrhizin [65]. Overall, utilizing GO-derived hydrogel offers a novel route to incorporate various bio-compatible additives for specific bio-applications.

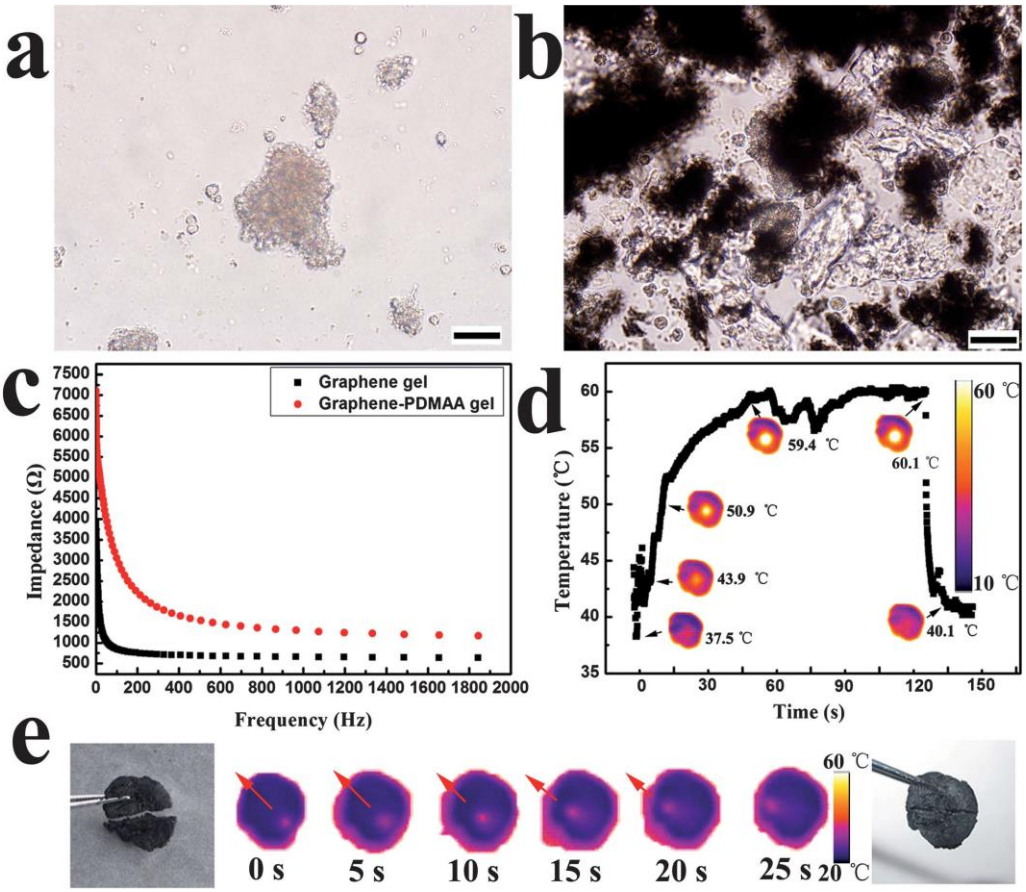

Figure 6. Self-healing of graphene–PDMAA gels under NIR laser irradiation and their infrared thermal images. Reproduced with permission from Ref 65. Copyright 2012, Royal Society of Chemistry.

1.1.4.2. Supercapacitor

Supercapacitors, comprising of pseudo-capacitor and electric double-layer capacitor (EDLC), are a class of energy storage devices which exhibit large power density and energy density simultaneously (Figure 7). Carbon-based EDLCs demonstrate several advantages, such as low-cost, high energy density and intrinsic robust nature [66-70]. Among the carbon nanomaterials used for EDLC electrodes, such as CNT, activated carbon, carbon nanofiber (CNF) and mesoporous carbon, graphene has emerged as an alternative due to intrinsically high specific surface area, large flexibility, high electric conductivity and outstanding mechanical stability. These excellent properties of graphene make it suitable for application in supercapacitor electrode. Multi-dimensional graphene structure is also appreciated, due to increased surface area for efficient electrolyte diffusion. Furthermore, replacing graphene to RGO has attracted researchers for cost-effectiveness and facile scalability of RGO for industrial application.

Lee *et al.* proposed preparation of metal-oxide nanofiber coated RGO network by freeze-drying and thermal reduction methodologies [71]. By dispersing metal-oxide nanofibers in GO solution and subsequent freeze-drying, 3D GO network with well-decorated metal-oxide nanofiber was prepared and additionally reduced. The final nanostructure exhibited high specific

capacitance of 446 F/g due to hybridization of pseudo-capacitance of metal-oxide nanofiber and EDLC capacitance of RGO. Wu *et al.* took a different approach of producing 3D RGO network by mixing of ammonia boron trifluoride (NH_3BF_3) with GO solution prior to hydrothermal reduction [72]. Nitrogen and boron element in NH_3BF_3 play a role as a dopant on RGO network, thus increasing charge transfer between original carbon atoms and doped nitrogen/boron atoms. This nitrogen/boron doped 3D RGO network was applied as a solid-state supercapacitor with polyvinyl alcohol (PVA)/sulfuric acid electrolyte, showing specific capacitance of 26.2 F/g. Chen *et al.* added organic amine or ammonia in GO solution and subsequent hydrothermal reduction of the corresponding solution for 12 h at 180 ^oC [73]. The resultant hydrogel electrode exhibited high power density of 205 kW/kg and specific capacitance of 113.8 F/g. At last, 3D porous MnO_2/RGO composite film prepared by RGO coating on polystyrene (PS) microsphere template and MnO_2 deposition also worked as a supercapacitor electrode due to large surface area of initial PS template [74].

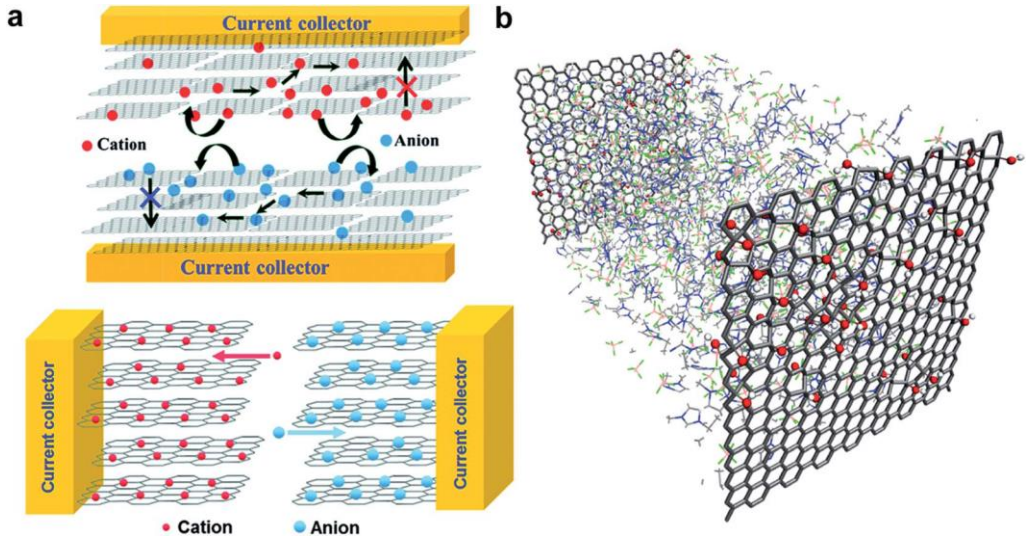

Figure 7. Preparation of supercapacitor: supercapacitor mechanism. Reproduced from Ref 66. with permission from the Royal Society of Chemistry.

1.1.4.3. Sensor

Due to increase in specific surface area and surface reactivity, preparation of novel material in nano-regime and its sensor application has always been a primary interest among nanomaterial researchers. Advent of graphene era has aroused a huge attention toward the fabrication of graphene-based sensors for chemical/biological detection for superior electric conductivity, large specific surface area of graphene itself [75-77]. Besides graphene, GO and RGO-based sensors are also thoroughly investigated, due to facile immobilization of enzyme, active metal nanomaterials or other bio-receptor molecules on functional groups of GO or RGO. The previous studies have shown that the preparation of 3D architecture also presents increased sensing performance [78]. 3D RGO network has also been applied in strain sensor application, where intrinsically robust nature and high electric conductivity of graphene have been exploited.

For example, 3D RGO micropillar structure on PDMS template was fabricated and tyrosinase enzyme was immobilized on the RGO surface to be utilized as a phenol detection sensor [79]. To obtain 3D structure of RGO, PDMS micropillars were prepared by photolithography technique and negative GO sheets were adsorbed on positively functionalized PDMS, followed by chemical reduction. Using this method, target phenol molecules were detected

in detection limit of 50 nM. Similar form of RGO micropillar arrays were prepared by Penmatsa *et al.* and hydrogen peroxide (H_2O_2) was detected with this fine-coated RGO micropillar structure [80]. Penmatsa *et al.* used electrostatic spray deposition method to obtain fine RGO coating on micropillar array. On the other hand, Liu *et al.* employed inorganic nanoparticles for efficient detection of nitrogen dioxide (NO_2) [81]. Utilizing $SnCl_4$ as a tin oxide precursor and GO as a RGO precursor, the $SnCl_4$/GO solution undergoes hydrothermal reduction for 10 h at 200 ^oC to synthesize SnO_2/RGO aerogel. The SnO_2/RGO aerogel selectively respond to 50 ppm NO_2 gas due to unique electron transfer from the aerogel to NO_2 gas to form NO gas.

The 3D RGO gel can be used in detection of bio-molecules, such as glucose. Yuan *et al.* reported preparation of bimetallic PdCu nanoparticle on RGO hydrogel to detect glucose without addition of enzyme on the surface [82]. Using mild hydrothermal reduction of Pd/Cu precursor/GO solution, as-prepared PdCu/RGO hydrogel can detect glucose molecules at the detection limit of 20 μM in the presene of chloride ions.

Additionally, a hierarchically structured RGO foam fabricated from freeze-drying of GO suspension and subsequent thermal treatment (Figure 8) [83]. Since the material possesses macroporous honeycomb-like structure and

exhibits superior compression recovery, it was utilized as a strain-gauge sensor. As compressive strain applied on the RGO foam, the electrical resistance of the material showed linear change behavior along with fast response time. The preparation of RGO foam illuminates a promising route in preparation of real-time monitoring device for human health.

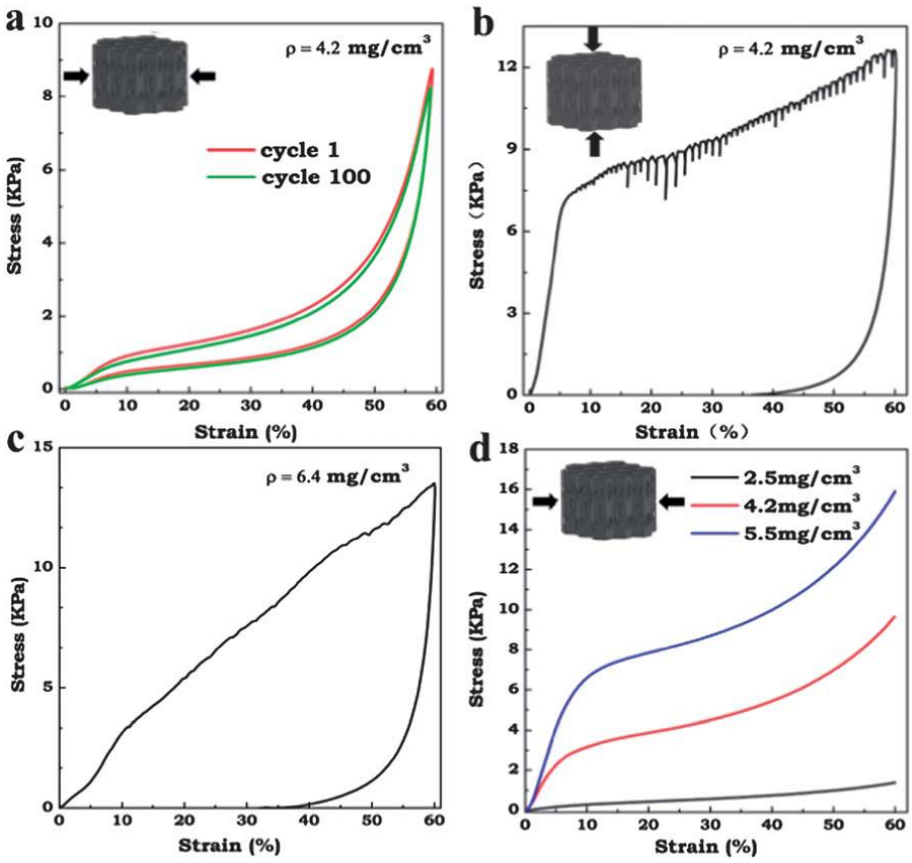

Figure 8. Typical compressive stress–strain curves of the ReG foam: a) in-plane direction and b) out-of-plane direction. c) A typical compressive stress–strain curve of the graphene foam prepared by the hydrothermal method. d) Stress– strain curves of the ReG foams with different density values along the in-plane direction. Reproduced from Ref 83 with permission from the Royal Society of Chemistry.

1.1.4.4. Latent heat storage

Thermal energy control in nano-electronics and industrial plant has been regarded as a critical issue. And also, utilization of surplus solar energy and storage of solar energy as thermal energy have been investigated, due to vast amount of solar energy projected by the sun [84]. Phase change materials (PCMs) are a class of materials that display different physicochemical properties when the ‘phase’ of corresponding material change from one to another [85]. These PCMs undergoes structural change in phase transition, and are applied in fields of non-volatile memory device [86], solar energy storage [87], controlled drug release [88] and *etc*. In case of thermal energy management, many organic materials like paraffin, fatty acid and eutectic mixtures are applied as PCMs due to large latent heat storage in solid-liquid phase transition (Figure 9 and 10). These organic PCMs exhibit a variety of thermophysical properties according to the number of carbon atoms or intrinsic chemical structure (Table 3 and 4). However, the organic PCMs tend to lose their stable shape when phase changes from solid to liquid, which is not appreciated in practical application. And the PCMs exhibit relatively low thermal/electric conductivities and these properties lower the thermal energy transfer rate.

Therefore, use of graphene in multi-dimensional structure can greatly

enhance the weak properties of current PCM used. Ye *et al.* reported preparation of RGO aerogel encapsulating paraffin [89]. The paraffin-encapsulated RGO aerogel was prepared by mixing of paraffin/cyclohexane solution and GO/water solution to obtain GO/paraffin emulsion. This emulsion was then reduced by hydrothermal method and resultant gel was lyophilized acquire paraffin/RGO aerogel. Since the paraffin PCM is directly 'embedded' in porous RGO aerogel structure, the shape-stability of paraffin is maintained during the latent heat storage process. Besides paraffin, fatty acids are a class of PCMs frequently used among researchers. Zhong *et al.* also synthesized RGO aerogel by hydrothermal reduction of GO solution, and molten octadecanoic acid was impregnated into the RGO aerogel by immersion technique [90]. The octadecanoic acid/RGO aerogel showed increased thermal conductivity of 2.635 W/mK at RGO loading fraction of 20 volume %, which is a 14 times value of pristine octadecanoic acid. Nonetheless, the results described above utilizes hydrothermal reduction which requires tightly sealed container and the RGO loading fraction should be very high for appreciable increase in thermal/electric conductivity values.

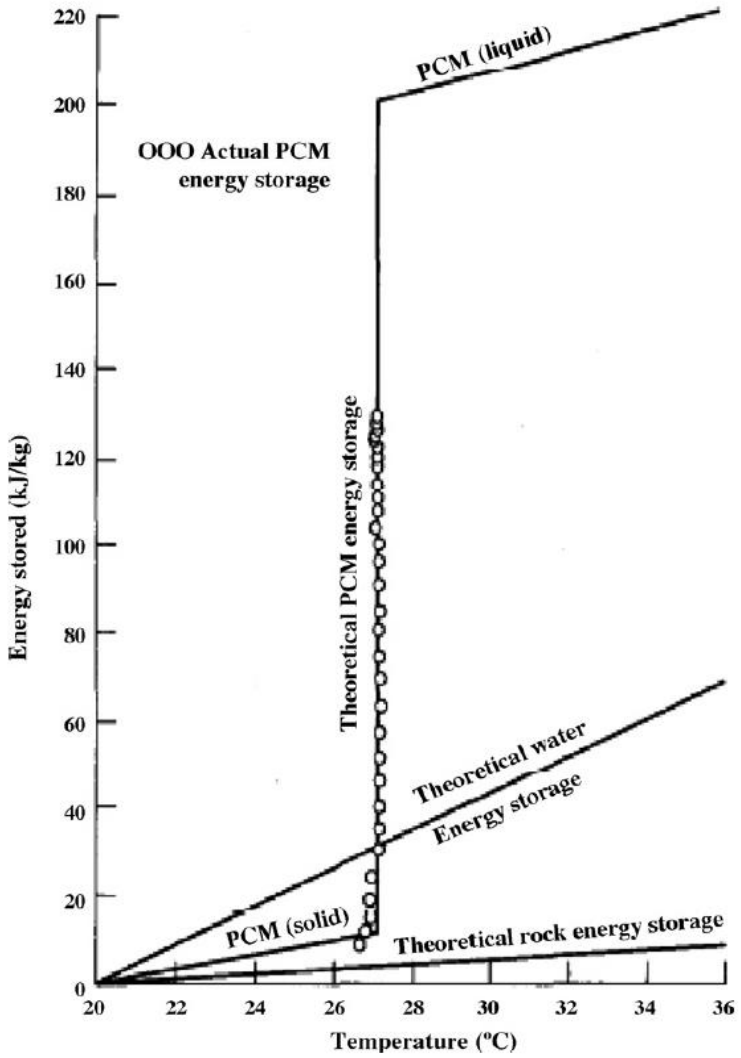

Figure 9. Performance comparison of PCM, water and rock storage system. Reprinted with permission from ref 85. Copyright 2007 Elsevier.

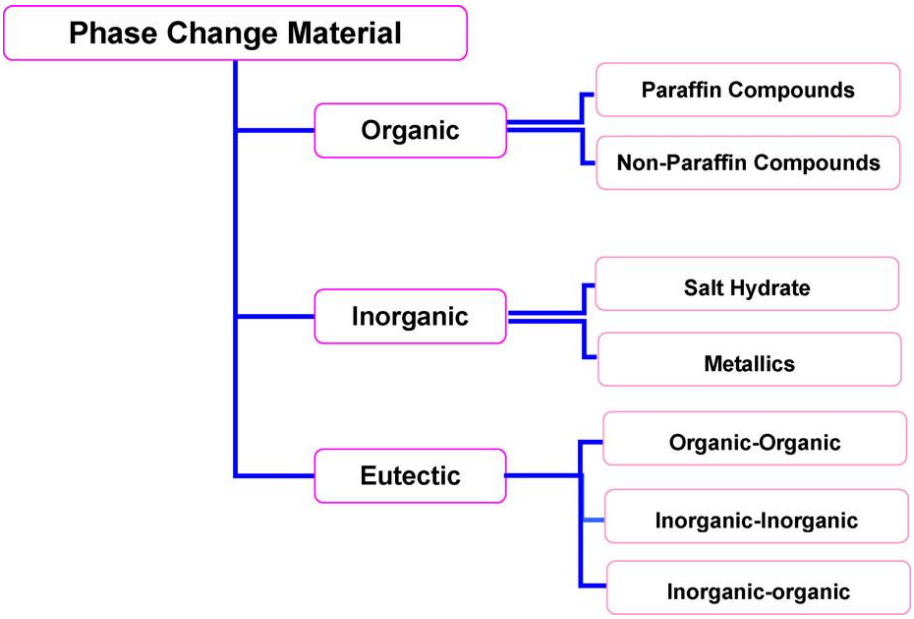

Figure 10. Categorization of phase change materials: Organic, inorganic and eutectic PCMs. Reprinted with permission from ref 85. Copyright 2007 Elsevier.

Table 3. Thermophysical parameters of paraffin according to number of carbon atoms in the paraffin structure. Reprinted with permission from ref 85. Copyright 2007 Elsevier.

Melting point and latent heat of fusion: paraffins

No. of carbon atoms	Melting point (°C)	Latent heat of fusion (kJ/kg)	Group[a]
14	5.5	228	I
15	10	205	II
16	16.7	237.1	I
17	21.7	213	II
18	28.0	244	I
19	32.0	222	II
20	36.7	246	I
21	40.2	200	II
22	44.0	249	II
23	47.5	232	II
24	50.6	255	II
25	49.4	238	II
26	56.3	256	II
27	58.8	236	II
28	61.6	253	II
29	63.4	240	II
30	65.4	251	II
31	68.0	242	II
32	69.5	170	II
33	73.9	268	II
34	75.9	269	II

[a] Group I, most promising; group II, promising; group III, less promising; — insufficient data.

Table 4. Thermophysical properties of non-paraffin organic PCMs. Reprinted with permission from ref 85. Copyright 2007 Elsevier.

Melting point and latent heat of fusion: non paraffins

Material	Melting point (°C)	Latent heat (kJ/kg)	Group[a]
Formic acid	7.8	247	III
Caprilic acid	16.3	149	–
Glycerin	17.9	198.7	III
D-Lattic acid	26	184	I
Methyl palmitate	29	205	II
Camphenilone	39	205	II
Docasyl bromide	40	201	II
Caprylone	40	259	II
Phenol	41	120	III
Heptadecanone	41	201	II
1-Cyclohexylooctadecane	41	218	II
4-Heptadacanone	41	197	II
p-Joluidine	43.3	167	–
Cyanamide	44	209	II
Methyl eicosanate	45	230	II
3-Heptadecanone	48	218	II
2-Heptadecanone	48	218	II
Hydrocinnamic acid	48.0	118	–
Cetyl alcohol	49.3	141	–
α-Nepthylamine	50.0	93	–
Camphene	50	238	III

1.2. Objectives and Outline of the Study

1.2.1. Objectives

In the previous section, the significance of 3D graphene network was introduced from the academic viewpoint and practical applications. The goal of this dissertation is to present two different synthetic methodologies to fabricate 3D reduced graphene oxide (RGO) networks in terms of 'plasma-reduction' and 'L-AA reduction'. Furthermore, the formation mechanism of the respective 3D RGO networks is systematically investigated, and their application fields are also presented: electrochemical energy storage application of the plasma-reduced GO film and latent heat storage application of the plasma-reduced GO film and L-AA-reduced graphene monolith as support material for organic PCMs.

1.2.2. Outline

This dissertation involves the following subtopics:

I. Preparation of 3-dimensional expanded RGO film *via* atmospheric plasma treatment on GO film
    1. Preparation of GO film *via* vacuum suction of GO solution
    2. Preparation of HRGO film *via* hydrazine-reduction
    3. Fabrication of 3-dimensional expanded RGO film *via* atmospheric

plasma

II. Fabrication of 3-dimensional RGO monolith *via* reduction of GO with L-ascorbic acid (L-AA)

1. Preparation of graphene oxide
2. Reduction of graphene oxide solution with L-AA

III. Applications

1. Fabrication of 3-dimensional, expanded RGO film as a free-standing supercapacitor electrode
2. Fabrication of free-standing 3D RGO film embedded with organic PCMs for latent heat storage
3. Fabrication of 3-dimensional graphene monolith with paraffin *via* L-AA reduction for PCM application

A detailed outline of the study is as follows:

1. As a ‘plasma-reduction’, the free-standing 3D expanded reduced graphene oxide (RGO) films are fabricated using a rapid thermal exfoliation and deoxygeneation process of graphene oxide (GO) thin film *via* brief atmospheric plasma treatment. To obtain 3D RGO structure, the GO thin film prepared from vacuum suction of GO solution is used as a starting material. The 3D RGO films are formed by brief atmospheric plasma

treatment on GO film, with sufficient argon flow. The electrons in the plasma glow reacts with oxygen-functional groups of GO surface and the sudden elimination of oxygen groups result in rapid reduction of GO. Due to formation of oxygen-related gases during thermal exfoliation, the RGO sheets are expanded outward to form 3D network of physically linked RGO sheets. In addition, the 3D RGO films can be formed without any toxic reducing agent and possess increased specific surface area.

2. As an ‘L-AA reduction’, 3D graphene monoliths are formed spontaneously during the mild L-ascorbic acid (L-AA) reduction of GO solution. Although the actual mechanism of formation of 3D graphene structure remains unknown, the spontaneous production of 3D graphene monolith by L-AA help reduce the additional step to convert 2D graphene sheets into 3D architecture. The pore size and density of the 3D graphene monoliths can be easily tuned by manipulating the concentration of GO solution. This new methodology can illuminate a great possibility for fabricating 3D graphene network material with controlled architecture.
3. The 3D expanded RGO film prepared from brief atmospheric plasma reduction is utilized as an active material for supercapacitor electrode. The utilization of carbon nanomaterials as electric double layer capacitor (EDLC) has attracted a great deal of interest because of the high surface

area and large electric conductivity of carbon nanomaterials. The increased contact area of electrolyte-electrode interface and superb electric conductivity of carbon nanomaterials help obtain large specific capacitance of carbon-EDLC system. Furthermore, the intrinsic strong nature of carbon materials is also an advantage, since long-term stability of electrode is required. In this study, as-prepared 3D RGO structure showed excellent electrochemical properties and good cyclability, for its high surface area and intrinsic physical/chemical stability.

4. The ability to control thermal energy storage is important in many technological applications, especially in electronic micro-devices and industrial plant where latent heat should be carefully controlled for stability of the devices and machines. In particular, phase change materials (PCMs) have received much attention due to their unique thermophysical properties. The PCMs, including paraffin or metal hydrates, store or release thermal energy during the phase-phase transition process. Among the PCMs, the organic PCMs like paraffin, fatty acid and polymers are less-expensive and can be processed easily. However, the thermal/electric conductivities and shape-stability of the organic PCMs are usually very low. In this work, a simple and effective pathway is demonstrated to study the latent heat storage properties of the organic PCMs/3D plasma-RGO (PRGO) film

comoposites assisted by immersion method. The PCM/PRGO composites demonstrate increased thermal/electric conductivities with retained latent heat of fusion.

5. The 3D pRGO monoliths prepared from mild L-AA reduction of GO solution are utilized as a support of paraffin. Due to low-cost and large latent heat of fusion, paraffin has been exploited as a representative PCM in industrial application. However, the paraffin itself has low thermal/electric conductivities and low shape-stability during solid-liquid transition. Therefore, the 3D pRGO monoliths are immersed in molten paraffin and the solidified paraffin is adsorbed in the 3D RGO monoliths to produce paraffin/pRGO composites. The pore size and the density of the 3D pRGO monoliths are adjusted by using different concentration of GO solution in initial reduction process. As the concentration of GO solution increases, the density of the resultant monolith increases and the physical properties of the corresponding paraffin/pRGO composite enhanced. This simple immersion method provides the feasible candidate for the practical applications of 3D RGO network in PCM industries.

2. EXPERIMENTAL DETAILS

2.1. Preparation of 3-dimensional expanded RGO film *via* atmospheric plasma treatment on GO film

2.1.1. Preparation of GO film *via* vacuum suction of GO solution

200 mesh Graphite (≤ 74 μm) was purchased from Alfa Aesar, USA. Sodium nitrate ($NaNO_3$, 99 %) and hydrazine monohydrate (N_2H_4•H_2O, 98 %) were purchased from the Sigma-Aldrich Co. Potassium permanganate ($KMnO_4$, 99.3 %) and phosphorus pentoxide (P_2O_5, extra pure) were acquired from the Junsei Chemical Co. Sulfuric acid (H_2SO_4, 95 %), hydrochloric acid (HCl, 35~37 %) and hydrogen peroxide (H_2O_2, 30~35.5 %) were supplied from the Samchun Chemical Co. Potassium persulfate ($K_2S_2O_8$, 99 %) was purchased from the Kanto Chemical Co.

Initially, graphene oxide (GO) solution was prepared by a slightly modified Hummers' method [91]. For pre-oxidation process, 5 g of graphite powder, 2.5 g of P_2O_5 and 2.5 g of $K_2S_2O_8$ was mixed with 30 ml of H_2SO_4 in a flask and the whole solution was heated at 80℃ for 6 h. The solution was filtered through mixed cellulose acetate filter (ADVANTEC) with excess deionized water and remaining residue was stored in vacuum oven for 24 h. The 2.5g of $NaNO_3$ was then dissolved in 115 ml of H_2SO_4 with vigorous stirring. The dried graphite powder was poured into well-mixed $NaNO_3$/H_2SO_4 solution

with vigorous stirring, while kept in ice bath. In this state, 15 g of $KMnO_4$ was slowly added to the solution for 30 min, while keeping the temperature lower than 20℃. After 30 min, ice bath was removed and whole solution was heated at 45℃ for 12 h, turning the color of solution to brownish gray. Then 230 ml of deionized water was slowly poured into the paste, keeping the temperature below 40℃. 700 ml of deionized water was poured again and 25 ml of H_2O_2 was added dropwise to the solution, forming bright yellow color in solution. This graphitic oxide solution was washed with 10 wt % HCl solution for three times and deionized water for several times until the pH of solution turned into 7. This solution was ultrasonicated for 1 h to exfoliate graphitic oxide into GO. Then the solution was centrifugated at 4000 rpm for 30 min to exclude residue. The GO solution was dried in vacuum oven and GO powder was obtained.

After complete drying, the GO powder was re-dissolved in ultra-pure water to make 0.2 wt% GO solution. The aqueous GO 0.2 wt% solution was vacuum-filtered through 47mm AAO membrane (Whatman®) with vacuum-suction apparatus for 12 h. After complete suction, GO film was peeled off from the AAO membrane and was kept from humidity.

2.1.2. Preparation of HRGO film via hydrazine-reduction

The hydrazine-reduced GO (HRGO) film was prepared *via* vapor phase treatment of hydrazine on GO film. The GO film prepared from chapter 2.1.1 was put in a glass jar and 0.1 ml of hydrazine solution was dropped inside of the jar, while kept away from the GO film. The jar was sealed with teflon tape and was put in a dry oven. The hydrazine reduction proceeded for 6 h at 100 ^{o}C. As-prepared HRGO film was then put in a vacuum oven before further use.

2.1.3. Fabrication of 3-dimensional expanded RGO film *via* atmospheric plasma

In order to produce 3-dimensionally expanded plasma-reduced GO (PRGO) film, the dried GO film was treated with atmospheric plasma using handheld plasma apparatus. An atmospheric plasma curtain was produced by radio-frequency discharge on cathode ray tube of handheld plasma apparatus with 13.56 MHz radio-frequency and inert argon flow (Flow rate : 8 L/min). The distance from the surface of GO film and the cathode ray tube was set up to be 1 cm. After luminous plasma curtain was produced, the GO film was exposed to plasma curtain for up to 20 seconds. After 20 second-exposure, PRGO film was produced with sudden change of color from gray to black. The as-prepared PRGO film was kept in vacuum oven before further use.

2.2. Fabrication of 3-dimensional RGO monolith *via* reduction of GO with L-ascorbic acid (L-AA)

2.2.1. Preparation of graphene oxide

200 mesh Graphite (≤ 74 μm) was supplied from Alfa Aesar. Hydrogen peroxide (H_2O_2, 30~35.5 %), sulfuric acid (H_2SO_4, 95 %) and hydrochloric acid (HCl, 35~37 %) were acquired from the Samchun Chemical Co. Potassium permanganate ($KMnO_4$, 99.3 %) and phosphorus pentoxide (P_2O_5, extra pure) were purchased from the Junsei Chemical Co. L-ascorbic acid (99 %), sodium nitrate ($NaNO_3$, 99 %) and hydrazine solution (35 % in H_2O) were purchased from the Sigma-Aldrich Co. Potassium persulfate ($K_2S_2O_8$, 99 %) was purchased from the Kanto Chemical Co.

Graphene oxide (GO) solution was prepared by a slightly modified Hummers' method [91]. Solid $NaNO_3$ (0.5 g) was mixed with H_2SO_4 (23 ml) at vigorous stirring. Fine graphite powder (1 g) was then poured into well-mixed $NaNO_3$/ H_2SO_4 solution with vigorous stirring in ice bath. After thorough mixing for 1 h, $KMnO_4$ (3 g) was slowly poured into the solution, while keeping the temperature lower than 40 ^oC. After 30 min, ice bath was removed and whole solution was heated at 45 ^oC for 12 h, turning the black solution to brownish gray paste. Then deionized water (46 ml) was slowly poured into the paste, keeping the temperature below 20 ^oC using ice bath. Then deionized

water (140 ml) was additionally poured and H_2O_2 (5 ml) was slowly dropped to the solution, forming graphitic oxides in solution. The H_2O_2 reacts with the residual metal ions in the solution and cleave them away. This graphitic oxide solution was washed with 10 wt % aqueous HCl solution for three times and deionized water for several times until the pH of solution turned to 7. This solution was ultra-sonicated for 1 h at 450 W power to exfoliate graphitic oxide into GO. Then the solution was centrifugated at 4000 rpm for 30 min to exclude residue. As-prepared GO solution was dried as powder and kept in vacuum oven before further use.

2.2.2. Reduction of graphene oxide solution with L-AA

After complete drying, the GO powder was re-dissolved in ultra-pure water to prepare 0.01, 0.05 and 0.5 wt% GO solution. The 3D pRGO monolith was synthesized by the reduction method presented by Li's group with slight modification [46]. L-ascorbic acid (L-AA) powder was added to the corresponding GO solution, to make the weight ratio of GO in the corresponding solution to L-ascorbic acid as 2 to 1. After L-AA addition, the solution was stirred vigorously for 30 min until all the L-AA powder dissolved. After complete mixing, the solution was put in a glass jar and the jar was stored in 100 ^{o}C oven for 30 min to obtain 3D pRGO monoliths with different pore sizes, according to the different initial concentration of GO solution used. After thermal treatment, the 3D pRGO monoliths were kept in ice bath for 30 min and then moved to 200 ^{o}C oven for 8 h. The 3D pRGO monoliths were then lyophilized for 48 h. Finally, the lyophilized 3D pRGO monoliths were stored in vacuum oven to be kept away from moisture.

2.3. Applications

2.3.1. 3-dimensional expanded RGO film as a free-standing supercapacitor electrode

The GO film and HRGO film were fabricated by the method described in chapter 2.1.1 and 2.1.2, respectively. The 3-dimensional expanded RGO film was prepared by the method described in chapter 2.1.3.

For microscopic analyses, scanning electron microscope (SEM) images were obtained with a JSM-6701F (JEOL, Japan). High-resolution transmission electron microscope (HR-TEM) images were acquired with a JEM-3010 transmission electron microscope. For HR-TEM analysis, few mg of samples were readily dispersed in ethanol and was transfered on copper grid. All X-ray photoelectron spectroscopy (XPS) analyses were conducted with a Thermo-VG (Sigma Probe, UK). Thermogravimetric analysis (TGA) spectra were obtained with a Perkin-Elmer Pyris TGA 6 thermogravimetric analyzer. All TGA analyses were conducted in inert nitrogen atmosphere and the target temperature was 700 ^{o}C at the ramping rate of 10 ^{o}C/min. UV-Vis absorption spectroscopy measurements were performed with a Lambda 35 (Perkin-Elmer) UV-Vis spectrometer. For UV-Vis analyses, the samples were readily dispersed in distilled water. X-ray diffraction (XRD) was conducted using a Bruker New D8 Advance with a Cu-Kα radiation source (λ: 1.5406 Å) at 12

kW power. All XRD analyses were done using the film-type samples, without any modification. Brunauer–Emmett–Teller (BET) surface areas of PRGO films were measured using a ASAP 2000 Micromeritics surface area analyzer (Micromeritics Co., USA). Fourier-Transform Infrared (FT-IR) spectra measurement was conducted with a Perkin-Elmer Frontier FT-NIR/MIR Spectrometer, using universal-ATR mode.

All plasma treatment was conducted using a MyPL 200 handheld plasma apparatus with 13.56 MHz radio-frequency glow discharge and 8 L/min argon flow (APP Co. Ltd., Korea). The distance between the target GO film and the cathode ray tube of the handheld plasma apparatus was set to be 1 cm. The applied plasma power was varied from 100 W to 200 W, and the operating time was fixed at 20 sec.

The cyclic voltammetry (CV) and galvanostatic charge/discharge tests of GO, HRGO and PRGO films were conducted with a Wonatech WBCS 3000 potentiostat/galvanostat instrument to study the electrochemical performances of the samples. All electrochemical measurements were performed in a 3-electrode system with 1M H_2SO_4 solution as the electrolyte at room temperature, where the counter and reference electrodes were Pt wire and Ag/AgCl, respectively. The film itself was directly employed as the working electrode for all sample species. The potential range for CV and galvanostatic

charge/discharge tests was 0.0 to 0.8 V. The electrochemical behavior was first characterized by the CV test at scan rates ranging from 10 mV/s to 250 mV/s. After that, the galvanostatic charge/discharge test of the PRGO film was carried out at a current density of 1, 3 and 5 A/g to precisely evaluate the gravimetric capacitance, C_m (F/g). The gravimetric capacitances (C_m) were calculated by using the equation $C_m = (I \times \Delta t)/(m \times \Delta V)$, where C_m is the gravimetric capacitance in F/g , I is the constant discharge current in mA, Δt is the discharge time in second, m is the total mass of the active material in mg, ΔV is the potential window in V. The cycle stability of the PRGO film was measured by the galvanostatic charge/discharge test at a current density of 1 A/g in 1M H_2SO_4 solution.

2.3.2. 3-dimensional expanded RGO film as a foothold for organic phase change materials

The 3-dimensional expanded RGO film (PRGO film) was prepared by the method described in chapter 2.1.3. For this experiment, polyethylene glycol (M.W. 20000, extra pure) was acquired from Junsei Chemical Co. Fluorene (98%) and octanoic acid (98%) were purchased from Sigma-Aldrich Chemical Co. Paraffin (C_nH_{2n+2}, melting point: 42~44 ^oC) were purchased from Kanto Chemical Co. All of the reagents were used as received without further purification.

For fabrication of the PCM/PRGO composites, solid paraffin and PEG flake, 10 g respectively, were stuffed in 70 ml glass bottle and heated to 60 ^oC and 75 ^oC for melting of the solid PCMs, respectively. The PRGO films were then immersed in the molten paraffin and PEG for 30 min. After complete adsorption of molten PCMs, the PRGO films stuffed with paraffin and PEG were retracted from the glass bottle and were dried in room temperature (RT) to obtain the paraffin/PRGO composite and PEG/PRGO composite, respectively. 40 ml of octanoic acid (in liquid state) was also poured to 70 ml glass bottle and the PRGO film was then immersed in the liquid octanoic acid at RT for 30 min. After complete soaking for 30 min, the PRGO film stuffed

with octanoic acid was collected out and was dried in RT to obtain the octanoic/PRGO composite.

For microscopic analyses, scanning electron microscope (SEM) images were acquired with a JSM-6701F (JEOL, Japan). Fourier-Transform Infrared (FT-IR) spectra measurement was conducted with a Perkin-Elmer Frontier FT-NIR/MIR Spectrometer, using universal-ATR mode. The PCM/PRGO composites were pelletized and the corresponding pellet was measured. X-ray diffraction (XRD) measurement was conducted using a Bruker New D8 Advance with a Cu-Kα radiation source (λ: 1.5406 Å) at 12 kW power. Differential scanning calorimetry (DSC) measurement was conducted with a Perkin-Elmer differential scanning calorimeter DSC 6000. The long-term thermal cyclability of the PCM/PRGO composites was also evaluated with a Perkin-Elmer differential scanning calorimeter DSC 6000. Thermogravimetric analysis (TGA) spectra were obtained with a Perkin-Elmer Pyris TGA 6 thermogravimetric analyzer. All TGA analyses were operated in inert nitrogen atmosphere at ramping rate of 10 ^{o}C/min. The thermal conductivity of the PCM/PRGO composites were determined by modified Flynn and Levin method using a Perkin-Elmer differential scanning calorimeter DSC 6000 [92-93]. For the thermal conductivity measurement, fluorine pellet (5 mm diameter) was utilized as sensor material. The pristine PCMs and the

PCM/PRGO composites were cut into thin, round pellet by razor blade with 6.5 mm diameter. For thermal conductivity measurement, the thickness of sample must be measured. For the DSC analyses, two kinds of experiments were conducted: First, melting curves of the sole fluorine pellet was measured. After then, the melting curves of the PCMs and the composites were measured by using fluorine pellet and sample pellet in one alumina holder. The contact between fluorine pellet and sample pellet must be firm in order to obtain accurate result. After measurement, the slope values of the melting curve were calculated and was converted to thermal resistance to determine the thermal conductivity of the samples. The electric conductivity of the PCM/PRGO composites was measured using a four-point probe system (Mode Systems Co., Korea) equipped with a current source meter (Keithley 2400, Keithley Co., USA).

2.3.3. 3-dimensional pRGO monolith for adsorption of paraffin as a phase change material

The 3-dimensional pRGO monoliths were prepared by the method described in chapter 2.2.2. In this work, paraffin (C_nH_{2n+2}, melting point: 42~44 ^oC) were aquired from Kanto Chemical Co. All of the reagents were used as received without further purification.

For fabrication of paraffin/RGO composites, 10 g of solid paraffin was added to 70 ml glass bottle and the bottle was heated up to 60 ^oC until all paraffin melted. The 3D pRGO monoliths with different pore sizes were then immersed in the molten paraffin for 30 min until the 3D pRGO monoliths were completely soaked with liquid paraffin. After 30 min, the 3D pRGO monoliths with stuffed paraffin were collected out of the molten paraffin and were dried in room temperature to obtain the paraffin/pRGO composites.

For microscopic analysis, scanning electron microscope (SEM) analyses were conducted with a JSM-6701F (JEOL, Japan). X-ray diffraction (XRD) was conducted using a Bruker New D8 Advance with a Cu-Kα radiation source (λ: 1.5406 Å) at 12 kW power. Fourier-Transform Infrared (FT-IR) spectra were acquired with a Perkin-Elmer Frontier FT-NIR/MIR Spectrometer, using universal-ATR measurement on pelletized samples. Differential scanning calorimetry (DSC) measurement was done with a Perkin-Elmer differential

scanning calorimeter DSC 6000. Thermogravimetric analysis (TGA) spectra were obtained with a Perkin-Elmer Pyris TGA 6 thermogravimetric analyzer. All TGA measurements were operated in inert nitrogen atmosphere. The thermal conductivity of paraffin/RGO composites was measured by the DSC-based method described in chapter 2.3.2. The electric conductivity of the paraffin/pRGO composites was measured using a four-point probe system (Mode Systems Co., Korea) equipped with a current source meter (Keithley 2400, Keithley Co., USA).

3. RESULTS AND DISCUSSION

3.1. 3-dimensional, expanded RGO film as a free-standing supercapacitor electrode

3.1.1. Preparation of PRGO film *via* atmospheric plasma

In Figure 11, the process of plasma-assisted reduction of GO film to produce 3D expanded PRGO film is demonstrated. In this work, GO powder was prepared *via* a slightly modified Hummers' method. Among the various oxidation pathways of graphite, the Hummers' method enables mass-production of graphitic oxide with less harmful residues to be washed. The produced graphitic oxide solution was readily ultra-sonicated and few-layer GO powers were obtained after repeated washing. The GO was dispersed in water to prepare 0.2 wt % aqueous GO solution (Figure 11a). This dilute solution was vacuum-suctioned on AAO membrane to produce few μm-thick GO thin film (Figure 11b). This GO film was then treated with atmospheric argon plasma for 20 sec using hand plasma apparatus with 13.56 MHz radio-frequency (RF). When the plasma reached the surface of GO film, the color of the film surface changed suddenly from brownish grey to black, forming expanded PRGO film (Figure 11c). During this plasma treatment, argon plasma curtain induce sudden thermal exfoliation and deoxygenation on GO film to produce 3-dimensionally expanded structure of RGO.

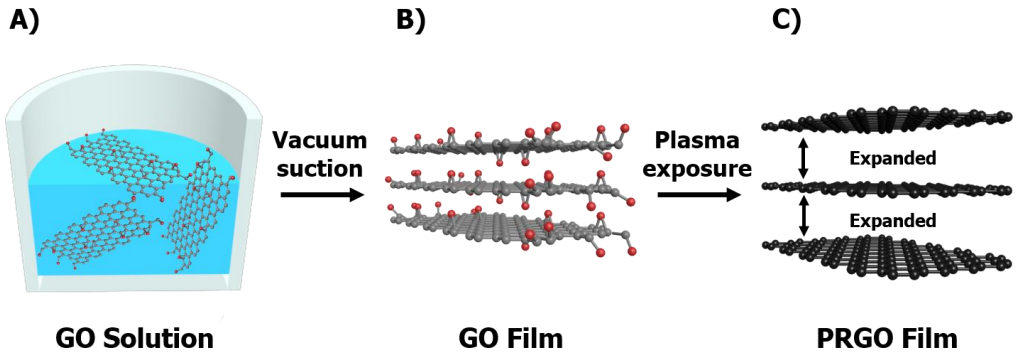

Figure 11. Schematic illustration of preparation of PRGO film. a) Dilute GO solution prepared by Hummers' method; b) GO thin film prepared by vacuum-filtration of the GO solution on AAO. Red dots stand for oxygen-related groups on GO structure; c) Expanded structure of PRGO film produced by atmospheric argon plasma treatment on GO thin film for 20 sec at 200W plasma power.

In SEM image of GO thin film (Figure 12a), GO sheets were stacked vertically to produce 10 μm-thick GO film after vacuum-suction of 10 ml 0.2 wt% GO solution onto AAO membrane. After brief atmospheric plasma treatment on GO film for 20 sec, the as-reduced GO sheets in the PRGO film expanded outward and the distance between individual RGO sheets increased. In Figure 12b, overall thickness of as-prepared PRGO film reached *ca.* 400 μm after plasma treatment. Digital photograph of the PRGO film (Figure 13) demonstrate that the structure of free-standing RGO film with 38 mm diameter was well preserved after plasma-reduction. The film demonstrated flexibility and change in color, referring to successful reduction of GO. In Figure 14, the transmission electron microscopy (TEM) analysis on PRGO film demonstrated that the planar RGO sheet was observed after brief plasma treatment on GO sheet.

The reduction mechanism of GO film by brief plasma treatment can be described as a combined effect of rapid thermal exfoliation and deoxygenation process. When atmospheric argon plasma curtain reaches the GO surface, various reactive species, such as electrons and ions, in plasma detach the oxygen-related functional groups (epoxide, carbonyl, carboxyl and hydroxyl groups) from the surface. These oxygen groups were rapidly eliminated compared to previous vacuum plasma process [39, 41, 95], which is verified by

rapid transition of color of the GO film. Additionally, this sudden deoxygenation generate oxygen-related gases like CO or CO_2 from oxygen groups and these gases evolve into stacked graphene sheets and induce high pressure to expand adjacent graphene sheets outward. Judging from the SEM results, atmospheric argon plasma treatment on GO film and subsequent reduction showed similar behavior with expansion of GO sheets in thermal reduction process [25].

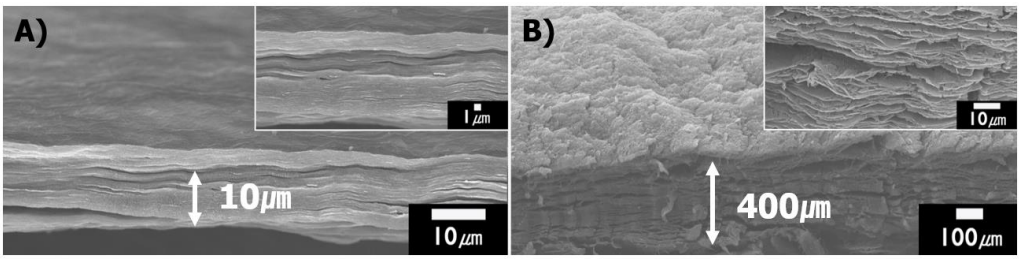

Figure 12. SEM images of GO film and PRGO film. a) x2000 SEM image of GO thin film (Inset: magnified image of GO thin film); b) x100 SEM image of PRGO film after 200W plasma treatment for 20 sec (Inset: magnified image of PRGO film).

.

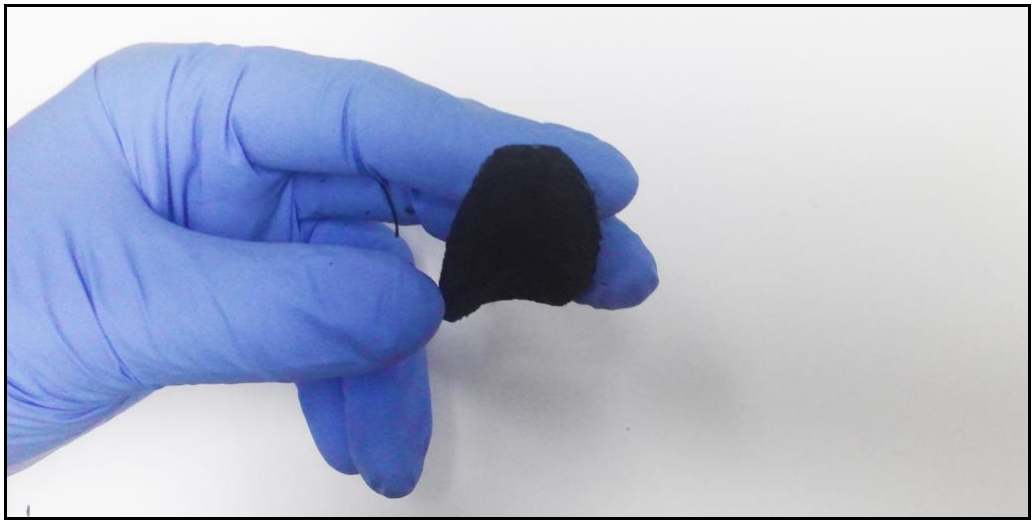

Figure 13. Digital photograph of the free-standing PRGO film.

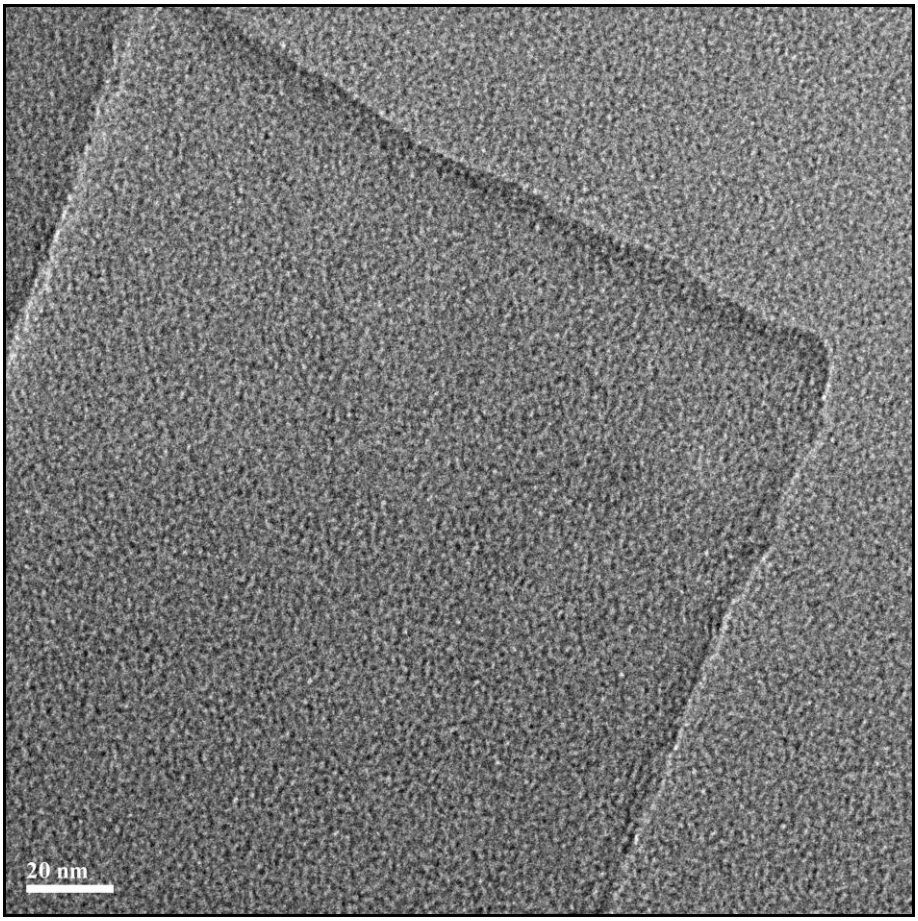

Figure 14. TEM image of PRGO film (Plasma treatment condition: 200W power for 20 sec).

3.1.2. Characterization of PRGO film

X-ray photoelectron spectroscopy (XPS) C1s analysis on PRGO film with different applied plasma power was conducted to investigate the effect of plasma condition on the degree of reduction of GO film (Figure 15 and 16). In the GO film spectrum, a distinct peak for single/double bond between carbon and carbon (C-C/C=C)) at 284.5 eV and a peak for C-O single bond at 286.5 eV is emphasized, as reported in previous work [41]. However, at plasma power exceeding 110 W, the C-O single bond peak was decreased and C-C/C=C bond peak was increased, which stands for cleavage of oxygen groups and restoration of C-C graphitic structure. Although C=O double bond peak at 287.8 eV and carboxyl (COOH) peak at 290 eV were still observed in the C1s spectra, the peak intensity of overall oxygen-related group was decreased (Figure 15). As the applied power increased to 200W, the percentage of carbon element on the surface of resultant PRGO film rose from 80.0 % at the power of 100W to 91.1 % at 200W. Meanwhile, the percentage of oxygen element declined from 20 % at 100W to 8.9 % at 200W (Figure 16). As a result, O/C ratio of PRGO film surface decreased to 0.116 when the applied power reached 200 W. The C1s XPS results indicate that the plasma reduction of GO completed in 20 sec with more than 110 W plasma power, reaching lowest O/C ratio of 0.116 at applied power of 200W.

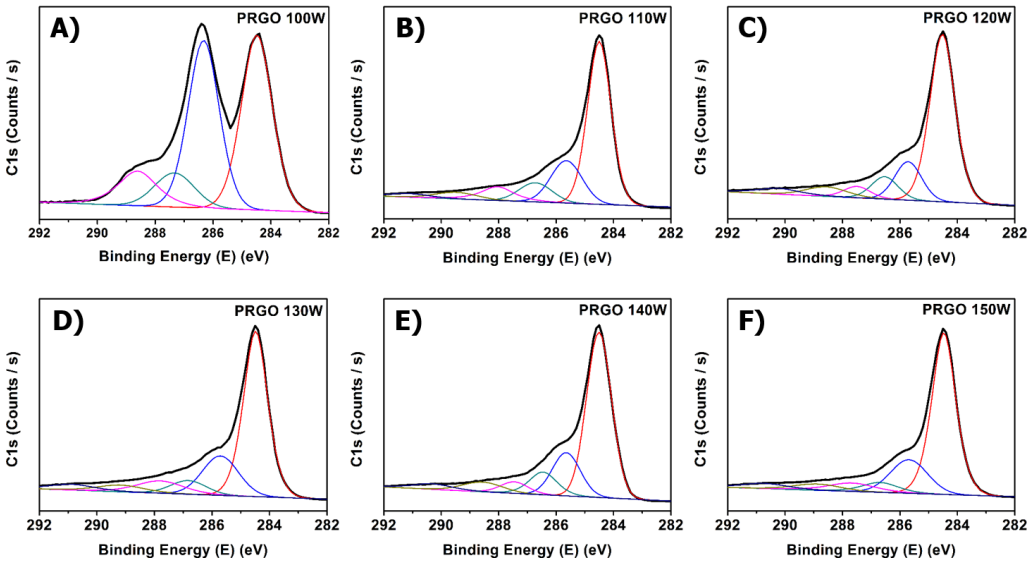

Figure 15. Deconvoluted XPS C1s spectra of PRGO film with varying applied plasma power from 100 to 150 W. a) 100W treatment; b) 110W treatment; c) 120W treatment; d) 130W treatment; e) 140W treatment; f) 150W treatment.

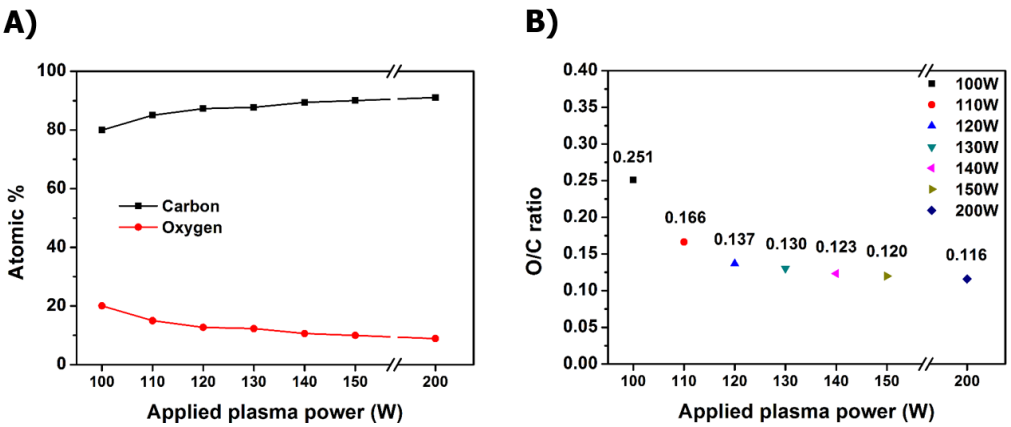

Figure 16. XPS analyses of PRGO film after plasma treatment. a) Atomic percentage of carbon (C) and oxygen (O) calculated from XPS analysis on PRGO film; b) O/C ratio values of PRGO film plotted over various applied plasma power (ranging from 100W to 200W). All plasma processing was conducted within 20 sec.

N1s XPS analyses were additionally conducted to clarify the effect of reduction on the surface atomic structure of PRGO film. Especially, hydrazine-reduced GO (Further denoted as HRGO) was prepared to compare the degree of reduction and the hetero-atom doping effect (Figure 17). For the comparison, HRGO films were synthesized by vapor-phase reduction of GO film with 0.1 ml hydrazine solution at 100 ℃ for 6 h. PRGO film produced at 200W plasma power (Further denoted as PRGO 200W) was used for this comparison experiment due to its lowest O/C ratio. In Figure 17a, a small N1s peak around 400 eV in overall XPS spectrum is present in HRGO, while a negligible N1s peak is detected in overall XPS spectrum of PRGO 200W. In Figure 18b, various nitrogen-related peaks, from pyridinic (*ca.* 399 eV) to pyrrolic (*ca.* 400.2 eV) and quaternary nitrogen (*ca.* 401.3 eV) peak, were spotted in deconvoluted HRGO N1s spectrum. In PRGO 200W spectrum, small nitrogen-related peaks were found and GO also showed small peak in N1s spectrum. These results indicate that the use of nitrogen-containing reducing agent like hydrazine or its relatives in reduction of GO might lead to considerable doping of nitrogen elements in target graphene structure, while atmospheric argon plasma treatment resulted in a minute hetero-atom incorporation on graphene structure. Since the atmospheric plasma treatment proceeded in normal atmospheric condition, N_2 gases in the air might be converted to nitrogen-

related reactive species and the reactive species might contact with graphene structure for insignificant nitrogen-doping on PRGO 200W.

UV-Vis measurement on GO, HRGO and PRGO 200W was done to study atomic structural change of PRGO film after plasma reduction process (Figure 18). First, the corresponding samples were finely dispersed in water and bath-sonicated prior to measurement. In UV-Vis spectra, the red-shift of broad absorption peak from 230 nm of GO to 283 nm of PRGO 200W after 200W plasma treatment reveals that C-C/C=C bonding was re-generated in plasma reduction process [96]. This vathochromic shift of absorption peak of PRGO 200W exceeds that of absorption peak of HRGO, suggesting superior reduction effect of plasma reduction.

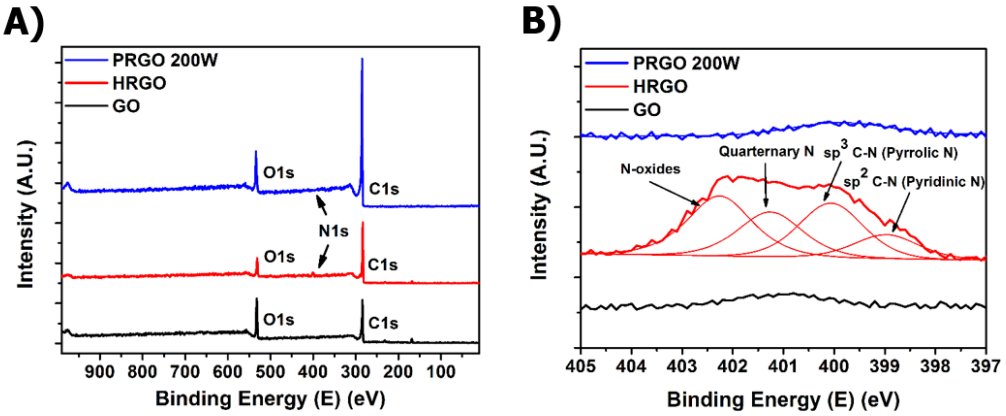

Figure 17. a) XPS wide spectra of GO, HRGO and PRGO 200W; b) deconvoluted XPS N1s spectra of GO, HRGO and PRGO 200W.

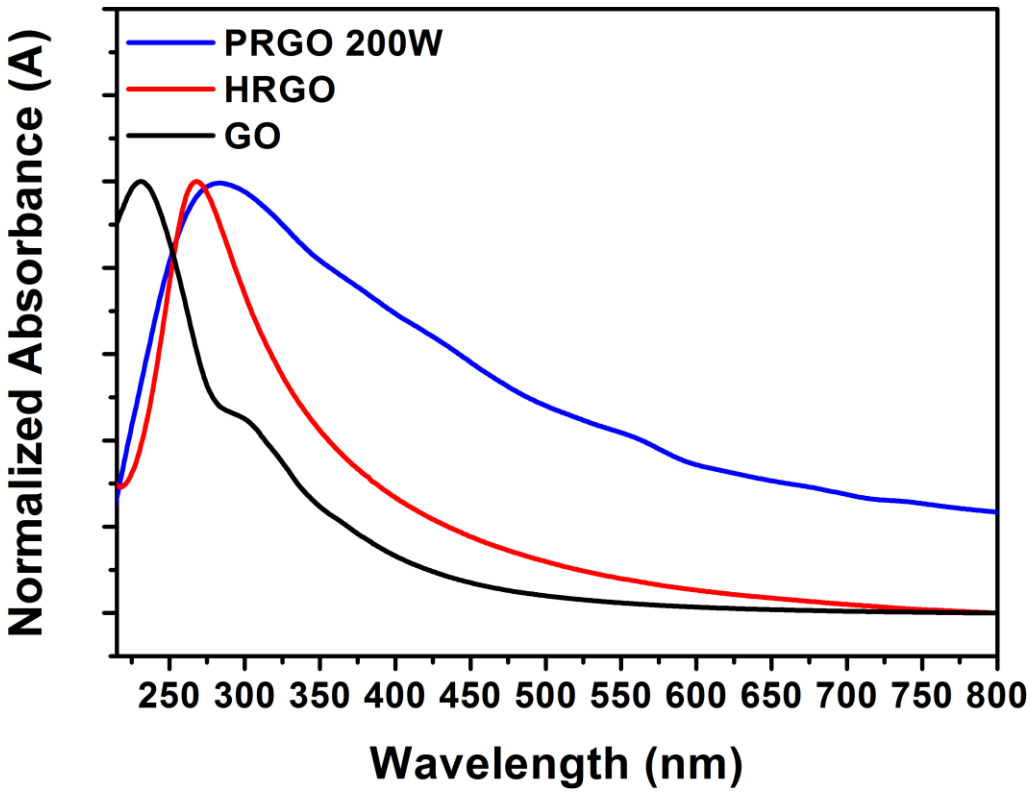

Figure 18. UV-Vis spectra of GO, HRGO and PRGO 200W.

C1s XPS analyses were additionally conducted to scrutinize the structural change of GO film after chemical and plasma reduction, in the viewpoint of change in oxygen-related functional groups on the surface (Figure 19). The peak area values were calculated by intergration of area under each deconvoluted C1s peak. In Figure 19, the C-O single bond peak at 286.5 eV occupied 14.1 % of peak area in GO film spectrum, while the C-C/C=C bond peak area percentage at 284.5 eV was 45.9 %. After each reduction process, corresponding C-O single bond peak area in HRGO and PRGO 200W diminished to 9 and 8.1 %, respectively. Meanwhile, the C-C/C=C bond peak area at 284.5 eV increased from to 48.8 % and 53.7 %, respectively. The result suggests that the plasma reduction exhibited better cleavage of oxygen-related groups after reduction process and the overall graphene structure is more repaired in plasma reduction.

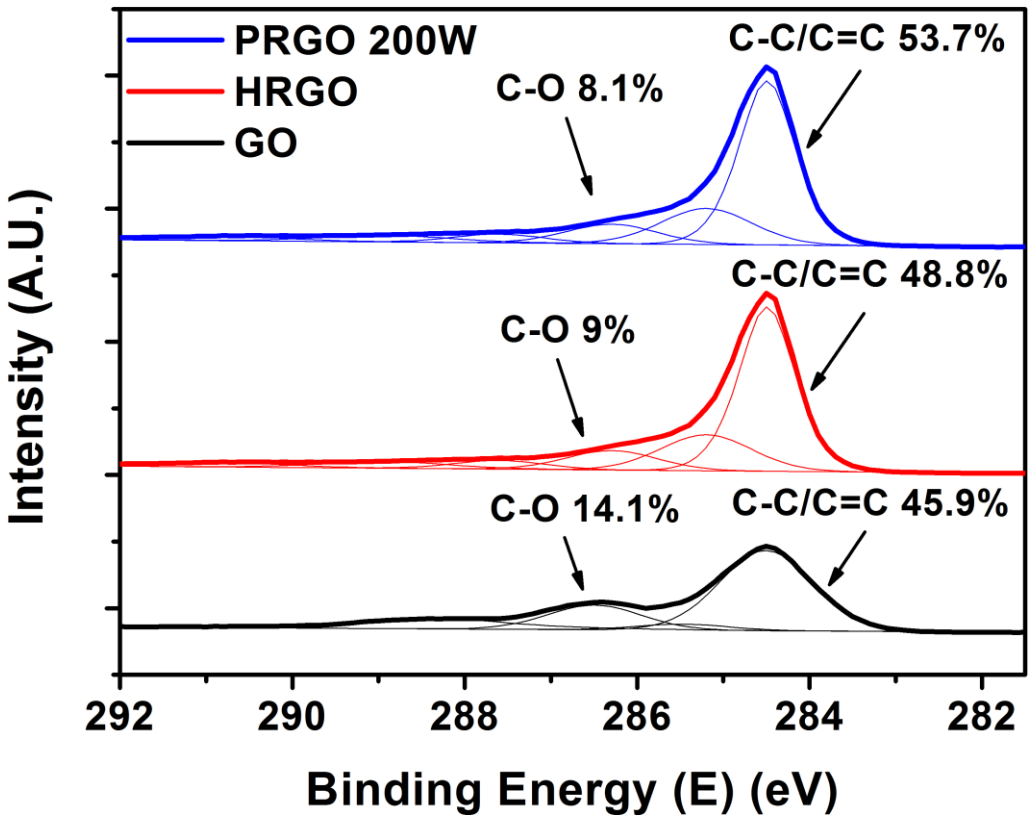

Figure 19. Comparison graph of XPS C1s spectra of GO, HRGO and PRGO 200W.

X-ray diffraction (XRD) analyses on GO film revealed that GO thin film possesses a well-ordered, stacked layers of GO sheets, as can be seen from a sharp d_{001} peak (Figure 20). The exact 2Θ value for the d_{001} peak was 10.22, corresponding to a d-spacing value of 8.65 Å, and this value is due to presence of water molecule layer with hydrogen bonding on two GO sheets [97]. In the XRD spectra of HRGO and PRGO 200W, the characteristic peak of GO at 2Θ = 10 to 12 is absent, and a new broad peak is observed at 2Θ = 24.73 and 24.78 for HRGO and PRGO 200W, respectively. These values correspond to the d-spacing of 3.60 Å and 3.59 Å, which are comparable with the d-spacing of 3.35 Å for graphite. The change in the value of d-spacing can be attributed to cleavage of oxygen groups on basal plane and restoration of π-π interaction between neighboring RGO sheets. These broad peak also indicates the existence of 3D-expanded structure of PRGO and the restoration of the graphitic structure after plasma reduction, almost similar with the ordered structure of graphite. Supplementary Brunauer–Emmett–Teller (BET) analysis exhibited that PRGO 200W sample showed Type IV hysteresis with high surface area of 312 m^2/g after plasma reduction process (Figure 21). From these results, the plasma reduction of GO thin film at 200W power generated a graphitic ordered 3D RGO structure with high surface area.

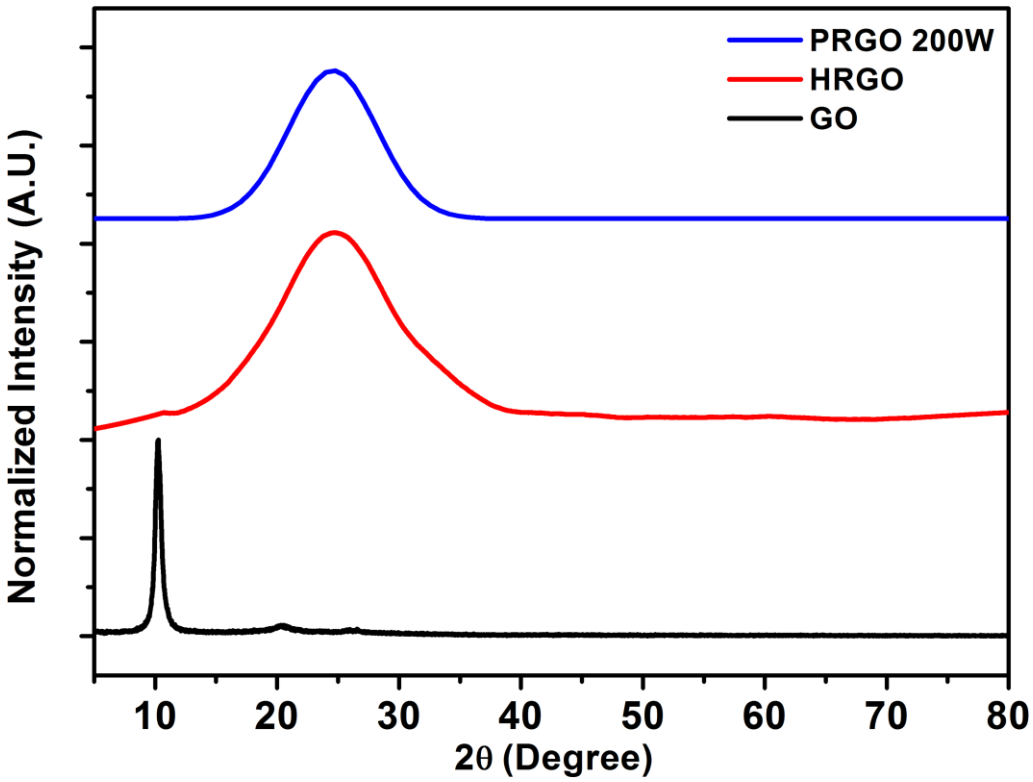

Figure 20. Normalized XRD spectra of GO, HRGO and PRGO 200W.

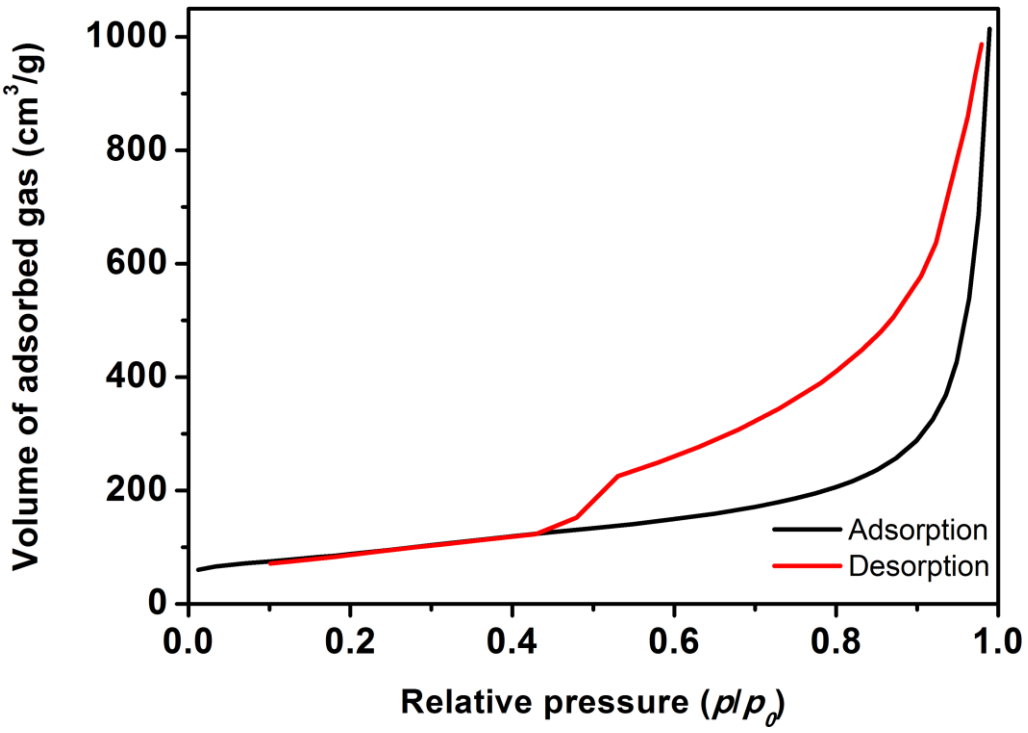

Figure 21. Brunauer–Emmett–Teller (BET) curve of PRGO 200W.

In the following Fourier-Transform infrared (FT-IR) analysis, a broad peak at *ca.* 3400 cm^{-1} was assigned to the O-H stretching of hydroxyl group and a small peak at *ca.* 1715 cm^{-1} was designated for C=O double bond vibration of carbonyl group on GO in GO FT-IR spectrum (Figure 22). The intensity of these peaks were diminished in the FT-IR spectra of HRGO and PRGO 200W, which indicates the cleavage of oxygen-related groups after the hydrazine/plasma reduction.

Figure 23 describes the Raman analyses results of GO, HRGO and PRGO 200W. The Raman spectra of GO, HRGO and PRGO 200W displayed G peaks for E_{2g} vibration of sp^2 C-C structure at *ca.* 1595 cm^{-1} and D peaks for structural defects at *ca.* 1344 cm^{-1}. In previous work, the I_D/I_G ratio of chemically reduced GO after reduction was calculated to be larger than that of GO due to smaller sp^2 domain [26]. However, in this study, the I_D/I_G ratio decreased from 0.97 of GO to 0.83 of the PRGO 200W, in comparison with 1.15 of the hydrazine-reduced HRGO. It can be assumed from the Raman results that production of RGO by plasma reduction with atmospheric argon plasma prompted the removal of structural defects and the conversion of sp^3 to sp^2 C-C structure, leading to increase in the G peak [98]. Therefore, this brief plasma treatment can produce RGO structure with less deformation compared with that from traditional chemical reduction pathway.

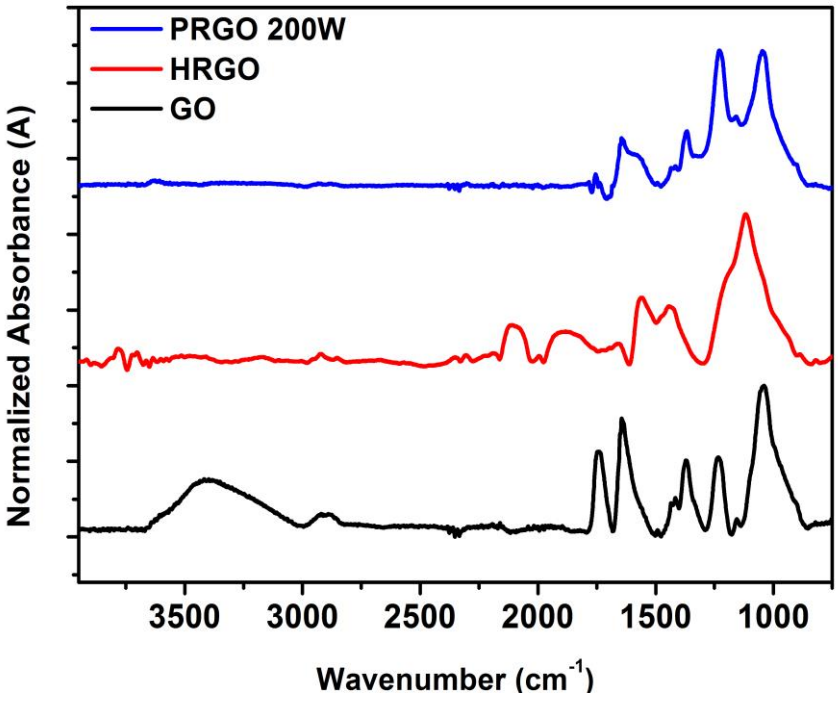

Figure 22. Normalized FT-IR spectra of GO, HRGO and PRGO 200W.

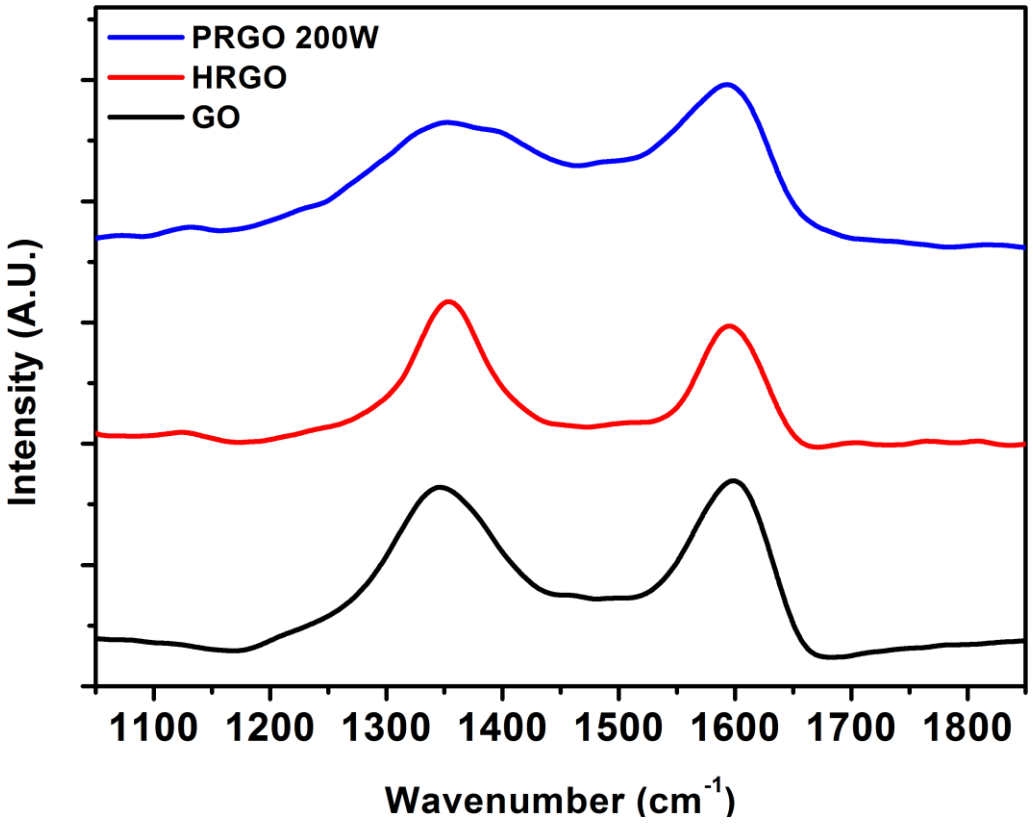

Figure 23. Raman spectra of GO, HRGO and PRGO 200W.

In order to evaluate the processability of as-prepared PRGO 200W for future application in solution-based process, PRGO 200W film was ground to flakes and was dispersed in following various organic solvents: Toluene, dimethyl formamide (DMF), 2-propanol (also known as IPA), N-methyl-2-pyrrolidone (NMP), water, ethanol, tetrahydrofuran (THF), n-hexane, acetone and acetonitrile. The concentration was set to be 0.05 wt% for each solution. The ground PRGO 200W flakes were readily dispersed in each solvent by vigorous mixing for 30 min and the mixed solutions in vials were placed on the flat table for 30 min. After 30 min, the PRGO 200W flakes were observed to be finely dispersed in all solvents except n-hexane (Figure 24). After placing the solution vials on the flat table for 7 days, the dispersability of PRGO 200W in the organic solvent decreased, which is witnessed by precipitated PRGO solutes in toluene, water, THF, n-hexane and acetone. The PRGO 200W flakes were observed to be well-dispersed in 2-propanol and NMP after 7 day storage.

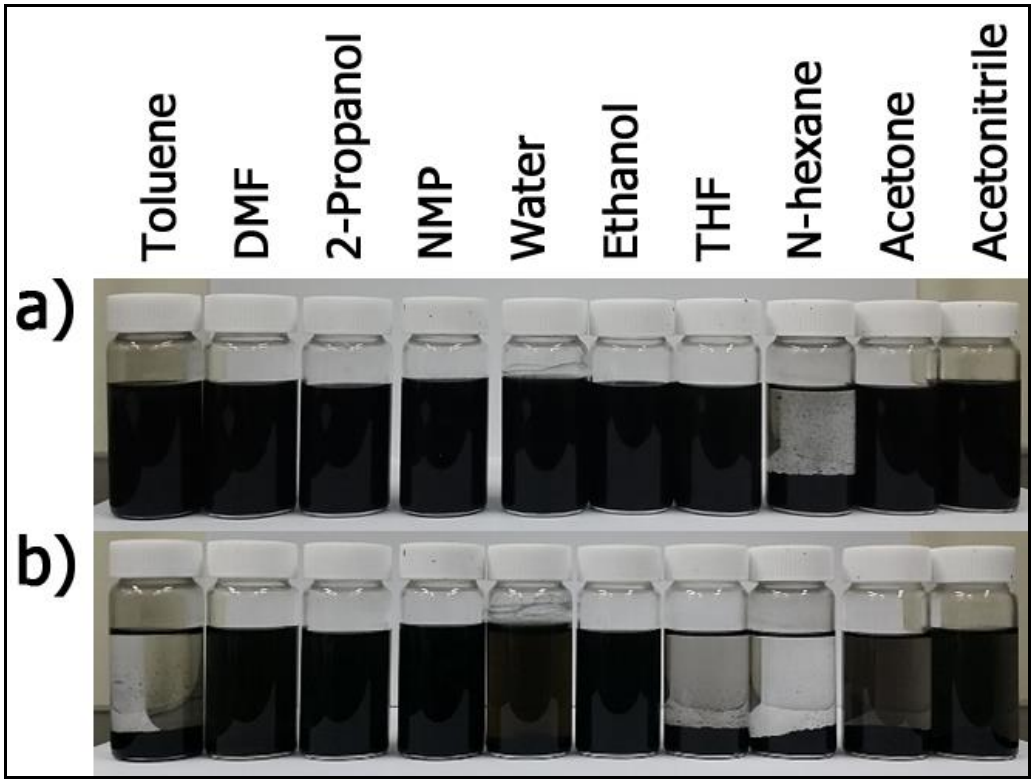

Figure 24. Dispersion result of PRGO 200W in various organic solvents. a) Digital photograph of PRGO 200W powder dispersion in toluene, DMF, 2-propanol, NMP, water, ethanol, THF, n-hexane, acetone and acetonitrile taken after 30 min dispersion. b) Digital photograph of PRGO 200W powder dispersion in the same solvents taken after 7 days later.

Additional thermo-gravimetric analysis (TGA) was conducted to evaluate the thermal stability of GO, HRGO and PRGO 200W up to 700 ℃ (Figure 25). The weight loss curve of GO in Figure 25 exhibited a linear, continuous loss of weight up to around 300 ℃ due to gasification of oxygen-functional groups on the GO basal plane as CO or CO_2 gases. The GO, HRGO and PRGO 200W all displayed a weight loss starting from ca. 550 ℃ and this loss can be attributed to thermal degradation of C-C structure of graphene [99]. Nonetheless, the PRGO 200W exhibited only 13 % weight reduction up to 700 ℃, comparable with 14 % weight loss of HRGO produced from harsh hydrazine reduction. Judging from these data, the atmospheric plasma treatment induced successful cleavage of oxygen-related groups on GO surface to produce thermally stable RGO structure. Plus, the PRGO 200W demonstrates the enhanced thermal barrier property comparable with hydrazine-treated RGO.

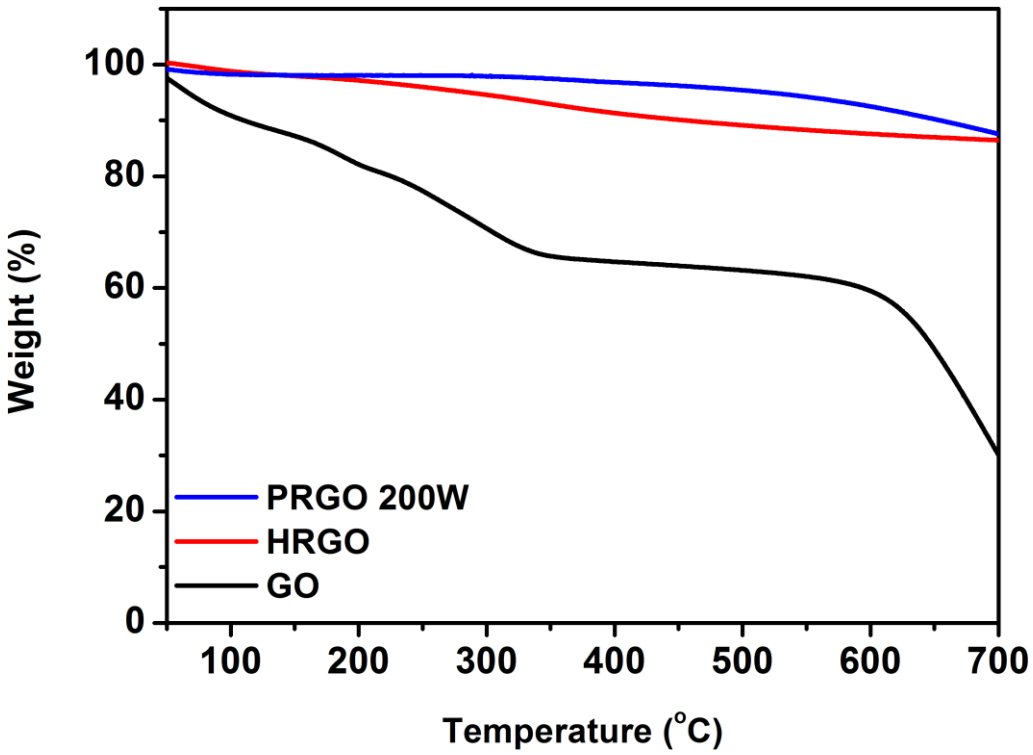

Figure 25. Thermogravimetric analysis (TGA) spectra of GO, HRGO and PRGO 200W.

3.1.3. Supercapacitor performance of PRGO film

Figure 26a displays electrochemical evaluation results of the GO, HRGO and PRGO 200W at the scan rate of 50 mV/s. All electrochemical tests, cyclic votammetry (CV), cyclability test and galvanostatic charge-discharge test, were proceeded using free-standing film samples as working electrodes in 3-electrode system. The CV measurement showed that the PRGO 200W electrode demonstrates larger capacitance than GO and HRGO, which is indicated by larger CV curve area.

In the galvanostatic measurement at current density of 1 A/g, the PRGO 200W electrode displayed a tri-angular charge-discharge curve with minute internal resistance (IR) drop, possibly due to the removal of oxygen-functional groups from GO surface (Figure 26b). In comparison with GO and HRGO, the PRGO 200W electrode exhibited gravimetric capacitance of 150 F/g at current density of 1 A/g. This enhancement in capacitance value of PRGO 200W can be attributed to successful restoration of sp^2 hexagonal lattice in RGO structure and increased surface area of 3D PRGO structure. The capacitance of PRGO 200W electrode in this work surpasses the electrochemical performance of the hydrazine-reduced GO electrodes in previous works [100-102] and the gravimetric capacitance of 100 F/g of the RGO electrode prepared from microwave reduction method [103].

The detailed electrochemical behavior of PRGO 200W electrode was additionally evaluated by conducting CV measurement by changing scan rates from 10 mV/s to 250 mV/s (Figure 26c). As scan rate increased from 10 mV/s to 250 mV/s, the area under CV curve gradually decreased, which means that the analogous specific capacitance also reduced. The decrease in the capacitance at higher scan rates of PRGO 200W can be explained by the limitation of diffusion inside the micro-pores of PRGO 200W at higher rates. Lastly, the long-term stability of PRGO 200W electrode was evaluated at a scan rate of 50 mV/s. After cycling test for 1000 cycles, 82 % retention of initial capacitance of PRGO 200W electrode was determined, demonstrating acceptable stability as a supercapacitor electrode material (Figure 27).

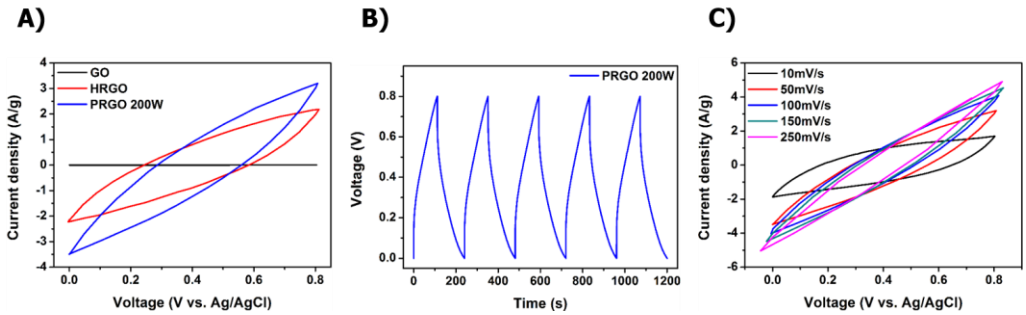

Figure 26. Electrochemical characterization of PRGO film. a) Cyclic voltammetry (CV) graph of GO, HRGO and PRGO 200W at 50 mV/s scan rate; b) 5-consecutive charge-discharge curve of PRGO 200W at 1 A/g current density; c) Cyclic voltammetry graph of PRGO with various scan rates, from 10 to 250 mV/s. All electrochemical analyses were conducted using 1M H_2SO_4 liquid electrolyte in 3-electrode system.

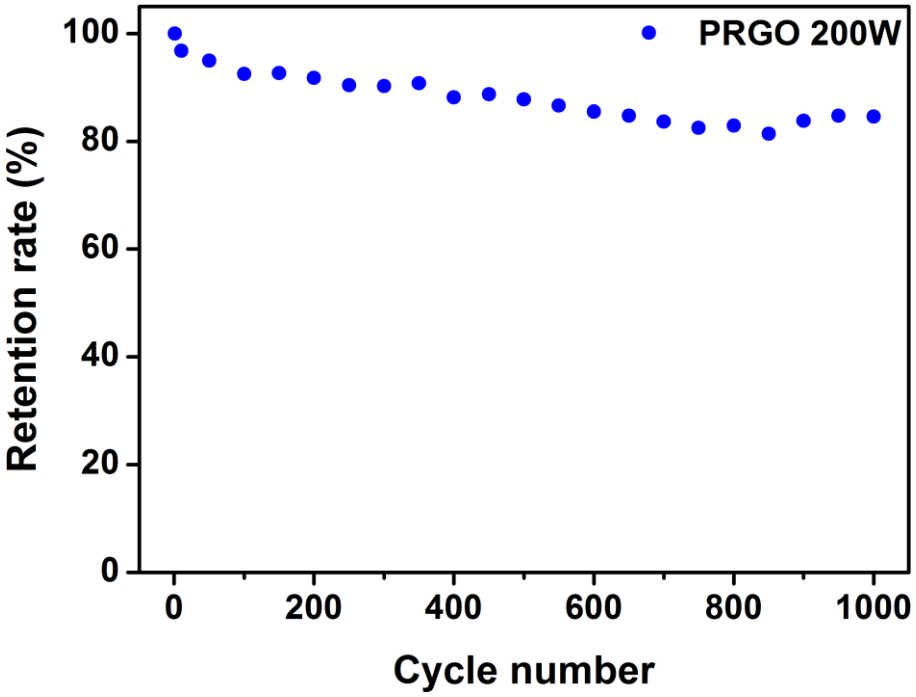

Figure 27. Cyclability test of PRGO 200W for 1000 cycles.

In conclusion, a novel type of 3-dimensional, expanded PRGO structure was prepared *via* brief and direct atmospheric argon plasma treatment on GO thin film. The thin GO film with 10 μm thickness was transformed into 3-dimensionally expanded PRGO film with up to 400 μm thickness without any toxic chemical treatment. The 3D PRGO film was produced with applied plasma power exceeding 110 W in less than 20 seconds, and the lowest O/C ratio for PRGO film was approximately 0.116 at 200W plasma power. Systematic surface analyses announced that oxygen-related functional groups were cleaved from RGO sheet after combined process of rapid thermal exfoliation and deoxygenation. The PRGO 200W was then used as a free-standing supercapacitor electrode, displaying 150 F/g of specific capacitance at the current density of 1 A/g and 82 % of initial capacitance was retained after 1000 charge-discharge cycles. Considering the longer plasma exposure time, complex device set-up, and high vacuum condition needed for plasma reduction reported in previous works, this rapid, environmental-friendly method can illuminate a novel way of producing 3D RGO structure for energy storage applications.

3.2. Fabrication of free-standing 3D RGO film embedded with organic PCMs for latent heat storage

3.2.1. Preparation of PCM/PRGO composites

Figure 28 describes the preparation of the PCM/PRGO composites by simple immersion of the 3D PRGO network in liquid-state organic PCMs. At first, dried GO powders synthesized by a modified Hummers' method were readily dispersed in deionized water and the concentration of the GO solution was set to 0.2 wt %. Prior to synthesis of expanded PRGO network, the 0.2 wt% GO solution (10 ml) was vacuum-filtered on commercialized AAO membrane (Pore size: 100 to 300 nm) for 12 h to acquire GO thin film (Figure 28a). As-prepared GO film was peeled off from the membrane and was reduced with atmospheric plasma apparatus to synthesize the PRGO network. (Figure 28b). The fabrication of as-synthesized PRGO network is realized by rapid thermal exfoliation/deoxygenation during the atmospheric plasma treatment and the oxygen-related groups on the GO surface are annihilated to make physically-linked RGO network [40]. The 3D, expanded structure of PRGO network was realized by production of oxygen-derived gas, such as CO_2, in the rapid thermal exfoliation process. These gases evolve into the stacked graphene sheets and induce sudden pressure to drive the graphene framework outward. Due to increased distance between RGO sheets during the thermal

exfoliation process, various organic PCMs are readily impregnated into the network by a facile immersion method (Figure 28c).

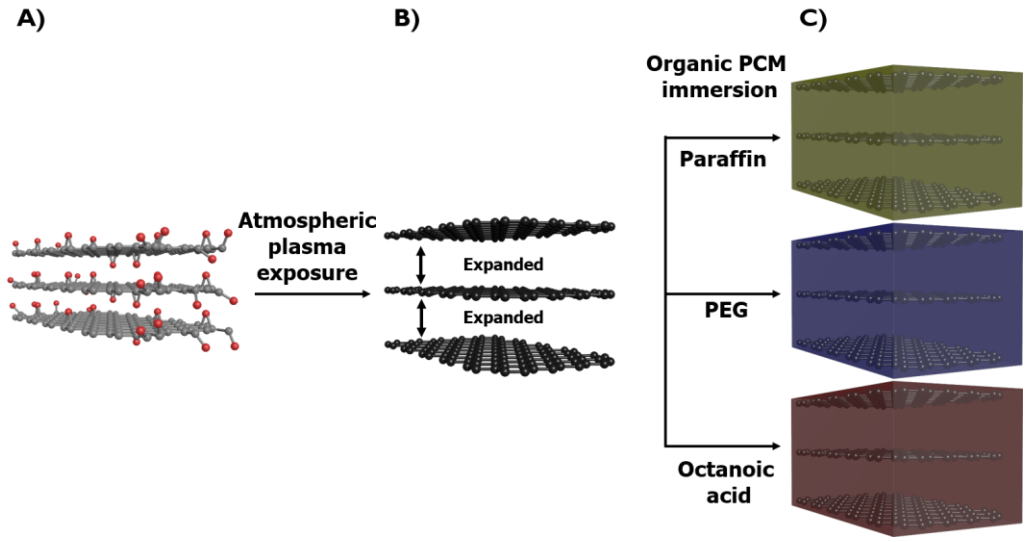

Figure 28. Fabrication process of the PCM/PRGO composites. a) Illustration of proposed chemical structure of GO film. Red dots indicate oxygen-related groups; b) PRGO network prepared by plasma treatment on GO film; c) Preparation of the PCM/PRGO composites by immersion of PRGO network into each PCM (in liquid state) for 30 min.

The surface morphologies of the as-prepared PCM/PRGO composites were investigated by scanning electron microscopy (SEM) in order to evaluate the successful introduction of organic PCMs into PRGO network (Figure 29). The surfaces of the 3D PRGO network prepared from atmospheric plasma reduction on GO film display cork-like expanded structure of connected graphene sheets (Figure 29a) [46]. As illustrated above, the open, percolated structure of PRGO network with inter-layer distances ranging from *ca.* 500 nm to few μm provides an opportunity of sufficient organic PCM introduction in the network by simple immersion. Figure 29b to 29d exhibits SEM images of the three PCM/PRGO composites after immersion process. The open structures of pristine PRGO network are successfully saturated with paraffin (Figure 29b), polyethylene glycol (PEG) (Figure 29c) and octanoic acid (Also known as caprylic acid) materials (Figure 29d). The three different reagents all represent organic PCMs, which require a shape-stabilizer for further industrial application. From the SEM results, the PRGO network provides a room for adsorption of organic PCMs with enhanced shape stability.

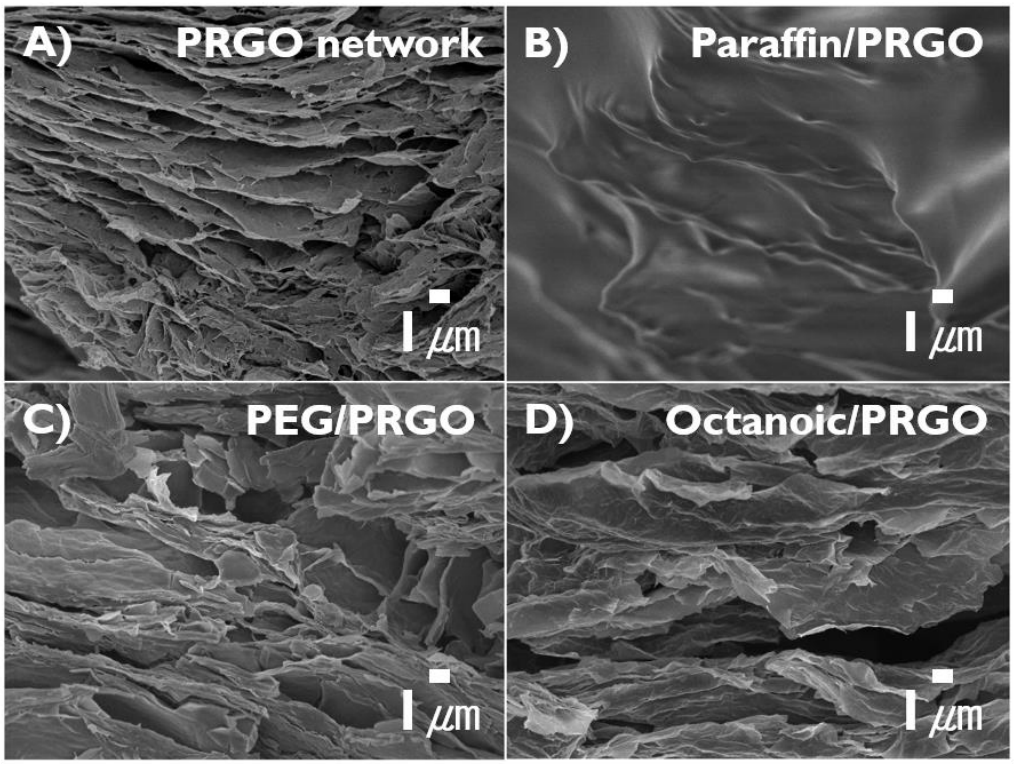

Figure 29. SEM images of the PCM/PRGO composites. a) Pristine PRGO network; b) paraffin/PRGO; c) PEG/PRGO and d) Octanoic/PRGO.

3.2.2. Characterization of PCM/PRGO composites

X-Ray diffraction (XRD) analyses were conducted to understand the structrural change after immersion of organic PCMs in 3D PRGO network to form PCM/PRGO composites. In Figure 30, the XRD spectra presents a broad peak at *ca.* 25° for PRGO network spectrum and this peak stands for typical RGO structure with d-spacing of 3.56 Å [90]. In the XRD spectra of the PCM/PRGO composites, two protruding peaks of paraffin at 21° and 23° are displayed in paraffin/PRGO, while two peaks att 19.2° and 23.4° for PEG and a broad peak at 20.5° for octanoic acid are present in PEG/PRGO and octanoic/PRGO, respectively. According to the previous works, the three PCM/PRGO composites display almost the same XRD d-spacing values with the result of pristine PCMs [104-105]. The XRD results also demonstrate that the introduction of paraffin, PEG and octanoic acid into the 3D PRGO network resulted in no substantial structural change of the corresponding PCM, while almost no PRGO peak was found due to extremely lower concentration (less than 4 wt %) of PRGO network composition in the composites.

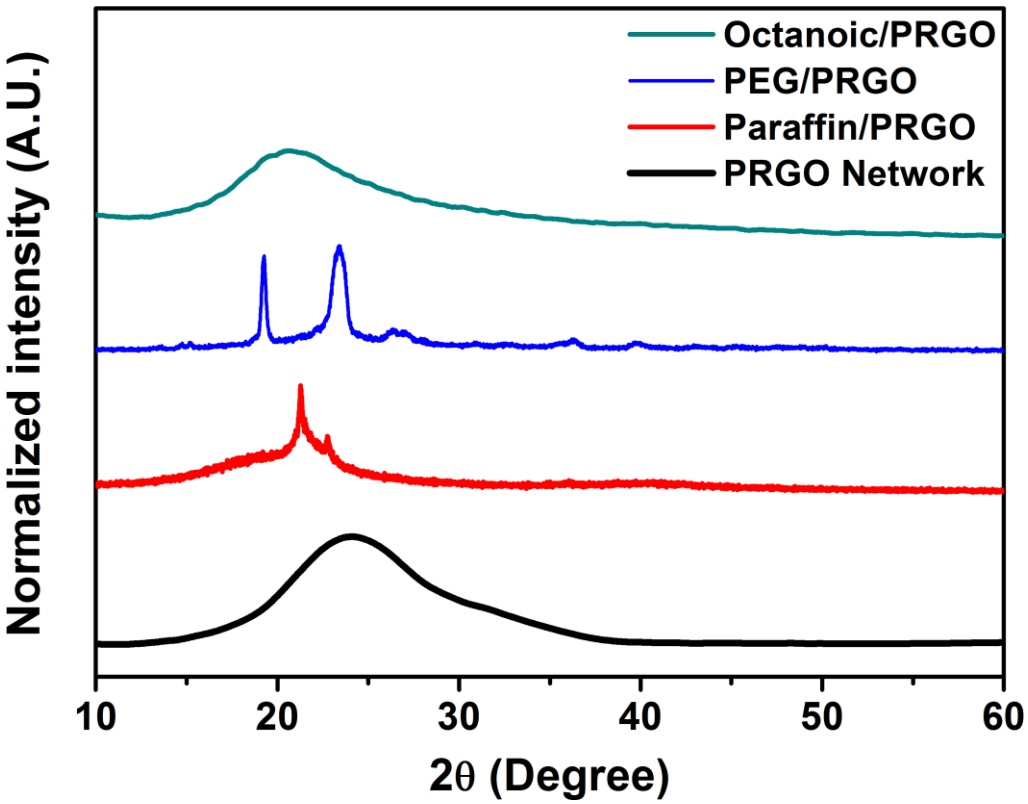

Figure 30. Normalized XRD analysis graph of the PCM/PRGO composites.

To verify the successful introduction of organic PCMs in the PRGO network, additional FT-IR analyses on the PCM/PRGO composites were conducted (Figure 31). In the FT-IR spectra of the PCM/PRGO composites, the two distinct peaks at *ca.* 2850 cm^{-1} and 2940 cm^{-1} for the paraffin/PRGO composite stand for the -CH bond stretching of the structure of paraffin (C_nH_{2n+2}) inside the PRGO network [106-107]. In the PEG/PRGO composite, the stretching peak of the -CH bonds at 2860 cm^{-1}, the C=O double bond vibration peak at 1635 cm^{-1}, the deformation peak of the -CH bonds at 1467 and 1341 cm^{-1}, the hydroxyl (-OH) group bending peak at 1280 and 1240 cm^{-1} and the C–O stretching vibration peak at *ca.* 1148 cm^{-1} in the PEG/PRGO composite all indicate the characteristic -CH chains and hydroxyl groups of PEG polymer backbone in the composite [105]. In the octanoic/PRGO composite FT-IR spectrum, two protruding peaks for the stretching vibration of -CH groups at 2860 cm^{-1} and 2920 cm^{-1}, a sharp C=O carbonyl peak at 1710 cm^{-1} and a small C-O stretching peak at 1270 cm^{-1} represent alkyl chains and the carboxyl groups of octanoic acid in the octanoic/PRGO composite [108]. Owing to small weight fraction of the PRGO network in the PCM composites, a distinct FT-IR peak for the PRGO network was not found. The FT-IR analyses again show that the pristine PCMs are well adsorbed in the PRGO network without significant change in chemical structure.

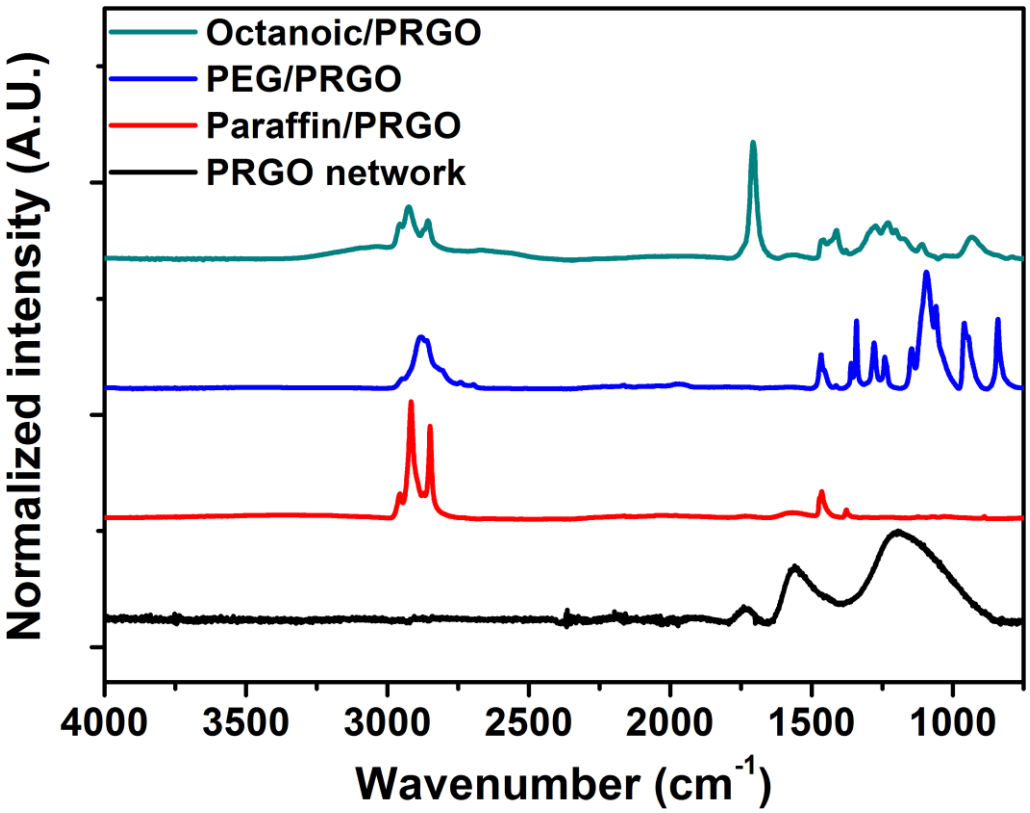

Figure 31. Normalized ATR-FT-IR curve of the PCM/PRGO composites.

The thermophysical properties of the PCM/PRGO composites were evaluated by differential scanning calorimetry (DSC) examination. The change in heat flow was recorded as a function of temperature change (Figure 32). The peak melting temperature and the value of latent heat of fusion for the pristine PCMs and the PCM/PRGO composites were measured as well. In the pristine PCM measurement, three combined peaks protruded at pristine paraffin spectrum, showing peak melting temperature at *ca.* 51 ℃ to completely consume *ca.* 119 J/g heat energy for solid-to-liquid phase transition. The DSC curves of pristine PEG and octanoic acid also demonstrated energy consumption of *ca.* 191 J/g and 144 J/g, at 70 ℃ and 18 ℃, respectively. Especially, the PEG polymer possesses the largest heat of fusion in course of thermal cycling process. In the DSC analyses on the PCM/PRGO composites, the paraffin/PRGO composite displayed an endothermic melting process starting at 26 ℃ and ending at 50 ℃ to completely consume 115 J/g heat energy for solid-to-liquid phase transition. The PEG/PRGO and octanoic/PRGO composites exhibited heat absorption of 184 J/g and 140 J/g, respectively, after DSC measurement at ramping rate of 5 ℃/min (Summarized in Table 5). By comparing the values, the latent heat of fusion of the PCMs after formation of the composites was almost retained. In the previous works, the values of latent heat of fusion were significantly lowered due to

incorporation of large amount of heterogeneous fillers in the PCM matrix, with decreasing weight fraction of the PCMs and the overall thermal stability [109-111]. Nonetheless, since the 3D PRGO network possesses less than 5 % weight fraction of the overall composites, the values of overall latent heat of fusion for the PCM/PRGO composites remain intact.

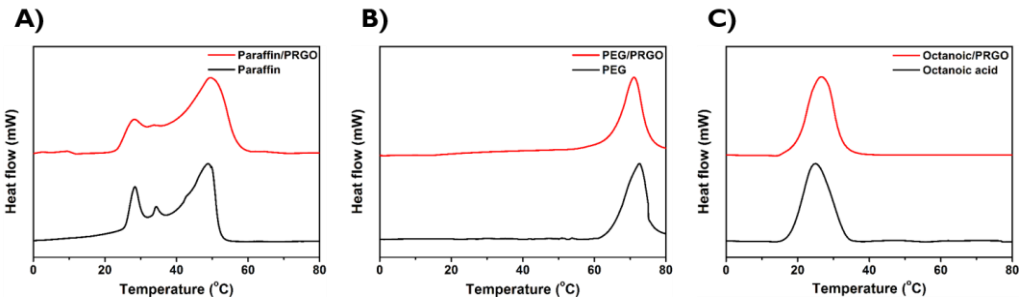

Figure 32. DSC curve of the PCM/PRGO composites.

Table 5. Summarized value of the DSC analysis on the PCM/PRGO composites.

Sample	Peak melting temperature(^{o}C)	Latent heat of fusion (△H)
Paraffin	49.2	119.2
Paraffin/PRGO	49.0	115.3
PEG	72.7	190.9
PEG/PRGO	71.0	184.0
Octanoic acid	25.2	144.4
Octanoic/PRGO	25.0	140.1

The thermal stability of the PCM/PRGO composites was further studied with thermogravimetric analysis (TGA) experiments. Figure 33 displays the TGA curves of the pristine PCMs and the prepared PCM/PRGO composites. Pristine paraffin exhibits a single-step weight loss starting at 201 ℃ and the maximum weight loss behavior at 275 ℃, due to thermal decomposition of the paraffin chain. The paraffin/PRGO composite species also exhibit a one-stage weight loss behavior and the maximum weight loss increased up to 290 ℃. For the pristine PEG, the weight loss begins at 318 ℃ and the maximum weight loss occurs at 383 ℃, while the PEG/PRGO exhibits the maximum weight loss at 391 ℃. For the octanoic/PRGO, the maximum weight loss was increased up to 145 ℃ from 138 ℃ of the pristine octanoic acid. The PRGO network is robust enough to protect the impregnated PCMs from degrading at the ordinary boiling point, thus enhancing the onset decomposition temperature of composite PCMs.

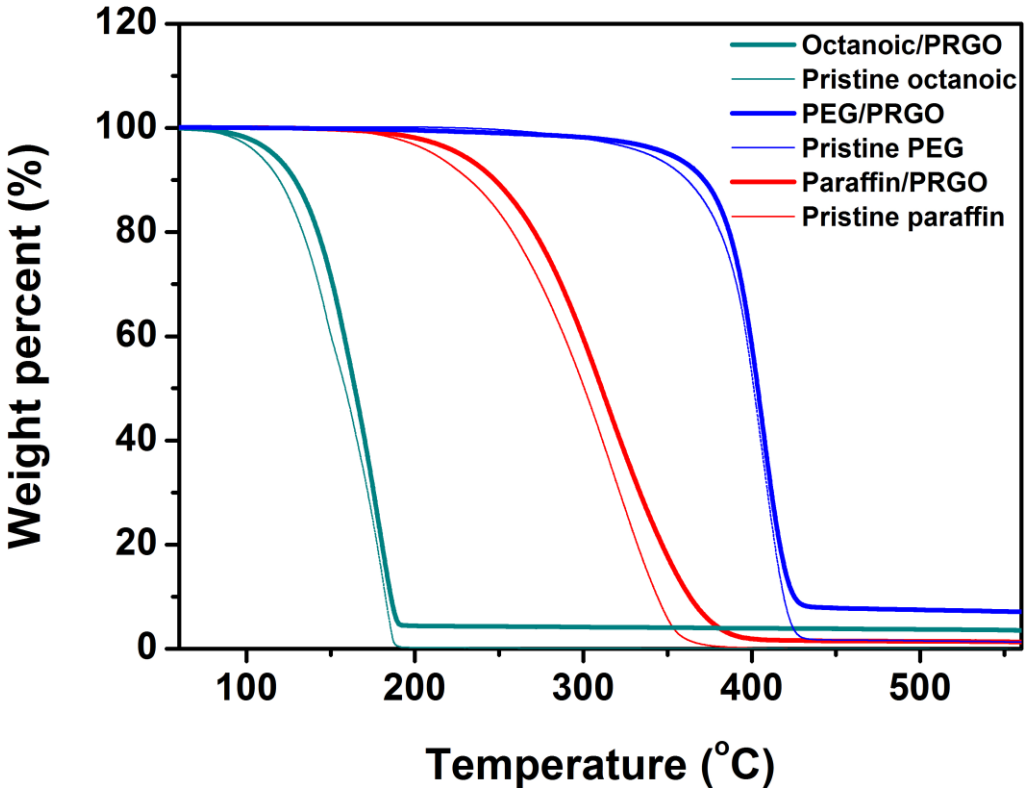

Figure 33. TGA graph of the PCM/PRGO composites. The TGA experiments were conducted in inert N_2 atmosphere.

3.2.3. Enhanced PCM performance of PCM/PRGO composites

The long-term thermal cyclability of the PCM/PRGO composites was examined by DSC measurement for 30 cycles (Figure 34). In the DSC graph, the shape of the DSC curve for 1st cycle and the DSC curves for the later cycles are slightly different for all three composites, with changes in the position of protruding peak. The slight modification in DSC curves can be explained as a re-positioning of the PCM materials in the PRGO network, followed by stabilization. Furthermore, after recurring DSC measurement on the three PCM/PRGO composites for 30 cycles, less than 3 % reduction in the value of latent heat of fusion was measured, as presented in Figure 35. The minute reduction in the latent heat of fusion for the three PCM/PRGO composites can be attributed to slight PCM evaporation phenomena during the 30-cycle DSC measurement [112]. From the DSC cyclability results, the PRGO network worked as a successful shape-stabilizer/container, and re-positioning of the PCM materials in the overall composites induced insignificant change in the amount of latent heat of fusion.

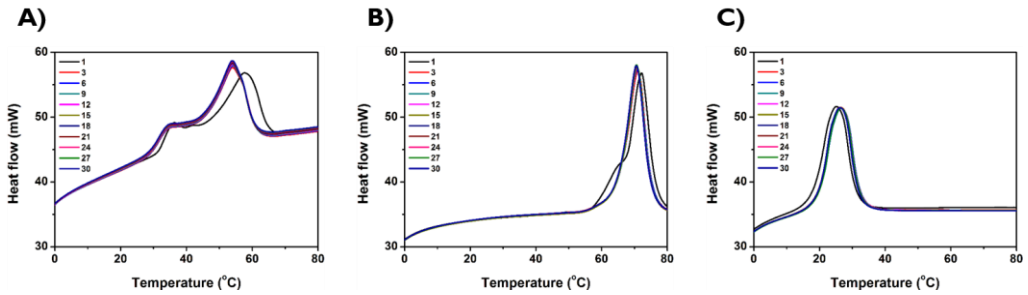

Figure 34. DSC heating curves of the PCM/PRGO composites for 1 to 30 cycle. a) DSC curves of the paraffin/PRGO composite; b) DSC curves of the PEG/PRGO composite; c) DSC curves of the octanoic/PRGO composite. All experiments were conducted in inert N_2 atmosphere.

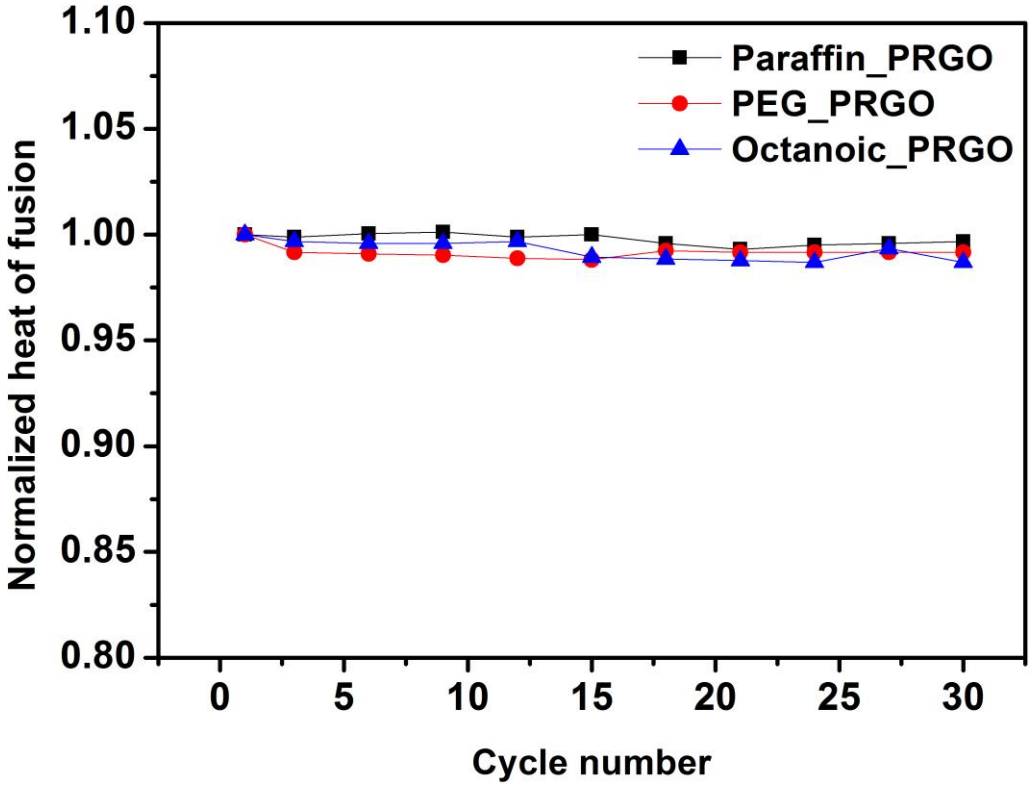

Figure 35. Normalized value of latent heat of fusion of the PCM/PRGO composites after 30-cycle DSC measurement.

The influence of the introduction of PRGO network on the thermal/ electric conductivities of the PCM/PRGO composites were studied (Figure 36, Figure 37 and Table 6). The thermal conductivity of the pristine PCMs and the PCM/PRGO composites was measured by the method using DSC [92-93]. Using fluorine (melting point: 112 ℃) as a reference material, thermal conductivity of the PCM/PRGO composites was determined by the difference in the slope of the DSC endothermic curves of fluorine and the target material. The thermal conductivity measurement was done three times for each sample and the calculated thermal conductivity values were averaged (Figure 36). By DSC mode calculation, thermal conductivities of the paraffin/PRGO, PEG/PRGO and octanoic/PRGO were calculated to be 0.62, 0.06 and 0.38 W/ m•K, respectively (Table 6). Compared with the thermal conductivity values of the pristine PCMs, where the values are 0.24, 0.04 and 0.146 W/ m•K for the paraffin, PEG and octanoic acid, the thermal conductivities of the PCM/PRGO composite increased by up to *ca.* 2.5-fold (Figure 37). Considering the small weight fraction of the PRGO network in the composites, the 2.5-fold increase in the thermal conductivity of the PCM/PRGO composites overwhelm the previous work using RGO aerogel as a filler for PCM [89].

The electric conductivity of the PCM/PRGO composites were also calculated by 4-probe method. Owing to the insulating properties of traditional

PCMs, the utilization of the PCMs in electronic devices has been restricted. In this work, the PCM/PRGO composites exhibited enhanced electric conductivity values ranging from $5*10^{-3}$ to $8*10^{-2}$ S/cm (Table 6). From these conductivity measurement results, the PCM/PRGO composites offer a potential use in thermal energy storage application due to the increased heat transfer action by greater thermal/electric conductivity.

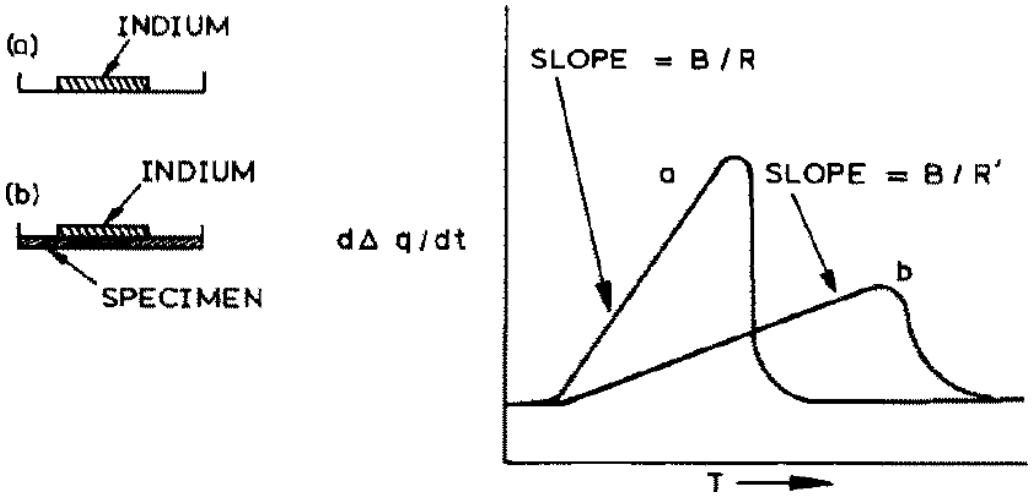

Figure 36. DSC curves for melting of indium: a) indium; b) indium+specimen sheet. Reprinted with permission from ref 92. Copyright 1988 Elsevier.

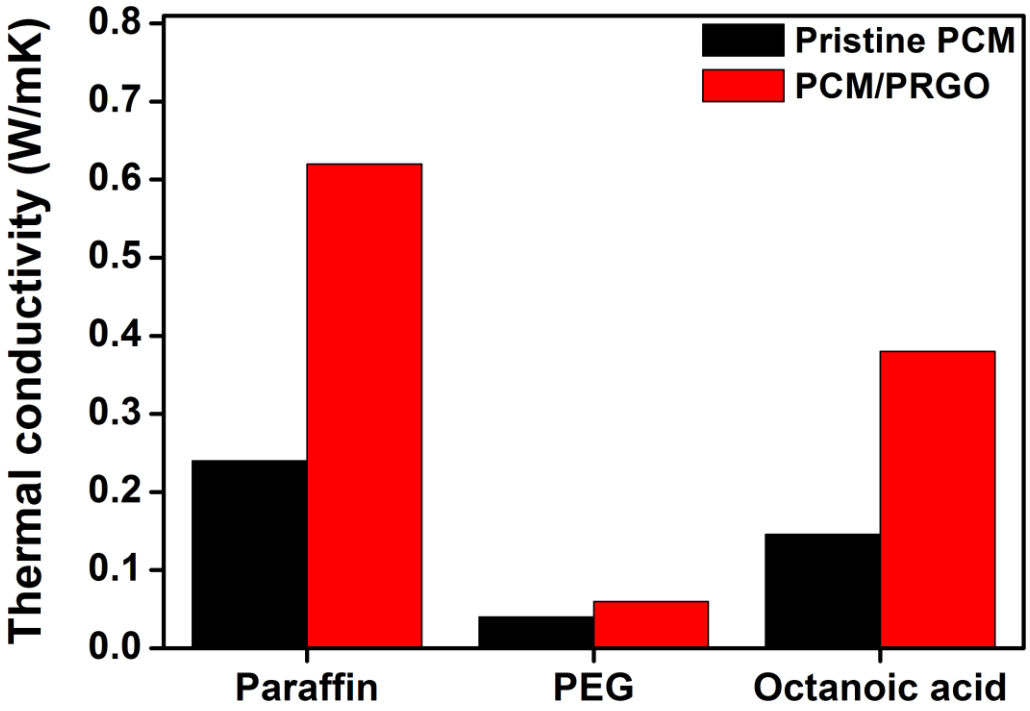

Figure 37. Comparison graph of thermal conductivity values of pristine PCMs and the PCM/PRGO composites.

Table 6. Physical parameters of the PCM/PRGO composites.

Sample	Thermal conductivity (W/m·K)	Electric conductivity (S/cm)
Pristine paraffin	0.24	- (insulating)
Paraffin/PRGO	0.62	$5.23 * 10^{-3}$
Pristine PEG	0.04	- (insulating)
PEG/PRGO	0.06	$5.45 * 10^{-3}$
Pristine octanoic acid	0.146	- (liquid state)
Octanoic acid/PRGO	0.38	$8.33 * 10^{-2}$

Herein, the PCM/PRGO composites comprised of 1) 3D PRGO network generated by atmospheric plasma reduction on GO film and 2) three different organic PCMs (paraffin, PEG and octanoic acid) were prepared by facile immersion of the as-fabricated PRGO network in liquid-state organic PCMs. Instead of compact structure of stacked GO sheets, open, percolated PRGO network with inter-connected RGO sheets enable simple impregnation of liquid-state PCMs into the network by capillary forces. The PRGO network work as a shape-stabilizer and property enhancer of the organic PCMs. Compared with each pristine PCM, the PCM/PRGO composites exhibited increased shape-stability and the values of latent heat of fusion were retained owing to low weight fraction of PRGO network in the composites. At last, the PCM/PRGO composites exhibited enhanced thermal/electric conductivities, demonstrating up to 2.5-fold increase of thermal conductivities compared with pristine PCMs. This methodology opens a promising route in use of the RGO-incorporated PCMs in industrial thermal energy control of solar panel and lithium ion batteries.

3.3. Fabrication of 3-dimensional graphene monolith with paraffin *via* L-AA reduction for PCM application

3.3.1. Preparation of paraffin/pRGO composites

Figure 38 illustrates the preparation of the paraffin/pRGO composites by simple immersion method. At first, the dried GO powders synthesized from a slightly modified Hummers' method were dissolved in DI water and the concentration of the GO solution was set to 0.01, 0.05, and 0.5 wt % (Figure 38a). The porous structure of partially reduced graphene oxide (pRGO) monoliths are not generated at the higher concentration of GO than 0.5 wt %. To fabricate pRGO monoliths, the GO solution was mixed with L-ascorbic acid (L-AA) powder with vigorous stirring (mass ratio of GO: L-AA = 2:1). After complete mixing, the L-AA/GO solution was transferred to appropriate vessel and kept in 100 ºC oven for 30 min. The pRGO monolith was then formed in shape of black cylinder floating on the water (Figure 38b) [46]. After freezing for 30 min and thawing for 30 min, the pRGO monoliths were further lyophilized to eliminate water residue on the monoliths. Li *et al.* described that the reduced GO sheets are pushed away by ice to form cork-like structure in freezing step, and the ice are eliminated in thawing & lyophilization process (Figure 39). The as-prepared 3D pRGO monolith samples were then immersed in molten paraffin at 60 ºC for 30 min to obtain the paraffin/pRGO composites

(Figure 38c). Due to percolated, open structure of pRGO monoliths, molten paraffin is easily impregnated into the monolith and solidifies.

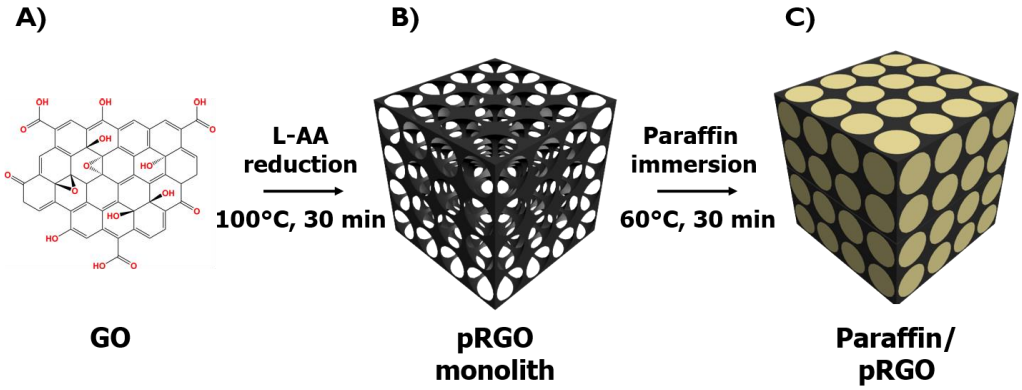

Figure 38. Schematic illustration of the preparation of the paraffin/pRGO composites. a) GO powders were dispersed in distilled water with varying concentration; b) Porous pRGO monolith formed after reduction of GO solution with L-AA at 100 ºC for 30 min; c) Paraffin/pRGO composite obtained after immersion of cylindrical pRGO monolith in molten paraffin for 30 min.

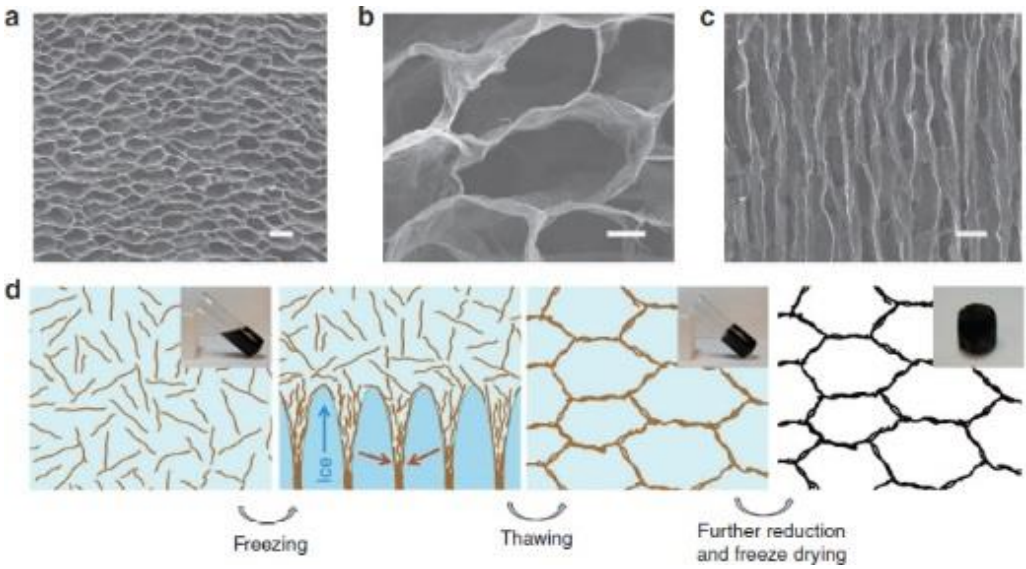

Figure 39. Formation mechanism of pRGO monolith via L-AA reduction of GO. Reprinted with permission from Ref 46. Copyright 2012 Right Managed by Nature Publishing Group.

The micro-scale morphologies of the pristine pRGO monoliths and the paraffin/pRGO composites were examined by SEM analyses (Figure 40). In Figure 40a to 40c, the SEM images of pristine pRGO monoliths synthesized from reduction of GO solutions with different concentration (0.01, 0.05 and 0.5 wt %) exhibited cork-shaped micro structure of inter-connected RGO sheets. In the inset images of Figure 40, the average pore size reduced as the initial GO concentration increases, from *ca.* 2 ~ 5 μm of pRGO_0.01 to *ca.* 0.5 ~ 1 μm of pRGO_0.05. During this reaction process, the dispersed RGO sheets are accumulated to generate diverse shape of micro-porous scaffold with respect to the GO solution concentration and the shape of vessel [45-46]. Figure 40d to 40f displays SEM images of the paraffin/pRGO composites. From the SEM analyses, the micro-pores of the three different pRGO monoliths were soaked with paraffin materials, which are seen to be glittering in the SEM images. From the results, it can be inferred that the pores of pRGO monolith provided a room for paraffin packing, and the interaction between solidified paraffin and the surface of pRGO monolith was sturdy enough to preserve the overall composite structure.

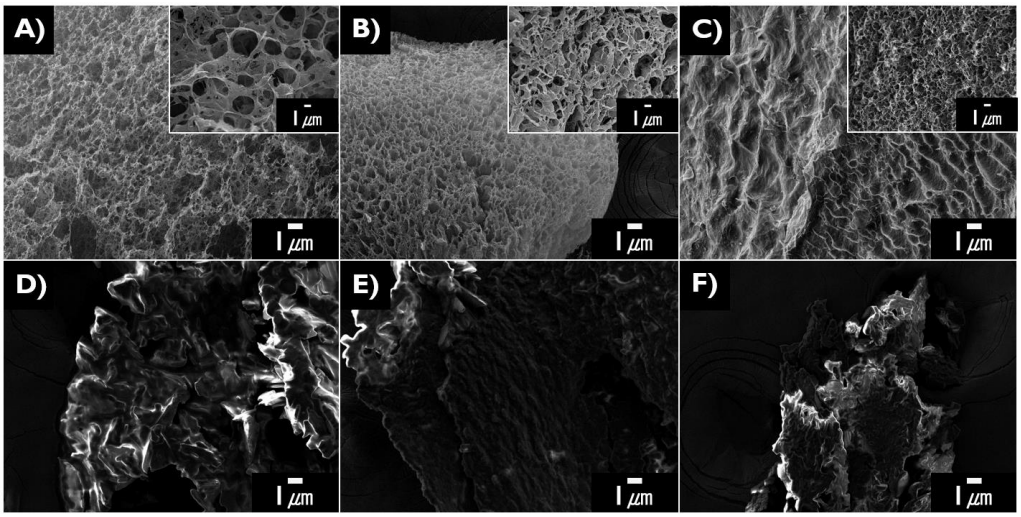

Figure 40. SEM images of a) pristine pRGO_0.01, b) pristine pRGO_0.05 and c) pristine pRGO_0.5 (Inset images: X5000 magnification of each pristine pRGO sample); SEM images of d) paraffin/pRGO_0.01, e) paraffin/pRGO_0.05 and f) paraffin/pRGO_0.5.

3.3.2. Characterization of paraffin/pRGO composites

XRD analysis (Figure 41) was conducted to verify successful immersion of paraffin materials in pRGO monolith. In Figure 41, the XRD graph for the paraffin/pRGO composites shows two prominent peaks at 21° and 23°, the characteristic peaks of pristine paraffin [104]. Concurrently, the pristine pRGO monoliths exhibited broad peak at *ca.* 25° for typical RGO structure [90]. The broad peak demonstrates the various degree of reduction or pRGO sheets in the monolith. In the XRD graph, characteristic d_{002} peak for the paraffin/pRGO composites was not changed significantly. The result indicates that the immersion of molten paraffin into the pRGO monolith and solidification induced no crucial structural change of the intrinsic paraffin material. And also almost no pRGO-related peak was detected in the XRD curve of the paraffin/pRGO composites, due to lower fraction (less than 5 wt %) of pRGO scaffold weight in the composites.

Additional FT-IR investigation on the paraffin/pRGO composites were done to verify successful introduction of paraffin in the pRGO monoliths (Figure 42). Two small peaks at 1050 cm^{-1} and 1715 cm^{-1} were observed and these peaks respectively indicate minute C-O stretching vibration and C=O double bond vibration. The mild reduction by L-AA on GO left small fraction of carboxyl groups, while annihilating hydroxyl groups on basal plane. The FT-

IR spectrum of pristine paraffin displays two strong -CH peaks at *ca.* 2850 cm^{-1} and 2940 cm^{-1} and these peaks represent the alkyl chain structure of paraffin. In the FT-IR spectra of the paraffin/pRGO composites, only two protruding peaks at *ca.* 2850 cm^{-1} and 2940 cm^{-1} again prove that the alkyl chain structure of paraffin remains inside the pRGO monolith. From these results, the FT-IR analyses show that the paraffin materials were successfully incorporated in the composite without modification in chemical structure, with trivial pRGO-related peaks were found due to low fraction of pRGO in the composites.

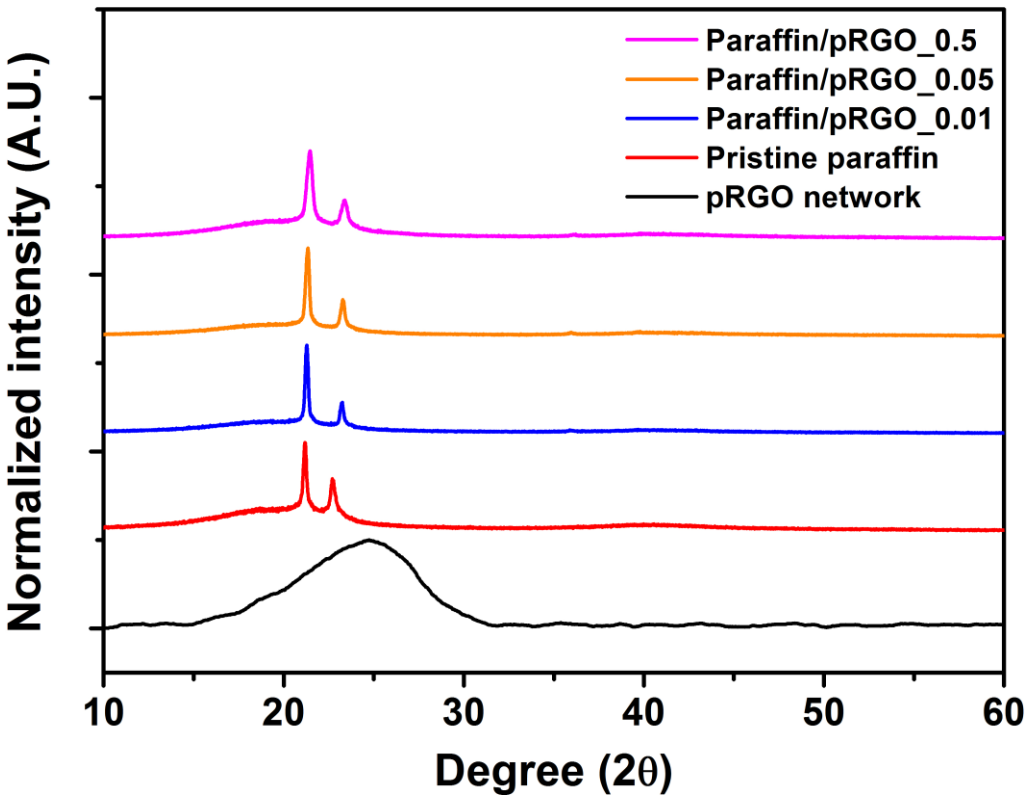

Figure 41. Normalized XRD analysis graph of the paraffin/pRGO composites.

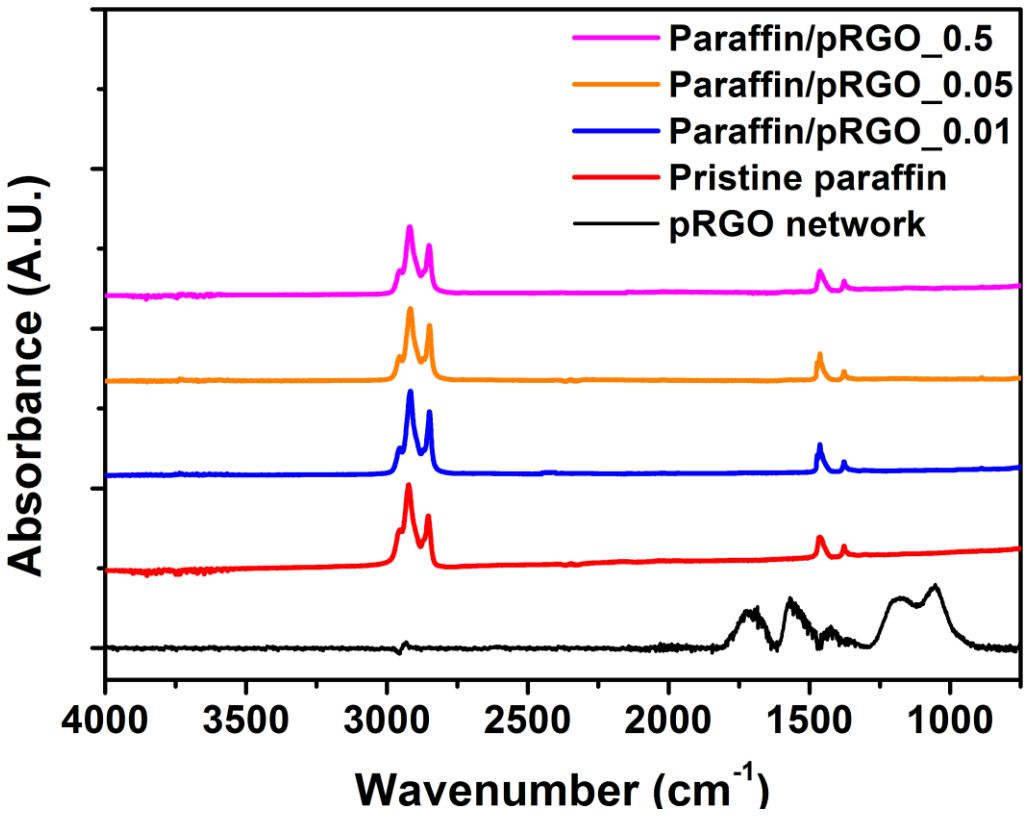

Figure 42. FT-IR curve of the paraffin/pRGO composites.

The thermal behavior of the paraffin/pRGO composites were examined by adjusting condition parameters such as the initial concentration of corresponding pRGO monolith. The change in heat flow was recorded as a function of temperature change in differential scanning calorimetry (DSC) examination (Figure 43). The peak melting temperature and the value of latent heat of fusion were also measured. In the case of DSC analyses on the pristine paraffin and the paraffin/pRGO composites, the pristine paraffin exhibited heat of fusion of 119.2 J/g after DSC measurement at ramping rate of 10 ℃/min. In case of the paraffin/pRGO composites, the latent heat of fusion after formation of the composites was almost maintained, exhibiting 116.0 J/g, 115.9 J/g and 115.2 J/g for paraffin/pRGO_0.01, paraffin/pRGO_0.05 and paraffin/pRGO_0.05, respectively. The peak melting temperature of the composites demonstrated slight change, ranging from 48.8 to 49.7 ℃. In previous works, the value of latent heat of fusion might be lowered due to incorporation of large amount of graphitic fillers in the PCM matrices, decreasing the thermal stability. Nonetheless, the 3D pRGO monolith occupies less than 4 % weight of the overall composites, with the overall latent heat of fusion maintained.

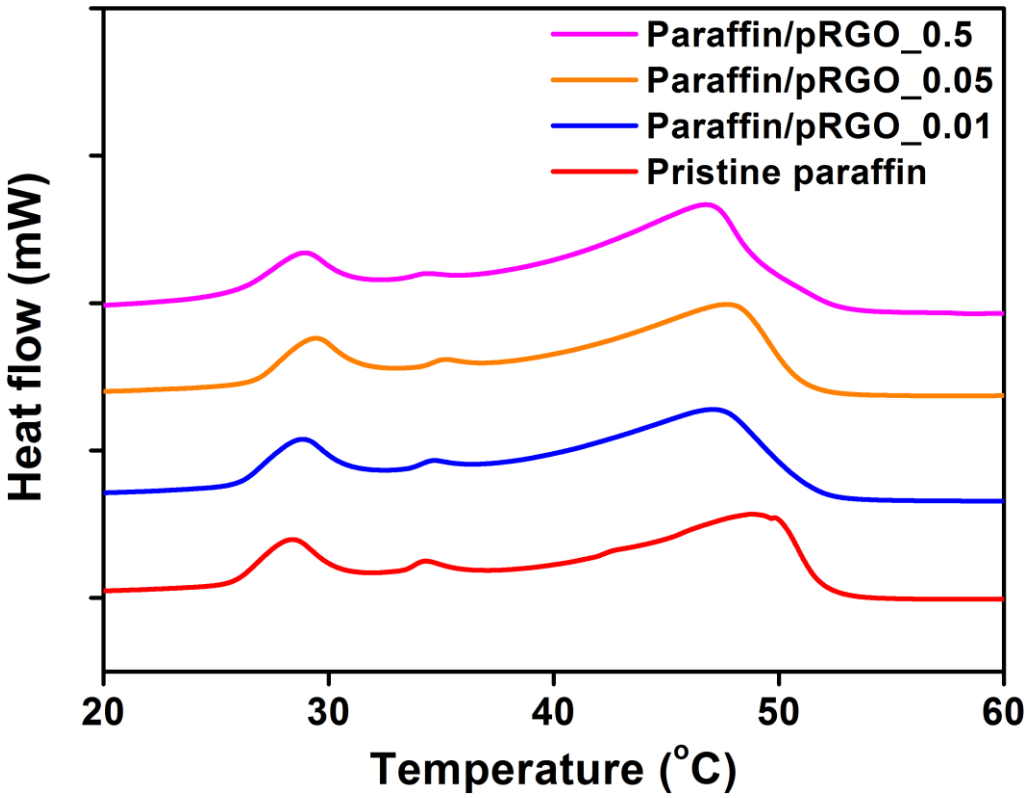

Figure 43. DSC curve of the paraffin/pRGO composites. The DSC experiments were conducted in inert N_2 flow.

Table 7. Summarized value of the DSC analysis on the paraffin/pRGO composites.

Sample	Peak melting temperature(^{o}C)	Latent heat of fusion (ΔH)
Paraffin	48.8	119.2
Paraffin/pRGO 0.01	48.5	116.0
Paraffin/pRGO 0.05	47.5	115.9
Paraffin/pRGO 0.5	46.8	115.2

The thermal barrier properties of the paraffin/pRGO composites was studied by TGA analyses to measure the maximum weight loss temperature (Figure 44). In the TGA graph, the weight loss occurring at a temperature range from 200 to 400 ℃ is due to thermal degradation of the alkyl chains of paraffin molecules, and the remaining weight fraction over 500 ℃ belongs to the pRGO monoliths.

The detailed 1st derivative thermogram of the TGA weight-loss curves of the paraffin/pRGO composites (Figure 45) presents that the value of onset decomposition temperature of the paraffin/pRGO composites increased from 216.32 ℃ of the pristine paraffin to 236.54 ℃ of the paraffin/pRGO_0.5 sample, and the maximum weight loss temperatue also increased from 289.82 ℃ to 332.45 ℃ (Summarized in Table 8). Since the pRGO monolith made from 0.01 wt % GO solution is relatively lower in density, its fraction in the paraffin/pRGO_0.01 is extremely low and therefore increase in onset decomposition temperature was relatively small, from 216.32 to 216.8 ℃. Nonetheless, the gradual increase in the onset decomposition temperature and maximum weight loss temperature indicates that the paraffin/pRGO composites acquired higher thermal stability by introducing pRGO monoliths as thermal barrier materials.

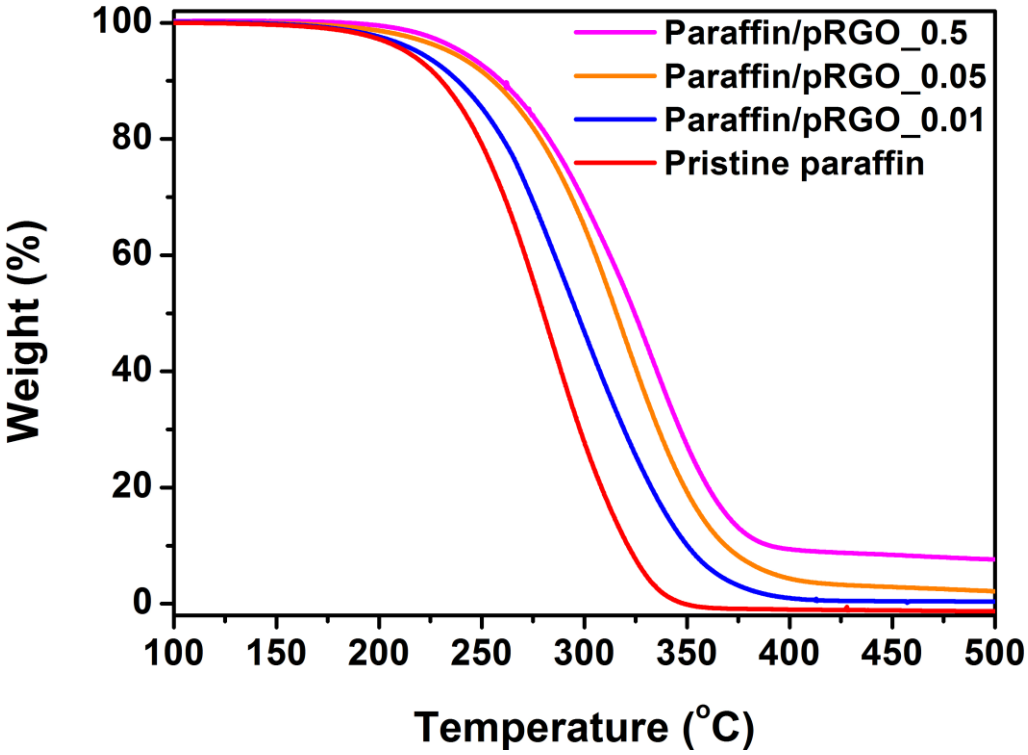

Figure 44. TGA graph of the paraffin/pRGO composites. The TGA experiments were conducted in inert N_2 atmosphere.

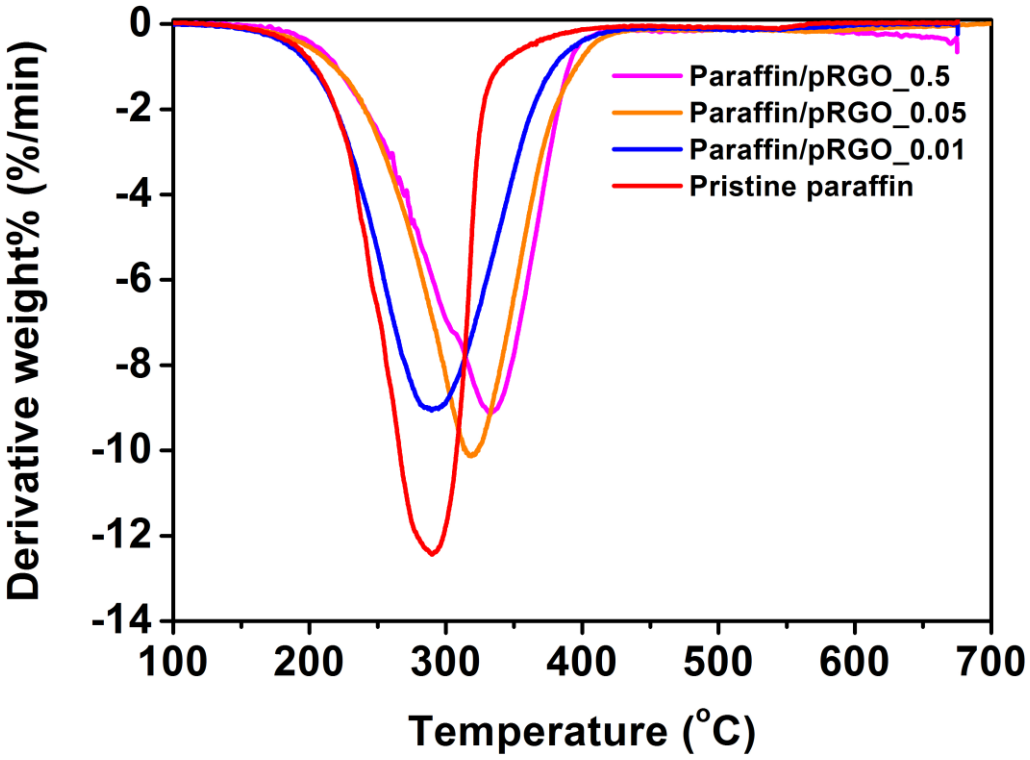

Figure 45. 1st derivative graph of the TGA curve.

Table 8. Onset decomposition temperature and maximum weight loss temperature of the paraffin/pRGO composites after TGA analyses.

Sample	Onset decomposition temperature (ºC)	Maximum weight loss temperature (ºC)
Paraffin	216.32	289.82
Paraffin/pRGO 0.01	216.8	290.31
Paraffin/pRGO 0.05	235.51	318.32
Paraffin/pRGO 0.5	236.54	332.45

3.3.3. Enhanced PCM performance of paraffin/pRGO composites

The long-term cycling stability of the paraffin/pRGO composites was carefully examined by DSC cycling for 30 solid–liquid phase-transition cycles (Figure 46). In Figure 46, the 1st DSC cycle of the paraffin/pRGO materials exhibited a protruding peak at 32 ^{o}C. As cycling test proceeded to 30 times, however, the intensity of protruding peak at 32 ^{o}C was slightly diminished and the peak positions were slightly modified. Overall, the DSC heat flow curves stabilized from 3rd cycle to 30th cycle. From the DSC curves, it can be concluded that the paraffin chain was re-organized in the cycling process and the chain stabilized after sufficient cycling. In the viewpoint of heat storage capability, only *ca.* 2 % reduction in the value of latent heat of fusion was observed for the paraffin/pRGO_0.01. The *ca.* 1 % reduction in latent heat of fusion for the paraffin/pRGO_0.05 and the paraffin/pRGO_0.5 was also found (Figure 47). This small reduction in the latent heat of fusion for the paraffin/pRGO composites can be attributed to minute loss during the DSC process owing to evaporation of PCMs [112]. Overall, this results indicate that the paraffin/pRGO composites maintain their heat storage capacity for long cycling process.

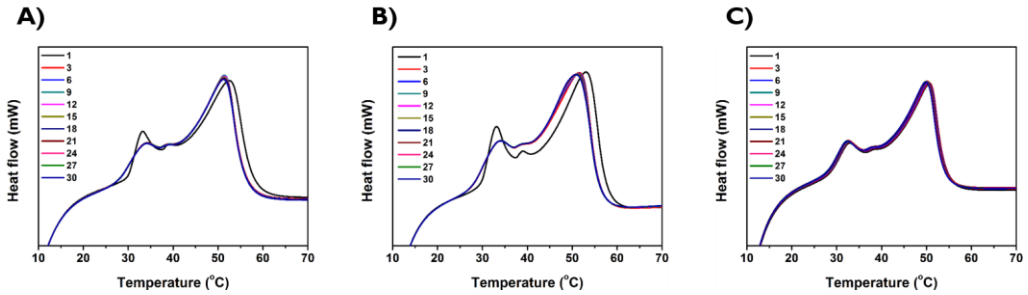

Figure 46. a) DSC curve of the paraffin/pRGO_0.01 after 30 solid–liquid phase-transition. The DSC experiments were conducted in N_2 flow; b) DSC curve of the paraffin/pRGO_0.05 after 30 solid–liquid phase-transition; c) DSC curve of the paraffin/pRGO_0.5 after 30 solid–liquid phase-transition.

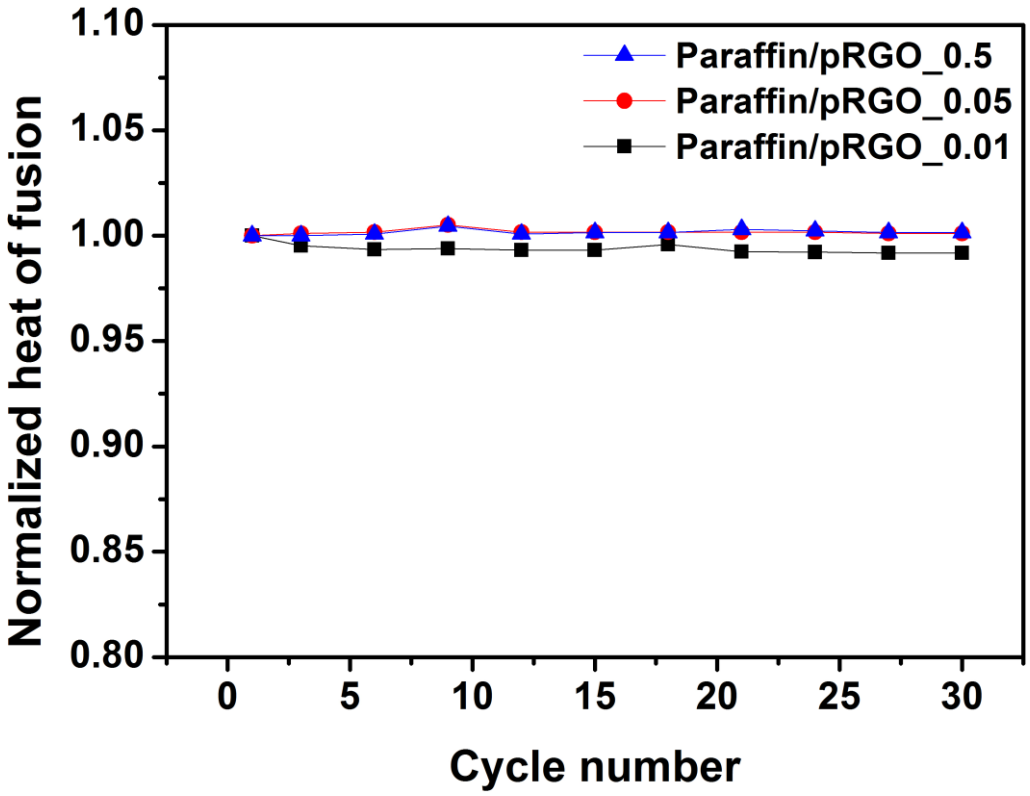

Figure 47. Normalized latent heat of fusion values of the paraffin/pRGO composites.

The enhancement in the thermal/electric conductivities of the paraffin/pRGO composites were investigated with DSC-based thermal conductivity measurement method and 4-probe method (Figure 48 and Table 9). The thermal conductivity of the pristine paraffin and the paraffin/pRGO composites was calculated by DSC-based method [92-93] (Details described in section 3.2.3). By DSC calculation, thermal conductivities of the pristine paraffin and paraffin/pRGO_0.01, paraffin/pRGO_0.05 and paraffin/pRGO_0.5 were calculated to be 0.24, 0.52, 0.68 and 0.97 W/ m•K, respectively (Table 9). In comparison with the thermal conductivity values of the pristine paraffin, the thermal conductivity measurement of the paraffin/pRGO composites exhibited *ca.* 4 times increase in thermal conductivity (Figure 48). Considering the small weight fraction of the pRGO monolith in the composites, the 4-fold increase in the thermal conductivity of the paraffin/pRGO composites might provide a promising route in enhancement in the rate of heat uptake and release in thermal energy storage process.

On account of the basic insulating properties of paraffin, the paraffin utilization in electronic devices has been quite obstructed. Nonetheless, introduction of super-conductive pRGO monolith in PCM might open a new route in the future application of pRGO-reinforced PCMs in electronic devices.

To investigate the enhancement in electric conductivity of the paraffin/pRGO compsites, the electric conductance was measured by 4-probe method. For electric conductivity measurement, all samples were cut into flat, round pellet with known thickness. From the conductivity measurement, the paraffin/pRGO composites showed increased electric conductivity values from $3.8*10^{-3}$ to $4.2*10^{-1}$ S/cm as the initial GO concentration increased from 0.01 to 0.5 wt % (Table 9). This result is due to the fact that the densely packed pRGO sheets of the pRGO monolith from highest GO concentration induced higher electric conductance. From these conductivity measurement results, the paraffin/pRGO composites present a promising route in application of RGO-reinforced paraffin PCM in various thermal/electronic application.

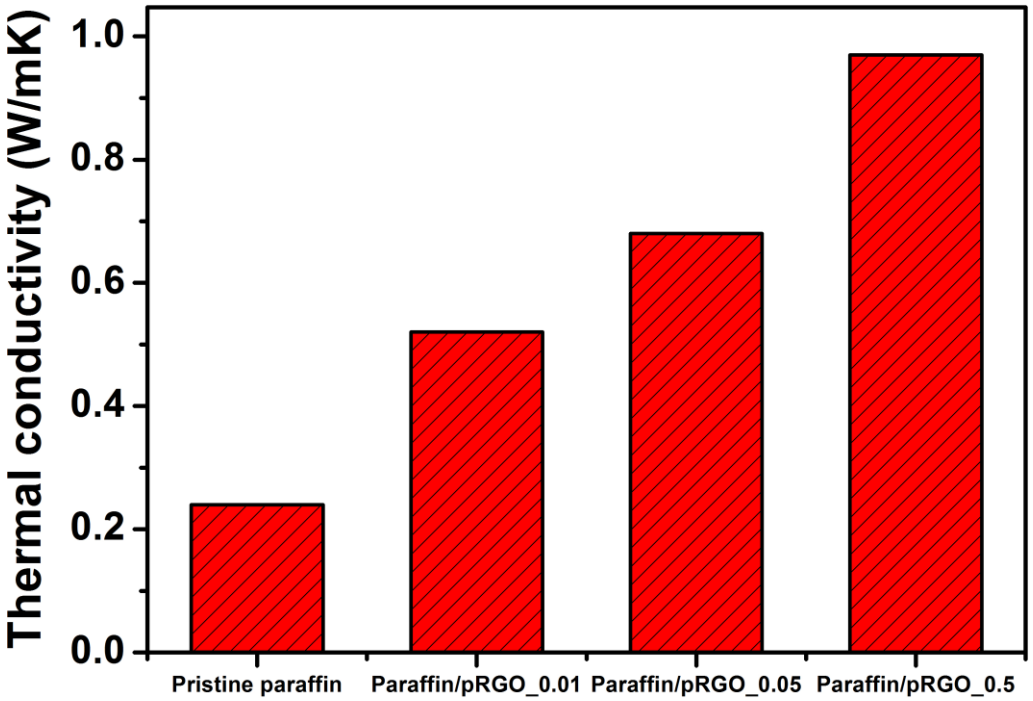

Figure 48. Comparison graph of thermal conductivity values of pristine paraffin and the paraffin/pRGO composites.

Table 9. Physical parameters of the paraffin/pRGO composites.

Sample	Thermal conductivity (W/(m·K))	Electric conductivity (S/cm)
Pristine paraffin	0.24	-
Paraffin/pRGO_0.01	0.52	$3.8*10^{-3}$
Paraffin/pRGO_0.05	0.68	$8.5*10^{-2}$
Paraffin/pRGO_0.5	0.97	$4.2*10^{-1}$

In summary, the composite materials composed of paraffin and 3D pRGO monoliths were successfully prepaerd by two-step process: 1) fabrication of pRGO monolith by mild L-AA reduction of three different GO solutions (0.01, 0.05 and 0.5 wt %) and 2) subsequent immersion of the pRGO monoliths in molten paraffin for complete soaking. These paraffin/pRGO composites were then applied as phase change material (PCM) with increased thermophysical/electric properties. Compared with conventional paraffin, the paraffin/pRGO composites exhibited greatly enhanced thermal stability and retained latent heat of fusion. The thermal stability of all composites was observed to improve with increasing primary concentration of GO solution (0.01 to 0.5 wt %) in reduction process, due to excellent barrier properties of denser graphene network from 0.5 wt % solution. Additionally, the paraffin/pRGO composites showed superb thermal/electric conductivities, showing a promising pathway for industrial and practical applications such as thermal energy storage device for solar panel and nano-electronics.

4. CONCLUSIONS

1. Free-standing, 3D expanded plasma-reduced graphene oxide (PRGO) films are synthesized using a rapid thermal exfoliation/deoxygeneation process of graphene oxide (GO) thin film *via* brief atmospheric plasma treatment. This synthetic methodology is termed as 'plasma reduction' throughout this dissertation. The 3D PRGO films are formed by brief atmospheric plasma treatment (less than 20 sec) on GO film, with sufficient argon flow. Due to sudden formation of oxygen-related gases during thermal exfoliation, the RGO sheets are expanded outward to form 3D network of physically linked RGO sheets. Systematic analyses confirmed that the 3D PRGO films can be formed without any hetero-atom incorporation and possess increased specific surface area.
2. 3D RGO monoliths are formed spontaneously during the mild reduction of GO using L-ascorbic acid (L-AA). This reduction method is referred as 'L-AA reduction' throughout this dissertation. The spontaneous production of 3D RGO monolith by L-AA reduction facilitates the conversion of 2D graphene sheets into 3D architecture. The pore size and density of the 3D RGO monoliths can be easily adjusted by manipulating the concentration of GO solution. This new methodology can illuminate a great possibility for fabricating 3D graphene network material with

controlled architecture.

3. The 3D expanded PRGO film prepared from plasma reduction is utilized as an active material for supercapacitor electrode. The increased contact area of electrolyte-electrode interface and high electric conductivity of 3D PRGO films help obtain large specific capacitance of carbon-EDLC system. By 200W plasma treatment, PRGO film possess lowest O/C ratio of 0.116 and highest surface area of 312 m^2/g. In this study, as-prepared 3D PRGO structure showed largest specific capacitance of 150 F/g at 1 A/g and maintained 82 % capacitance retention after 1000 cycles, for its high surface area and intrinsic physical/chemical stability. In comparison with the RGO film prepared with harsh hydrazine treatment, the PRGO film exhibited superior performance and the plasma reduction method illuminates a promising pathway for environmental-friendly production of supercapacitor electrode.
4. The 3D expanded PRGO films prepared by 200W atmospheric plasma treatment are utilized as supporting material for various organic phase change materials (PCMs). In this work, three representative organic PCMs, paraffin, polyethylene glycol and octanoic acid, are incorporated into the 3D PRGO film by simple immersion method. In order to enhance the intrisically low thermal/electric conductivities and shape-stability of

the organic PCMs, the 3D PRGO film act as a property-enhancer and shape-stabilizer simultaneously. The composite material of PCM and PRGO demonstrate increase in thermal/electric conductivities with retained latent heat of fusion. Thermal cyclability test confirmed that the composite materials maintain its latent heat of fusion after 30 cycles, showing its potential application in nano-electronics and energy storage devices.

5. The 3D pRGO monoliths prepared from mild reduction of GO solution using L-AA are utilized as a property-enhancer/shape-stabilizer of paraffin. Although paraffin has been used as representative PCM for its low-cost and large latent heat of fusion, the material possesses quite low thermal/electric conductivities and exhibit low shape-stability during solid-liquid transition. Therefore, the molten paraffin is impregnated into 3D pRGO monoliths by simple immersion and then solidified to produce paraffin/RGO composites. The pore size and the density of the 3D pRGO monoliths are adjusted by using different concentration of GO solution (from 0.01 to 0.5 wt %) in initial reduction process. As the concentration of GO solution increases, the density of the resultant monolith increases and the physical properties of the corresponding paraffin/pRGO composite enhanced, showing 3-fold enhancement of thermal

conductivity. Due to low fraction of pRGO monolith in the composites, the overall latent heat of fusion is retained. This simple immersion pathway provides the possible candidate for the practical applications of 3D RGO network in PCM industries.

In summary, two different methods in preparation of 3D RGO network were demonstrated as plasma reduction and L-ascorbic acid (L-AA) reduction of GO. In plasma reduction, the 3D expanded RGO film is produced from brief atmospheric argon plasma treatment on GO film due to rapid thermal exfoliation/deoxygenation process. The degree of reduction is controlled by adjusting applied plasma power on GO film. In L-AA reduction, 3D, cylindrical RGO monoliths were manufactured using mild reduction of GO with L-AA. The density and pore size of the resultant monoliths were readily controlled with change in concentration of GO solution. These new reduction pathways do not require a high temperature annealing process, and the reduction proceeds in non-toxic way. The simple process can be used as an alternative tool for the fabrication of multi-dimensional RGO structure with controlled design.

The 3D RGO networks prepared by the two methods described in this dissertation have been successfully applied in electrochemical/thermal energy storage application. The outstanding properties of these materials may be beneficial in further applications related to electrochemical energy storage and conversion, chemical/biological/pressure sensor, bio-compatible support, nano-electronic devices, and management in thermal energy storage.

REFERENCES

[1] J. H. Chen, C. Jang, S. Xiao, M. Ishigami, M. S. Fuhrer, *Nat. Nanotechnol.*, **2008**, *3*, 206.

[2] A. K. Geim, P. Kim, *Sci. Am.*, **2008**, *298*, 90.

[3] A. P. Demchenko, M. O. Dekaliuk, *Methods Appl. Fluoresc.*, **2013**, *1*, 042001.

[4] K. S. Novoselov, A. K. Geim, S. V. Morozov, D. Jiang, Y. Zhang, S. V. Dubonos, I. V. Grigorieva, A. A. Firsov, *Science*, **2004**, *306*, 666.

[5] M. I. Katsnelson, *Mater. Today*, **2007**, *10*, 20.

[6] K. S. Novoselov, V. I. Fal´ko, L. Colombo, P. R. Gellert, M. G. Schwab, K. Kim, *Nature*, **2012**, *490*, 192.

[7] P. Blake, E. W. Hill, A. H. Castro Neto, K. S. Novoselov, D. Jiang, R. Yang, T. J. Booth, A. K. Geim, *Appl. Phys. Lett.*, **2007**, *91*, 063124.

[8] D. D. L. Chung, *J. Mater. Sci.*, **1987**, *22*, 4190.

[9] X. Lu, M. Yu, H. Huang, R. Ruoff, *Nanotechnology*, **1999**, *10*, 269.

[10] Y. Zhu, S. Murali, W. Cai, X. Li, J. W. Suk, J. R. Potts, R. S. Ruoff, *Adv. Mater.*, **2010**, *22*, 3906.

[11] C. Berger, Z. M. Song, T. B. Li, X. B. Li, A. Y. Ogbazghi, R. Feng, Z. T. Dai, A. N. Marchenkov, E. H. Conrad, P. N. First, W. A. De Heer, *J. Phys. Chem. B*, **2004**, *108*, 19912.

[12] C. Berger, Z. Song, X. Li, X. Wu, N. Brown, C. Naud, D. Mayou, T. Li,

J. Hass, A. N. Marchenkov, E. H. Conrad, P. N. First, W. A. de Heer, *Science*, **2006**, *312*, 1991.

[13] W. A. de Heer, C. Berger, X. Wu, P. N. First, E. H. Conrad, X. Li, T. Li, M. Sprinkle, J. Hass, M. L. Sadowski, M. Potemski, G. Martinez, *Solid State Commun.*, **2007**, *143*, 92.

[14] J. Hass, W. A. de Heer, E. H. Conrad, *J. Phys.: Condens. Matter*, **2008**, *20*, 323202.

[15] K. V. Emtsev, A. Bostwick, K. Horn, J. Jobst, G. L. Kellogg, L. Ley, J. L. McChesney, T. Ohta, S. A. Reshanov, J. Rohrl, E. Rotenberg, A. K. Schmid, D. Waldmann, H. B. Weber, T. Seyller, *Nat. Mater.*, **2009**, *8*, 203.

[16] Z. Chen, W. Ren, L. Gao, B. Liu, S. Pei, H.-M. Cheng, *Nat. Mater.*, **2011**, *10*, 424.

[17] Y. Dedkov, A. Shikin, V. Adamchuk, S. Molodtsov, C. Laubschat, A. Bauer, G. Kaindl, *Phys. Rev. B*, **2001**, *64*, 035405.

[18] P. W. Sutter, J.-I. Flege, E. A. Sutter, *Nat. Mater.*, **2008**, *7*, 406.

[19] Y. S. Dedkov, M. Fonin, C. Laubschat, *Appl. Phys. Lett.*, **2008**, *92*, 052506.

[20] Y. Hernandez, V. Nicolosi, M. Lotya, F. M. Blighe, Z. Y. Sun, S. De, I. T. McGovern, B. Holland, M. Byrne, Y. K. Gun'ko, J. J. Boland, P.

Niraj, G. Duesberg, S. Krishnamurthy, R. Goodhue, J. Hutchison, V. Scardaci, A. C. Ferrari, J. N. Coleman, *Nat. Nanotechnol.*, **2008**, *3*, 563.

[21] W. S. Hummers Jr., R. E. Offeman, *J. Am. Chem. Soc.*, **1958**, *80*, 1339.

[22] C. Soldano, A. Mahmood, E. Dujardin, *Carbon*, **2010**, *48*, 2127.

[23] B. C. Brodie, *Phil. Trans. R. Soc. Lond.*, **1859**, *149*, 249.

[24] L. Staudenmaier, *Ber. Dtsch. Chem. Ges.*, **1898**, *31*, 1481.

[25] S. Pei, H.-M. Cheng, *Carbon*, **2012**, *50*, 3210.

[26] S. Stankovich, D. A. Dikin, R. D. Piner, K. A. Kohlhaas, A. Kleinhammes, Y. Jia, Y. Wu, S. T. Nguyen, R. S. Ruoff, *Carbon*, **2007**, *45*, 1558.

[27] V. H. Pham, T. V. Cuong, T.-D. Nguyen-Phan, H. D. Pham, E. J. Kim, S. H. Hur, E. W. Shin, S. Kim, J. S. Chung, *Chem. Commun.*, **2010**, *46*, 4375.

[28] A. Ambrosi, C. K. Chua, A. Bonanni, M. Pumera, *Chem. Mater.*, **2012**, *24*, 2292.

[29] H.-J. Shin, K. K. Kim, A. Benayad, S.-M. Yoon, H. K. Park, I.-S. Jung, M. H. Jin, H.-K. Jeong, J. M. Kim, J.-Y. Choi, Y. H. Lee, *Adv. Funct. Mater.*, **2009**, *19*, 1987.

[30] P. Cui, J. Lee, E. Hwang, H. Lee, *Chem. Commun.*, **2011**, *47*, 12370.

[31] I. K. Moon, J. Lee, R. S. Ruoff, H. Lee, *Nat. Commun.*, **2010**, *1*, 73.

[32] S. Pei, J. Zhao, J. Du, W. Ren, H.-M. Cheng, *Carbon,* **2010**, *48*, 4466.

[33] G. Wang, J. Yang, J. Park, X. Gou, B. Wang, H. Liu, J. Yao, *J. Phys. Chem. C*, **2008**, *112*, 8192.

[34] Y. Liu, Y. Li, Y. Yang, Y. Wen, M. Wang, *J. Nanosci. Nanotechnol.*, **2011**, *11*, 10082.

[35] Z.-J. Fan, W. Kai, J. Yan, T. Wei, L.-J. Zhi, J. Feng, Y.-m. Ren, L.-P. Song, F. Wei, *ACS Nano*, **2011**, *5*, 191.

[36] X. Mei, J. Ouyang, *Carbon,* **2011**, *49*, 5389.

[37] T. A. Pham, J. S. Kim, J. S. Kim, Y. T. Jeong, *Colloids Surf., A,* **2011**, *384*, 543.

[38] V. H. Pham, H. D. Pham, T. T. Dang, S. H. Hur, E. J. Kim, B. S. Kong, S. Kim, J. S. Chung, *J. Mater. Chem.*, **2012**, *22*, 10530.

[39] M. Baraket, S. G. Walton, Z. Wei, E. H. Lock, J. T. Robinson, P. Sheehan, *Carbon,* **2010**, *48*, 3382.

[40] T. N. Lambert, C. C. Luhrs, C. A. Chavez, S. Wakeland, M. T. Brumbach, T. M. Alam, *Carbon,* **2010**, *48*, 4081.

[41] S. W. Lee, C. Mattevi, M. Chhowalla, R. M. Sankaran, *J. Phys. Chem. Lett.*, **2012**, *3*, 772.

[42] J.-H. Kim, G. Liu, S. H. Kim, *J. Mater. Chem.*, **2006**, *16*, 977.

[43] M. J. Fernández-Merino, L. Guardia, J. I. Paredes, S. Villar-Rodil, P.

Solís-Fernández, A. Martínez-Alonso, J. M. D. Tascón, *J. Phys. Chem. C*, **2010**, *114*, 6426.

[44] C. K. Chua, M. Pumera, *Chem. Soc. Rev.*, **2014**, *43*, 291.

[45] W. Chen, L. Yan, *Nanoscale*, **2011**, *3*, 3132.

[46] L. Qiu, J. Z. Liu, S. L. Chang, Y. Wu, D. Li, *Nat. Commun.*, **2012**, *3*, 1241.

[47] X. Wang, L. Zhi, K. Mullen, *Nano lett.*, **2008**, *8*, 323.

[48] B. Shen, W. Zhai, W. Zheng, *Adv. Funct. Mater.*, **2014**, *24*, 4542.

[49] Y. Zhu, S. Murali, M. D. Stoller, A. Velamakanni, R. D. Piner, R. S. Ruoff, *Carbon*, **2010**, *48*, 2106.

[50] R. S. Sundaram, C. Gomez-Navarro, K. Balasubramanian, M. Burghard, K. Kern, *Adv. Mater.*, **2008**, *20*, 3050.

[51] M. Zhou, Y. Wang, Y. Zhai, J. Zhai, W. Ren, F. Wang, S. Dong, *Chem. Eur. J.*, **2009**, *15*, 6116.

[52] D. R. Dreyer, S. Park, C. W. Bielawski, R. S. Ruoff, *Chem. Soc. Rev.*, **2010**, *39*, 228.

[53] X. Cao, Z. Yin, H. Zhang, *Energy Environ. Sci.*, **2014**, *7*, 1850.

[54] H. Huang, L. Xu, Y. Tang, S. Tang, Y. Du, *Nanoscale*, **2014**, 6, 2426.

[55] Z. Xu, B. Zheng, J. Chen, C. Gao, *Chem. Mater.*, **2014**, *26*, 6811.

[56] Y. Zhou, Q. Bao, L. A. L. Tang, Y. Zhong, K. P. Loh, *Chem. Mater.*,

2009, *21*, 2950.

[57] H. Wang, J. T. Robinson, X. Li, H. Dai, *J. Am. Chem. Soc.,* **2009**, *131*, 9910.

[58] S. Dubin, S. Gilje, K. Wang, V. C. Tung, K. Cha, A. S. Hall, J. Farrar, R. Varshneya, Y. Yang, R. B. Kaner, *ACS Nano,* **2010**, *4*, 3845.

[59] J. H. Kim, W. S. Chang, D. Kim, J. R. Yang, J. T. Han, G. W. Lee, J. T. Kim, S. K. Seol, *Adv. Mater.,* **2015**, *27*, 157.

[60] C. Zhu, T. Y. Han, E. B. Duoss, A. M. Golobic, J. D. Kuntz, C. M. Spadaccini, M. A. Worsley, *Nat. Commun.*, **2015**, *6*, 6962.

[61] S. Ryu, C. Lee, J. Park, J. S. Lee, S. Kang, Y. D. Seo, J. Jang, B. S. Kim, *Angew. Chem. Int. Ed.,* **2014**, *53*, 9213.

[62] S. W. Crowder, D. Prasai, R. Rath, D. A. Balikov, H. Bae, K. I. Bolotin, H. J. Sung, *Nanoscale*, **2013**, *5*, 4171.

[63] H. Y. Yue, S. Huang, J. Chang, C. Heo, F. Yao, S. Adhikari, F. Gunes, L. C. Liu, T. H. Lee, E. S. Oh, B. Li, J. J. Zhang, T. Q. Huy, N. V. Luan, Y. H. Lee, *ACS Nano,* **2014**, *8*, 1639.

[64] C. Hou, Y. Duan, Q. Zhang, H. Wang, Y. Li, *J. Mater. Chem.,* **2012**, *22*, 14991.

[65] L. Chen, B. Wei, X. Zhang, C. Li, *Small,* **2013**, *9*, 2331.

[66] Z. Yu, L. Tetard, L. Zhai, J. Thomas, *Energy Environ. Sci.,* **2015**, *8*, 702.

[67] J. J. Yoo, K. Balakrishnan, J. Huang, V. Meunier, B. G. Sumpter, A. Srivastava, M. Conway, A. L. Reddy, J. Yu, R. Vajtai, P. M. Ajayan, *Nano lett.*, **2011**, *11*, 1423.

[68] S. Han, D. Wu, S. Li, F. Zhang, X. Feng, *Adv. Mater.*, **2014**, *26*, 849.

[69] J. Jang, J. Bae, M. Choi, *Carbon*, **2005**, *43*, 2730.

[70] M. Choi, B. Lim, J. Jang, *Macromol. Res.*, **2008**, *16*, 200.

[71] J. S. Lee, C. Lee, J. Jun, D. H. Shin, J. Jang, *J. Mater. Chem. A,* **2014**, *2*, 11922.

[72] Z. S. Wu, A. Winter, L. Chen, Y. Sun, A. Turchanin, X. Feng, K. Mullen, *Adv. Mater.*, **2012**, *24*, 5130.

[73] P. Chen, J.-J. Yang, S.-S. Li, Z. Wang, T.-Y. Xiao, Y.-H. Qian, S.-H. Yu, *Nano Energy*, **2013**, *2*, 249.

[74] B. G. Choi, M. Yang, W. H. Hong, J. Choi, Y. S. Huh, *ACS Nano*, **2012**, *6*, 4020.

[75] Y. P. Dan, Y. Lu, N. J. Kybert, Z. T. Luo, A. T. C. Johnson, *Nano Lett.*, **2009**, *9*, 1472.

[76] L. H. Tang, Y. Wang, Y. M. Li, H. B. Feng, J. Lu, J. H. Li, *Adv. Funct. Mater.*, **2009**, *19*, 2782.

[77] Y. Ohno, K. Maehashi, Y. Yamashiro, K. Matsumoto, *Nano Lett.*, **2009**, *9*, 3318.

[78] C. Sharma, S. Patil, S. Saurabh, A. Sharma and R. Venkatragavan, *Bull. Mater. Sci.*, **2009**, *32*, 239.

[79] F. Liu, Y. Piao, J. S. Choi, T. S. Seo, *Biosens. Bioelectron.*, **2013**, *50*, 387.

[80] V. Penmatsa, T. Kim, M. Beidaghi, H. Kawarada, L. Gu, Z. Wang, C. Wang, *Nanoscale*, **2012**, *4*, 3673.

[81] X. Liu, J. Cui, J. Sun, X. Zhang, *RSC Adv.*, **2014**, *4*, 22601.

[82] M. Yuan, A. Liu, M. Zhao, W. Dong, T. Zhao, J. Wang, W. Tang, *Sensor Actuat. B-Chem*, **2014**, *190*, 707.

[83] J. Kuang, L. Liu, Y. Gao, D. Zhou, Z. Chen, B. Han, Z. Zhang, *Nanoscale*, **2013**, *5*, 12171.

[84] A. Abhat, *Solar energy*, **1983**, *30*, 313.

[85] A. Sharma, V. V. Tyagi, C. R. Chen, D. Buddhi, *Renew. Sustainable Energy Rev.*, **2009**, *13*, 318.

[86] S. Raoux, W. Welnic, D. Ielmini, *Chem. Rev.*, **2010**, *110*, 240.

[87] S. M. Shalaby, M. A. Bek, A. A. El-Sebaii, *Renew. Sustainable Energy Rev.*, **2014**, *33*, 110.

[88] D. C. Hyun, N. S. Levinson, U. Jeong, Y. Xia, *Angew. Chem. Int. Ed.*, **2014**, *53*, 3780.

[89] S. Ye, Q. Zhang, D. Hu, J. Feng, *J. Mater. Chem. A*, **2015**, *3*, 4018.

[90] Y. Zhong, M. Zhou, F. Huang, T. Lin, D. Wan, *Sol. Energ. Mat. Sol. Cells*, **2013**, *113*, 195.

[91] M. Kim, C. Lee, J. Jang, *Adv. Funct. Mater.*, **2014**, *24*, 2489.

[92] J. H. Flynn, D. M. Levin, *Thermochim, Acta*, **1988**, 126, 93.

[93] C. P. Camirand, *Thermochim, Acta*, **2004**, *417*, 1.

[94] S. W. Lee, C. Mattevi, M. Chhowalla, R. M. Sankaran, *J. Phys. Chem. Lett.*, **2012**, *3*, 772.

[95] M. Cardinali, L. Valentini, P. Fabbri, J. M. Kenny, *Chem. Phys. Lett.*, **2011**, *508*, 285.

[96] Y-K. Kim, M-H. Kim, D-H. Min, *Chem. Commun.*, **2011**, *47*, 3195.

[97] D. A. Dikin, S. Stankovich, E. J. Zimney, R. D. Piner, G. H. Dommett, G. Evmenenko, S. T. Nguyen, R. S. Ruoff, *Nature*, **2007**, *448*, 457.

[98] M. Cheng, R. Yang, L. Zhang, Z. Shi, W. Yang, D. Wang, G. Xie, D. Shi, G. Zhang, *Carbon*, **2012**, *50*, 2581.

[99] C. Zhu, S. Guo, Y. Fang, S. Dong, *ACS Nano*, **2010**, *4*, 2429.

[100] M. D. Stoller, S. Park, Y. Zhu, J. An, R. S. Ruoff, *Nano Lett.*, **2008**, *8*, 3498

[101] S. D. Perera, R. G. Mariano, N. Nijem, Y. Chabal, J. P. Ferraris, K. J. Balkus Jr., *J. Power Sources*, **2012**, *215*, 1.

[102] Q. Wu, Y. X. Xu, Z. Y. Yao, A. R. Liu, G. Q. Shi, *ACS Nano*, **2010**, *4*,

1963.

[103] A. V. Murugan, T. Muraliganth, A. Manthiram, *Chem. Mater.*, **2009**, *21*, 5004.

[104] Q. Tang, J. Sun, S. Yu, G. Wang, *RSC Adv.*, **2014**, *4*, 36584.

[105] C. Wang, L. Feng, H. Yang, G. Xin, W. Li, J. Zheng, W. Tian, X. Li, *PCCP*, **2012**, *14*, 13233.

[106] M. Mehrali, S. T. Latibari, M. Mehrali, H. S. C. Metselaar, M. Silakhori, *Energ, Convers. Manage.*, **2013**, *67*, 275.

[107] D. Wu, W. Wen, S. Chen, H. Zhang, *J. Mater. Chem. A*, **2015**, *3*, 2589.

[108] Y. Konuklu, M. Unal, H. O. Paksoy, *Sol. Energ. Mat. Sol. Cells*, **2014**, *120*, 536.

[109] J.-N. Shi, M.-D. Ger, Y.-M. Liu, Y.-C. Fan, N.-T. Wen, C.-K. Lin, N.-W. Pu, *Carbon*, **2013**, *51*, 365.

[110] F. Yavari, H. R. Fard, K. Pashayi, M. A. Rafiee, A. Zamiri, Z. Yu, R. Ozisik, T. Borca-Tasciuc, N. Koratkar, *J. Phys. Chem. C*, **2011**, *115*, 8753.

[111] J. Wang, H. Xie, Z. Xin, Y. Li, C. Yin, *J. Appl. Phys.*, **2011**, *110*, 094302.

[112] H. Ji, D. P. Sellan, M. T. Pettes, X. Kong, J. Ji, L. Shi, R. S. Ruoff, *Energy Environ. Sci.*, **2014**, *7*, 1185.

국문초록

한 층의 탄소 원자로 이루어진 2차원 탄소 동소체인 그래핀은 지난 2004년의 획기적 발견 이후 전 세계적으로 집중적인 관심을 받아 왔다. 그래핀 물질은 높은 비표면적, 역학적 안정성 그리고 뛰어난 열/전기 전도도 등의 특별한 성능을 보인다. 특히, 그래핀의 높은 비표면적과 역학적 안정성으로 인해 그래핀을 3차원 구조로 제조해 다양한 방면으로 응용하는 연구가 계속 진행되었으며, 지금까지 다양한 3차원 그래핀 구조체의 제조 방법이 개발되어왔다. 하지만, 저비용, 친환경적인 그래핀의 다차원 구조체 제조는 아직 많은 연구가 필요하다.

본 논문에서는 플라즈마 환원방법 / L-아스코르브산 환원방법을 이용하여 3차원의 환원된 그래핀 옥사이드 구조체를 제조하였으며, 이들의 형성 메커니즘을 체계적으로 고찰하였고, 아울러 슈퍼캐패시터 전극과 상변화물질의 지지체로의 응용에 대해 살펴보았다.

플라즈마 환원방법으로, 먼저 흑연을 화학적 박리하여 제조한 그래핀 옥사이드를 물에 분산시킨 후 진공 여과하여 얻은 그래핀 옥사이드 필름에 상압 플라즈마를 20초 간 처리하여 3차원으로 확장된 환원된 그래핀 옥사이드 필름을 제조하였다. 더불어, 사용하는 상압 플라즈마의 출력을 조절함에 따라서 최종적인 환원된 그래핀 옥사이드의 성질 또한 조절 할 수 있었다. 상기 방법은 기존의 환원 방식에서 사용하던 높은 에너지 출력과 하이드라진과 같은 유독성 화합물을 요구하지 않을뿐더러, 기존의

플라즈마 방식에서 필수적인 고진공 조건 없이도 우수한 성능의 그래핀 물질을 신속하게 제조할 수 있다는 장점이 있다.

L-아스코르브산 환원방법으로, 그래핀 옥사이드 용액을 L-아스코르브산을 이용해 환원 시 자발적으로 3차원 환원된 그래핀 옥사이드 구조체가 형성됨을 관찰하였다. 위 방식은 기존의 환원 방식과 달리 그래핀 옥사이드 용액의 환원 과정 중에 3차원 환원된 그래핀 옥사이드 구조체의 형성이 자발적으로 일어나며, 최초의 그래핀 옥사이드 용액의 농도를 조절함에 따라 얻어지는 환원된 그래핀 옥사이드 구조체의 기공 크기와 밀도가 조절됨을 관찰하였다. 또한 L-아스코르브산과 같은 친환경 환원제의 사용으로도 기존의 화학적 환원 방식과 비견될 수준의 고품질 3차원 그래핀 구조체를 제조할 수 있다는 장점이 있다.

본 연구에서 새롭게 개발한 플라즈마 환원방법 / L-아스코르브산 환원방법은 기공 및 밀도 조절이 가능하며 비표면적이 증대된 새로운 종류의 그래핀 구조체 제조에 적용될 수 있으며, 이를 통해 슈퍼캐패시터 전극과 상변화물질를 포함한 여러가지 응용분야에 폭넓게 활용될 수 있을 것으로 사료된다.

주요어: 탄소 나노물질, 그래핀, 다차원, 플라즈마 환원, L-아스코르브산, 슈퍼캐패시터 전극, 상변화 물질

학번: 2011-22930